



TECHNISCHE
UNIVERSITÄT
WIEN

Dissertation

Quantum Cascade Interband and Intersubband Ring Lasers

ausgeführt zum Zwecke der Erlangung des
akademischen Grades eines Doktors der technischen Wissenschaften

unter der Leitung von

Univ.Prof. Mag.rer.nat. Dr.rer.nat. Gottfried Strasser
Institut für Festkörperelektronik

eingereicht an der

TECHNISCHEN UNIVERSITÄT WIEN
FAKULTÄT FÜR ELEKTROTECHNIK UND INFORMATIONSTECHNIK

von

Dipl.-Ing. Martin Holzbauer, BSc

Matr.Nr. 0625138

Wiener Straße 78

A-2860 Kirchschlag

Wien, April 2018

1. Gutachter: Prof. Dr. Joachim Wagner
2. Gutachter: Prof. Dr. Karl Unterrainer

An investment in knowledge pays the best interest.

Benjamin Franklin

Abstract

Semiconductor ring lasers are compact devices that provide single-mode light emission in the vertical direction. The absence of cleave facets, together with the low beam divergence, makes these light sources perfectly suited for on-chip array integration. The light is out-coupled with a second-order distributed feedback grating and, due to the ring cavity, a symmetric far field pattern is obtained. Ring lasers with designable emission wavelengths from the mid-infrared to the terahertz spectral region can be fabricated using quantum cascade lasers and interband cascade lasers.

The focus of this thesis is the development of new concepts for ring lasers with interband and intersubband optical transitions. Ring quantum cascade lasers have a large emitting surface, which leads to better collimated emission beams compared to facet-emitting ridge devices. An even further focused far field pattern is obtained with an on-chip meta-material lens that is fabricated into the substrate of the laser. In combination with a modified distributed-feedback grating containing integrated abrupt phase-shifts an intensity maximum is created in the center. With two continuous π -phase-shifts also a central lobed far field can be generated. Furthermore, the rotation of the measured far field patterns allow to map the position of the whispering gallery modes inside the ring lasers. A new sensing platform is developed utilizing two concentric rings, which are fabricated from a bi-functional quantum cascade laser detector material. With an applied bias voltage the ring operates as laser and in the unbiased case as detector for the same wavelength. This on-chip monolithic integration of both laser and detector allows to build compact optoelectronic systems for infrared spectroscopy. The developed system with commutable laser and detector rings are used in gas absorption measurements. For mobile applications, the energy efficiency and thermal management of quantum cascade lasers is important. Techniques to improve the heat dissipation from ring quantum cascade lasers are investigated. Subsequently, metal-covered second-order distributed feedback gratings are developed. These devices incorporate an optimized grating, which is used for mode selection and out-coupling of the light towards the substrate. The metallized gratings enable compact high-performance laser devices with improved heat dissipation capabilities. Finally, the concept of ring lasers is transferred from intersubband devices to the emerging field of interband cascade lasers. The first ring interband cascade laser with vertical light emission is presented. This laser device features much lower power consumption than quantum cascade lasers and is therefore well-suited for input power-limited mobile applications.

Kurzfassung

Ringlaser auf Halbleiterbasis sind kompakte Bauelemente, welche monomodige Lichtemission in vertikaler Richtung ermöglichen. Durch das Fehlen von gespaltenen Kristallfacetten sowie der geringen Divergenz des Strahls sind diese Lichtquellen für eine Integration auf demselben Chip perfekt geeignet. Das Licht wird durch ein verteiltes Rückkopplungsgitter zweiter Ordnung ausgekoppelt und durch die Ringgeometrie des Resonators ergibt sich ein symmetrisches Fernfeld. Ringlaser mit einstellbarer Emissionswellenlänge können für den mittleren Infrarot- bis hin zum Fern-Infrarotbereich als Quantenkaskadenlaser und Interbandkaskadenlaser hergestellt werden.

Der Schwerpunkt dieser Dissertation liegt in der Entwicklung neuer Konzepte für Ringlaser mit optischen Interband- und Intersubband-Übergängen. Ringquantenkaskadenlaser haben eine große emittierende Oberfläche, welche zu einer besseren Kollimierung der Strahlen führt, während z.B. Streifenlaser über die Kante emittieren. Mit einer Metamaterial-Linse, welche in das Substrat prozessiert wird, kann eine noch bessere Fokussierung der emittierten Strahlen erreicht werden. In Kombination mit einem Rückkopplungsgitter, welches abrupte Phasenverschiebungen beinhaltet, kann ein Intensitätsmaximum im Zentrum erzeugt werden. Mit zwei kontinuierlichen π -Phasenverschiebungen kann ebenfalls ein Intensitätsmaximum im Fernfeldzentrum erzeugt werden. Darüber hinaus kann aus der Rotation des gemessenen Fernfelds auf die Position der Flüstergalerie-Moden im Ringresonator rückgeschlossen werden. Es wurde eine neue Sensorplattform mit zwei konzentrischen Ringen entwickelt, bei der beide Ringe aus dem gleichen bi-funktionalen Laser-Detektor-Material gefertigt wurden. Wird eine elektrische Spannung angelegt, so wird der Ring als Laser betrieben, während er bei derselben Wellenlänge ohne Spannung als Detektor arbeitet. Diese monolithische Integration von Laser und Detektor erlaubt das Bauen von kompakten optoelektronischen Systemen für Infrarotspektroskopie. Das entwickelte System mit vertauschbaren Laser- und Detektorringen wurde in Gasabsorptionsmessungen verwendet. Für mobile Applikationen spielen Energieeffizienz und das thermische Management eine entscheidende Rolle. Es wurden verschiedene Möglichkeiten zur Verbesserung der Wärmeabfuhr von Ringquantenkaskadenlasern untersucht. Dies führte in weiterer Folge zur Entwicklung verteilter Rückkopplungsgitter zweiter Ordnung, welche komplett mit Metall bedeckt sind. Diese Bauelemente bestehen aus optimierten Gitterstrukturen, welche für die Modenselektion und das Auskoppeln in Richtung Substrat verwendet werden. Die metallisierten Gitterstrukturen ermöglichen das Bauen kompakter, leistungsfähiger Laser mit verbesserter Wärmeabfuhr. Abschließend wurde das Konzept der Ringlaser von den Intersubband-Bauelementen in das aufstrebende Feld der Interbandkaskadenlaser transferiert. Der erste Ringinterbandkaskadenlaser mit vertikaler Lichtemission wird präsentiert. Dieser Laser zeichnet sich im Vergleich zum Quantenkaskadenlaser durch eine viel geringere Leistungsaufnahme aus und ist deshalb bestens für mobile Anwendungen mit begrenzter Eingangsleistung geeignet.

Contents

1	Introduction	1
1.1	Infrared light sources	3
1.1.1	Black-body radiators	3
1.1.2	Diode lasers	4
1.1.3	Quantum cascade lasers	5
1.1.4	Interband cascade lasers	5
1.1.5	Other coherent light sources	6
1.2	Outline of this work	6
2	Semiconductor lasers	7
2.1	Interband and intersubband transitions	7
2.1.1	Light-matter interaction	8
2.1.2	Intersubband selection rule	10
2.2	Cascading	11
2.3	Optical waveguides and resonators	13
2.3.1	Slab waveguide	14
2.3.2	Lossy media	15
2.3.3	Effective refractive index	16
2.3.4	Vertical mode confinement	18
2.3.5	Lateral mode confinement	21
2.3.6	Longitudinal mode confinement	23
2.3.7	Fabry-Pérot cavity	23
2.3.8	Circular-shaped cavities	29
2.4	Mode selection	35
2.4.1	Short cavity	35
2.4.2	Coupled cavities	36
2.4.3	External cavity	37
2.4.4	Distributed Bragg grating	38
2.4.5	Distributed-feedback grating	42
2.5	Device characterization setups	57
2.5.1	Electrical and optical characterization	58
2.5.2	Nearfield and farfield measurements	63
2.5.3	Measurement software	65
3	Quantum cascade lasers	67
3.1	A short historical review	68
3.2	Operation Principles	69

3.3	Materials	71
3.4	Ring quantum cascade lasers	74
3.5	Light propagation and polarization	76
3.6	Beam shaping	81
	3.6.1 Abrupt grating shifts	81
	3.6.2 Continuous grating shifts	82
	3.6.3 On-chip collimation	83
3.7	Remote sensing	86
3.8	Thermal management	89
	3.8.1 Thermal model	91
	3.8.2 Boundary conditions	94
	3.8.3 Materials	96
	3.8.4 Simulation results	97
3.9	Metal-covered ring quantum cascade lasers	106
	3.9.1 Lateral regrowth	108
	3.9.2 Direct wafer bonding	111
	3.9.3 Optimized grating design	112
4	Interband cascade lasers	125
4.1	A short historical review	128
4.2	Operation principles	129
	4.2.1 Semimetallic interface	131
	4.2.2 Active region	133
	4.2.3 Hole injector	134
	4.2.4 Electron injector	135
4.3	Materials	136
4.4	Waveguides	140
	4.4.1 Plasmon-enhanced waveguide	140
	4.4.2 Dielectric-metal hybrid cladding	142
4.5	Substrate-emitting ring interband cascade lasers	143
	4.5.1 Basic considerations	144
	4.5.2 Grating design	146
	4.5.3 Fabrication	151
	4.5.4 Results	154
5	Summary and Outlook	163
A	Appendix	167
A.1	Fundamentals	167
	A.1.1 Electromagnetic fields	167
	A.1.2 Wave propagation	168
	A.1.3 Energy transport	170
	A.1.4 Polarization	170
A.2	Absorption and recombination in semiconductors	173
	A.2.1 Free carrier absorption	173
	A.2.2 Inter-valley conduction band absorption	174
	A.2.3 Inter-valence band absorption	175

A.2.4	Recombination mechanisms	175
A.3	Growth sheets	183
A.3.1	Quantum cascade laser P51	183
A.3.2	Interband cascade laser ICL3	184
A.4	Device fabrication	184
A.4.1	Ring quantum cascade laser	184
A.4.2	Ring interband cascade laser	187
Abbreviations and Acronyms		191
List of Symbols		195
References		197
Acknowledgements		219
List of Publications		221
Curriculum Vitae		227

Introduction

Many molecules have characteristic absorption lines that are located in the infrared spectral region, which starts at around 700 nm and goes to long wavelengths at 1 mm. The reason for the optical response lies in the structure of the molecules, which allows to excite specific rotational and vibrational modes. An incident light can be absorbed by the molecule if the photon energy matches the transition energy. Especially the mid-infrared, roughly defined between 3 μm and 30 μm , is highly interesting for spectroscopy. Fig. 1.1 shows the absorption lines of various gases in this "fingerprint" spectral region.

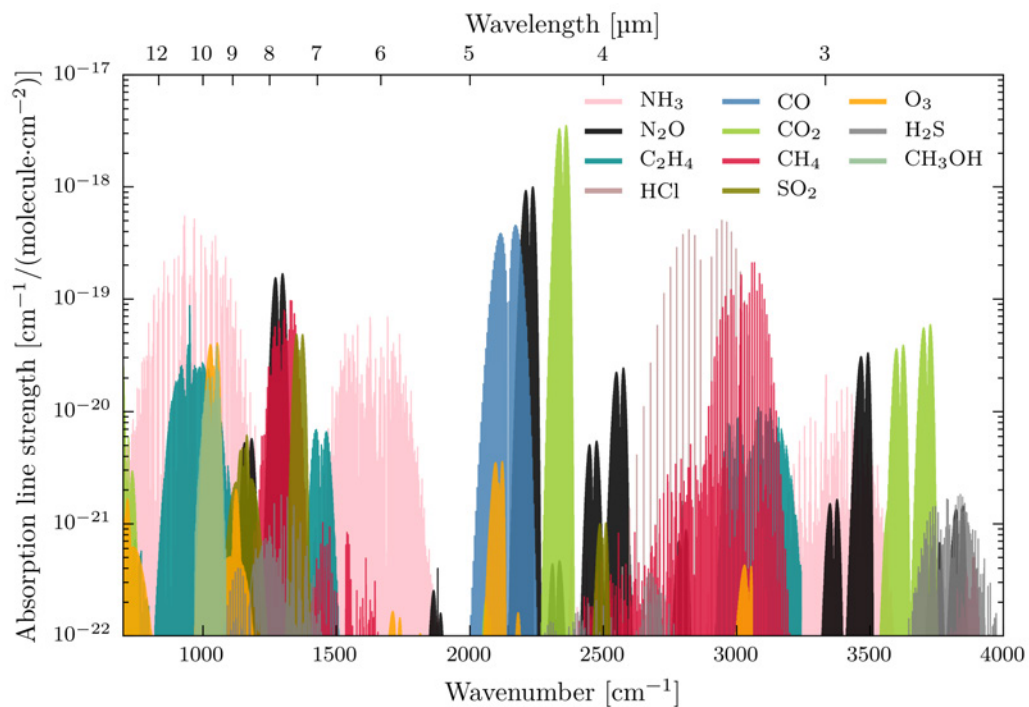


Fig. 1.1: Absorption lines of various molecules in the infrared spectral region. The source data is obtained from the HITRAN2016 database [1].

The strength of mid-infrared absorption lines can be several orders of magnitude larger than in the near-infrared region (750 nm to 3 μm), which allows to perform very sensitive measurements. As the molecules have various degrees of freedom, a rather complex frequency response is observed. However, the positions of the transition energies are well studied and documented for many substances, e.g. in the HITRAN database [1]. For the identification of a substance it can be sufficient to probe the absorbance at one specific wavelength if an interference with other analytes can be excluded. On the other hand, an extension of the measurement to more absorption lines can increase the spectral selectivity and robustness.

A major showstopper for spectroscopic measurements can be the water-vapor in the atmosphere. Fig. 1.2 shows the infrared absorption spectrum of a H_2O molecule. Water features a huge number of transition lines across the whole infrared spectral region, which would strongly attenuate the light. But there are also two atmospheric windows, roughly located between 3.3 μm – 4.7 μm and 8.5 μm – 13.8 μm , which allow free-space optical transmission or sensitive measurements of chemical substances. In order to identify and quantify molecules in low concentrations with high precision, powerful infrared light sources with designable emission wavelengths are demanded.

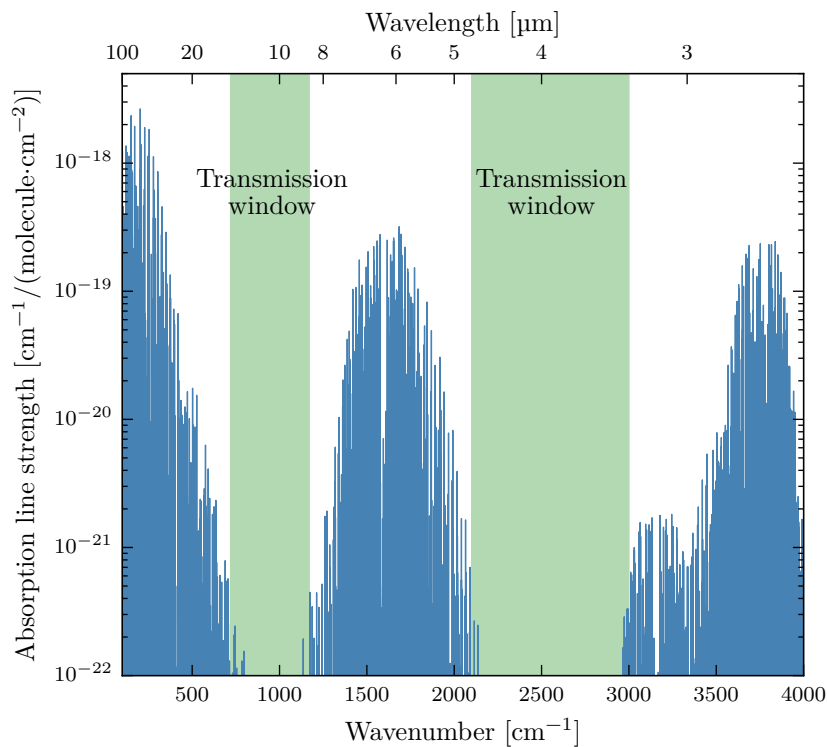


Fig. 1.2: Water strongly absorbs in the infrared spectral region. However, there are two atmospheric windows (green shaded areas), where the H_2O molecule is not active. The source data is obtained from the HITRAN database [1].

1.1 Infrared light sources

1.1.1 Black-body radiators

One of the simplest light source for generating infrared radiation is a black-body radiator. Hereby, electromagnetic radiation is emitted from an object that is heated to a certain temperature. The radiation intensity and the emission spectrum are determined by the temperature of the object. According to Planck's law, the spectral power density of a black-body radiator can be calculated by

$$B_{\lambda}(T) = \frac{2hc_0^2}{\lambda^5} \frac{1}{\exp\left(\frac{hc_0}{\lambda k_B T}\right) - 1}, \quad (1.1)$$

where h is Planck's constant, c_0 the speed of light in vacuum, λ the wavelength, k_B Boltzmann's constant and T the temperature of the object. Fig. 1.3 shows the electromagnetic radiation emitted from a black-body source, which is heated to different temperatures. The spectrum of the black-body radiator is broad-band and the emission intensity can only be adjusted with the temperature, which in turn changes the wavelength. However, this method of light generation is simple and effective. It is commonly used for the global source in Fourier-Transform infrared (FTIR) spectrometer, where a silicon-carbide rod is heated. Selective measurements at specific wavelengths can only be performed with additional filter elements or by engineering the emissivity of the object surface [2]. A more efficient way is to directly generate light at the desired emission wavelength with semiconductor lasers.

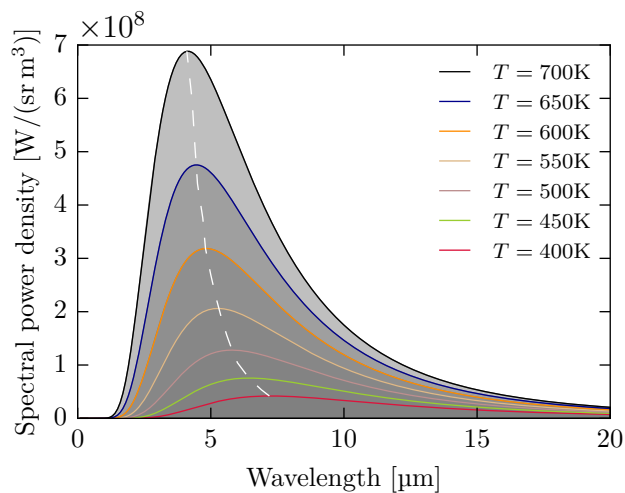


Fig. 1.3: Spectral power density of the radiation emitted from a black-body at different temperatures. The white dashed line marks the wavelength dependence of the emission peaks.

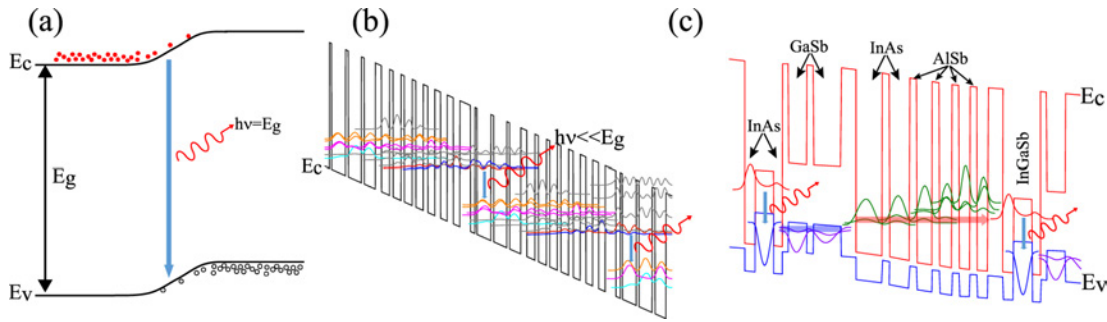


Fig. 1.4: Band diagrams for different infrared semiconductor lasers. (a) Conventional band gap diode laser, (b) quantum cascade laser (QCL) and (c) interband cascade laser (ICL). Reprinted with permission from [2].

1.1.2 Diode lasers

In conventional diode lasers, electrons in the conduction band and holes in the valence band are injected from opposite sides into an active region of a forward biased pn-junction. The term "active region" refers to the section where the light is generated via recombination of electrons and holes. Fig. 1.4(a) illustrates the band diagram with the optical transition for a diode laser. The wavelength of the emitted photon is determined by the band gap energy of the used material. Coherent light emission from GaAs pn-junctions was first observed in 1962 [3]. With liquid helium cooled InSb diode lasers, emission at $5.2\ \mu\text{m}$ has been observed at high magnetic fields [4]. A breakthrough in the field of semiconductor lasers was the invention of the so called *double heterostructure laser* by Kroemer, Alferov and Kazarinov at the Ioffe Institute of the Russian Academy of Sciences [5]. A narrow gap material is sandwiched between two wide band gap materials. This heterostructure provides good carrier confinement and also the light is confined in the active region due to the lower refractive index of the cladding material. Both properties lead to a strong reduction of the lasing threshold currents. Initial attempts with the lattice-mismatched GaAsP system allowed lasing only at liquid nitrogen temperatures. With the change to the chemical more stable AlGaAs system, lattice-matched layers could be grown that enable continuous-wave operation room-temperature operation of double heterostructure lasers [6]. Soon after, quantum well (QW) lasers have been explored. However, type-I quantum well lasers based on GaSb suffer from shallow hole confinement and increased Auger recombination at longer wavelengths. Adding more indium content to the quaternary AlInGaAsSb barriers allows to increase the valence band offset and emission up to $3.7\ \mu\text{m}$ has been demonstrated [7]. Multiple quantum wells (QWs) can be used to enhance the modal overlap, but an electron hole pair can still only emit a single photon. One of the first materials used for semiconductor light sources were II-VI and IV-VI (lead-salt or lead-chalcogenide) materials [2]. Lead-salt lasers have been the dominant semiconductor lasers from $3 - 30\ \mu\text{m}$ for about 30 years [8, 9]. Compared to narrow gap II-VI semiconductors, such as HgCdTe, lead-salt materials feature lower Auger recombination rates. However, the poor thermal properties of lead-salt lasers limit them to operation at cryogenic temperatures.

1.1.3 Quantum cascade lasers

The operation principle of quantum cascade lasers (QCLs) differs from conventional interband semiconductor lasers. Instead of using electron-hole recombinations across the band gap, the QCL relies on intersubband transitions of electrons within the conduction band. Therefore, it is also referred as an unipolar device. The first QCL was experimentally demonstrated in 1994 by Faist et al. in the group of Capasso at Bell Labs [10]. Fig. 1.4(b) shows a band diagram of a typical QCL together with the square moduli of the wavefunctions for selected eigenenergies. The electrons traverse through alternating layers of quantum wells and barriers, which have been designed to build an energy staircase. A single electron can emit multiple photons due to the cascading of many stages in series. The conduction band states in this heterostructure can be engineered by changing the thickness and composition of the material layers. With this design flexibility QCLs nowadays cover the spectral region from 3 – 25 μm up to the far-infrared (THz) region from 60 – 300 μm [11, 12]. The QCL is discussed more in detail in chapter 3.

1.1.4 Interband cascade lasers

The interband cascade laser (ICL) is a hybrid between a conventional diode laser and the quantum cascade laser. Hence, it combines conduction-to-valence band optical transitions with the cascading principle. Fig. 1.4(c) shows an ICL design with the typical "W" active region [13]. Electrons in the InAs layer recombine with holes in the Ga(In)Sb layer and traverse via interband tunneling into the next cascade. The broken gap type-II band alignment between layers of InAs and GaSb enables transition energies, which are below the band gaps of the bulk materials. Fig. 1.5 illustrates the band alignments in semiconductor heterostructures. The concept for ICLs was proposed by Yang in 1995, only one year after the first demonstration of the QCL [14]. The long upper state lifetimes allow to build laser devices with threshold current densities below 100 A/cm^2 [15]. ICLs perform best in the wavelength range of 3 – 4 μm , but also devices at 11 μm have been demonstrated [16]. The ICL is discussed more in detail in chapter 4.

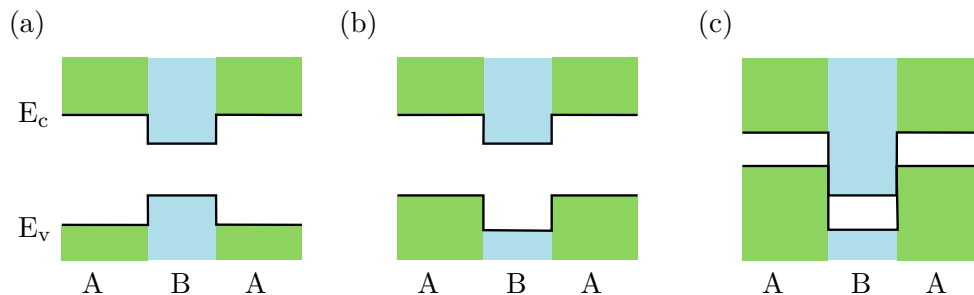


Fig. 1.5: Band alignments between conduction band edges E_c and valence band edges E_v in semiconductor heterostructures. (a) Straddling gap type-I. (b) Staggered gap type-II. (c) Broken gap type-II.

1.1.5 Other coherent light sources

Gas lasers with CO (5–6 μm) and CO₂ (9.4 μm and 10.6 μm) are very powerful, but limited to fixed wavelengths. Non-linear conversion with difference frequency generation or optical parametric amplifiers allows also to address other wavelength regions [17]. Therefore, often solid-state fiber lasers or diode lasers are used. Semiconductor lasers are technically also solid-state lasers, but their physical principles are different. Solid-state lasers can only be optically pumped since their gain medium consists of a dielectric, e.g. an erbium or neodymium doped YAG. A general overview of state-of-the-art and next-generation mid-infrared sources can be found in [2].

1.2 Outline of this work

The aim of this thesis is the development of new device concepts for quantum cascade and interband cascade lasers with ring-shaped cavities.

Chapter 2 provides the theoretical framework for infrared semiconductor lasers. Interband and intersubband transitions are discussed and the concept of cascading of multiple stages is introduced. Wave guiding as well as optical resonators are presented in a general way. Special focus is put on ring-shaped cavities and mode selection via distributed-feedback gratings. Finally, measurement setups for electrical and optical characterization of quantum cascade and interband cascade lasers are discussed.

Chapter 3 gives a general introduction into the field of quantum cascade lasers, their basic building blocks and commonly used materials. Ring quantum cascade lasers are elaborated more in detail with emphasize on light polarization and beam shaping. A compact sensing platform with two concentric rings featuring a commutable laser/detector operation is presented for gas measurements. An in-depth discussion of the thermal management together with possible bottlenecks are presented. Strategies to optimize the heat dissipation are investigated by simulation and experimentally. Finally, the design, fabrication and characterization of metal-covered ring quantum cascade lasers are presented.

Chapter 4 is dedicated to interband cascade lasers. The operation principles together with basic building blocks are discussed. The demonstration of the first substrate-emitting ring interband cascade lasers is discussed. Finally, polarization sensitive measurements of quantum cascade and interband cascade lasers are compared. These measurements reflect the different nature of optical transitions in interband and intersubband devices.

Chapter 5 summarizes the work and also gives an outlook for future research and applications.

Semiconductor lasers

In this chapter the fundamentals of semiconductor lasers are discussed, which applies to quantum cascade lasers as well as to interband cascade lasers. A laser consists of an optical gain medium, a pump source and a feedback mechanism provided by the resonator. Optical gain is achieved in semiconductor lasers with population inversion between two states. Electrons in the upper state can make a radiative transition to the lower state and transfer the energy difference to a photon. The main difference between quantum cascade laser and interband cascade laser is the nature of the optical transition.

2.1 Interband and intersubband transitions

Transitions between an occupied state in the conduction band (CB) and an empty state in the valence band (VB) are called an *interband* transitions. In contrast to that, transitions within the same band are known as *intersubband* or *intraband* transitions. The character of interband and intersubband transitions can be strongly different, as illustrated in Fig. 2.1. For interband processes, the transition energy is given by the sum of the energy of the confined states in conduction and valence band together with the bandgap energy. Since the bandgap energy is material dependent it determines a lower bound for the transition energy. On the other hand, intersubband transitions are not subjected to this bandgap limitation. There, the energy difference between initial and final state can be designed by engineering thickness and composition of the quantum well/barrier materials. This is an important property, because optical transitions and therefore also the emission wavelength of semiconductor lasers, can be changed in a wide spectral range. Considering intersubband transitions in the conduction band, then the upper bound for the transition energy is primarily determined by the conduction band offset. The gain spectrum of interband transitions, shown in Fig. 2.1(a), is broadened by the electron and hole distributions, which have opposite curvatures in the dispersion relation $E(k)$ [17]. The transition energy changes with the in-plane wavevector k_{\perp} . For intersubband transitions the in-plane dispersion has the same curvature (states within the same band), which leads to a delta-like gain spectrum that is broadened by scattering.

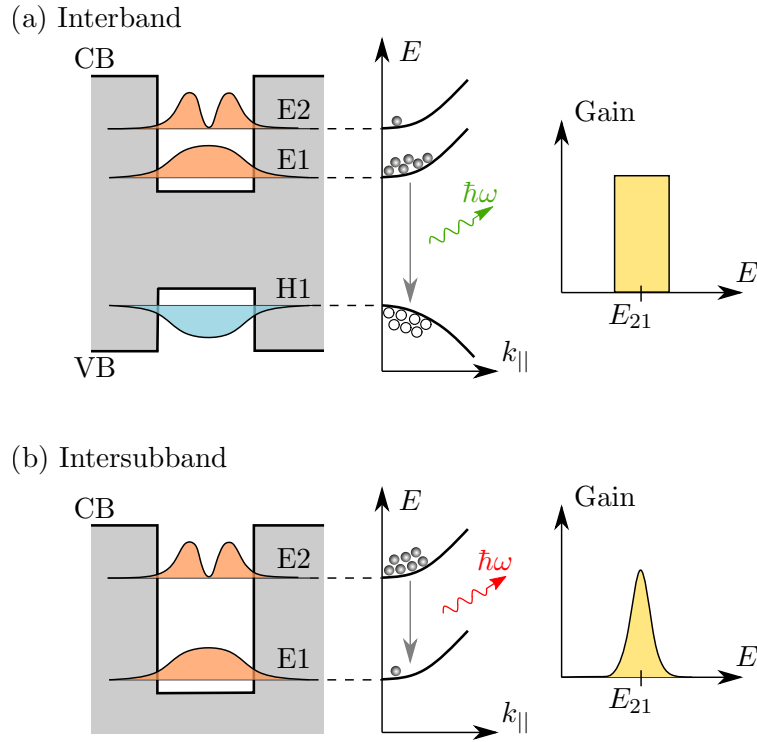


Fig. 2.1: Illustration of interband and intersubband transitions in quantum wells. (a) In the case of interband transitions an electron in the conduction band (CB) recombines with a hole in the valence band (VB). If the transition is radiative then the energy difference $E1 - H1$ is transferred to a photon. Due to the inverse curvature of the bands, the gain profile is broadened. (b) Intersubband transitions take place between confined energy states in the conduction band. The photon energy is determined by the energy difference $E2 - E1 = E_{21}$ and is typically much lower than the bandgap energy. A narrow gain peak is caused by the similar in-plane dispersion.

2.1.1 Light-matter interaction

Electronic states in the conduction and valence bands of semiconductors can be found by solving Schrödinger's equation

$$H_0\psi = E\psi, \quad (2.1)$$

$$\left[\frac{\mathbf{p}^2}{2m_0} + V(\mathbf{r}) \right] \psi = E\psi, \quad (2.2)$$

with the Hamiltonian of the crystal lattice H_0 , the wavefunction ψ and the energy E of the electron, the momentum operator \mathbf{p} , the free electron mass m_0 and the crystal potential $V(\mathbf{r})$. The wavefunctions can be expanded into the product of a plane wave and the Bloch function $u(\mathbf{k}, \mathbf{r})$ via

$$\psi = e^{j\mathbf{k}\cdot\mathbf{r}} u(\mathbf{k}, \mathbf{r}), \quad (2.3)$$

where \mathbf{k} is the wavevector of the electron and the Bloch part u resembles the same periodicity as the crystal lattice. In the envelope function approximation the wavefunction is represented as

$$\psi = F(\mathbf{r})u(\mathbf{r}), \quad (2.4)$$

with a slowly varying function $F(\mathbf{r})$ that ignores the fast changing crystal potential at each atom. The envelope function approximation allows to describe heterostructures, where different material layers are stacked on top of each other. In this approximation it is assumed that the Bloch function can be represented by the band-edge Bloch function $u(\mathbf{k}, \mathbf{r}) \approx u(\mathbf{k} = \mathbf{0}, \mathbf{r}) = u(\mathbf{r})$. An interaction of an electron with a photon is considered with the magnetic vector potential [18]

$$\mathbf{A}(\mathbf{r}, t) = \hat{\mathbf{e}} \operatorname{Re} \left[A(\mathbf{r}) e^{j\omega t} \right], \quad (2.5)$$

where the unit polarization vector $\hat{\mathbf{e}}$ points in the direction of \mathbf{A} . Hereby the photon is treated as an electromagnetic wave. For the light-matter interaction the momentum in the Schrödinger equation (2.2) is substituted by $\mathbf{p} \rightarrow (\mathbf{p} + e\mathbf{A})$. The Schrödinger equation for electron-photon interaction then reads

$$\left[\frac{\mathbf{p}^2 + 2e\mathbf{p} \cdot \mathbf{A} + (e\mathbf{A})^2}{2m_0} + V(\mathbf{r}) \right] \psi = E\psi, \quad (2.6)$$

where e is the charge of the electron. The original Hamiltonian H_0 is then expanded by a time-dependent perturbation H' and the new Hamiltonian is written as

$$H = H_0 + H', \quad (2.7)$$

$$= H_0 + \frac{e}{2m_0} [\mathbf{p} \cdot \mathbf{A} + \mathbf{A} \cdot \mathbf{p}]. \quad (2.8)$$

In this expansion the squared vector potential term has been neglected. The perturbation of the electromagnetic field induces transitions from an initial state $|i\rangle$ to the final state $|f\rangle$. The transition rate is described by Fermi's golden rule, which reads [19]

$$\hat{P}_{if} = \frac{2\pi}{\hbar} |\langle f | H' | i \rangle|^2 \delta(E_f - E_i - \hbar\omega), \quad (2.9)$$

where the transition energy $E_f - E_i$ between the two states equals the photon energy $\hbar\omega$.

On the other hand, a photon can also induce a transition $|f\rangle \rightarrow |i\rangle$, expressed with the transition rate \hat{P}_{fi} . Considering the occupation $f(E)$ of initial and final states, the energy loss of the electromagnetic wave per unit time is given by [20]

$$P = \hbar\omega \left(\hat{P}_{if}f(E_i)[1 - f(E_f)] - \hat{P}_{fi}f(E_f)[1 - f(E_i)] \right). \quad (2.10)$$

The occupation of a state is calculated with the Fermi-Dirac distribution function $f(E)$, which is defined as

$$f(E) = \frac{1}{1 + \exp[(E - \mu)/k_B T]}, \quad (2.11)$$

with the chemical potential μ , the Boltzmann constant k_B and the temperature T .

2.1.2 Intersubband selection rule

The different nature of interband and intersubband transitions can be seen by expanding the matrix element $|\langle f|H'|i\rangle|$ in (2.9). Therefore the perturbation part of the Hamiltonian is written as $H'(\mathbf{r}, t) = [H'(\mathbf{r}) \exp(j\omega t) + H'^*(\mathbf{r}) \exp(-j\omega t)]$, where the time-independent part is given by [18]

$$H'(\mathbf{r}) = \frac{e}{2m_0} A(\mathbf{r}) \hat{\mathbf{e}} \cdot \mathbf{p}. \quad (2.12)$$

Assuming that the wavelength of the electromagnetic wave is much larger than the atomic distances (dipole approximation) then the vector potential can be neglected in the matrix element. Initial and final states are expressed with envelope functions F_i and F_f in the corresponding bands with the Bloch functions u_g and u_h , respectively. The subscripts g and h label the bands. With this preparation the matrix element $|\langle f|H'|i\rangle|$ can now be written as [17]

$$\langle f|\hat{\mathbf{e}} \cdot \mathbf{p}|i\rangle = \langle F_i u_g|\hat{\mathbf{e}} \cdot \mathbf{p}|F_f u_h\rangle \quad (2.13)$$

$$= \langle F_i|\hat{\mathbf{e}} \cdot \mathbf{p}|F_f\rangle \langle u_g|u_h\rangle + \langle F_i|F_f\rangle \langle u_g|\hat{\mathbf{e}} \cdot \mathbf{p}|u_h\rangle \quad (2.14)$$

$$= \underbrace{\langle F_i|\hat{\mathbf{e}} \cdot \mathbf{p}|F_f\rangle}_{\text{Intersubband}} \delta_{gh} + \underbrace{\langle F_i|F_f\rangle \langle u_g|\hat{\mathbf{e}} \cdot \mathbf{p}|u_h\rangle}_{\text{Interband}} \quad (2.15)$$

The first term is non-zero only for transitions within the same band ($g = h$), which corresponds to intersubband transitions. On the other hand the second term is non-zero only if the transition occurs between different bands ($g \neq h$) and both subband indices have to match. This case corresponds to interband transitions. By including the polarization of the electromagnetic wave in the derivation it can be shown that intersubband transitions

only couple to light that is polarized in growth direction perpendicular to the semiconductor layers [17]. Electric field components parallel to the layer plane create a vanishing matrix element. The validity of this *intersubband selection rule* has been investigated in an experimental study by H.C. Liu et al. [21], The prediction, that intersubband transitions are only sensitive to transverse magnetic (TM) polarized light, was confirmed in absorption measurements with GaAs based quantum well infrared photodetectors. The photoresponse to transverse electric (TE) polarized light was less than 3% compared to TM absorption.

2.2 Cascading

Semiconductor quantum well lasers are well known to provide a good carrier confinement in the active region where the light is generated. However, there are several reasons to replace a single QW with a heterostructure consisting of multiple quantum wells. The gain of a single stage may not be enough to overcome all the losses caused by the waveguide and the mirrors. If these total losses are not compensated, the lasing threshold cannot be reached. Furthermore, the overlap of the waveguide mode with the active quantum well in a (narrow) single QW may not be sufficient. This issue becomes worse for devices emitting at longer wavelengths as the width of the waveguide mode extends even more, hence reducing the overlap further [22]. In principle, there are two options for assembling multiple QWs: Either connect the individual light-emitting units in parallel or in series. Both principles (non-cascaded and cascaded) are illustrated in Fig. 2.2. In order to point out the differences, a comparison in terms of currents, voltages and dissipated powers at the lasing threshold is given.

For the case of a parallel connection, the QWs are put next to each other and share the same upper and lower laser levels, as shown in Fig. 2.2(a). This arrangement is used in conventional diode lasers, where electrons/holes are injected into the conduction/valence band from opposite sides of the device. Ideally, all QWs are populated equally, thus the transit time of the carriers has to be faster than the electron-hole recombination rate due to radiative and/or non-radiative processes. Every of the N stages contributes a fraction $J_{\text{th},n} = J_{\text{th}}/N$ to the total threshold current density J_{th} , where $n = 1$ to N denotes the index of the QW. Since the stages are connected in parallel, the voltage drop across this configuration equals the voltage of a single QW. This threshold voltage V_{th} is determined by the photon energy $\hbar\omega$ and an additional small margin ΔE , which accounts for the losses that also need to be compensated [22]. Thus, the laser threshold voltage is given by

$$V_{\text{th,parallel}} = \frac{\hbar\omega + \Delta E}{q}, \quad (2.16)$$

where q is the electron charge. The voltage drop increases for shorter emission wavelengths λ because $\hbar\omega = hc/\lambda$, where h denotes Planck's constant and c the speed of light. In real devices also a resistance R_s , which is in series with the multiple QWs, has to be included. This resistance ($R_s = R_e + R_h$) accounts for all the losses from electrical contacts, cladding layers, connecting layers, and so on [22]. The dissipated threshold power density for a

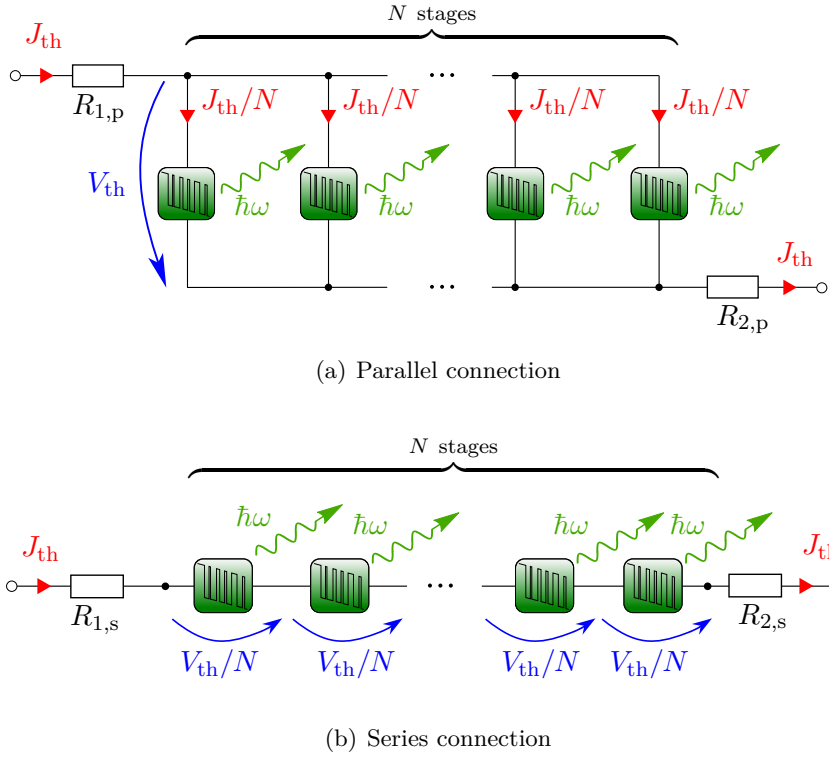


Fig. 2.2: Illustrations of the equivalent circuits for lasers consisting of multiple QWs. The parallel connection (a) is commonly used for conventional pn-junction diode lasers, where electrons are injected into the left contact and holes from the right hand side. A series connection (b) of light emitting stages is used in QCLs or ICLs.

parallel connection of QWs then reads as

$$P_{\text{th,parallel}} = (V_{\text{th}} + V_{\text{resistance}})J_{\text{th}} \quad (2.17)$$

$$= \left[\frac{(\hbar\omega + \Delta E)}{q} + R_s N J_{\text{th,n}} \right] N J_{\text{th,n}}, \quad (2.18)$$

where $J_{\text{th}} = N J_{\text{th,n}}$ is the total threshold current density of the carrier flowing from the left to the right contact.

In the case of a series connection, the injected carrier passes all QWs, as shown in Fig. 2.2(b). The threshold current density is the same in every stage, e.g. $J_{\text{th}} = J_{\text{th,n}}$. Such configuration is utilized in interband and intersubband cascade lasers, where carriers are extracted from a QW and injected into a higher energy level of the next QW. The total voltage drop across the device is determined by the sum of all stages and therefore given by

	Current density J_{th}	Voltage V_{th}	Power density P_{th}
parallel (non-cascaded)	$NJ_{\text{th},n}$	$\frac{\hbar\omega + \Delta E}{q}$	$\frac{(\hbar\omega + \Delta E)NJ_{\text{th},n}}{q} + N^2J_{\text{th},n}^2R_s$
series (cascaded)	$J_{\text{th},n}$	$N\frac{\hbar\omega + \Delta E}{q}$	$\frac{(\hbar\omega + \Delta E)NJ_{\text{th},n}}{q} + J_{\text{th},n}^2R_s$

Tab. 2.1: Summary of the derived formulas at lasing threshold for non-cascaded and cascaded arrangements of multiple QWs.

$$V_{\text{th,series}} = N\frac{\hbar\omega + \Delta E}{q} = NV_{\text{th,parallel}}. \quad (2.19)$$

A reduction in threshold current is achieved at the expense of an increased threshold voltage [23]. The total dissipated threshold power density, including a series resistance $R_s = R_{1,p} + R_{2,p} \approx R_{1,s} + R_{2,s}$, is written as

$$P_{\text{th,series}} = \left[\frac{N(\hbar\omega + \Delta E)}{q} + R_s J_{\text{th},n} \right] J_{\text{th},n}. \quad (2.20)$$

A summary of the derived formulas for cascading and non-cascading arrangements are presented in Tab. 2.1. First of all, both schemes are equivalent in terms of dissipated threshold power density P_{th} if the number of cascades $N = 1$ or the series resistance $R_s = 0$. Assuming a more realistic device with $N > 1$ and a finite series resistance, then only the second term in P_{th} is essential. In that case, a series connection of multiple QWs is more efficient because $P_{\text{th,parallel}} > P_{\text{th,series}}$. Or in other words, a non-cascaded arrangement causes more heating because more power is wasted on the series resistance R_s [24]. This statement becomes even stronger for longer emission wavelengths, where the photon energy $\hbar\omega$ decreases and the threshold current density as well as the number of cascades usually increase. The first term ($\propto NJ_{\text{th},n}$) becomes less important compared to the second term ($\propto N^2J_{\text{th},n}^2$) and cascading is the preferable connection for multiple QWs. Furthermore, a parallel arrangement relies on an uniform distribution of the injected carriers over all QWs. This requirement is harder to fulfill for devices emitting at longer wavelengths, where more stages are needed and the transport via diffusion is limited [24]. A more efficient and smoother carrier transport is achieved with resonant tunneling, which is utilized in cascaded heterostructures like the quantum cascade laser or the interband cascade laser.

2.3 Optical waveguides and resonators

The basic ingredients for a laser are stimulated photon emission in a gain medium together with a feedback mechanism. While the former is determined by the incorporated semiconductor materials and the quantum design, the latter can be implemented with

a resonator. The simplest realization of such a feedback mechanism is obtained with a Fabry-Pérot cavity, where the gain medium is sandwiched between two mirrors. To enable light out-coupling, at least one of the mirrors needs to be semitransparent. The resonator lengths for e.g. quantum cascade lasers are typically in the order of $\sim 1 - 5$ mm. Therefore, it is essential to guide the light, which is generated in the gain medium, along the resonator. Otherwise, the electromagnetic field spreads with propagation distance and hence reduces the spatial overlap with the gain medium. A possible solution is to use e.g. a dielectric waveguide, where the light is confined to a core layer due to a variation of the refractive index. In the following, the planar slab waveguide is introduced and different types of cavities are discussed. An introduction into the fundamentals of electromagnetic waves and their properties is given in the appendix A.1.

2.3.1 Slab waveguide

The mode confinement in a slab waveguide is achieved by surrounding the guiding layer (refractive index n_g) with materials of lower refractive indices ($n_c, n_s < n_g$). An illustration of such a material stack is shown in Fig. 2.3.

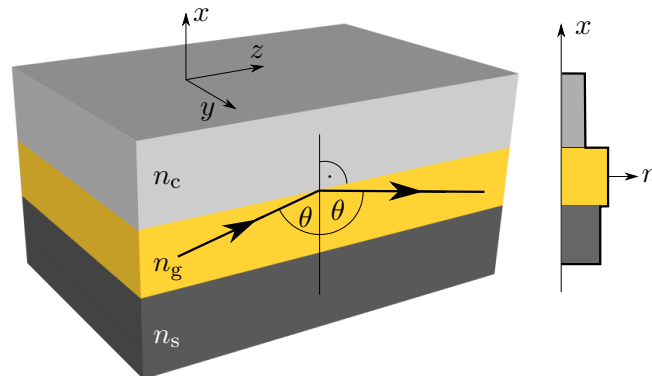


Fig. 2.3: Slab waveguide: The light is guided due to reflections at the interface between dielectric materials with high and low refractive indices. The light guiding layer is sandwiched between a cladding on top and the substrate layer at the bottom. The refractive indices of the cladding n_c and the substrate layer n_s need to be lower than n_g . A wave propagating in z -direction is then confined in the vertical dimension (x -direction) due to total internal reflection. Based on [25]

The electromagnetic wave experiences total internal reflection at the boundaries between the guiding and cladding/substrate layers. This results in confinement in vertical direction (along the x -axis). A condition for total internal reflection can be expressed by starting with the plane wave ansatz for the incident, reflected and transmitted (i, r, t) waves at the interface between the guiding and the cladding layer. With the projection of the wavevector \mathbf{k}_{\parallel} onto the interface, the plane waves are given by

$$\mathbf{E}^{i,r,t} = \mathbf{E}_0^{i,r,t} e^{j(\mathbf{k}_{\parallel}^{i,r,t} \cdot \mathbf{r} - \omega t)}, \quad (2.21)$$

where $\mathbf{E}_0^{i,r,t}$ is an amplitude function. Since the interface is translation invariant [25], the phases of the three waves have to match, which translates to $\mathbf{k}_{\parallel}^i = \mathbf{k}_{\parallel}^r = \mathbf{k}_{\parallel}^t$. Furthermore, each wavevector has to fulfill the dispersion relation in the corresponding medium, given by $|\mathbf{k}^{i,r,t}| = n^{i,r,t}\omega/c_0$. The tangential components of the wavevector can also be expressed with the angle θ , which is the angle between wavevector and normal vector of the interface, as illustrated in Fig. 2.3. Then the phase matching condition can be written as

$$n^i \frac{\omega}{c_0} \sin \theta_i = n^r \frac{\omega}{c_0} \sin \theta_r = n^t \frac{\omega}{c_0} \sin \theta_t. \quad (2.22)$$

With the refractive indices for the slab waveguide $n^i = n^r = n_g$ and $n^t = n_{c,s}$, equation (2.22) becomes

$$n_g \frac{\omega}{c_0} \sin \theta_i = n_{c,s} \frac{\omega}{c_0} \sin \theta_t, \quad (2.23)$$

which is also known as Snell's law. For total internal reflection, the angle of the transmitted beam is $\theta_t = 90^\circ$. In other words, the wavevector of the incident beam has to be larger than the wavevector of the beam in the cladding/substrate, which corresponds to the condition $n_g > n_c$. The critical angle for total internal reflection is given by the ratio of the refractive indices

$$\theta_{\text{crit}} := \theta_i = \arcsin \left(\frac{n_{c,s}}{n_g} \right). \quad (2.24)$$

For waves impinging under an angle greater than θ_{crit} to the surface normal, a guided propagation in z direction is possible. The slab waveguide thus provides light confinement in vertical direction, which in Fig. 2.3 is along the x -axis. However, not every incident optical wave leads to a stable waveguide mode. In a geometrical picture the wave has to merge with itself again after being reflected twice (e.g. at the interface guiding/cladding and guiding/substrate layer). Only if this self-consistency condition is fulfilled, a waveguide mode is established. It can be seen as the superposition of two plane waves. This eigenmode is characterized by a fixed transverse field distribution and polarization, which remains invariant for a propagation along the z -direction [26].

2.3.2 Lossy media

In general, the refractive index of a material is a complex-valued quantity, i.e. $\tilde{n} = n + j\kappa$. The imaginary part, also known as extinction coefficient, relates to the absorption losses introduced by the material. The wavelength-dependent optical response can be described with the Lorentz-Drude model. There, the motion of an electron is modelled with a damped harmonic oscillator. The permittivity is given by the relationship

$$\epsilon(\omega) = \epsilon_\infty \left(1 - \frac{\omega_p^2}{\omega^2 + j\omega/\tau} \right), \quad (2.25)$$

where $\omega = 2\pi c/\lambda$ and $\tau = \frac{\mu m^*}{e}$ is the electron scattering time and ϵ_∞ the high-frequency dielectric constant. The plasma frequency

$$\omega_p = \sqrt{\frac{Ne^2}{\epsilon_0 \epsilon_\infty m^*}} \quad (2.26)$$

is calculated for a material with an effective electron mass m^* and doping concentration N . The mobility μ can be expressed with the empirical Caughey-Thomas equation [27]

$$\mu = \frac{\mu_{\max} - \mu_{\min}}{1 + (N/N_{\text{ref}})^\alpha} + \mu_{\min}, \quad (2.27)$$

with the fitting parameters μ_{\min} (high doped material) and μ_{\max} (low- or undoped) in units of $[\text{cm}^2/\text{Vs}]$. N_{ref} is the doping concentration at which $\mu = (\mu_{\max} + \mu_{\min})/2$ and the exponent α is also a fitting parameter. This model takes lattice and impurity scattering into account. The relaxation time τ can also be calculated using the Hilsum formula [28], which provides an empirical expression for the doping-dependent mobility

$$\mu = \frac{\mu_0}{1 + \sqrt{N/N_0}}, \quad (2.28)$$

where μ_0 and N_0 are fitting parameters that can be obtained from e.g. Hall measurements. The material parameters used for the simulations in this thesis are calculated with the Lorentz-Drude model. Actual values and model parameters are given in the sections 3.9 and 4.5 together with the corresponding waveguide and grating simulations.

2.3.3 Effective refractive index

For a plane wave propagating in z -direction the following ansatz is used

$$\mathbf{E}(\mathbf{r}, t) = \mathbf{E}(x, y, z, t) = \mathbf{E}_0(x, y) e^{j\omega t} e^{-j\beta z}, \quad (2.29)$$

with the propagation constant $\beta = n_g(\omega/c_0) \sin \theta_i = nk_0 \sin \theta_i$ and the amplitude function $\mathbf{E}_0(x, y)$, which remains constant along the propagation direction and only varies in the perpendicular x - y plane. The spatial (second-order) derivative is then given by

$$\vec{\nabla}^2 \mathbf{E}(\mathbf{r}, t) = [\vec{\nabla}^2 \mathbf{E}_0(x, y) - \beta^2 \mathbf{E}_0(x, y)] e^{j\omega t} e^{-j\beta z}. \quad (2.30)$$

Using this relation, the Helmholtz equation $[\vec{\nabla}^2 + \mu\epsilon\omega^2]\mathbf{E}(\mathbf{r}, t) = 0$ then becomes

$$\vec{\nabla}^2 \mathbf{E}_0(x, y) + (\mu\epsilon\omega^2 - \beta^2) \mathbf{E}_0(x, y) = 0. \quad (2.31)$$

With the relation $\sqrt{\mu\epsilon} = \sqrt{\mu_0\epsilon_0}\sqrt{\mu_r\epsilon_r} = (1/c_0)n$, the second term can be rewritten to $\mu\epsilon\omega^2 - \beta^2 = (n/c_0)^2\omega^2 - \beta^2 = n^2k_0^2 - \beta^2$ and hence (2.31) is equivalent to

$$\vec{\nabla}^2 \mathbf{E}_0(x, y) + (n^2k_0^2 - \beta^2) \mathbf{E}_0(x, y) = 0. \quad (2.32)$$

Solutions of this equation are characterized by the mode order m , which corresponds to a complex propagation constant $\beta^{(m)}$ with an angle of incidence $\theta_i^{(m)}$. Each waveguide mode has a phase velocity $v_{\text{phase}}^{(m)} = \omega/\beta^{(m)}$ that is given by [25]

$$v_{\text{phase}}^{(m)} = \frac{\omega}{\beta^{(m)}} = \frac{\omega}{n_g k_0 \sin \theta_i^{(m)}} = \frac{c_0}{n_{\text{eff}}^{(m)}}, \quad (2.33)$$

where the relation $c_0 = \omega/k_0$ for the phase velocity in free-space is used. The effective refractive index $n_{\text{eff}}^{(m)}$, also known as modal effective index, links the waveguide propagation constant β with the free-space propagation constant k_0 . It depends on the mode order and is explicitly defined as

$$n_{\text{eff}}^{(m)} = n_g \sin \theta_i^{(m)} = \frac{\beta^{(m)}}{k_0}. \quad (2.34)$$

The value of the effective refractive index commonly lies between the refractive index of the core layer and the cladding material, i.e. $n_{c,s} < n_{\text{eff}} < n_g$. However, n_{eff} is not simply an averaged refractive index between the core and cladding material weighted by the mode intensity overlaps. It is related to the phase change and in general a complex-valued quantity $\tilde{n}_{\text{eff}} = n + j\kappa$, caused by the complex refractive indices of the waveguide layers. The waveguide loss (intensity loss) for a particular mode in the waveguide is given by

$$\alpha_{\text{wg}} = -2 \text{Im}\{\beta\} = -2k_0 \text{Im}\{\tilde{n}_{\text{eff}}\} = -\frac{4\pi}{\lambda_0} \text{Im}\{\tilde{n}_{\text{eff}}\}, \quad (2.35)$$

where λ_0 is the wavelength of the electromagnetic wave in free space. The concept of the effective refractive index is very useful for the computation of multilayer systems, such as the example illustrated in Fig. 2.4. There, the refractive index of a material stack, e.g. the active region, is represented by \tilde{n}_{eff} . Instead of considering a larger number of layers for the computation, it is sufficient to calculate/estimate the effective refractive index for the whole layer sequence once and then use this value for representing the multilayer system in other simulations. With this approach it is easier to calculate the mode profile also in "large" waveguides without considering all the thin layers. Once the effective refractive index of the layer stack is known, the electromagnetic field distribution in e.g. the laser can be simulated with a coarser mesh grid. The grid size for optical simulations is typically

around $(1/10)\lambda_0/n$ and finer, where n is the refractive index of the material. Hence, at least more than 10 grid points per material wavelength should be considered to get accurate results. Adaptive mesh grid refinements can be used in the regions of interest, e.g. corners or material interfaces. The effective refractive index method is also applied to the simulations of different waveguides presented in the following.

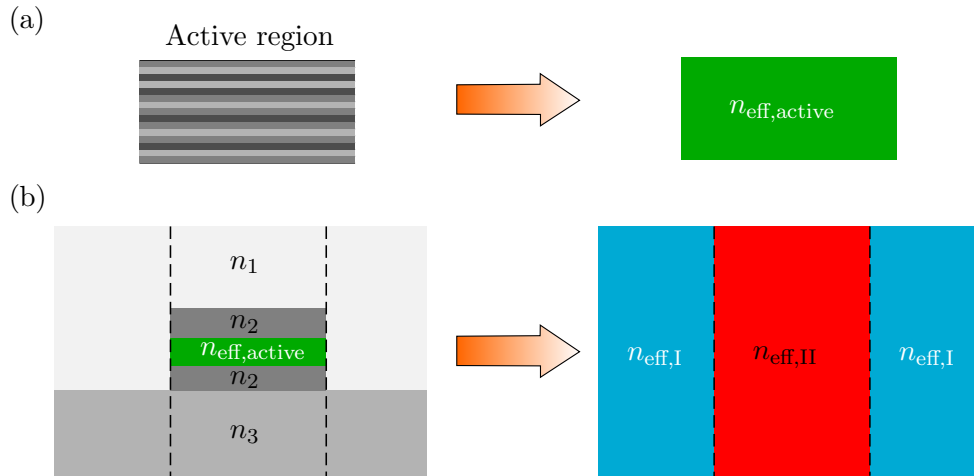


Fig. 2.4: Application of the effective refractive index method to a semiconductor laser. (a) The multiple layers of the active region are represented by a homogeneous material with the effective refractive index $n_{\text{eff,active}}$. This parameter is then used for the calculation of a more complex arrangement as shown in (b). The model for the semiconductor laser consists of several material regions and refractive indices. For the calculation of the mode profile, the semiconductor laser is separated into different simulation domains, indicated by the vertical dashed lines. The horizontal mode profile can now easily be calculated, considering the effective refractive indices of the regions.

2.3.4 Vertical mode confinement

A confinement of the optical mode in vertical direction (growth direction) is achieved in the slab waveguide by surrounding the light guiding core layer with materials that have lower refractive indices. There, the waveguide consists of dielectric materials only. In addition, laser waveguides can also be composed of other materials, such as e.g. metals or highly-doped metal-like semiconductors [29]. Three common waveguide configurations, such as the pure dielectric, the metal-dielectric and the double-metal waveguide, are discussed in the following. Fig. 2.5 shows an illustration of a semiconductor ridge laser with confinement in vertical, lateral and longitudinal direction. The mode confinements in the other two directions are discussed in the subsequent sections.

Pure dielectric waveguide

Simulations of the electric field distributions in a pure dielectric waveguide are shown in Fig. 2.6(a). The solutions of the Helmholtz equation, derived in the appendix (A.17), are grouped into TM and TE polarized waveguide modes. Due to the continuity condition

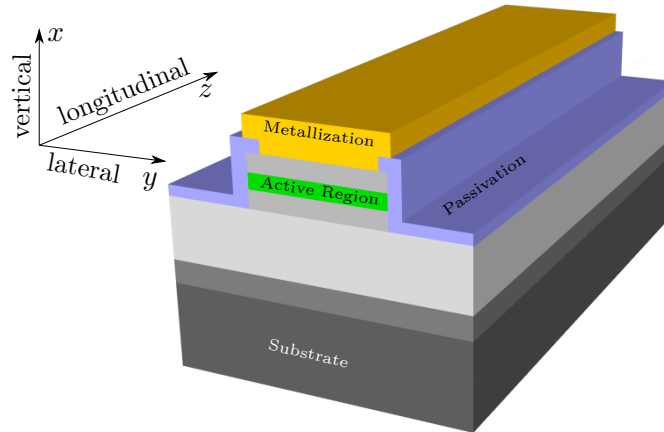


Fig. 2.5: Illustration of a ridge waveguide together with the naming convention for the vertical, lateral and longitudinal direction.

of the normal component of the displacement field $\mathbf{D} = \epsilon\mathbf{E}$ at the interface, the electric field in the material with the lower refractive index (cladding or substrate) has to be discontinuous (see (A.8) in the appendix). As a result, the electric field in vertical direction has a higher value in the cladding/substrate for TM modes, which leads to the jump in the field distributions. As can be seen, the light substantially penetrates into the cladding and substrate layer. In a real laser device the guiding layer corresponds to the gain medium (active region), where light amplification takes place. The overlap of the mode with the active region is an important quantity for the waveguide design and it is expressed as confinement factor

$$\Gamma = \frac{\int_{\text{active}} |E(x, y)|^2 dx dy}{\int_{-\infty}^{\infty} \int_{-\infty}^{\infty} |E(x, y)|^2 dx dy}, \quad (2.36)$$

which becomes smaller as the mode penetrates more in the surrounding materials. One goal of the waveguide design is to maximize the overlap with the active region to generate as many photons as possible via the process of stimulated emission. Besides the pure dielectric waveguides, also dielectric-metal or double metal waveguides are used for infrared laser sources. A comparison of different waveguides is shown in Fig. 2.6.

Metal-dielectric waveguide

The dielectric-metal waveguide, shown in Fig. 2.6(b), still has a dielectric substrate, but the cladding layer is replaced by a metal. Due to the refractive index contrast, an interface plasmon mode is created and therefore it is also called a single-plasmon waveguide. The interface plasmon is a guided TM mode at the interface between materials with opposite signs of the dielectric constant. Although the metal layer may introduce losses at first

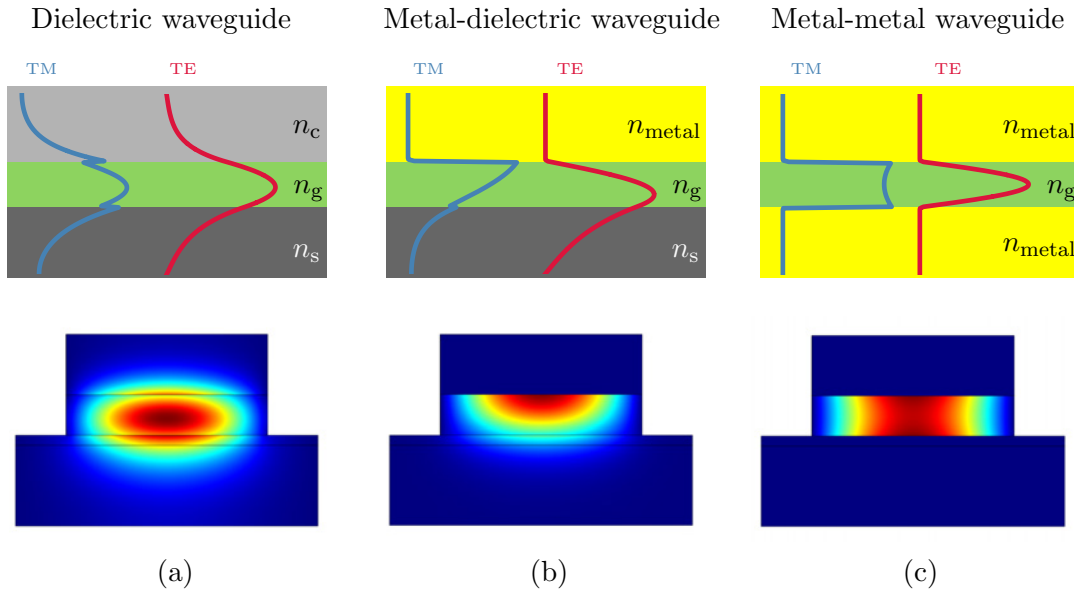


Fig. 2.6: Different planar waveguide configurations for vertical light confinement together with the normalized electric fields. The blue curves correspond to the fundamental TM polarized fields, whereas the red curves show the TE polarization. In the second row the full two-dimensional mode profiles for TM polarized light are shown for typical waveguide geometries with vertical and also lateral confinement. The data is extracted from a mode analysis ($\lambda = 8 \mu\text{m}$) performed with COMSOL. For the laser core (guiding layer) a refractive index of $n_g = 3.2$ is assumed. (a) Pure dielectric waveguide with the cladding $n_c = 2.5$ and the substrate $n_s = 2.8$. (b) Metal-dielectric waveguide where the cladding is replaced by a metal with $n_{\text{metal}} = 4.9 - j57$. Such a configuration is also known as a single plasmon waveguide. (c) In the double-metal waveguide the light is strongly confined with a metal layer below and above.

sight, this configuration offers distinct advantages especially for lasers operating at longer wavelengths [30]. The penetration depth of the guided mode into the metal decreases with increasing wavelength and hence the metal related losses are lowered. In the case of dielectric waveguides the cladding thickness needs to be increased at longer wavelengths to ensure a good mode confinement. However, one runs into several issues with pure dielectric waveguides. First of all, long growth times are necessary, which are technologically problematic due to the drift of the flux rates. An even more severe drawback of the pure-dielectric waveguide stems from the free-carrier absorption loss [17] that is calculated to

$$\alpha_{\text{fc}} = -\frac{4\pi}{\lambda_0} \text{Im}\{\tilde{n}\} = \frac{e^2 N \lambda^2}{4\pi^2 c^3 \epsilon_0 n_{\text{eff}} m^* \tau}, \quad (2.37)$$

which scales with λ^2 . Since the cladding has to be doped sufficiently to ensure a good current transport, the inherent losses are also increased. A metal-dielectric waveguide on the other hand enables a much stronger mode confinement than with a pure dielectric waveguide. It is commonly used in long-wavelength MIR and THz QCLs, where the metal induced losses become comparable to the free-carrier losses in pure dielectric waveguides [29]. A related approach is utilized for MIR QCLs, where the semiconductor cladding is

doped to such extent that it behaves optically like a metal. The dielectric constant $\epsilon = n^2$ changes its sign at the interface, which again enables a much stronger mode confinement than with a pure dielectric waveguide. Furthermore, the waveguide can be engineered to match certain properties for a specific wavelength by adjusting the doping and hence the plasma resonance in the cladding. The mode in this so-called plasmon-enhanced waveguide [31] is pushed towards the core layer. It has been successfully demonstrated for QCLs based on GaAs, InAs and InP substrates [32, 33, 34]. With this approach much thinner waveguides can be used, which is crucially for long-wavelength lasers.

Double-metal waveguide

A high quality crystal growth of appropriate cladding layers for QCLs emitting in the THz region ($\lambda \sim 100 \mu\text{m}$) is not feasible since the necessary thickness of these layers would be also in the same order. The single metal-dielectric waveguide confines the waveguide mode due to the formation of an interface plasmon between the materials. A similar effect can be achieved with a thin highly doped cladding layer, which then shows a metal-like behavior (but not as good as a real metal). However, the mode overlap with the guiding region is reduced due to penetration of the mode into the substrate layer. The confinement can be drastically improved by employing a double-metal waveguide, which is nothing else than a microstrip resonator commonly implemented with microwave technology [35, 36]. Fig. 2.6(c) shows the normalized electric field in the layer stack. The guiding region, which can be the active region of a laser, is sandwiched between two metal layers, commonly made of Au or Cu. For THz QCLs, this waveguide enabled the highest operating temperature [36]. On the downside, the far-field pattern is highly divergent due to the impedance mismatch at the laser facet [17].

2.3.5 Lateral mode confinement

For the slab waveguides in the previous section, an infinite extent in the y - z plane was assumed (see Fig. 2.3). There, the refractive index contrast of the individual layers leads to a light confinement in vertical x -direction. These epitaxial layers are typically grown with molecular beam epitaxy (MBE) or metal-organic chemical vapor deposition (MOCVD) systems. The thickness of the mono-crystalline layers in vertical direction are technologically limited by the achievable growth time. However, for means of mode control and light guiding in a real laser device, also a finite lateral dimension of the waveguide has to be taken into account.

The confinement of light in lateral direction is achieved using processing technologies such as etching, deposition, implantation or regrowth. Some possible configurations are shown in Fig. 2.7. The simplest approach is the gain guided structure, shown in Fig. 2.7(a). The current flow is restricted to a small area below the contact due to isolation layers (e.g. SiN or SiO₂). Hence, optical gain is available in this pumped region. Unfortunately, the current is only weakly confined and can spread in lateral direction. Furthermore, there is no refractive index step in lateral direction, which results in a poor photon confinement and hence high optical losses. In the ridge configuration, shown in Fig. 2.7(b), a

cavity is created by etching the semiconductor material away. The quality of the etched sidewalls plays an important role, as roughness induces losses for the optical mode. This configuration offers good current and moderate photon confinement and is commonly used for QCLs and ICLs. Fig. 2.7(c) illustrates the approach based on proton implantation with hydrogen ions. The implantation process leads to the creation of defects, which make the material almost insulating. For high-performance lasers a so-called buried-heterostructure process is used, illustrated in Fig. 2.7(d). The lateral regrowth with e.g. iron-doped InP allows the formation of semi-insulating layers with low refractive indices. It offers good current and photon confinement together with excellent thermal properties.

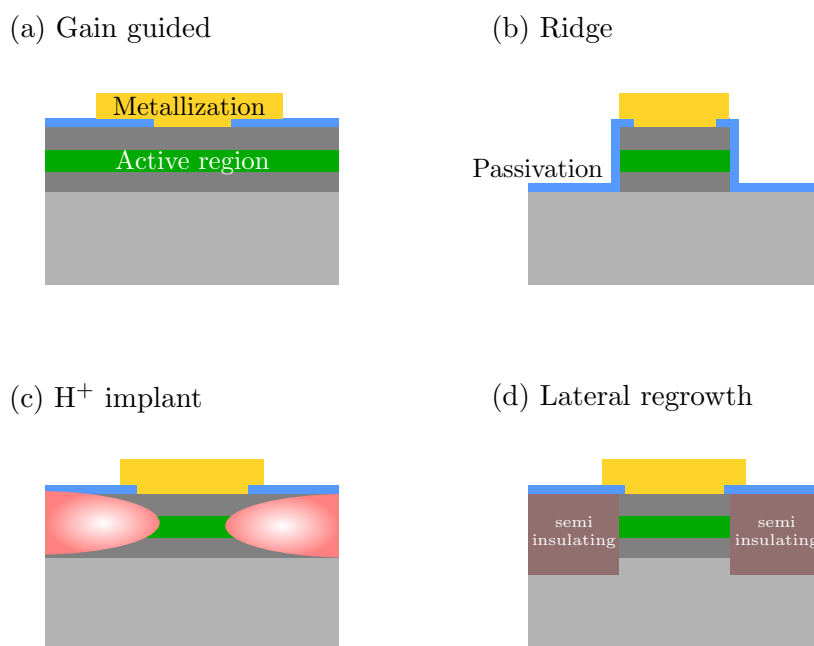


Fig. 2.7: Some structures for lateral confinement in semiconductor lasers. (a) Gain guided structure, (b) ridge configuration, (c) proton implantation with hydrogen ions and (d) lateral regrowth with semi-insulating material.

The waveguide width is of great importance for the emission behavior, since it determines which lateral modes can reach the lasing threshold. Ideally, only a single lateral mode is excited, but if the lateral waveguide size becomes too wide, also higher-order modes may be present. Simulations of a straight ridge waveguide, which supports several lateral modes, are shown in Fig. 2.8. For the simulation it is assumed that the structure is translation-invariant in vertical and longitudinal direction (into the paper plane). Thus, it can again be treated as a slab waveguide, but now with confinement in horizontal direction. Finally, it has to be noted that the ridge width also determines the divergence of the emitted beam. A narrow ridge has a smaller facet, which leads to a broader emission pattern in the far-field.

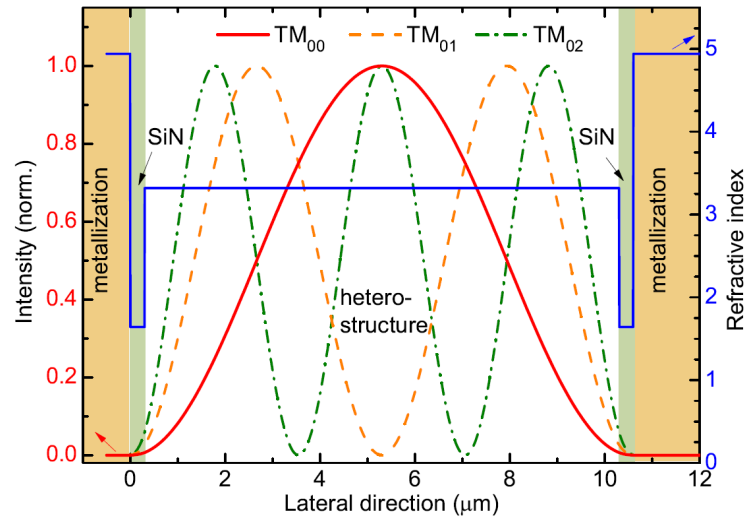


Fig. 2.8: Fundamental and higher-order lateral modes (transverse-magnetic polarized) in a semiconductor laser. Reprinted with permission from [37].

2.3.6 Longitudinal mode confinement

One advantage of semiconductor lasers is the approximately 3 times higher refractive index of the gain medium than in air. This allows to build optical resonators simply by removing the surrounding material, e.g. by etching or cleaving the crystal. Due to the high refractive index contrast, good waveguides are inherently created. The longitudinal mode confinement is caused by the finite length of the laser device. As it will be shown in the subsequent discussion about Fabry-Pérot cavities, the length of the device determines the wavelengths at which stationary eigenmodes are supported.

2.3.7 Fabry-Pérot cavity

In the context of semiconductor lasers the Fabry-Pérot cavity is a device that can be easily fabricated. There, a gain medium is embedded in a ridge waveguide, which is manufactured using photolithographic techniques and standard etch processes. An illustration of such a Fabry-Pérot resonator is shown in Fig. 2.9. The facets, where the light is partly out-coupled and reflected back into the cavity, can be formed by etching or preferably cleaving. The latter approach has the advantage that the semiconductor crystal breaks along the crystal axis, which creates very smooth surfaces. The facets act as high-quality optical mirrors, which are essential for the laser operation. In general, the reflectivity (at normal incidence) between two materials with different refractive indices is given by

$$R = \left(\frac{n - n_0}{n + n_0} \right)^2 = \left(\frac{n/n_0 - 1}{n/n_0 + 1} \right)^2, \quad (2.38)$$

where n is the refractive index of e.g. the semiconductor and n_0 the other material. As

the ratio n/n_0 increases, also the reflectivity increases. For a semiconductor with e.g. $n = 3.2$ and air as the surrounding material with $n_0 = 1$, a reflectivity of $R = 27\%$ is calculated. In general, the reflectivity between two materials depends on the polarization (σ or π) of the light and also the incidence angle [25]. Hence, the same waveguide has different reflectivities for TM and TE-polarized light [38]. Furthermore, the reflectivity of the mirrors can be engineered by tilting facets [39]. In the Fabry-Pérot device, shown in Fig. 2.9, the light is emitted from both facets. However, for certain applications it may be required to use only a single facet as emitting area. For example, this can be the purpose for building lasers with high output power. In this case, the other facet is covered with a high-reflectivity coating, which can be either metallic or dielectric. While the former type acts like an almost perfect mirror with reflectivities close to unity, the latter can be composed of different materials that can be designed to provide a frequency selective reflectivity. Hereby, a stack of alternating dielectric layers with high/low refractive indices serves as a distributed Bragg mirror (DBR) that has a high reflectivity in the stopband around the design wavelength. The DBR is described more in detail in section 2.4.4. For applications where the laser is coupled to e.g. an external cavity, it is necessary that the generated light is out-coupled from the facet without any back-reflections. In other words, the Fabry-Pérot cavity needs to be destroyed to suppress its characteristic resonances. Therefore, an anti-reflection coating is applied on the resonator facet and as a result the laser cavity is dictated by the external cavity.

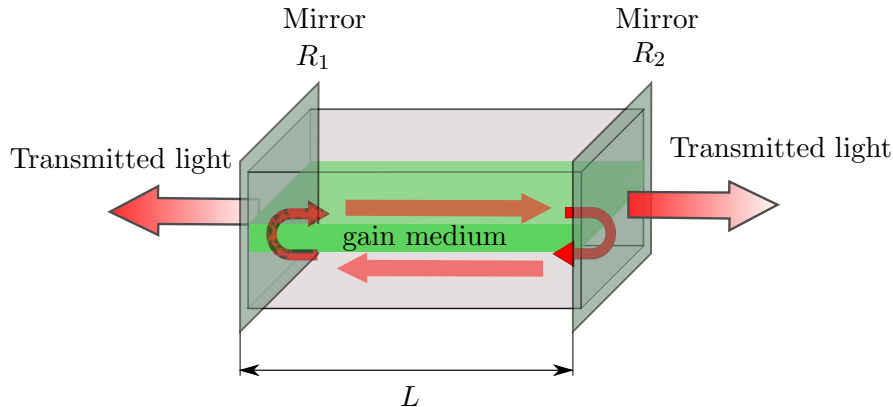


Fig. 2.9: The light in a Fabry-Pérot laser is partially transmitted via the facets and reflected back into the cavity.

The Fabry-Pérot cavity shows characteristic resonance frequencies, which are determined by the length L of the resonator. A stationary mode can only be established if it satisfies the following condition

$$L = m \frac{\lambda_{\text{mat}}}{2}, \quad (2.39)$$

with the reduced wavelength in the material $\lambda_{\text{mat}} = \lambda/n_{\text{eff}}$ and a positive integer m . Rearranging the equation to

$$\lambda = \frac{2n_{\text{eff}}L}{m} \quad (2.40)$$

shows that only certain eigenmodes with mode index m at the wavelength λ are supported by the cavity. The effective refractive index n_{eff} in general has a wavelength-dependence. Starting from a mode at a wavelength λ , the next mode at the wavelength $\lambda + \Delta\lambda$ is given by

$$\lambda + \Delta\lambda = \frac{2L(n_{\text{eff}} + \Delta n_{\text{eff}})}{m + \Delta m}. \quad (2.41)$$

For the calculation of the spacing between adjacent modes ($\Delta m = 1$), a linear approximation $\partial n_{\text{eff}}/\partial\lambda = \Delta n_{\text{eff}}/\Delta\lambda$ is used, which leads to

$$\Delta\lambda = \frac{2L(n_{\text{eff}} + \Delta\lambda\partial n_{\text{eff}}/\partial\lambda)}{m + 1} - \lambda. \quad (2.42)$$

Inserting (2.40) into the above formula and rearranging the terms gives an expression for the distance between two modes, the so-called free-spectral range (FSR),

$$\text{FSR}_\lambda = |\Delta\lambda| = \left| \frac{-\lambda^2}{2L \left(n_{\text{eff}} - \lambda \frac{dn_{\text{eff}}}{d\lambda} \right) + \lambda} \right| \quad (2.43)$$

$$\approx \frac{\lambda^2}{2L \left(n_{\text{eff}} - \lambda \frac{dn_{\text{eff}}}{d\lambda} \right)}. \quad (2.44)$$

In spectroscopy the spectrum is often expressed in terms of wavenumbers, which is defined as $\nu = 1/\lambda$ with the unit $[\text{cm}^{-1}]$. Although the name repetency is recommended, as it is a physical quantity with a unit and not only a number, the wavenumber is commonly used in the scientific community. However, a similar derivation as before gives a formula for the mode spacing expressed in wavenumbers

$$\text{FSR}_\nu = |\Delta\nu| \approx \frac{1}{2L \left(n_{\text{eff}} + \nu \frac{dn_{\text{eff}}}{d\nu} \right)}. \quad (2.45)$$

The brackets term in the denominator is identified as the group refractive index

$$n_{\text{group}} = n_{\text{eff}}(\lambda) - \lambda \frac{dn_{\text{eff}}(\lambda)}{d\lambda} \quad (2.46)$$

$$= n_{\text{eff}}(\nu) + \nu \frac{dn_{\text{eff}}(\nu)}{d\nu}, \quad (2.47)$$

which can deviate substantially from the effective refractive index n_{eff} in presence of gain and/or dispersive materials. The longitudinal mode spacing in a Fabry-Pérot cavity is therefore given by

$$|\Delta\lambda| = \frac{\lambda^2}{2n_{\text{group}}L} \quad (2.48)$$

$$|\Delta\nu| = \frac{1}{2n_{\text{group}}L}. \quad (2.49)$$

In a resonator with 2 mm length and neglected dispersion $n_{\text{group}} \approx n_{\text{eff}} = 3.2$ the spacing between adjacent modes would be $\Delta\nu = 0.78 \text{ cm}^{-1}$. Furthermore, a typical QCL gain material with a spectral gain width of $2\gamma = 10 \text{ meV}$, which corresponds to $2\gamma/(hc_0) \approx 80 \text{ cm}^{-1}$, is assumed. Dividing this number by the mode spacing shows that 103 longitudinal modes are located within the gain spectrum. If no mode discrimination mechanism is incorporated, then this Fabry-Pérot laser will feature multimode operation. However, for spectroscopic applications it is mandatory to have a light source emitting at a single wavelength, which can also be tuned over a certain wavelength range. In order to get single mode emission one could narrow the gain bandwidth, decrease the cavity length or add a mode-selecting element, such as distributed Bragg or distributed feedback gratings, which will be discussed later in 2.4. On the other hand, the large number of longitudinal modes can also be utilized to build so-called frequency combs [40]. Hereby, a broadband gain material together with a locking mechanism, e.g. four-wave mixing, is used to generate a series of equally spaced phase-locked modes. The modes in an ordinary multi-mode Fabry-Pérot laser are usually not coupled and also not exactly equidistant due to the wavelength dependence of the group refractive index, expressed in (2.49). Hence, a multimode laser alone is not sufficient to get a frequency comb. In fact, to ensure a fixed phase relationship over a wide frequency range, the group velocity dispersion in the cavity needs to be compensated.

Threshold gain and losses

The first photon in the laser is generated by spontaneous emission. This event can be seen as the launch of an electromagnetic wave, which propagates in the cavity towards a mirror. There, it is partially transmitted and reflected back into the cavity. For simplicity, the wave, which propagates in z -direction, is described as an one-dimensional plane wave

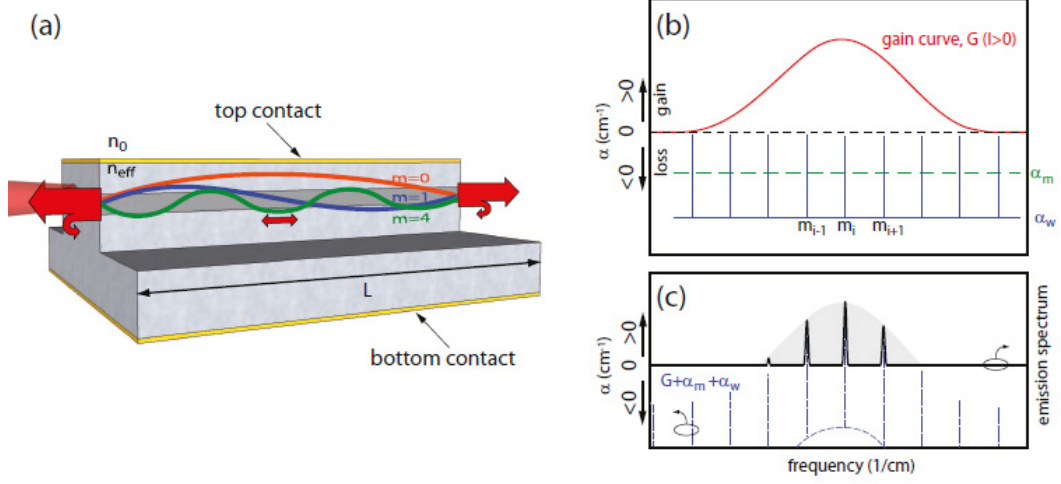


Fig. 2.10: (a) Due to the geometrical size of the cavity, several longitudinal modes are supported. (b) The separation between the modes is given by the free spectral range (FSR), which is inverse proportional to the resonator length. The material in the active region determines the wavelength-dependent gain. (c) Only the modes, which are located within the gain spectrum of the laser, can be excited and may reach threshold. Reprinted with permission from [41].

$$E(z, t) = E_0 e^{j(\omega t - \tilde{\beta}z)} R_1 R_2, \quad (2.50)$$

with the mirror reflectivities R_1 and R_2 . The complex propagation constant is given by

$$\tilde{\beta} = k_0 \tilde{n}_{\text{eff}} = \frac{2\pi}{\lambda_0} \text{Re}\{\tilde{n}_{\text{eff}}\} + j \frac{g - \alpha_{\text{wg}}}{2}. \quad (2.51)$$

The net gain $g - \alpha_{\text{wg}}$ in the imaginary part of $\tilde{\beta}$ causes amplification, determined by the gain material, and damping due to various losses such as mirror and waveguide losses. The latter is caused mainly by free-carrier absorption loss of the materials and scattering losses due to rough sidewalls. In the following, an expression for the threshold gain value is derived. Therefore, the amplitude of the wave after one round-trip (distance $2L$) has to at least reach the initial amplitude E_0 . Since only stationary solutions are of interest, the time-dependence is omitted. For the wave the condition then reads

$$E_0 e^{-j\tilde{\beta}2L} R_1 R_2 \stackrel{!}{=} E_0. \quad (2.52)$$

Inserting (2.51) into (2.50) together with $R = R_1 R_2$ gives

$$e^{-j2Lk_0 \text{Re}\{\tilde{n}_{\text{eff}}\}} e^{2L \frac{g - \alpha_{\text{wg}}}{2}} = \frac{1}{R}. \quad (2.53)$$

The condition on the phase implies that $2Lk_0 n_{\text{eff}} = m2\pi$, with an integer number m .

From this it follows that stationary modes are restricted to wavelengths of $\lambda_0 = 2n_{\text{eff}}L/m$. This result has been implicitly applied earlier in (2.40). Besides the phase condition also the amplitude condition $2L(g - \alpha_{\text{wg}})/2 = \ln(1/R)$ needs to be satisfied, which gives an expression for the threshold gain

$$g_{\text{th}} = \alpha_{\text{wg}} + \frac{1}{L} \ln\left(\frac{1}{R}\right) = \alpha_{\text{wg}} + \alpha_{\text{m}}. \quad (2.54)$$

A similar expression can be derived for the intensity instead of the amplitude. Thereby, a factor 1/2 appears in the formula for the losses. The total losses of the laser cavity are given by the sum of mirror and waveguide losses, $\alpha_{\text{total}} = \alpha_{\text{m}} + \alpha_{\text{wg}}$. The mirror losses are a measure for the amount of light that is out-coupled from the cavity through the semi-transparent mirrors. Thus, they represent the emission losses which are usually specified in units of $[\text{cm}^{-1}]$. For a Fabry-Pérot cavity the mirror losses (intensity) for both facets are given by

$$\alpha_{\text{m}} = \frac{1}{2L} [\ln(R_1) + \ln(R_2)] = \frac{1}{2L} \ln(R_1 R_2). \quad (2.55)$$

Considering the overlap of the mode with the active region via the overlap factor Γ in a generalized form

$$\Gamma = \frac{\int_{\text{active}} |\mathbf{E} \times \mathbf{H}| \, d\mathbf{r}}{\int_{\text{cavity}} |\mathbf{E} \times \mathbf{H}| \, d\mathbf{r}}, \quad (2.56)$$

an expression for the modal gain (material gain) can be found by

$$\Gamma g = \alpha_{\text{total}} = \frac{1}{2L} \ln(R) + \alpha_{\text{wg}}. \quad (2.57)$$

In other words, the laser reaches threshold if all losses are compensated by an optical gain. The required threshold current density is then given by [34]

$$J_{\text{th}} = \frac{\alpha_{\text{wg}} + \alpha_{\text{m}}}{\Gamma g}. \quad (2.58)$$

An increase of the pump current drives the laser above threshold and light emission for certain modes, specified by (2.40), becomes possible. Fig. 2.11 shows simulations of the mode distributions for the fundamental mode and the second lateral mode in a straight ridge waveguide. The waveguide is simulated for a wavelength of $\lambda = 8.7 \mu\text{m}$ and a waveguide width of $10 \mu\text{m}$.

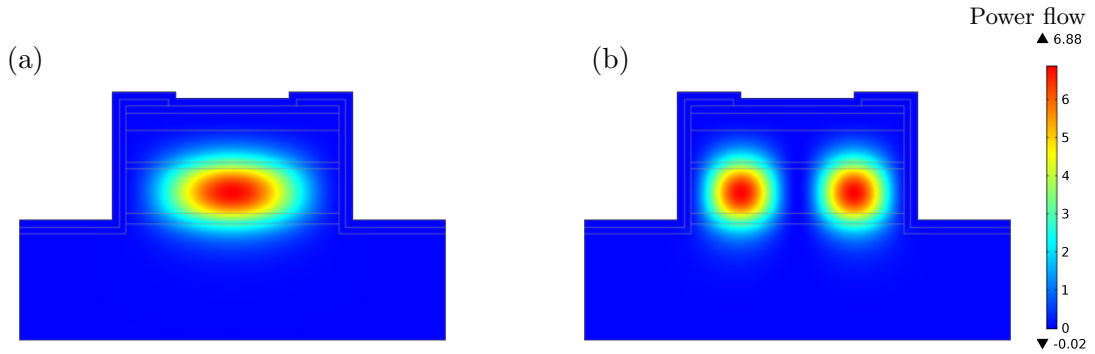


Fig. 2.11: Mode profile (time-averaged power flow) of a straight Fabry-Pérot resonator for a wavelength of $\lambda = 8.7\ \mu\text{m}$ and a waveguide width of $10\ \mu\text{m}$. (a) The fundamental mode has the maximum intensity in the waveguide center ($n_{\text{eff},1} = 3.195 - j8 \times 10^{-4}$). (b) Higher order lateral mode with the effective mode index $n_{\text{eff},2} = 3.114 - j1 \times 10^{-3}$. The simulated heterostructure corresponds to the P51 QCL design (see growthsheet in A.3.1), which is used for the intersubband devices in this work.

2.3.8 Circular-shaped cavities

Besides the straight ridge resonator, light can also be confined in circular symmetric cavities. The light is guided due to total internal reflection at the circular boundary between the inside material with refractive index n_1 and the surrounding material n_2 , as illustrated in Fig. 2.12(a). According to Snell's law (2.23), the angle of incidence θ_i is related to the angle of refraction θ_r via

$$n_1 \sin \theta_i = n_2 \sin \theta_r. \quad (2.59)$$

Total internal reflection occurs if the angle of incidence is larger than $\theta_{\text{crit}} = \arcsin(n_2/n_1)$, as already used in (2.24). Light is reflected at the circular boundaries and trapped inside the symmetric cavity. Therefore, the radius of the cavity has to be larger than the wavelength. The waveguide modes inside the cavity are also known as *whispering-gallery modes* (WGMs). Compared to straight ridge cavities, the center of mass of the modes are shifted towards the curved boundary. Originally, WGMs were first observed for acoustic waves rather than electromagnetic waves. In 1910, Lord Rayleigh described the propagation of a sound whisper along the circular gallery in St. Pauls Cathedral [42]. In this whispering gallery the sound waves have the tendency to cling to the concave sidewalls, which allows them propagate over a long distance. Two persons near the wall, but at different positions in the gallery, can even hear the whisper of each other. Whispering galleries have been built long time before the effect was understood theoretically, such as e.g. the Echo Wall in the Temple of Heaven in China or the Gol Gumbaz Mausoleum in India [43]. In the following, an analytical expression for the electromagnetic field inside the circular-shaped cavities is derived and afterwards simulations of the whispering-gallery modes are presented.

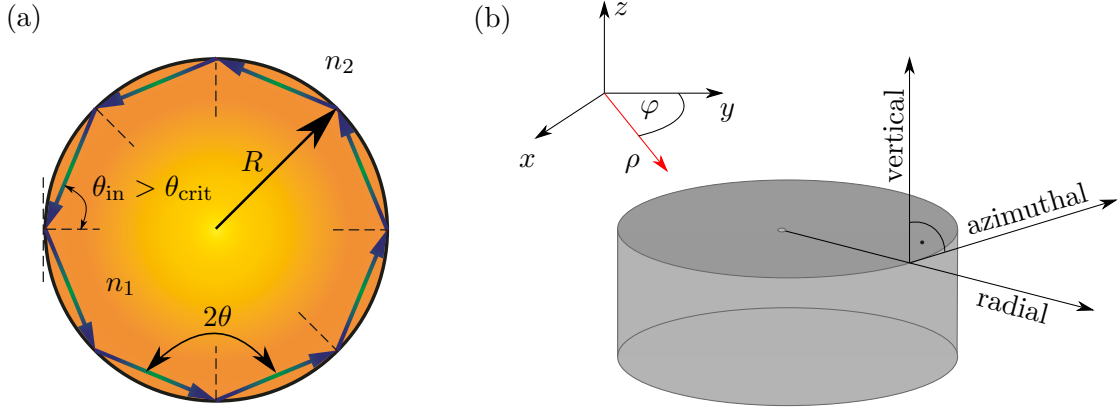


Fig. 2.12: (a) A light ray propagating inside a cavity with $n_1 > n_2$ is reflected at the circular boundaries if the angle of incidence is larger than the critical angle $\theta_{\text{crit}} = \arcsin(n_2/n_1)$. (b) Coordinate system and naming convention for circular-shaped resonators.

Whispering-gallery modes

Starting point for the derivation of the electromagnetic field distribution in circular-shaped resonators is the Helmholtz equation for source-free and homogeneous media. It has been derived in the appendix (A.12) and is given by

$$\left[\nabla^2 + \mu\epsilon\omega^2 \right] \tilde{\mathbf{E}}(\mathbf{r}, \omega) = 0. \quad (2.60)$$

Due to the axisymmetric geometry, it is convenient to switch from a cartesian to a cylindrical coordinate system, as shown in Fig. 2.12(b). There, the Nabla-operator then has the form

$$\vec{\nabla} = \mathbf{e}_\rho \frac{\partial}{\partial \rho} + \mathbf{e}_\varphi \frac{1}{\rho} \frac{\partial}{\partial \varphi} + \mathbf{e}_z \frac{\partial}{\partial z}, \quad (2.61)$$

with the unit vectors \mathbf{e}_ρ , \mathbf{e}_φ and \mathbf{e}_z in ρ , φ and z direction, respectively. Here, ρ denotes the radial coordinate, φ is the azimuthal angle and z the vertical coordinate. Inserting (2.61) into (2.60) gives the Helmholtz equation in cylindrical coordinates

$$\left(\frac{\partial^2}{\partial \rho^2} + \frac{1}{\rho} \frac{\partial}{\partial \rho} + \frac{1}{\rho^2} \frac{\partial^2}{\partial \varphi^2} + \frac{\partial^2}{\partial z^2} + n^2 k_0^2 \right) \tilde{\mathbf{E}}(\rho, \varphi, z, \omega) = 0, \quad (2.62)$$

where the free-space wavevector $k_0 = \omega/c_0$ and the refractive index $n = \sqrt{\mu_r \epsilon_r}$ are used for the substitution $\mu\epsilon\omega^2 = \mu_0 \epsilon_0 \mu_r \epsilon_r k_0^2 c_0^2 = n^2 k_0^2$. To simplify the derivation, only the z -component of the electric field is considered. The partial differential equation can be solved with a separation ansatz [44]. The field is decomposed into functions that only depend on a single coordinate,

$$E_z(\rho, \varphi, z) = R(\rho)\Phi(\varphi)Z(z). \quad (2.63)$$

Inserting (2.63) into (2.62) and dividing the whole equation by $R\Phi Z$ gives

$$\frac{1}{R} \frac{\partial^2 R}{\partial \rho^2} + \frac{1}{R} \frac{1}{\rho} \frac{\partial R}{\partial \rho} + \frac{1}{\Phi} \frac{1}{\rho^2} \frac{\partial^2 \Phi}{\partial \varphi^2} + \frac{1}{Z} \frac{\partial^2 Z}{\partial z^2} + n^2 k_0^2 = 0. \quad (2.64)$$

The third term is the only one that depends on z and since the whole left hand side of this equation has to sum up to zero, the term has to equal some constant

$$\frac{1}{Z} \frac{\partial^2 Z}{\partial z^2} = -\beta^2. \quad (2.65)$$

Using β as the variable is on purpose since $Z(z) = e^{j\beta z}$ is a solution to this differential equation and therefore β corresponds to the propagation constant. Inserting (2.65) into (2.64) and multiplying the equation with ρ^2 gives

$$\frac{\rho^2}{R} \frac{\partial^2 R}{\partial \rho^2} + \frac{1}{R} \rho \frac{\partial R}{\partial \rho} + \frac{1}{\Phi} \frac{\partial^2 \Phi}{\partial \varphi^2} + (n^2 k_0^2 - \beta^2) \rho^2 = 0. \quad (2.66)$$

Again, the second term is the only one that depends φ , hence this term also needs to equal a constant. Therefore, the azimuthal dependence can be described by a function $\Phi(\varphi) = e^{jm\varphi}$, which is a solution of the differential equation

$$\frac{1}{\Phi} \frac{\partial^2 \Phi}{\partial \varphi^2} = -m^2. \quad (2.67)$$

Replacing the second term in (2.66) with $-m^2$ and multiplying with R gives a (Bessel) differential equation that only depends on the radial coordinate

$$\rho^2 \frac{\partial^2 R}{\partial \rho^2} + \rho \frac{\partial R}{\partial \rho} + R [(n^2 k_0^2 - \beta^2) \rho^2 - m^2] = 0. \quad (2.68)$$

The solutions are given by the superposition of Bessel functions of first kind (J_m) and second kind (Y_m). The original partial differential equation from (2.64) has now been separated into three independent equations (2.68), (2.67) and (2.66), respectively. In each case the solution depends only on a single coordinate: $R(\rho)$ in radial direction, $\Phi(\varphi)$ in azimuthal direction and $Z(z)$ axial direction. The solution for the electric field in (2.62) is given by the multiplication of the solutions of the three partial differential equations

$$E_z(\rho, \varphi, z) = (A J_m + B Y_m) e^{j\beta z} e^{jm\varphi}, \quad (2.69)$$

with the coefficients A and B . In a similar manner, also the magnetic field H_z can be separated into three individual contributions. With the appropriate boundary conditions, the electromagnetic field distribution in circular-shaped cavities (e.g. disks or rings) can be calculated. Fig. 2.13 shows finite-element eigenfrequency calculations of ring resonators, using COMSOL. The eigenmodes are determined by the azimuthal mode number m and the radial order l . The whispering-gallery mode solutions are further separated into transverse-electric $TE_{l,m}$ or transverse-magnetic $TM_{l,m}$ polarized. For quantum cascade lasers the modes are dominantly TM-polarized, while a TE polarization has to be considered for interband devices.

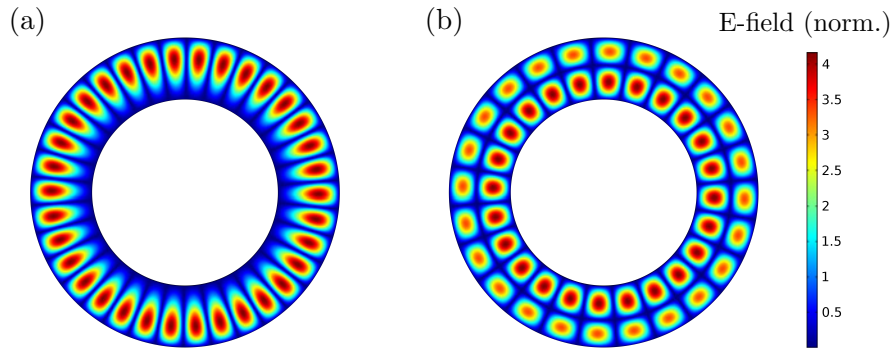


Fig. 2.13: Finite-element simulations of the whispering-gallery modes in ring cavities. (a) Fundamental WGM ($l = 0$) and (b) first-order lateral mode ($l = 1$). The ring with a waveguide width of $40 \mu\text{m}$ and an outer radius of $100 \mu\text{m}$ is simulated for a wavelength of $\lambda = 100 \mu\text{m}$.

Compact disk-shaped optical whispering-gallery mode sensors are used e.g. for optomechanics or biosensing and disk lasers have also been realized with quantum cascade lasers in the mid-infrared, as well as in the THz spectral region [45, 46, 47, 48]. However, in disk lasers unwanted higher-order radial modes are easily excited. A reduction of the lateral waveguide width to a size, which is on the order of the wavelength, allows to suppress these modes and lasing in the fundamental WGM is possible. With a ring geometry, not only lateral modes can be efficiently suppressed, but also the pump power is reduced compared to disk lasers. The waveguide modes in ring lasers can also be calculated with the method of conformal transformation [49, 50]. There, the coordinates (ρ, φ, z) are transformed into a new coordinate system (u, v, z) , while still preserving the angles of the grid. For a ring geometry the coordinate transformation is given by [41]

$$u = R_{\text{out}} \ln \left(\frac{\rho}{R_{\text{out}}} \right) \quad (2.70)$$

$$v = R_{\text{out}} \varphi, \quad (2.71)$$

where φ is the angle, ρ is the local coordinate and R_{out} is the outer radius of the ring, which serves as reference radius. With this coordinate transformation, a ring shape is mapped onto a straight rectangle. An illustration of the mapping is shown in Fig. 2.14. The transverse refractive index profile $n(\rho)$ in the original coordinate system (ρ, φ, z) is also

transformed and reads in the new coordinate system $n_t(u) = n \exp(u/R_{\text{out}})$ [41]. Hence, the refractive index profile in the transformed rectangular waveguide increases towards the outer sidewall. An intuitive explanation is that the optical path is longer for light travelling closer to the outer sidewall of the ring. This translates to a lower phase velocity ($v_{\text{phase}} = c_0/n$) and hence an increased refractive index for the straight ridge [51]. Fig. 2.15 shows the simulated radial (lateral) whispering-gallery modes in a ring cavity with an outer diameter of $400 \mu\text{m}$ and waveguide width of $10 \mu\text{m}$.

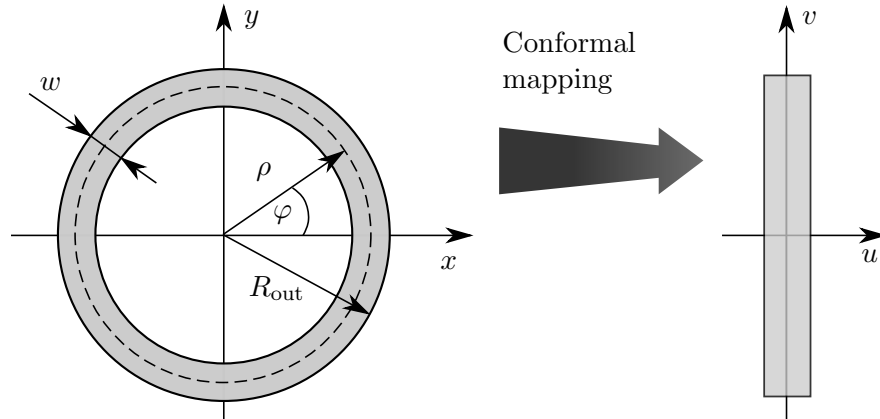


Fig. 2.14: Conformal transformation of a bent waveguide to a straight geometry via the angle-preserving mapping of the coordinates $(r, \varphi, z) \rightarrow (u, v, z)$.

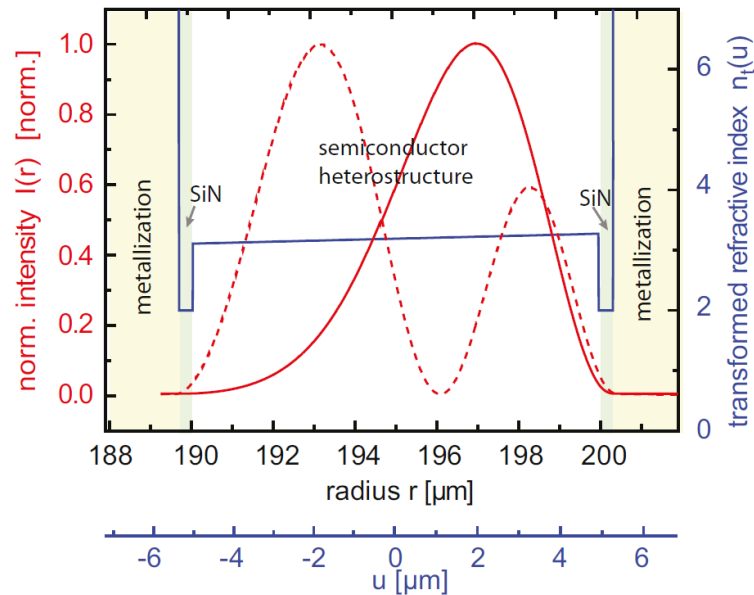


Fig. 2.15: Calculation of the whispering-gallery modes (WGMs) in a ring cavity with the method of conformal transformation. The refractive index (blue line) increases in the transformed coordinate system (u, v, z) towards the outer sidewall. For illustration, also the radius in the original coordinate system is plotted. The intensity maximum of the fundamental WGM is shifted in a ring cavity closer to the outer sidewall at $200 \mu\text{m}$. The main peak of the first-order radial (lateral) mode (dashed line) is shifted to the inner sidewalls. Reprinted with permission from [41].

Similar to Fabry-Pérot cavities (see section 2.3.7), the spacing between adjacent modes in ring cavities is determined by the size of the resonator. The eigenmodes in circular cavities have to satisfy the phase condition given by

$$m \frac{\lambda}{n_{\text{eff}}} = L_{\text{eff}}, \quad (2.72)$$

with the azimuthal/longitudinal mode index m , the free-space wavelength λ , the effective refractive index n_{eff} and the effective cavity length $L_{\text{eff}} = 2\pi r_{\text{eff}}$. For the effective radius r_{eff} the mode's center of gravity in radial direction is used. In the case of the fundamental radial mode, r_{eff} commonly lies between the outer radius R_{out} of the waveguide and the center radius $r_{\text{center}} = (R_{\text{out}} - R_{\text{in}})/2$, with R_{in} as the inner waveguide radius. The spacing between the azimuthal (longitudinal) modes (free-spectral range, FSR) is given by

$$\text{FSR}_{\nu} = |\Delta\nu| = \frac{1}{n_{\text{group}} L_{\text{eff}}} = \frac{1}{n_{\text{group}} 2\pi r_{\text{eff}}}, \quad (2.73)$$

where n_{group} is the group refractive index, defined in (2.47). Fig. 2.16 shows simulations of the the fundamental whispering-gallery mode and the second lateral (radial) mode in a ring waveguide. The waveguide is simulated for a wavelength of $\lambda = 8.7 \mu\text{m}$, a waveguide width of $10 \mu\text{m}$ and an outer ring radius of $200 \mu\text{m}$. Compared to the straight ridge waveguide, shown in Fig. 2.11, the intensity maximum of the fundamental whispering-gallery mode is shifted towards the outer sidewall of the ring. This spatial shift becomes even more pronounced if rings with a smaller diameters are considered.

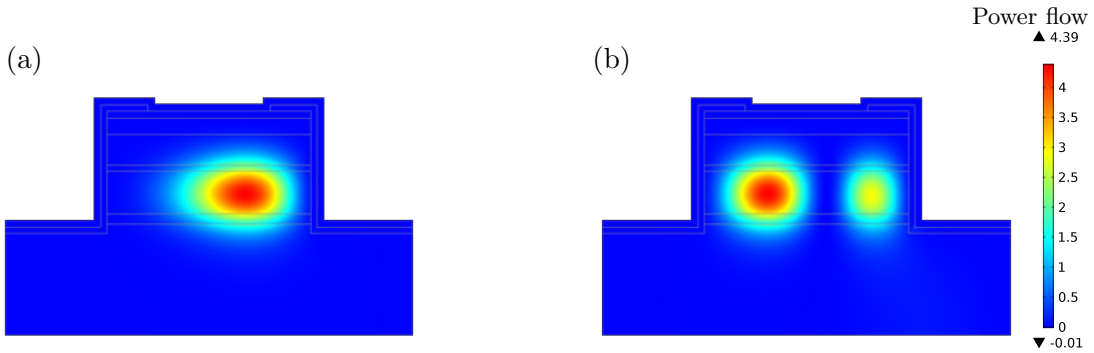


Fig. 2.16: Mode profile (time-averaged power flow) of a ring resonator for a wavelength of $\lambda = 8.7 \mu\text{m}$. The waveguide width is $10 \mu\text{m}$ and the outer ring radius is $200 \mu\text{m}$. (a) The intensity maximum fundamental mode is shifted towards the outer sidewall ($n_{\text{eff},1} = 3.185 - j8.6 \times 10^{-4}$). (b) Higher order lateral mode with the effective mode index $n_{\text{eff},2} = 3.113 - j1 \times 10^{-3}$. The simulated heterostructure corresponds to the P51 QCL design (see growthsheet in A.3.1), which is used for the intersubband devices in in this work.

2.4 Mode selection

A semiconductor laser is not necessarily inherent single-mode. Instead, simultaneous emission at multiple wavelengths may be observed. The light amplifying material in the active region provides a finite bandwidth for the gain and several waveguide modes within this wavelength band can reach threshold, as explained in section 2.3.7. For many applications, a single-mode operation of the laser source is required. More specifically, the laser should oscillate in the fundamental transversal, lateral and longitudinal mode. To excite only one lasing mode, the losses of the other waveguide modes have to be selectively increased. This can be achieved with simple geometrical constraints or more complex structures such as coupled cavities or gratings. In the following, several concepts to achieve single-mode emission with semiconductor lasers are discussed.

2.4.1 Short cavity

For single-mode operation, a mode discrimination mechanism has to be incorporated into the cavity. A very simple approach is to reduce the length of the laser. The spacing between two adjacent modes (free spectral range, FSR) is according to (2.49) inversely proportional to the cavity length. Thus, if the cavity is short enough and hence the mode spacing large enough, only a single longitudinal mode remains in the gain spectrum. However, a short cavity is only feasible if the gain of the laser is high enough to compensate the (increased) mirror losses. From (2.55) it can be seen that the mirror losses are also inversely proportional to the cavity length. Short cavities are commonly used in bandgap lasers with typical cavity lengths of $\sim 50 \mu\text{m} - 300 \mu\text{m}$ [52]. Fig. 2.17 illustrates the mode selection with a short laser cavity.

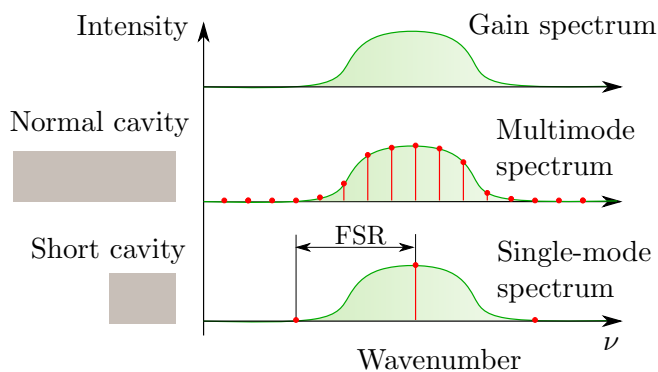


Fig. 2.17: Illustration of the mode selection with a short cavity. In a normal cavity several longitudinal modes fit into the gain spectrum of the active region material. As a result, the laser will excite multiple modes. If the cavity length is shortened to such an extent that the mode spacing (FSR) becomes larger than the gain bandwidth, only a single mode can reach threshold.

In addition, small gain regions are also utilized in vertical-cavity surface-emitting lasers (VCSEL) [53, 54], where high quality Bragg mirrors (reflectivities $\sim 99\%$) are grown above and below the active region. The high mirror reflectivities are needed to keep the mirror losses sufficiently low. On the other hand, the high gain in band gap devices allows to artificially increase the slope efficiency η_s , which is written as [55]

$$\eta_s = \frac{dP}{dI} = \eta_i \frac{N\hbar\omega}{e} \frac{\alpha_m}{\alpha_m + \alpha_{wg}}, \quad (2.74)$$

with the optical output power P , the drive current I , the internal quantum efficiency η_i , the number of periods N , the photon energy $\hbar\omega$, the electron charge e , the mirror loss α_m and the waveguide loss α_{wg} . The slope efficiency can be increased by increasing the mirror losses (assuming constant waveguide losses) and thus by decreasing the length of the laser cavity. In QCLs, with their much lower gain on the order of $\sim 15 \text{ cm}^{-1}$, the mirror losses cannot be compensated easily.

2.4.2 Coupled cavities

In the coupled cavities configuration the generated light of the laser is passed through at least one additional optical cavity [56]. Light amplification only occurs for modes at those wavelengths, where the resonances of the two cavities coincide. Fig. 2.18 illustrates one possible configuration of coupled cavities. The geometrical length of cavity 1 leads to a sequence of equally spaced modes. Only those longitudinal modes are amplified, which match the resonances of cavity 2. In this two-section device cavity 2 is used as a modulator, where the refractive index in the cavity can be changed by current injection or heating. Hence, the position of the resonance can be tuned and a single longitudinal mode is selected.

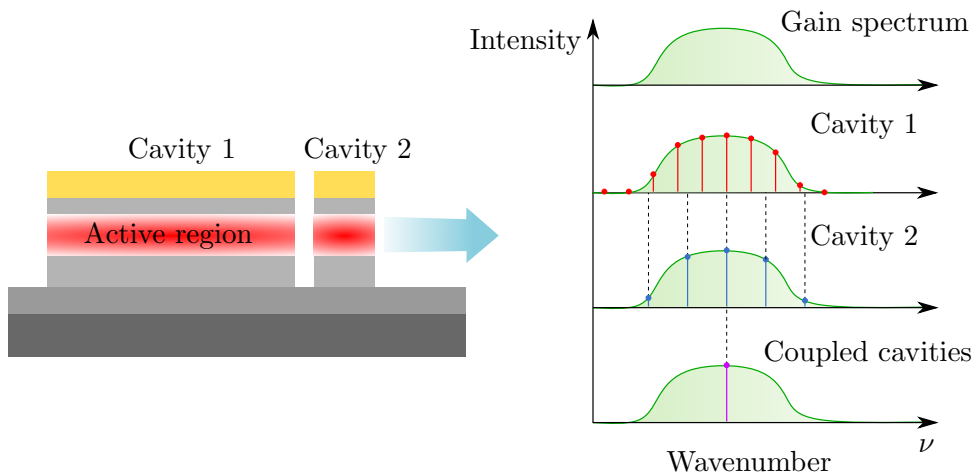


Fig. 2.18: Illustration of a coupled cavities configuration. Only those frequencies, where the resonances of both cavities match, are amplified. As a result, only a single mode remains in the spectrum of the coupled cavities.

2.4.3 External cavity

Semiconductor lasers can provide a broad gain spectrum, which in principle allows to achieve single-mode emission over a wide spectral range. For QCLs, the width of the gain curve can be around 120 cm^{-1} . However, due to a limited tuning range, not all wavelengths within the gain spectrum are accessible. For instance, with distributed-feedback gratings the emission wavelength can be tuned with temperature by $\sim 10 \text{ cm}^{-1}$ and with current tuning by only $\sim 1 \text{ cm}^{-1}$ [17]. There are concepts to extend the tuning range of distributed-feedback lasers with e.g. different grating periods in multi-segment devices. However, such sampled gratings [57, 58] or binary superimposed gratings [59, 60] require a more sophisticated fabrication and may still lack of continuous wavelength-tunability. The on-chip integrated distributed feedback gratings are discussed more in detail in section 2.4.5. To access different wavelengths over a broad spectral region, an external tunable optical filter can be used instead. Therefore, the laser is covered with an anti-reflection coating (e.g. a quarter-wave layer Al_2O_3) on the front facet and the output beam is collimated with a lens and directed onto a wavelength-selective grating. The anti-reflection coating is necessary to suppress the Fabry-Pérot modes of the semiconductor laser. The back facet of the ridge laser is preferably covered with a high-reflection coating. Two mainly used external cavity configurations [61] are illustrated in Fig. 2.19.

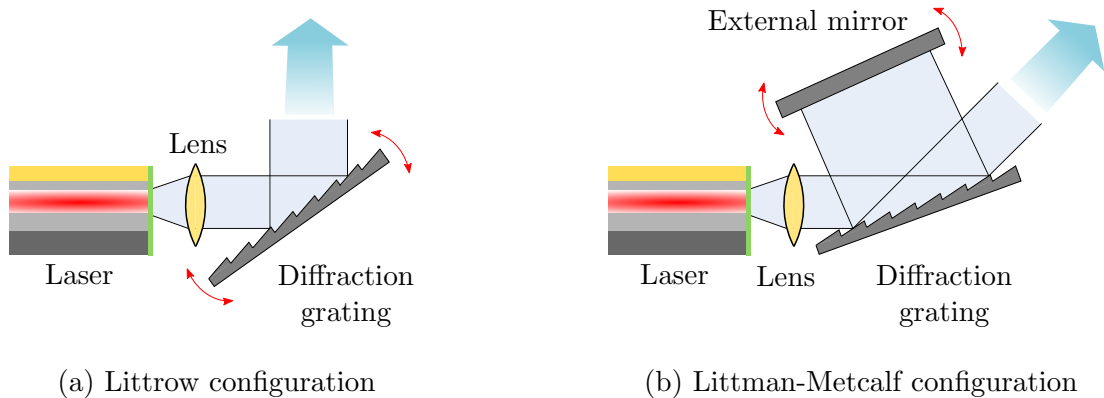


Fig. 2.19: Illustration of an anti-reflection coated semiconductor laser in external cavity configurations. (a) In the Littrow configuration, the wavelength is selected by rotating the diffraction grating. With the rotation, also the direction of the output beam changes. (b) For the Littman-Metcalf configuration, the grating remains fixed and the wavelength is tuned by rotating the mirror. The direction of the output beam is fixed, but at the expense of a reduced output power compared to the Littrow configuration.

In the Littrow configuration, shown in Fig. 2.19(a), the wavelength is tuned by rotating the diffraction grating. The wavelength-dependent reflectivity of the diffraction grating serves as the end mirror of the cavity. Hence, the optical cavity is not just determined by the semiconductor laser itself, but also by the external configuration. The emitted beam from the laser is collimated by the lens and impinges at an angle θ_i on the diffraction grating. The first-order diffracted beam exits the grating under an angle of $\theta_{r,m}$ and is fed back into the laser. The angle of the diffracted beam depends on the diffraction order m and can be calculated with the grating equation, given by [62]

$$d [\sin(\theta_i) + \sin(\theta_{r,m})] = m\lambda, \quad (2.75)$$

where d is the grating period and λ is the wavelength. The grating spatially separates the incident polychromatic beam by diffracting different orders under different angles $\theta_{r,m}$. For a maximum optical feedback, incident and diffracted beams need to be colinear ($\theta_{r,m} = \theta_i$), which represents a Bragg reflection with

$$2d \sin(\theta_G) = \lambda_G, \quad (2.76)$$

where the wave at λ_G is diffracted by the grating under an angle θ_G . The first-order diffracted beam is reflected back into the laser chip and experiences amplification, whereas the other wavelengths see higher losses. One drawback of the Littrow arrangement is the change of the emission angle with the tuning of the wavelength. This issue can be solved by placing a reflector after the grating and using the other laser facet as output. Another external cavity arrangement is the Littmann-Metcalf configuration [63], which is shown in Fig. 2.19(b). There, the diffraction grating is fixed and the wavelength is tuned by rotating an external mirror. The emission angle remains the same, which is preferable for many spectroscopic applications. Furthermore, the selectivity and the linewidth are commonly narrower due to the fact that the diffraction occurs twice per cavity round trip. However, in comparison to the Littrow configuration, a lower output power is obtained because the zero-order diffracted beam from the mirror is lost [64]. Compared to e.g. distributed-feedback gratings, external cavity configurations are more bulky and sensitive to mechanical vibrations. But they have the advantage of providing a fast tuning over a broad spectral range and also the phase noise in external cavity lasers is reduced due to the longer resonator length. Furthermore, they allow to incorporate other optical elements in the beam path. For mode-locking, e.g. elements such as saturable absorbers and optical filters can be easily integrated in the resonator. External cavity quantum cascade lasers can be used for stand-off detection of surface-contaminations with e.g. explosives [65]. With the development of broadband QCL gain materials, external cavity lasers achieve a tuning range of 432 cm^{-1} for light emission from 7.6 to $11.4 \mu\text{m}$ [66]. Microelectromechanical systems (MEMS) technology can improve the tuning capabilities and mechanical stability of tunable external cavity lasers significantly [9, 67, 68, 69].

2.4.4 Distributed Bragg grating

A plane wave impinging under normal incidence on the interface between two materials is partly transmitted and reflected. The reflectivity can be calculated with the Fresnel equation (2.38) considering the refractive indices n_1 and n_2 in both materials. A stack of alternating materials with the thicknesses d_1 and d_2 can form a so-called Bragg reflector (DBR). Fig. 2.20 schematically illustrates such material stack.

This structure behaves like a wavelength-dependent mirror due to a periodic variation of the refractive index. The incoming wave is partly reflected at each interface and the total

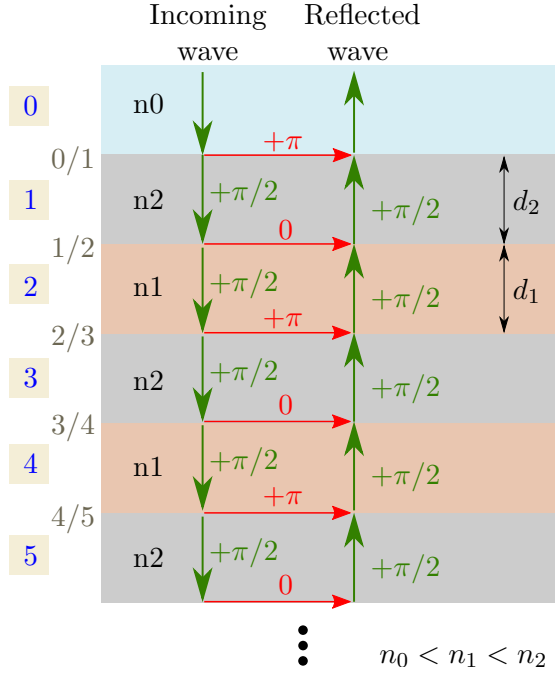


Fig. 2.20: Schematic illustration of the constructive superposition of the wave reflected at each interface in a distributed Bragg mirror. A plane wave propagating through a material of thickness $d_{1,2} = \frac{1}{4} \lambda_B / n_{1,2}$ experiences a phase shift of $\pi/2$. In addition, the reflections at the interfaces cause either a phase shift of π ($n_0, n_1 \rightarrow n_2$) or no shift ($n_2 \rightarrow n_0, n_1$). A plane wave incident from a material with refractive index n_0 , with $n_0 < n_1 < n_2$, experiences a total phase shift of $\pi, 3\pi, 5\pi$ etc. due to transmission through the materials and back reflection at the interfaces. Based on [70].

reflectivity is given by the sum over all contributions. For a constructive interference, the thicknesses of the materials need to be one quarter of the material wavelength,

$$d_1 = \frac{1}{4} \frac{\lambda_B}{n_1} \quad \text{and} \quad d_2 = \frac{1}{4} \frac{\lambda_B}{n_2}, \quad (2.77)$$

where λ_B is the Bragg wavelength in free-space. The wave then accumulates a phase shift of $\pi/2$ when travelling through a single layer (2π phase change over one wavelength). For a transition from a low index to a high refractive index material, the phase changes by π at reflection. For a transition from a high to a low index material, there is no phase change. A wave coming from layer 0, being reflected at the interface 1/2 and transmitted back to the surface experiences a total phase shift of $\pi/2 + 0 + \pi/2 = \pi$. A wave reflected at the interface 3/4 accumulates a total phase shift of $3 \times \pi/2 + 0 + 3 \times \pi/2 = 3\pi$. This can be continued for all interfaces and one arrives at an expression for the total phase shift between incoming and reflected wave $\Delta\phi = (2m + 1)\pi = \pi, 3\pi, 5\pi$ and so on ($m = 0, 1, 2, 3, \dots$). In this example, the reflected wave is shifted by a phase of π compared to the incoming plane wave. The whole material stack acts like a narrowband reflector around the Bragg wavelength. Defining the grating period Λ_g as the sum of the two layers gives

$$\Lambda_g = d_1 + d_2 = \frac{\lambda_B}{2} \left(\frac{1}{2n_1} + \frac{1}{2n_2} \right). \quad (2.78)$$

The term in the bracket can be written as an averaged refractive index $\bar{n} = 2/(1/n_1 + 1/n_2)$. With this relation, the Bragg wavelength can then be calculated to

$$m\lambda_B = 2\bar{n}\Lambda_g, \quad (2.79)$$

with the diffraction order $m = 1, 2, 3, \dots$ and the propagation constant at the Bragg wavelength reads $\beta_B = 2\pi/(\lambda_B/\bar{n})$. For small variations of the refractive indices of the materials $\Delta n = |n_2 - n_1| \approx 10^{-3}$, the total reflectivity can be calculated with coupled-mode theory [71]. It depends on the detuning $\Delta\beta = \beta - \beta_B$ of the light ($\beta = 2\pi/\lambda$) from the Bragg wavelength λ_B . The total (power) reflectivity for small detunings ($\Delta\beta < \kappa$) then reads [70]

$$R = \frac{\sinh^2(SL)}{\cosh^2(SL) - (\Delta\beta/\kappa)^2}, \quad (2.80)$$

with L the length of the grating, κ the coupling coefficient between forward and backward propagating wave and the complex-valued $S = \sqrt{|\kappa|^2 - \Delta\beta^2}$. Fig. 2.21 shows the reflectivity spectrum of a distributed Bragg grating. Within the stop band, the multilayer structure shows high reflectivities. For zero detuning ($S = |\kappa|$), the reflectivity at the Bragg wavelength is $R_{\text{Bragg}} = \tanh^2(|\kappa|L)$. Using a typical coupling strength of $|\kappa|L \approx 2$, the reflectivity can reach values of $R > 93\%$.

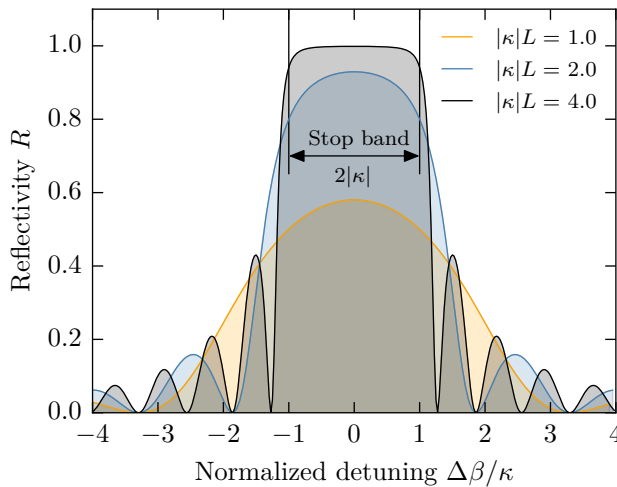


Fig. 2.21: Reflectivity spectrum of a distributed Bragg grating for different coupling strengths $|\kappa|L$. The detuning from the Bragg wavelength is given by $\Delta\beta = \beta - 2\pi/\lambda$. In the middle of the stop band, exactly at the Bragg wavelength ($\Delta\beta/\kappa = 0$), a peak reflectivity of $R_{\text{Bragg}} = 93\%$ is calculated for the multilayer structure with $|\kappa|L = 2$.

For larger refractive index steps, e.g. $\Delta n \approx 0.5$, the coupled-mode theory is not appropriate anymore [70]. The amplitude of the optical field changes significantly over propagation distance and in this case the grating problem is commonly treated by transfer-matrix methods [72].

Lateral Bragg grating

In lasers with a lateral distributed-Bragg grating, the active region is spatially separated from the frequency-selective grating. The corrugated gratings can be either single-sided with a cleaved facet on the other side or sandwich the active core from both sides. Fig. 2.22

illustrates a semiconductor laser with two passive lateral DBRs. Light emitted from the optical gain region in the plane of the grating experiences a feedback. The left- and right-going waves are coupled by the periodic modulation of the refractive index, leading to high reflectivities within the stop band. With current injection, the gain curve of the active region can be shifted spectrally (temperature-induced shift). However, as the reflector section is separated and not pumped electrically, the reflectivity of the DBR does not change. As a result, the lasing mode eventually shifts to a lower reflectivity region of the DBR section. The laser then can hop to another mode, which experiences lower losses by the mirror [73]. Lasers with lateral DBR gratings require a more sophisticated processing of the surface. Grating grooves need to be patterned and perhaps also regrown. Furthermore, the coupling region between active laser core and passive gratings is essential and requires more engineering effort.



Fig. 2.22: Illustration of a lateral distributed-Bragg reflector grating.

Vertical Bragg grating

A distributed-Bragg reflector grating can also be used in a vertical arrangement. The most prominent device which utilizes feedback in vertical direction is the vertical-cavity surface-emitting laser (VCSEL) [53]. An illustration of such a VCSEL device is shown in Fig. 2.23. The active region is sandwiched between two multilayer DBR mirrors, often also referred as Bragg stack. In contrast to lateral DBR layers, high reflectivities are obtained on a much shorter distance [70]. This is essential for the VCSEL, with the optical resonator oriented in growth direction, since the height of the active region is only on the order of the wavelength. This short cavity enables an inherent single-mode emission, as discussed in section 2.4.1. Within the plane-wave approximation, the reflectivity of the grating is given by [43, 74]

$$R_{\text{DBR}} = \left(\frac{1 - \gamma^{2N}}{1 + \gamma^{2N}} \right)^2, \quad (2.81)$$

with the refractive index contrast $\gamma = n_{\text{low}}/n_{\text{high}}$ between the two materials and the number of periods N . In order to reduce the thickness of the grown mirror, γ has to be increased. This shortens on one hand the growth time and is also beneficial for the thermal management of the structure. Depending on the device type and the target wavelength different material combinations are used for the alternating layers. For near-IR devices ($\lambda \approx 1 \mu\text{m}$) these can be a GaAs/AlAs multilayer structure or for interband cascade lasers ($\lambda \approx 4 \mu\text{m}$) an epitaxial AlAsSb/GaSb bottom mirror with a ZnSe/Ge dielectric top mirror. To achieve reflectivities close to unity, typically 20 – 25 periods are necessary.

With vertical Bragg gratings, very compact surface-emitting devices can be fabricated [75, 54]. Another advantage is the possibility to make a two-dimensional integration of multiple devices in an array [76, 77].

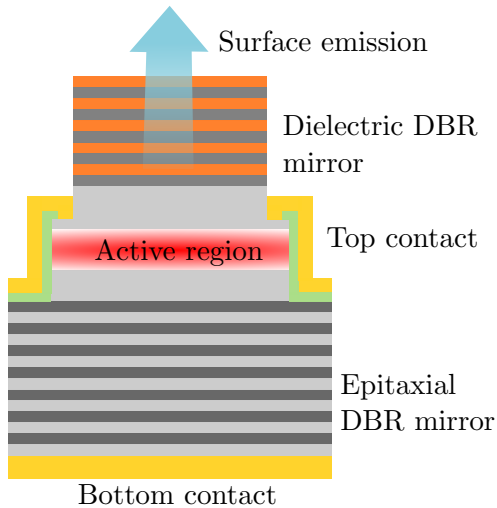


Fig. 2.23: Schematic illustration of a vertical-cavity surface-emitting laser VCSEL with distributed-Bragg mirrors below and on top of the active region. The DBRs act as frequency-selective reflectors for light propagating in growth direction. High reflectivities of the mirrors are necessary to compensate for the short gain region.

2.4.5 Distributed-feedback grating

Similarly to a DBR, the distributed-feedback DFB grating relies on the periodic modulation of the refractive index. In contrast to DBRs, the grating is integrated along the whole active region of the laser and thus no active-passive transition regions as in DBR lasers are needed. Furthermore, the refractive index contrast is usually smaller compared to DBR gratings. The DFB grating is etched into the waveguide layers of the laser device, as illustrated in Fig. 2.24.

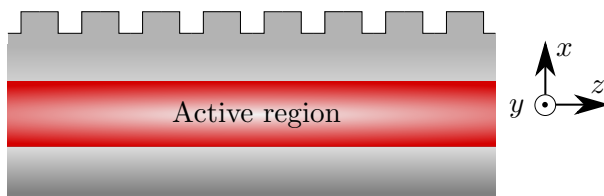


Fig. 2.24: Illustration of a DFB laser with the corrugated grating integrated along the active region.

The grating couples forward and backward propagating waves via Bragg scattering and constructive interference is only achieved for certain wavelengths. Spatial periodic structures of layered materials are of great importance in e.g. solid state electronics, mechanics, acoustics or optics. Knowledge of the physical behavior of such crystal-like material stacks enables to create new artificial materials with designable properties. Although these disciplines may examine different aspects and goals in engineering, the underlying mathematical description of periodical structures remains almost the same. Similarly to the formation of an energy band gap in semiconductors, caused by the periodic potential of the atoms,

also forbidden bands occur in optics. Due to the modulation of the refractive index, a photonic band gap arises in which no wave is allowed to propagate. Fig. 2.25 shows the simulated dispersion relation in a multilayer structure. The infinite crystal structure, illustrated in Fig. 2.25(a), consists of alternating material layers with refractive indices n_1 and n_2 , respectively. At the left and right boundaries Floquet periodicity conditions are used for the 2D-model implemented in COMSOL. The eigenfrequencies of the waveguide mode are computed for different wavevectors. A linear dispersion is observed when both materials have the same refractive index, shown in Fig. 2.25(b). The modulation of the refractive index $n_2 = n_1 + \Delta n$ results in the formation of a photonic band gap in the dispersion relation, as can be seen in Fig. 2.25(c) for $\Delta n = 0.5$. In Fig. 2.25(d) the index contrast between the two materials is increased to $\Delta n = 1$. As a result also the stop band increases. Engineering the optical properties of materials allows to control the flow of light. This design freedom is heavily used in e.g. photonic crystals [78].

Grating order

Similar to the DBR grating discussed in the previous section, also a DFB grating has to fulfill the Bragg condition at the free-space wavelength λ_B . It is given by

$$m \frac{\lambda_B}{2n_{\text{eff}}} = \Lambda_g, \quad (2.82)$$

with the grating order $m = 1, 2, 3, \dots$, the effective refractive index n_{eff} and the grating period Λ_g . In other words, for a second-order DFB grating ($m = 2$) the grating period has to equal the (reduced) wavelength λ_B/n_{eff} in the semiconductor material. If the condition from (2.82) is not met, then the grating is detuned and acts as a normal diffraction grating without feedback. As a result the light will be coupled out from the laser at an angle α to the surface normal. Fig 2.26 illustrates such a case, where a mode in a semiconductor is coupled by a diffraction grating into surface radiation.

To understand why the emission takes place under an angle α the projections of the propagation vectors on the surface are considered. The propagation vector of the guided laser mode is $\beta = \mathbf{k}_0 n_{\text{eff}}$, with the free-space propagation vector $|\mathbf{k}_0| = 2\pi/\lambda$ and the effective refractive index n_{eff} of the semiconductor. The (reciprocal) grating vector $|\mathbf{G}| = 2\pi/\Lambda_g$ is fixed by the grating period. At the interface semiconductor/air the tangential components of the vectors must satisfy

$$\mathbf{k}_0 n_0 \sin(\alpha) = \beta - m\mathbf{G}. \quad (2.83)$$

After rearranging the terms, the emission angle for radiation into a medium with refractive index n_0 (e.g. air with $n_0 = 1$) is given by

$$\alpha = \arcsin \left(\frac{n_{\text{eff}}}{n_0} - m \frac{\lambda}{\Lambda_g} \frac{1}{n_0} \right). \quad (2.84)$$

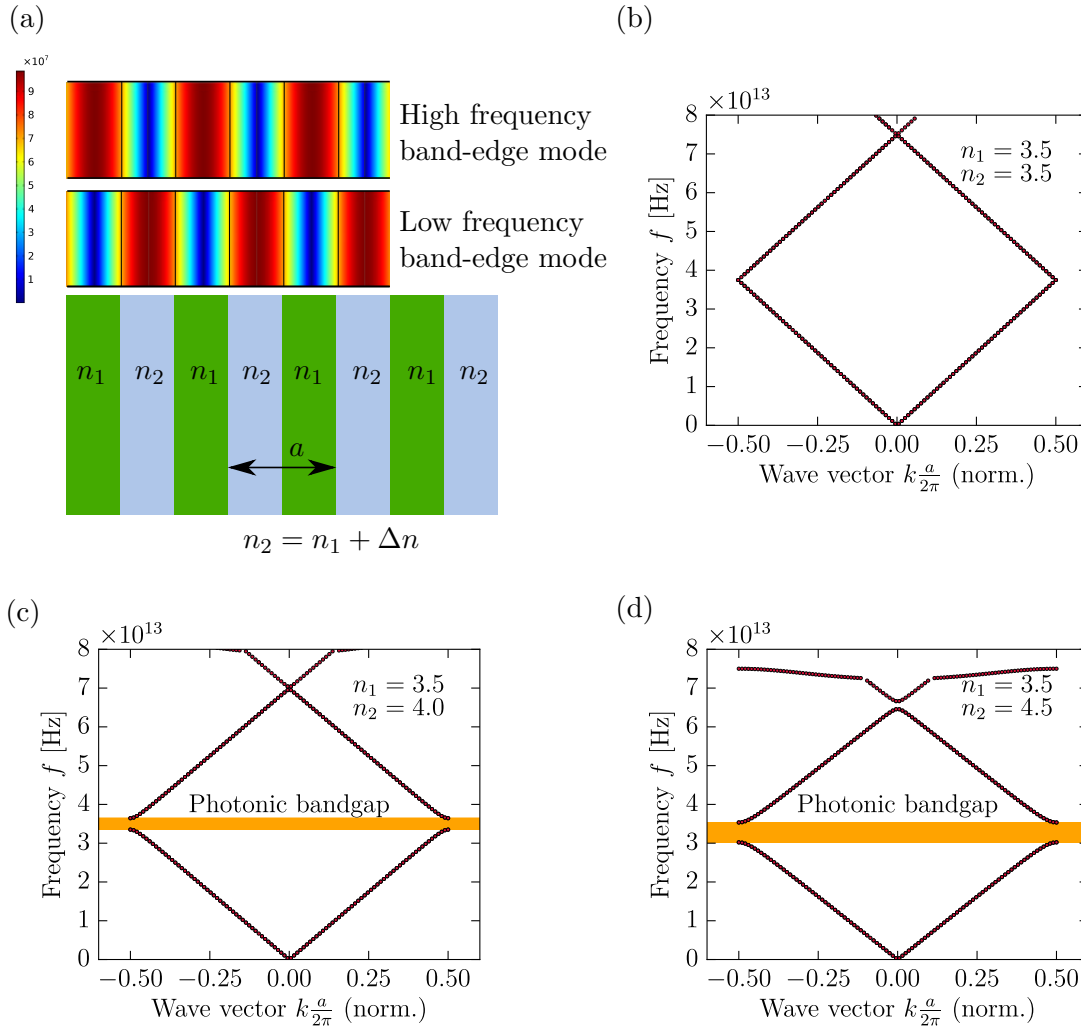


Fig. 2.25: Dispersion relation of a periodic structure. (a) The multilayer structure consists of alternating layers with refractive indices $n_1 = 3.5$ and $n_2 = n_1 + \Delta n$. Each layer has the same thickness $a/2$, where $a = 1.14 \mu\text{m}$ is the grating period. The multilayer stack is modelled with Floquet periodicity conditions at the left and right boundaries of an unit cell. Low and high frequency band-edge modes are plotted as normalized electric fields. (b) Dispersion relation for the case of zero refractive index contrast ($n_2 = n_1$). The wave vector k is swept in the 2D COMSOL simulation from $-\pi/a \dots +\pi/a$ and plotted against the eigenfrequencies of the obtained solutions. (c) With the modulation of the refractive index $\Delta n = 0.5$, a photonic bandgap opens in which wave propagation is forbidden (indicated by the orange shaded area). (d) An increase of the index contrast to $\Delta n = 1$ also increases the width of the frequency stop band. Based on [79, 78].

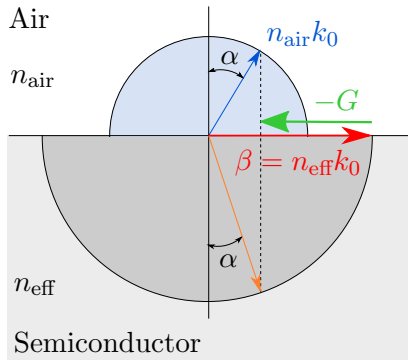


Fig. 2.26: Diffraction grating with a slightly detuned grating period Λ_g . The mismatch between grating vector $|\mathbf{G}| = 2\pi/\Lambda_g$ and the propagation vector $|\boldsymbol{\beta}| = n_{\text{eff}}2\pi/\lambda$ of the laser mode leads to an emission at the angle α .

In most cases however, the grating is intended to provide feedback at the Bragg wavelength and therefore also the grating period is adjusted to meet this requirement. Coming back to (2.82) shows that different diffraction orders m satisfy the Bragg condition. Each diffraction order has its own properties, which shall be discussed in the following.

1. First-order DFB grating

The grating vector \mathbf{G} equals twice the propagation vector $\boldsymbol{\beta}$. This allows a coupling between two counter-propagating modes and provides optical feedback. The emission is then in-plane (in longitudinal direction) from the facets of e.g. a ridge laser. An illustration of a first-order DFB grating is shown in Fig. 2.27(a).

2. Second-order DFB grating

Fig. 2.27(b) illustrates the case of a second-order DFB grating. Compared to a first-order grating, the grating period is twice as large for a second-order grating. The length of the grating vector matches the length of the propagation vector of the guided mode $|\mathbf{G}| = |\boldsymbol{\beta}|$. Inserting this into (2.83) shows that the first-order Bragg scattering ($m = 1$) couples the guided laser mode to a radiating mode $\boldsymbol{\beta}_{\text{rad}} = \mathbf{k}_0 n_0 \sin(\alpha)$. From $\boldsymbol{\beta}_{\text{rad}} = \boldsymbol{\beta} - \mathbf{G} = \mathbf{0}$ it follows that the radiation is directed perpendicular to the grating with $\alpha = 0^\circ$ and 180° , corresponding to surface and substrate emission. The feedback however is only provided by the second-order Bragg scattering ($m = 2$). The DFB grating couples the laser mode $\boldsymbol{\beta}$ via two grating vectors into the counter-propagating mode $-\boldsymbol{\beta} = \boldsymbol{\beta} - 2\mathbf{G}$. Fig. 2.27(c) shows the dispersion diagram for the second-order DFB grating. Light out-coupling is only possible if $\boldsymbol{\beta}_{\text{rad}}$ lies within the light cone (blue-shaded area).

3. Higher-order DFB gratings

From (2.82) it can be seen that the grating order m of a DFB grating is direct proportional to the grating period Λ_g . Hence, higher-order gratings are technologically easier to fabricate as the width of the etched grooves are much larger. Therefore, gratings with integer multiples of a first-order DFB grating are used to avoid complicated lithographic patterning. For a laser emitting at $\lambda = 4 \mu\text{m}$ the grating period for a first-order grating is e.g. 625 nm , while a fourth-order grating with $\Lambda_g = 2.5 \mu\text{m}$ can be fabricated with standard photolithographic techniques. An interesting feature of third-order DFB gratings can be achieved if the waveguide is engineered in such a way that the effective refractive index becomes $n_{\text{eff}} = 3$. Then the grating vector is $\mathbf{G} = 2\boldsymbol{\beta}/3$ and the light is coupled out from the laser, but propagates in

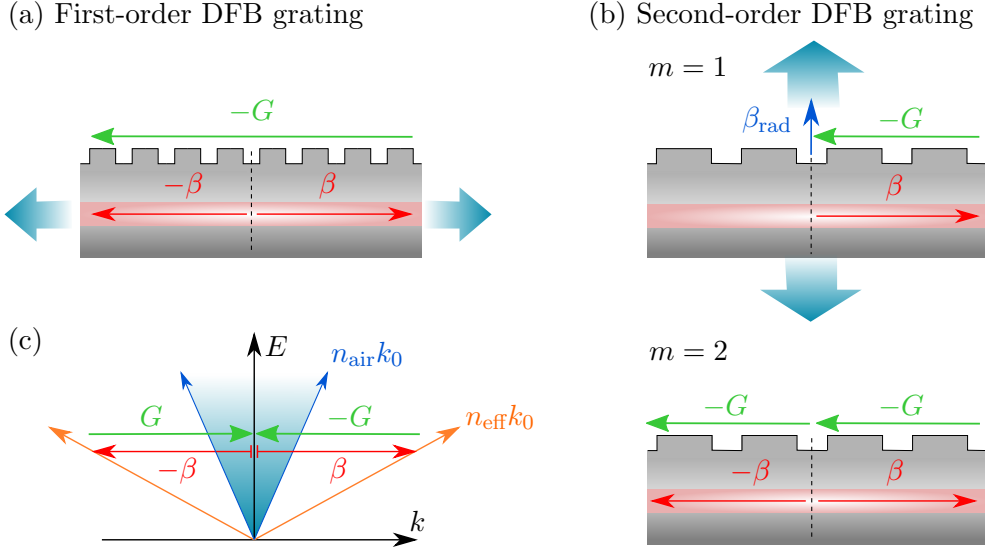


Fig. 2.27: Illustration of the diffraction behavior of (a) first-order DFB gratings and (b) second-order DFB gratings. In the latter case the first-order diffraction ($m = 1$) leads to surface/substrate emission, while the second-order diffraction ($m = 2$) couples the counter-propagating modes and hence is responsible for the optical feedback. (c) The dispersion diagram for the second-order grating shows that coupling from the laser mode β to a radiating mode is only possible if the grating provides such a feedback that the resulting vector β_{rad} lies within the light cone (blue-shaded area).

longitudinal direction parallel to the laser [80].

In this thesis the optical feedback and out-coupling from ring lasers is accomplished with second-order DFB gratings. The light is emitted towards the surface and the substrate in vertical direction. Hence, the total losses for a second-order DFB laser can be written as

$$\alpha_{\text{total}} = \alpha_{\text{wg}} + \alpha_{\text{surf}} + \alpha_{\text{sub}}, \quad (2.85)$$

where α_{wg} are the waveguide losses (absorption losses), α_{surf} are the surface emission losses and α_{sub} are the substrate emission losses, all in units of $[\text{cm}^{-1}]$. For common applications, light emission with high out-coupling efficiency just in one direction is required. Therefore, the grating has to be engineered to suppress the radiation in the opposite direction. This can be achieved by a proper waveguide and grating design. The grating parameters etch depth and duty-cycle influence the surface/substrate emission losses [81]. Finding a good and robust parameter set for the fabrication of the DFB grating demands for an accurate theoretical description of the problem.

In the following, theories for calculating the properties of spatial periodic structures are discussed more in detail. The most prominent is the *coupled-mode theory* by Kogelnik and Shank [71], which however is restricted to small periodic modulations only. The coupled

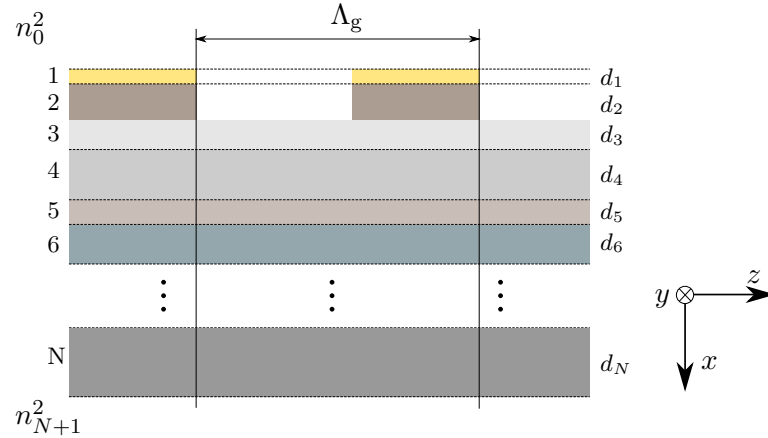


Fig. 2.28: Illustration of a multilayer structure with periodic repetition in z -direction. Each material layer has a certain thickness d and is represented by a complex-valued refractive index n . Based on [83].

mode theory provides only an approximation method for spatial periodic structures. A more general approach is based on the *Floquet-Bloch theory*, which is also applicable to strong index and gain modulations, which are present in e.g. DFB metal gratings. Herein, the exact Floquet-Bloch solutions of the infinite long waveguide structure are calculated. For small periodic perturbations the solutions match with those obtained by coupled-mode theory. The Floquet-Bloch theory is presented first as it describes the problem without any restrictions and afterwards the limited cases for the coupled-mode theory are discussed in further detail.

Floquet-Bloch theory

Starting point for calculating the properties of spatial periodic multilayer structures, as e.g. the one illustrated in Fig. 2.28, is the wave equation [82]

$$\frac{d^2 E}{dz^2} + k^2(\omega, z)E = 0, \quad (2.86)$$

where the amplitude of the electric field E oscillates with $\exp(j\omega t)$. The complex function $k(\omega, z)$ has the same periodicity Λ_g as the grating:

$$k(\omega, z) = k(\omega, z + \Lambda_g) = n(z)\frac{\omega}{c_0} + j\alpha(z). \quad (2.87)$$

The last term corresponds to a complex-valued refractive index, which is split here explicitly in real and imaginary part. The refractive index $n(z)$ and the gain $\alpha(z)$ have the same spatial periodicity

$$n(z) = n(z + \Lambda_g) \quad \text{and} \quad \alpha(z) = \alpha(z + \Lambda_g). \quad (2.88)$$

Type	Periodic function	$n(z)$	$\alpha(z)$
passive	$k(\omega, z) = n(z)\frac{\omega}{c}$	$\neq \text{const.}$	0
pure index modulation	$k(\omega, z) = n(z)\frac{\omega}{c} + j\alpha$	$\neq \text{const.}$	const.
pure gain modulation	$k(\omega, z) = n\frac{\omega}{c} + j\alpha(z)$	const. ≥ 1	$\neq \text{const.}$
combined modulation	$k(\omega, z) = n(z)\frac{\omega}{c} + j\alpha(z)$	$\neq \text{const.}$	$\neq \text{const.}$

Tab. 2.2: Characteristic wave equations for different types of spatial periodic structures with modulations of the refractive index $n(z)$ and/or the gain $\alpha(z)$.

From a mathematical point of view (2.86) is a second-order linear ordinary differential equation also known as *Hill's differential equation*. Solutions of this differential equation with the spatial periodic function k are described by the Floquet theory. Hill's differential equation appears in many applications in physics. For instance the time-independent one-dimensional Schrödinger equation for a particle in a periodic potential $V(x+a) = V(x)$, which is given by

$$\left[-\frac{\hbar^2}{2m} \vec{\nabla}^2 + V(x) \right] \psi(x) = E\psi(x), \quad (2.89)$$

also has the same mathematical structure as (2.86). For DFB lasers, the general solutions of the wave equation determine the properties of the modes for the infinite grating structure. A periodic perturbation of the laser with the period L leads to a periodic dispersion relation with the period $\Delta\beta = 2\pi/L$. Adding boundary conditions, which are dictated by the finite length of the laser, the resonance frequency as well as the threshold gain for each mode can be calculated [82]. Depending on the modulation of refractive index $n(z)$ and/or the gain $\alpha(z)$, different coupling schemes are distinguished. Tab. 2.2 summarizes different types of modulations in periodic structures. The passive structure corresponds to the aforementioned example of the one-dimensional Schrödinger equation. The cases of pure index or gain modulation and combined modulation are important for DFB laser.

Due to the periodicity of the refractive index in z -direction, the Floquet-Bloch theorem $\Phi(x, z + m\Lambda_g) = \exp(j\beta_0 m\Lambda_g)\Phi(x, z)$, with $m = 0, \pm 1, \pm 2, \dots$, can be applied to the electromagnetic field [83]. To give an idea how the Floquet-Bloch method is applied to the waveguide-grating problem, a representative multilayer structure is discussed. Considering the case where the electric field also changes along the x -axis (in growth direction). Fig. 2.28 shows the corresponding multilayer structure together with the coordinate system. The wave equation takes the form

$$\frac{d^2 E(x, z)}{dx^2} + \frac{d^2 E(x, z)}{dz^2} + k_0^2 n^2(x, z) E(x, z) = 0, \quad (2.90)$$

where $k_0 = 2\pi/\lambda$ is the free-space wavevector. The refractive index $n(x, z)$ is considered as complex-valued function, which already includes the gain/absorption. The electric field

can be expanded into a Fourier series

$$E(x, z) = \sum_{m=-\infty}^{\infty} E_m(x, z) e^{-j\beta_m z}, \quad (2.91)$$

where the partial waves $E_m(x, z)$ vary only slowly in z -direction. The propagation constant of the m -th partial wave is given by

$$\beta_m = \beta_0 + \frac{2\pi}{\Lambda_g} m. \quad (2.92)$$

Similar to the electric field, also the refractive index can be expanded into a Fourier series, which is given by

$$n^2(x, z) = n_0^2(x) + \sum_{q=-\infty, q \neq 0}^{\infty} A_q(x) e^{-j\frac{2\pi}{\Lambda_g} qz}, \quad (2.93)$$

where the zeroth-order term $n_0^2(x)$ is the dielectric function for which the grating is described by an average dielectric constant [84]. Inserting (2.91) and (2.93) into (2.90) gives an equation for TE-polarized waves [85]

$$\frac{d^2 E_m}{dx^2} + [k_0^2 n_0^2(x) - \beta_m^2] E_m = -k_0^2 \sum_{q=-\infty, q \neq 0}^{\infty} A_{m-q}(x) E_q(x). \quad (2.94)$$

The solutions of this equation are obtained by applying the continuity boundary condition at the interfaces between the layers, shown in Fig. 2.28. The calculated partial waves E_m are then summed up in (2.91) to get the electric field in the waveguide. However, for practical purposes the infinite set of Floquet-Bloch partial waves is truncated to orders of e.g. $m = \pm 20$ to ± 100 . This finite set of plane waves leads to relative errors of typically 10^{-4} for $\text{Re}\{\beta_0\}$ and below 2% for $\text{Im}\{\beta_0\}$ [86]. At resonance, the guided partial wave E_0 ($m = 0$) propagates in the $+z$ direction, while the surface/substrate emission field E_{-1} radiates perpendicular in growth direction. With a similar partial-wave expansion as presented above, also the magnetic field can be decomposed into partial waves

$$H(x, z) = \sum_{m=-\infty}^{\infty} H_m(x, z) e^{-j\beta_m z}. \quad (2.95)$$

A theoretical approach for calculating the Floquet-Bloch solutions for TM-polarized second-order DFB grating structures is developed by Finger and Gornik [86]. The simulations of the DFB gratings in this thesis are based on a program implemented by N. Finger in MATLAB [83]. It can handle TE- and TM-polarized grating structures with different grating orders and allows to calculate important design parameters based on the Floquet-

Bloch formalism. As there is no restriction to weak periodic refractive index modulations, also strong gratings incorporating metals with permittivity contrasts of $\Delta\epsilon = 10^2 \dots 10^4$ and deep grating etch depths can be analyzed.

Calculations of Noll and Macomber [84] suggest that there are only two resonant solutions for the infinite grating problem, which is a symmetric and an antisymmetric mode. This result is similar to the energy splitting of an electron in the periodic potential of a lattice. At the edge of the Brillouin zone, two solutions with different energies exist for the same wave vector. Fig. 2.29 shows the mode profiles (TM) for an infinite long DFB grating (second-order) with the two resonant solutions. The symmetric mode is identified as the radiating mode, while the antisymmetric solution is non-radiating towards the surface. For the latter case, magnetic field and z-polarized electric field E_z feature lobes of opposite sign between the grating teeth. The field destructively interferes and therefore no surface emission takes place.

Connection to coupled-mode theory The successful coupled-mode theory [71], which will be discussed more in detail in section 2.4.5, has the advantage of providing the physical picture of two counter-propagating modes, being responsible for the coupling and thus the grating feedback behavior. In order to relate the Floquet-Bloch approach to the coupled-mode theory, the former method is extended to provide comparable quantities such as radiation coefficients and coupling constants. Therefore, the Floquet-Bloch solutions of the infinite grating problem are used to calculate the properties of the finite-length grating. For instance the total magnetic field in the finite-length structure is obtained by a linear superposition

$$H(x, z) = A(z)H^+(x, z) + B(z)H^-(x, z), \quad (2.96)$$

where H^+ and H^- are the right-going and left-going Floquet solutions with the corresponding propagation constants β_0 and $-\beta_0$. The amplitudes $A(z)$ and $B(z)$ are assumed to vary slowly. In this conventional coupled-mode formalism forward- and backward propagating modes are considered [71, 84, 86]. Another similar approach uses a superposition of symmetric and antisymmetric eigenmodes of the infinite DFB grating [87, 88]

$$H(x, z) = A^s(z)H^s(x, z) + B^a(z)H^a(x, z) \quad (2.97)$$

$$= A(z) \left[\frac{H^s(x, z) + H^a(x, z)}{2} \right] + B(z) \left[\frac{H^s(x, z) - H^a(x, z)}{2} \right], \quad (2.98)$$

with the symmetric and antisymmetric eigenmodes H^s and H^a . Comparing (2.98) to the conventional ansatz (2.96) shows that the superposition of symmetric and antisymmetric eigenmodes is only an approximation. The terms $(H^s + H^a)$ and $(H^s - H^a)$ already contain components of the forward- and backward-propagating plane waves [87]. However,

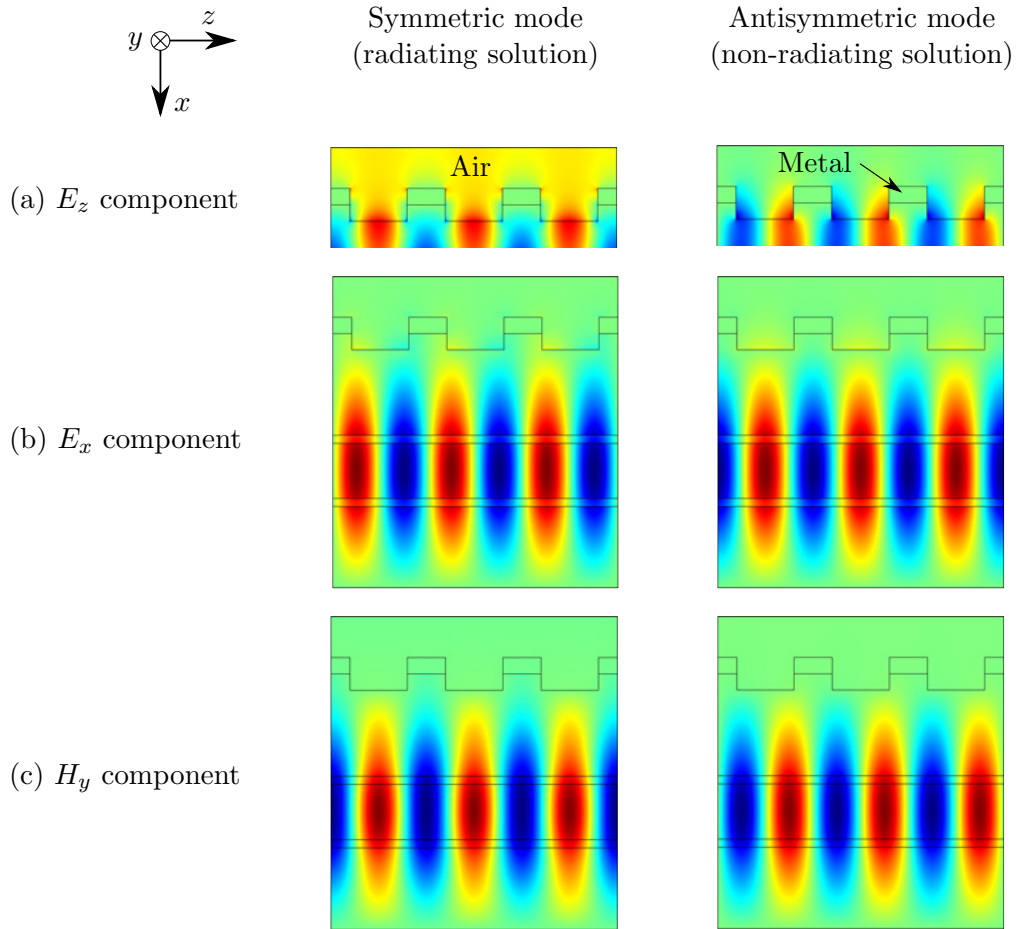


Fig. 2.29: Simulation of symmetric and antisymmetric modes in an infinite-long waveguide with a second-order DFB grating. A grating period of $2.34\ \mu\text{m}$ is chosen for the surface-emitting DFB laser at $\lambda \approx 8\ \mu\text{m}$. Periodic boundary conditions are set at the left and right edges. (a) Electric field (E_z -component) in the upper part of the waveguide and the DFB grating section. (b) Distribution of the electric field (E_x component) and (c) the magnetic field (H_y component) in the laser. The mode in the first column has an eigenfrequency of $f_{\text{sym}} = 3.7934 \times 10^{13}\ \text{Hz}$ and the field distribution is symmetric with respect to E_z . Therefore the field constructively interferes and surface emission in vertical direction is possible. On the other hand, the mode in the second column has an eigenfrequency of $f_{\text{asym}} = 3.7943 \times 10^{13}\ \text{Hz}$ and is antisymmetric in E_z . The field destructively interferes in the grating openings and hence this solution is referred as non-radiating.

in both cases the amplitudes $[A(z), B(z)]$ or $[A^s(z), B^s(z)]$ satisfy the same coupled-mode equations, which are discussed more in detail in the next section 2.4.5. An important parameter for DFB gratings is the complex coupling coefficient κ . It is derived from the overlap integrals of the rigorously computed Floquet-Bloch waves at resonance and the unperturbed waveguide fields. Details about the calculation can be found in [86, 83]. Absorption and radiation losses cause an exponential decay of the Poynting vector $S(x, z) \propto e^{-\alpha z}$ with the power attenuation constant $\alpha = 2 \text{Im}\{\beta_0\}$ [83]. The emitted power towards the surface is evaluated at the interface grating layer/vacuum by applying Poynting's theorem (A.20). From this, the radiation losses are calculated [86] to be

$$\alpha_{\text{surf,TE}} = \frac{|\mathbf{k}_0|}{|\mathbf{G}|} |R_{\text{surf}}|^2 \text{Re}\{n_0\} \quad \text{for TE polarization,} \quad (2.99)$$

$$\alpha_{\text{surf,TM}} = \frac{|\mathbf{k}_0|}{|\mathbf{G}|} |R_{\text{surf}}|^2 \text{Re}\left\{\frac{1}{n_0}\right\} \quad \text{for TM polarization,} \quad (2.100)$$

with the free-space wave vector $|\mathbf{k}_0| = 2\pi/\lambda$, the grating vector $|\mathbf{G}| = 2\pi/\Lambda_g$, the amplitude of the radiation field R_{surf} and the refractive index of vacuum $n_0 = 1$. Similarly, the substrate radiation loss is governed by

$$\alpha_{\text{sub,TE}} = \frac{|\mathbf{k}_0|}{|\mathbf{G}|} |R_{\text{sub}}|^2 \text{Re}\{n_{\text{sub}}\} \quad \text{for TE polarization,} \quad (2.101)$$

$$\alpha_{\text{sub,TM}} = \frac{|\mathbf{k}_0|}{|\mathbf{G}|} |R_{\text{sub}}|^2 \text{Re}\left\{\frac{1}{n_{\text{sub}}}\right\} \quad \text{for TM polarization,} \quad (2.102)$$

with the amplitude R_{sub} evaluated at the interface cladding/substrate and the refractive index n_{sub} of the substrate material. The total losses α_{total} are then the sum of absorption and radiation losses. Goal of the grating design is to achieve low absorption losses together with sufficient out-coupled radiation.

Coupled-mode theory

The "coupled-wave theory" for distributed-feedback lasers was developed by Kogelnik and Shank in 1972 [71]. It is also based on the scalar wave equation (2.86) but restricts itself to only small perturbations of the refractive index and the gain along the propagation direction. It is worth to mention that the name of the theory has changed since their initial publication. Nowadays, the term "coupled-mode" theory is used instead throughout the literature. Kogelnik and Shank solved the grating problem for pure index and gain coupling, where the coupling coefficient κ is either real or imaginary. The coupled-mode theory was further developed by Streifer et al. [89] by including radiation effects, the complex coupling scheme and other wave interactions. Kazarinov and Henry proposed in 1985 a theoretical study of a semiconductor laser with a second-order DFB grating for

surface emission [90]. The mode selection between two modes is based on engineering the radiation losses. The radiation can be seen as the result of the superposition of two counter-propagating waves that form the waveguide mode.

In the following, the basic theoretical framework of coupled-mode theory is discussed. Assuming a DFB grating along the z -direction, then the weak periodic spatial modulation of the refractive index $n(z)$ and the gain (loss) $\alpha(z)$ can be written as

$$n(z) = n_0 + \Delta n \cos\left(\frac{2\pi}{\Lambda_g} z\right) \quad (2.103)$$

$$\alpha(z) = \alpha_0 + \Delta\alpha \cos\left(\frac{2\pi}{\Lambda_g} z\right), \quad (2.104)$$

where n_0 and α_0 are the average values of the parameters of the medium, Δn and $\Delta\alpha$ are the amplitudes of the modulation and $|\mathbf{G}| = G = 2\pi/\Lambda_g$ is the (reciprocal) grating vector. Furthermore, the theory assumes that the laser oscillates close to (or at) the Bragg wavelength ($\lambda \approx \lambda_B$) with only weak perturbations $\Delta n \ll n_0$ and $\Delta\alpha \ll \alpha_0$. With that assumptions, the complex Hill's differential equation (2.86) simplifies to *Mathieu's differential equation*. The periodic function then reduces to $k(z) = k_0 + \Delta k \cos(z)$, which corresponds to the zeroth and first order components of a Fourier series. In contrast to the Floquet-Bloch approach, the higher order terms are neglected in the coupled-mode approximation. The electric field in the structure is constructed by the superposition of two counter-propagating waves

$$E(z) = R(z)e^{-j\beta_0 z} + S(z)e^{j\beta_0 z}, \quad (2.105)$$

where $R(z)$ is the complex amplitude of the "reference" wave and $S(z)$ of the "signal" wave. This terminology has been introduced by Kogelink for thick hologram gratings [91]. Only these two waves approximately fulfill the Bragg condition, while all other diffraction orders violate it and therefore are neglected. Inserting the ansatz (2.105) into the wave equation (2.86) gives a pair of coupled-mode equations [71]

$$-\frac{dR(z)}{dz} + [\alpha - j\delta] R(z) = j\kappa S(z), \quad (2.106)$$

$$\frac{dS(z)}{dz} + [\alpha - j\delta] S(z) = j\kappa R(z), \quad (2.107)$$

with the detuning from the Bragg frequency $\delta = (\beta^2 - \beta_0^2)/2\beta \approx \beta - \beta_0$. The coupling coefficient κ is calculated to be

$$\kappa = \frac{\pi\Delta n}{\lambda_B} + j\frac{\Delta\alpha}{2}. \quad (2.108)$$

It is a measure for the mutual coupling between forward and backward propagating wave and hence determines the strength of the feedback provided by the grating [71]. For second-order DFB gratings another self-coupling coefficient $j\zeta$ needs to be added to the term in the square brackets in (2.107) [84]. Once the coupling κ and the device geometry are known, the coupled-mode equations (2.107) can be solved by applying the appropriate boundary conditions, e.g. $R(z = -L/2) = S(z = L/2) \stackrel{!}{=} 0$, for a laser of length L . The solutions $R(z)$ and $S(z)$ then describe the distribution of the electromagnetic mode in the laser with the DFB grating. Finally, the threshold gain (intensity) can be derived, which is given by [84]

$$g_{\text{th}} = 2\alpha + \alpha_{\text{wg}}, \quad (2.109)$$

with the absorption loss in the waveguide α_{wg} . An important quantity for surface-emitting DFB lasers is the outcoupling efficiency [92]

$$\eta_{\text{surf}} = \alpha_{\text{surf}} \frac{k_0 \operatorname{Re}\{n_{\text{active}}\}}{G} \frac{\int |R(z) + S(z)|^2 dz}{\int |R(z)|^2 + |S(z)|^2 dz}, \quad (2.110)$$

with the magnitude of the free-space wave vector $k_0 = 2\pi/\lambda$, the grating wave vector $G = 2\pi/\Lambda_g$, the refractive index n_{active} of the active region, the confinement factor Γ and the gain g_0 in the active region. The surface emission loss α_{surf} has been already calculated in (2.99). In a similar fashion the outcoupling efficiency η_{sub} for substrate-emitting second-order DFB gratings can be calculated, considering the substrate radiation loss α_{sub} derived in (2.102).

Coming back to the coupling coefficient κ defined in (2.108), the coupling strength $|\kappa|L$ indicates whether the DFB grating enables a stable single-mode emission. Typical values are $|\kappa|L \sim 1$ to 5, as an undercoupled grating with $|\kappa|L \ll 1$ most likely cannot provide enough feedback. Furthermore, special cases for DFB gratings can be distinguished.

Depending on the real and imaginary part of κ , gratings are categorized in index coupled (κ real), gain coupled (κ imaginary) and complex coupled (κ mixed). Each coupling type has its characteristic properties, which manifest in certain mode spectra and threshold gains. Fig. 2.30 shows a comparison between an index and a gain coupled DFB laser.

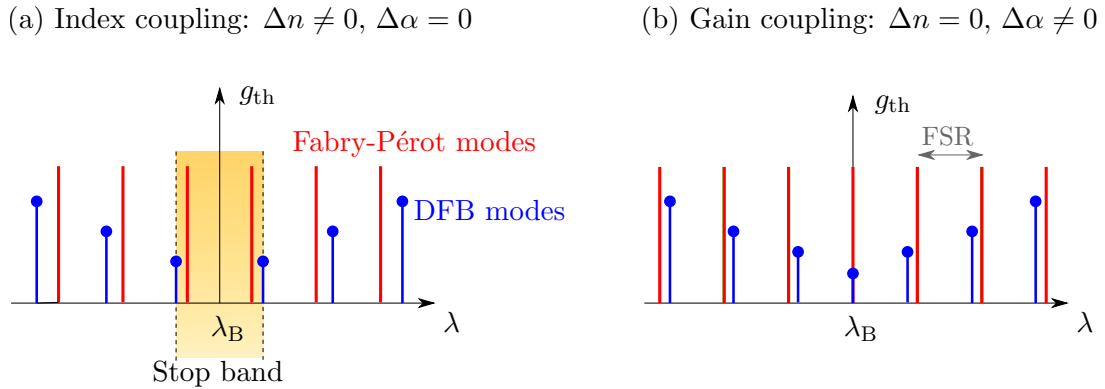


Fig. 2.30: (a) Illustration of the mode spectrum and corresponding threshold gains g_{th} for index coupling. Two DFB modes at edges of the stop band feature the lowest threshold gains. There is no mode the Bragg wavelength λ_{B} , because propagation is forbidden within the stop band. (b) On the other hand, a gain coupled DFB grating can excite a mode at λ_{B} . There is no stop band for gain coupling. Similar to index coupling the threshold gain increases with increasing spacing from the Bragg wavelength. For a small coupling the DFB modes are close to the Fabry-Pérot modes of the unperturbed resonator, which are separated by the free spectral range (FSR).

Index coupling

If the modulation of the real part $\Delta n \neq 0$ and the gain/loss modulation is $\Delta\alpha = 0$, then the coupling coefficient κ in (2.108) is also real-valued. A more detailed analysis with e.g. coupled-mode theory shows that lasers with index coupling show no emission at the Bragg wavelength λ_{B} . However, a frequency stop band is found, which is centered at λ_{B} . Two modes at the edges of the stop band experience the lowest (equal) threshold gains. For larger detunings from the Bragg wavelength more resonances occur, but the threshold gains are higher for these modes. An illustration is shown in Fig. 2.30(a). With increasing coupling coefficient κ , an increase of the stop band (symmetric with respect to λ_{B}) width can be observed. The degeneracy of the two band edge modes can be lifted by destroying the symmetry of the grating e.g. by modifying the mirror reflectivity at one facet. With this approach the losses for one of the two modes increases and only a single mode remains. Another possibility is to incorporate a phase shift of $\lambda/4$ in the center of the grating. The quarter wave shift leads to an exponentially decaying defect mode within the photonic band [79]. In contrast to the modes at the edges of the stop band, this defect-mode is then located at the Bragg wavelength.

Real devices are never perfect symmetrical and hence most likely only one of the two band-edge modes will be excited. An asymmetric gain/loss profile or unavoidable imperfections in the fabrication process may increase the losses for one mode. However, a priori it is not

known which one of the two modes this will be. A laser with an unpredictable emission wavelength is not useful for spectroscopic applications.

Gain coupling

In the case of gain coupling, lasing is possible at the Bragg wavelength, as illustrated in Fig. 2.30(b). The modulation $\Delta n = 0$, but the periodic gain/loss modulation is $\Delta\alpha \neq 0$, which results in a purely imaginary coupling coefficient κ . The DFB grating can be created by gain, absorption or radiation loss gratings [93]. An absorption grating may not be the best choice, since it relies on periodic losses, which waste energy and cause the laser to heat up. Radiation loss gratings can be realized with e.g. second-order DFB gratings. The longitudinal mode at λ_B experiences the lowest losses. All other modes have higher losses and the distance between two DFB modes is close to the intermodal spacing (FSR) of the free cavity modes, e.g. Fabry-Pérot modes. Despite the fact that no frequency stop band is apparent, a forbidden gap opens for the propagation constant β_0 [71].

Complex coupling

Fig. 2.31 illustrates the modal threshold gains for DFB gratings with a complex coupling coefficient. Here, $\Delta n \neq 0$ and $\Delta\alpha \neq 0$, which resembles a mixture between index and gain coupling. Depending on the magnitude of the real and imaginary contribution to the coupling constant, the frequency spectrum and threshold gains may change. However, the behavior of a complex coupled DFB laser is still closely related to the pure gain coupling scheme [82]. In general, complex coupling removes the degeneracy of the modes, which improves the mode selectivity [94]. Another aspect is introduced by the Kramers-Kronig relations, which link the real and imaginary part of the refractive index. A variation of the real part impacts the dissipation losses and vice versa [41]. The ring lasers presented in this thesis are commonly complex coupled second-order DFB lasers.

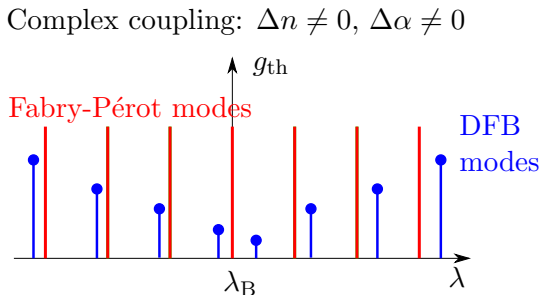


Fig. 2.31: Illustration of the threshold gain spectrum for a DFB grating with complex coupling. The presence of gain lifts the mode degeneracy and stable single-mode emission can be achieved. Depending on the relative strengths of the real and imaginary part of κ , the spectral behavior can be strongly asymmetric.

Ring DFB lasers

Solutions of the coupled mode theory are commonly derived for ridge lasers with first-order DFB gratings. An approach to extend the theory to surface-emitting ring lasers with

second-order DFB gratings is investigated together with C. Sigler and Prof. Botez from the University of Wisconsin-Madison. In contrast to finite-length ridges, the boundary conditions for ring-shaped resonators are given by

$$R(z) = R(z + 2\pi r_{\text{eff}}) \quad (2.111)$$

$$S(z) = S(z + 2\pi r_{\text{eff}}), \quad (2.112)$$

where $R(z)$ and $S(z)$ are the clock-wise and counter-clock-wise traveling waves and r_{eff} is the effective radius. After one roundtrip the waves have to merge with itself and therefore they need to be spatial periodic. This condition can be formulated in matrix notation

$$\begin{bmatrix} R(z_0 + z) \\ S(z_0 + z) \end{bmatrix} = \mathbf{M}(z, \alpha, \delta) \begin{bmatrix} R(z_0) \\ S(z_0) \end{bmatrix}, \quad (2.113)$$

with the reference position z_0 and the 2×2 matrix $\mathbf{M}(z, \alpha, \delta)$, which depends on the loss α and detuning δ of the DFB grating. The transfer matrix \mathbf{M} relates the forward and backward propagating field amplitudes [82]. With the boundary conditions (2.112) the matrix formulation of the problem then reads

$$\begin{bmatrix} R(z + 2\pi r_{\text{eff}}) \\ S(z + 2\pi r_{\text{eff}}) \end{bmatrix} = \begin{bmatrix} R(z) \\ S(z) \end{bmatrix} \quad (2.114)$$

$$= \mathbf{M}(2\pi r_{\text{eff}}, \alpha, \delta) \begin{bmatrix} R(z) \\ S(z) \end{bmatrix}, \quad (2.115)$$

which requires that \mathbf{M} has an eigenvalue of 1 for a particular set of (α, δ) . For an uniform ring the solutions are given by the infinite symmetric and antisymmetric modes. They naturally fulfill the boundary conditions and hence are solutions of the coupled-wave equations.

2.5 Device characterization setups

The characterization techniques used for interband and quantum cascade lasers are very similar. So they can be described before each technology is explained more in detail in the subsequent chapters. After the fabrication of the lasers the chip is soldered with indium or silver paste onto copper submounts (15 mm \times 25 mm). For electrical connection, the devices are ultrasonic wire bonded with $\sim 25 \mu\text{m}$ thick Au bond wires to a printed circuit board. For high duty-cycle or cw operation of the lasers, multiple wires are necessary as a single wire only sustains a maximum current of around 100 mA. This current limitation becomes

a more severe issue for devices mounted in an evacuated cryostat since the vacuum (10^{-5} to 10^{-6} mbar) prevents the heat dissipation from the wire. Depending on the size of the device and its electrical power requirement, typically 3 – 4 wires are sufficient for the ring lasers used in this work. The laser devices are characterized in terms of current/voltage, optical output power, spectral response and beam profile in the nearfield and farfield domain.

2.5.1 Electrical and optical characterization

Measurements of the optical output power (light), current and voltage (LIV characteristic) are performed either on the room-temperature (RT) stage or in an evacuated flow cryostat. An illustration of the self-made RT-stage is shown in Fig. 2.32. It consists of a custom-made copper mount, where the sample is fixed with four screws. For measurements of the substrate emission an additional adapter with a hole is used. Furthermore, a two-stage Peltier element together with water-cooling ensures a good heat dissipation. The temperature of the RT-stage is controlled with an Alpes Lasers TC-51. For device characterizations at lower temperatures the flow cryostat is used. There, the temperature can be adjusted between liquid nitrogen (78 K) and above room temperature due to an integrated heater element. The temperature of the cold finger in the flow cryostat is controlled with a CryoCon 32B unit. The ZnSe window in the cryostat provides a transmittance of 67% in the wavelength range between 4 – 10 μm for normal incidence.

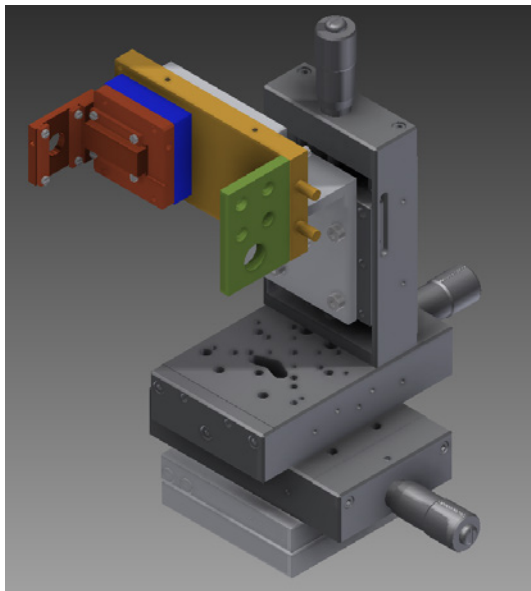


Fig. 2.32: Illustration of the laser stage designed for cw operation at room-temperature. The construction consists of three linear micrometer stages (x, y, z) where a water-cooled heatspreader (orange) is mounted. For active temperature stabilization a Peltier element (blue) is used. The sample itself is mounted on a copper block (red) and in this illustration also the 90° mount is shown. It is used for substrate-emitting devices and can be easily attached and removed with screws to achieve a stable mechanical connection and a good thermal contact. Connectors for SMA cables and the temperature controller are mounted on the green plate. The temperature is monitored with a temperature sensor, which is inserted into the drilled hole in the front face of the copper mount.

Fig. 2.33 shows the basic electrical wiring plan of the LIV characterization setup. Commonly the device is biased with a HP 8114A pulse generator, which can supply short pulses as well as high duty-cycle operation (up to nearly 100%). For LIV measurements the repetition rate is 5 kHz and the pulse duration is 100 ns, corresponding to a duty-cycle of 0.05%. Furthermore, a DC voltage can be added to the pulses, which allows cw testing. However, the pulser output voltage (\neq voltage on the sample) is limited to 100 V in the

”HIZ into $50\ \Omega$ ” mode. For higher voltages the AVTECH AVL-2-B pulse generator is used, which on the other hand is limited to short pulses with $5\ \text{kHz}/100\ \text{ns}$. The current through the laser is measured with a Tektronix AC Current Probe CT2, which is placed directly after the output of the pulse generator. This high-frequency current transformer delivers a voltage proportional to the current ($1\ \text{V}/1\ \text{A}$) and thus can only be used in pulsed operation. On the secondary side of the current probe a $50\ \Omega$ termination is required. The ”current” signal is fed into channel 1 of the high-impedance input of the oscilloscope (Tektronix TDS 3032B or Teledyne LeCroy HDO3034). Due to the pulsed operation at high frequencies, reflections (caused by unmatched impedances) can substantially distort the pulse shape. Therefore, all electrical connections are made with $50\ \Omega$ coaxial cables and appropriate interface connectors and terminators. For impedance matching, a series resistance of around $47\ \Omega$ is inserted before the laser device. Depending on the operation point the resistance of the laser is typically $R_{\text{laser}} \approx 8 - 15\ \Omega$, while the lower value can be assumed for ICLs and the latter one for QCLs. The voltage across the laser is measured with an additional wire on the printed circuit board. Again, to preserve the rectangular pulse shape the transmission line is terminated with a $50\ \Omega$ parallel resistor before the ”voltage” signal is feed into channel 2 of the oscilloscope. The inputs of the oscilloscope are switched to high-impedance mode for safety reasons. It would be also possible to use the internal $50\ \Omega$ resistors for impedance matching, but external resistors are easier and cheaper to replace in case of an measurement accident. To measure the actual current through the laser, the current through the $50\ \Omega$ resistor parallel to the laser device has to be subtracted from the total current (measured by the current probe). Data acquisition of both values, current and voltage, through and across the laser device are performed with the oscilloscope, which is read remotely via a GPIB or USB interface.

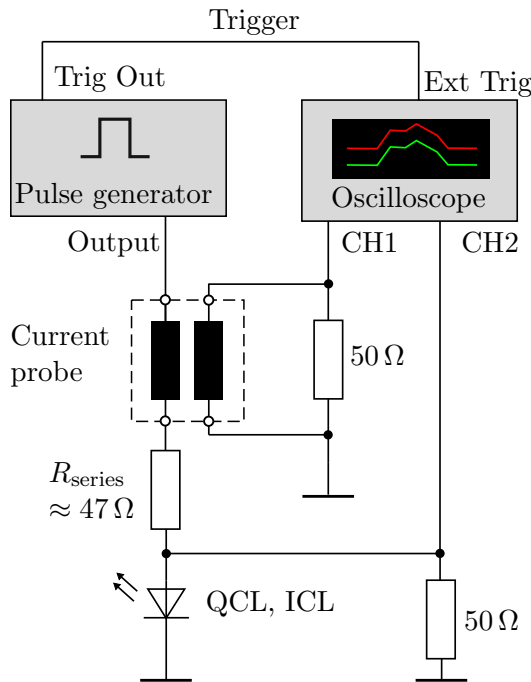


Fig. 2.33: Basic electrical wiring plan for light-current-voltage characterizations of the laser devices. The transmission lines are $50\ \Omega$ coaxial cables and for impedance matching parallel resistors are used on the high-impedance inputs of the oscilloscope. The current is measured with a high-frequency current transformer and needs to be corrected by the current through the $50\ \Omega$ resistor parallel to the device. A resistance in series with the laser device is used to improve the impedance matching and suppress possible reflections.

In Fig. 2.34 the complete setup for LIV measurements is illustrated. The laser (device

under test, DUT) is mounted either in an evacuated cryostat or on a room-temperature stage. The emitted light is collected with a ZnSe lens (focal length $f = 2''$ for the cryostat and $f = 1.5''$ for the RT-stage) and the parallel beam is directed through a KBr window into a Fourier-transform infrared spectrometer (FTIR). For standard characterization the optical signal is measured with the internal deuterated triglycine sulfate (DTGS) detector. The detector signal is fed into the lock-in amplifier (EG&G 5210 or EG&G 7265), which is triggered by the pulse generator. The lock-in amplifier is operated in the $R\theta$ -mode with an integration time constant of $t_c = 100$ ms. It delivers a voltage proportional to the optical signal, which is read via a GPIB interface from a remote computer. Depending on the laser type, its output power and the used detector, a full-scale sensitivity of $300 \mu\text{V} - 3 \text{ mV}$ is typically used on the lock-in amplifier. For more sensitive measurements, such as below lasing threshold, an external liquid-nitrogen cooled mercury-cadmium-telluride (MCT) detector (Judson J15D14-M204-S250U-60) is used instead of the DTGS. The detector element has the size $250 \times 250 \mu\text{m}^2$ and a peak specific detectivity of $4.18 \times 10^{10} \text{ cm}\sqrt{\text{Hz}}/\text{W}$ at 1 kHz, where a current of 3.23 mA is flowing. The pre-amplifier is operated at voltage of 15 V, which requires an external series resistance of 4.7 k Ω for the detector. The electrical signal from the MCT detector is amplified ($\times 1000$) with a Judson PA-101 pre-amplifier before it is fed into the lock-in amplifier.

For measurements of only the LIV characteristics, a FTIR spectrometer is not needed. But on the other hand, this setup allows to test the electrical/optical properties of a laser and also capture the spectrum within the same setup without moving anything. For measurements of the absolute power, a calibrated thermal detector (Ophir AN/2 or Thorlabs S401C) is placed directly in front of the emitting facet. Therefore the laser is operated with a higher duty-cycle or in cw mode. In this case the current probe and also the series resistance is removed.

Fourier-transform infrared spectroscopy

For the spectral characterization the laser is typically operated with 80 kHz/30 ns, corresponding to a duty-cycle of 0.24%. The spectrum is measured with a Bruker Vertex 70v FTIR spectrometer, which is equipped with a KBr window. Central component of the spectrometer is a Michelson interferometer, which for this particular instrument is realized with cube corner mirrors (retro-reflectors). The working principle of the Michelson interferometer is illustrated in Fig. 2.35.

The incident light from e.g. a laser is split by a semi-transparent mirror (beam splitter) into two beams. Ideally 50% of the intensity is transmitted into one path and the other 50% is reflected into the upper optical branch. One beam path is terminated with a fixed mirror, while in the other path a moving mirror is modulating the optical path length. After the light is reflected from the mirrors it is recombined again with the beam splitter and the resulting optical beam can be focused e.g. on a detector. For transmission experiments a sample can be placed in the optical path before the detector. Due to the 50% transmission of the beam splitter, half of the light emitted from the source is reflected back to it and therefore lost for the measurement. Depending on the mirror position of the moving mirror, and thus the optical path length, the signal measured with the detector is modulated. The

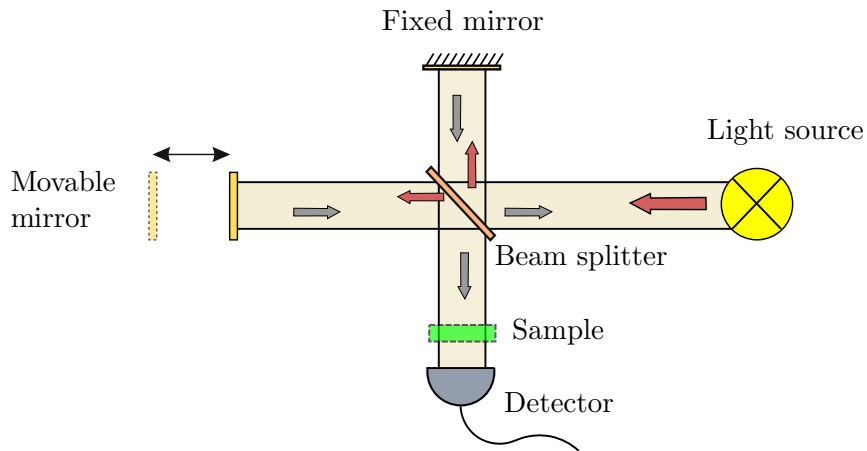


Fig. 2.35: Illustration of a Michelson interferometer.

optical path difference δ leads to constructive/destructive interference of the two beams. Constructive interference occurs if δ is an integer multiple of the wavelength λ . The measured signal on the detector is the so-called interferogram. It gives the intensity as function of the mirror position, which can be translated via Fourier-transformation into a spectrum. Fig. 2.36 shows a measured interferogram together with the corresponding spectrum of a broad-band light source (globar) equipped in the spectrometer. An ideal monochromatic laser source would have a sinusoidal interferogram, which gives a single spectral line.

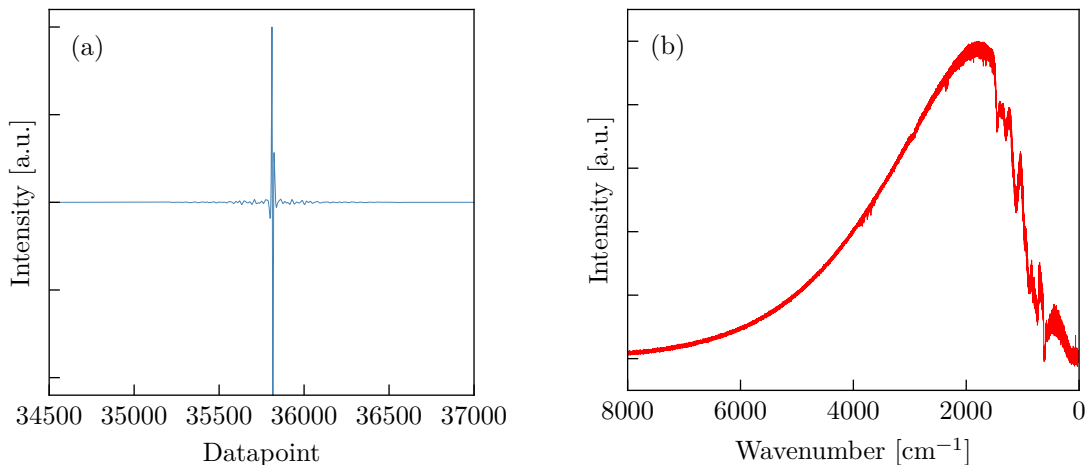


Fig. 2.36: (a) Interferogram measured with a FTIR spectrometer and (b) the corresponding spectrum of the internal black-body radiation source (globar). The spectrum is calculated from the interferogram data via Fourier-transformation.

The resolution of the spectrum is determined by the limited total driving distance of the moving mirror. The longer the travel distance of the moving mirror the better the attainable resolution ($\Delta\nu = 1/L_{\text{path}}$). A nominal resolution of $\Delta\nu = 0.21 \text{ cm}^{-1}$ is used

for the spectral measurements of the lasers. The actual mirror position is determined with an internal HeNe-laser emitting at 633 nm. The experimental measured intensity as a function of the mirror position is given by [95]

$$I(\delta) = \frac{2}{\pi} \int_0^{\infty} S(\nu) \cos(2\pi\nu\delta) d\nu, \quad (2.116)$$

where the spectral contribution at the wavenumber $\nu = 1/\lambda$ is determined by the Fourier component $S(\nu)$. With a Fourier-transformation this interferogram data can be converted into the spectrum, which then reads as

$$S(\nu) = 2 \int_0^{\infty} I(\delta) \cos(2\pi\nu\delta) d\delta. \quad (2.117)$$

An infinite integral boundary would require an infinite long travel distance of the mirror, which is practically impossible. Therefore, an apodization function (e.g. Happ-Genzel, Norton-Beer, Triangular etc.) is applied to the measured data. It serves as a truncation function, which forces the signal to zero values at the spatial limits. Furthermore, a phase correction (e.g. Mertz) is applied to account for the acquisition delay of the electronics (sampling), filter effects and other optical restrictions of the instrument.

The Vertex 70v spectrometer, used for the experiments, is evacuated with a vacuum pump to a pressure < 0.2 hPa, which allows to suppress residual water absorption within the instrument. For standard characterization the instrument is operated in rapid-scan mode and a wide-range MIR-FIR beam splitter is used in combination with a wide-range DTGS pyroelectric detector. For low intensity signals with a lot of background noise the step-scan technique can be used. There, the mirror is not moving continuously but step-wise, which gives a longer integration time per datapoint. Together with a lock-in amplifier this measurement technique can increase the signal-to-noise ratio significantly.

2.5.2 Nearfield and farfield measurements

Intensity profiles of the emitted laser light are captured with an uncooled micro-bolometer camera (IRM 160A). The VO_2/VO_x based camera has a resolution of 120×160 pixels, where each pixel is $50 \mu\text{m} \times 50 \mu\text{m}$. Farfield measurements only require the emitting laser source and the camera. For measurements of the projected nearfields, a ZnSe lens is placed between laser and camera. The lens is mounted on a translational stage and by varying the distance between laser, lens and camera the projection of the nearfield can be adjusted. In order to examine the polarization of the emitted light, a high density polyethylene (HDPE) polarizer (Tydex) is placed between lens and camera. For high-quality farfield measurements a MCT detector is mounted on a linear translation XY-stage in a distance of ~ 16 cm from the sample. With the stage, the liquid nitrogen cooled MCT detector is moved step-wise ($\Delta x = \Delta y = 0.6$ mm) in x- and y-direction over a scan area of around

24 mm \times 24 mm. The complete farfield image is obtained after a scan time of approximately 1 h. Therefore, the measured (x, y) data is converted to angle-dependent values (θ_x, θ_y) and corrected for the $1/r^2$ intensity loss and the projected area on the detector. Since the investigated ring lasers have low divergence angles, the measurement with a translational stage is justified. For ridge lasers with their typical small emitting facet areas, the use of a rotational stage is more appropriate. For measurements of interband cascade lasers at a wavelength $\sim 4 \mu\text{m}$ an InSb detector with 1 mm \times 1 mm detector size is used. The InSb photodetector has a specific detectivity of $D^* \sim 10 \times 10^{11} \text{ cm}\sqrt{\text{Hz/W}}$.

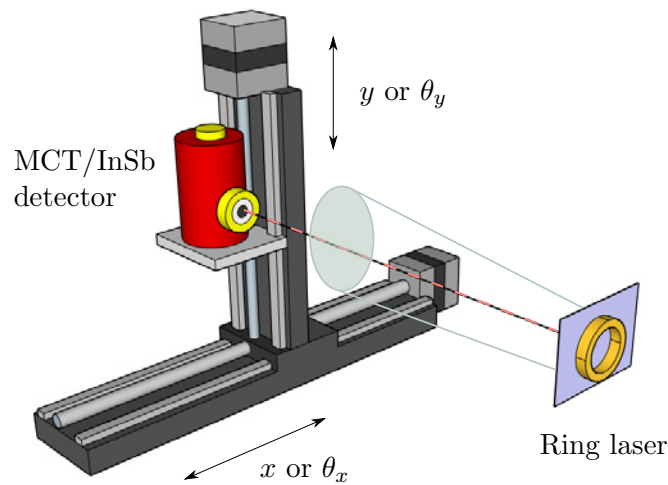


Fig. 2.37: Illustration of the measurement setup for farfield characterizations. The emission pattern is captured with a liquid nitrogen cooled MCT or InSb detector, which is mounted on a linear translational XY-stage.

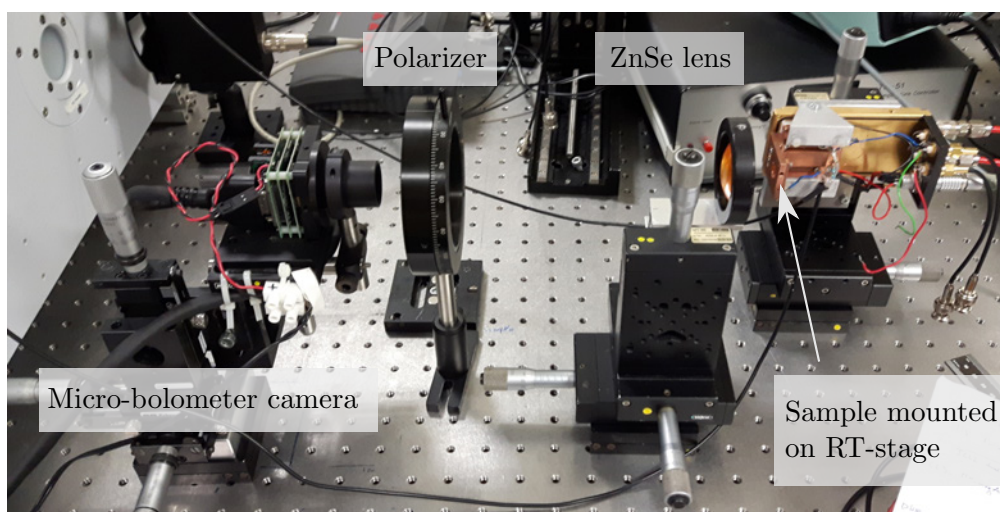


Fig. 2.38: Setup for polarization-sensitive nearfield measurements.

2.5.3 Measurement software

To enable automated measurements of the LIV characteristics and other laser properties, a software is developed with the Python programming language [96]. A screenshot of the graphical user interface of the measurement tool is shown in Fig. 2.39. While the equipment is controlled remotely via GPIB/USB from a computer, the software coordinates the whole measurement process. A variety of different instruments such as pulser, source meter units, lock-in amplifiers, oscilloscopes, multimeters, detectors and temperature controllers can be used. The software allows to quickly change parameters and settings of the instruments remotely. Furthermore, automated temperature-dependent sweeps can also be programmed. Finally, the measured data is automatically post-processed, plotted and saved as raw data as well as image file. All measurement settings can be saved and reloaded later again, which is important to reproduce a specific measurement.



Fig. 2.39: Graphical user interface of the self-developed Python program used to control and automate the measurement process.

Quantum cascade lasers

Already in the year 1971, Kazarinov and Suris proposed intersubband transitions in semiconductor quantum well structures as possible source for long wavelength emitters [97]. However, at that time the growth technology for these monolayer-thin nanostructures was not available. Only with the invention and development of the molecular beam epitaxy (MBE) [98, 99] and metal-organic chemical vapor deposition (MOCVD) [100], it was possible to produce high-quality crystal structures with designable electronic properties. The usage of intersubband transitions has the advantage that the emission wavelength can be tailored by engineering the thickness of the quantum wells. With that, the energy bandgap of a semiconductor material is not determining the emission wavelength. Fig. 3.1 illustrates a simple three-level laser system based on intersubband transitions.

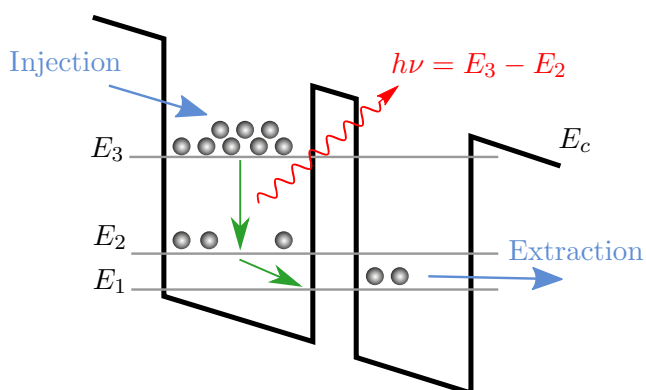


Fig. 3.1: Schematic illustration of the conduction band diagram and energy levels of an intersubband laser. The designable energy difference $E_3 - E_2$ determines the wavelength of the emitted photon. In quantum cascade lasers, multiple stages are connected in series.

The motion of the electron is quantized in direction perpendicular to the semiconductor layers. Artificially designed confined energy states determine the transitions for the electrons. With that, long wavelength lasers covering the mid-infrared up to the THz spectral region can be realized [101]. Electrons are excited and injected into the upper laser level E_3 , from which they can make a transition to E_2 . To establish intersubband gain, a population inversion between level 3 and 2 is required. In the case of a radiative transition, the energy difference $E_3 - E_2$ is emitted as photon. The lower laser level E_2 is depop-

ulated using fast scattering (~ 1 ps) with longitudinal-optical (LO) phonons to level E_1 . The LO phonon energy depends on the well material and is for instance $\hbar\omega_{LO} = 35$ meV in GaAs and $\hbar\omega_{LO} = 33.5$ meV in $\text{In}_{0.53}\text{Ga}_{0.47}\text{As}$ [102, 103]. Electrons are collected and injected into the next cascade, where the whole process is repeated. The cascading of multiple stages in series allows an electron to emit multiple photons as it moves through the heterostructure of the QCL. Furthermore, since there are no interband transitions involved, the electron remains in the conduction band only [34].

3.1 A short historical review

In the year 1994, the first laser based on intersubband transitions was experimentally demonstrated by J. Faist, F. Capasso, D.L. Sivco, C. Sirtori, A.L. Hutchinson and A.Y. Cho at Bell Labs [10]. This *quantum cascade laser* used photon-assisted interwell tunneling in a 3-well active region design ($\lambda = 4.26$ μm). The $\text{In}_{0.53}\text{Ga}_{0.47}\text{As}/\text{In}_{0.52}\text{Al}_{0.48}\text{As}$ heterostructure (25 stages) was grown by molecular beam epitaxy on an InP wafer. Despite the fact that the device operated only at cryogenic temperatures, this pioneering work provided the experimental proof-of-principle for the QCL concept. Shortly after, a plasmon-enhanced waveguide was introduced to reduce the optical losses for a laser emitting at a longer wavelength of 8.4 μm [31]. Already in 1997, a distributed-feedback QCL operated single-mode at room temperature [104]. The laser performance rapidly improved and continuous-wave operation of a buried heterostructure laser at room temperature was achieved in 2002 [105]. A detailed discussion of the progress and development of QCLs can be found in [34]. Moreover, QCLs are not limited to the mid-infrared spectral region. The design flexibility allows also to engineer long-wavelength laser sources without changing the material system. To date, THz QCLs cover the (far-infrared) spectral region from 1 – 5 THz but are still limited to operating temperatures below 200 K [36, 106]. Fig. 3.2 gives an overview of the maximum operating temperatures of QCLs in various wavelength regions.

Due to the increasing performance of mid-IR QCLs, far-infrared radiation can be also generated at room-temperature using intra-cavity difference frequency generation [107]. With the development of broadband gain materials, optical frequency combs [108] with phase-locked modes have been explored. Dual-comb spectroscopy is demonstrated with group velocity dispersion compensated QCLs [109, 40]. Nowadays, QCLs are capable to deliver up to 5.1 W optical output power in continuous-wave mode at room temperature [110]. They cover the spectral range between $\sim 2.6 - 25$ μm and 1.2 – 4.9 THz and reach wall-plug efficiencies of up to 21% (cw) [111, 112, 11, 101, 17, 113]. With a single-well injector design ($\lambda \sim 5$ μm) a record wall-plug efficiency of 53% is achieved at 40 K [114]. In this device, more light than heat is generated. Moreover, the heterostructures of intersubband devices can be used to detect infrared radiation, e.g. with quantum well infrared photodetectors (QWIPs) or quantum cascade detectors (QCDs). Integrated sensing platforms with a bi-functional quantum cascade laser and detector (QCLD) fabricated on the same chip have been demonstrated [115].

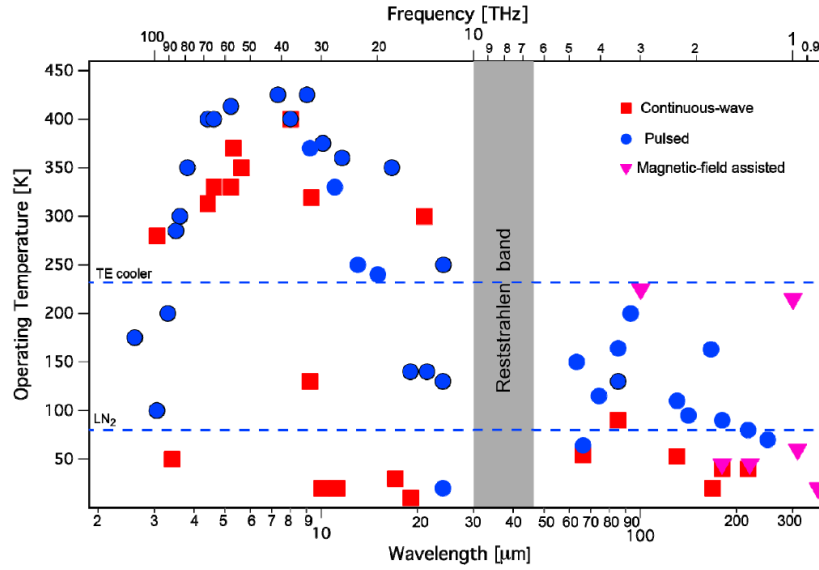


Fig. 3.2: Experimentally achieved maximum operating temperatures of QCLs from the mid-infrared to the THz spectral region. In the Reststrahlen band, phonon modes are excited in the semiconductor material, which strongly absorb the radiation. Reprinted with permission from [101].

3.2 Operation Principles

A single stage of a QCL consists of an injector, the active region and an extractor, which can be the injector for the subsequent stage. Fig. 3.3 shows the simulated conduction band diagram of the P51 QCL material, which is used for the intersubband devices in this thesis. The electron injector serves as reservoir, where electrons are collected from many energy levels (miniband) and injected into the upper laser level of the active region. To provide enough carriers, the injector section is partly doped. In addition, the position of the dopands is crucial for preventing ionized impurity scattering in the active region. The lasing transition takes place between upper and lower laser level $E_3 - E_2 = \hbar\omega$, which defines the wavelength $\lambda \approx 8 \mu\text{m}$ of the emitted photon. Hereby, the locations of the wavefunctions determine the dipole matrix element and hence the available gain. Within the effective mass approximation and by neglecting non-parabolicity effects, the dipole matrix element reads

$$z_{32} = \langle \varphi_3 | z | \varphi_2 \rangle, \quad (3.1)$$

with the wavefunctions φ_3 and φ_2 corresponding to the eigenenergies E_3 and E_2 , respectively. Under the assumption of parabolic subbands and a Lorentzian-shaped optical emission line, the peak intersubband material gain is given by [17]

$$G_p = \frac{4\pi e^2 z_{32}^2}{\epsilon_0 n_{\text{eff}} \lambda L_p} \frac{1}{2\gamma_{32}} (n_3 - n_2), \quad (3.2)$$

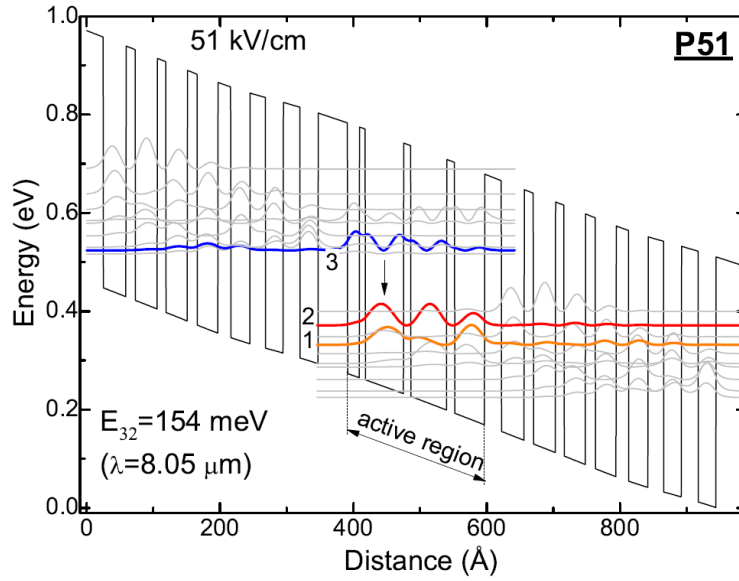


Fig. 3.3: Simulated conduction band diagram and squared moduli of some wavefunctions for the P51 quantum cascade laser material. The growthsheet can be found in the appendix A.3.1. The wavelength of the emitted photon is determined by the energy difference between upper laser level E_3 and lower laser level E_2 . Fast depopulation of the lower level is achieved by emission of LO phonons. Reprinted with permission from [37].

with the electron charge e , the refractive index n_{eff} , the length of one period L_p , the FWHM broadening of the transition $2\gamma_{32}$ and the sheet carrier densities n_3 and n_2 . The modal gain $G_m = G_p\Gamma$ depends on the overlap Γ of the mode with the gain region. In quantum heterostructures the optical gain can be increased by using materials with a low effective electron mass and by engineering the thicknesses of quantum wells and barriers. Concurring non-radiative processes, such as scattering with ionized impurities, alloy scattering, phonon scattering or electron-electron scattering provide alternative energy relaxation paths.

Stimulated emission requires a population inversion $n_3 > n_2$, which translates to a short lower state lifetime $\tau_{32} > \tau_2$. Or in other words, the electrons have to be extracted fast from the lower laser level, e.g. with resonant LO-phonon scattering [116]. The carriers rapidly decay to level 1, where they are collected by the extractor and injected into the upper laser level of the next stage (see Fig. 3.3). Typical QCL heterostructures consist of around 30 stages in which the electrons are "recycled". Cascading increases the overlap Γ between the optical mode and the gain regions, while the number of injected carriers per stage remains the same. The threshold current density for a three-level system can be estimated with a rate-equations model [17] that gives

$$J_{\text{th}} = e \frac{\alpha_{\text{total}}/G_m + n_2^{\text{therm}}}{\tau_{\text{eff}}}, \quad (3.3)$$

with the the effective lifetime $\tau_{\text{eff}} = \tau_3(1 - \tau_2/\tau_{32})$ and the total losses α_{total} that need

to be compensated by the gain. The term $n_2^{\text{therm}} = n_g \exp(-\Delta/k_B T)$ considers thermal backfilling of electrons into the lower laser level 2, where n_g is the injector sheet doping density and Δ the energy separation between level 2 and the Fermi level in the injector. A reduction of the threshold current density is achieved by lowering the waveguide losses α_{wg} , increasing the upper state lifetime τ_3 , decreasing the lower state lifetime τ_2 and by avoiding leakage paths and intersubband transitions, which lower the population inversion. Several active region concepts have been developed ranging from 1-well to 4-well designs, (chirped) superlattices, two-phonon resonances, bound-to-continuum designs and vertical/diagonal transitions. A detailed discussion of various design approaches can be found in [34, 17]. With an external bias voltage the alignment between the energy levels can be controlled. Fig. 3.4 shows a typical light-current-voltage curve of a QCL. For certain electric fields, a low resistance path is established for the electrons and resonant tunneling between adjacent quantum wells becomes possible. The presence of band alignments can be observed in the kink of the IV curve at point 1. Between points 1 and 2 the ring device shows spontaneous emission until it reaches lasing threshold at point 2. At point 2 the optical gain is high enough to compensate the losses in the laser cavity. The optical output power increases approximately linear with the injected current. A measurable quantity for the performance of lasers is the slope efficiency [17]

$$\eta_s = \frac{N_p \hbar \omega}{e} \frac{\alpha_m}{\alpha_{\text{total}}} \frac{\tau_{\text{eff}}}{\tau_{\text{eff}} + \tau_2}, \quad (3.4)$$

with the number of periods N_p and the mirror loss α_m of one facet. At high electric fields the energy levels start to misalign and the output power decreases again, which is indicated by the roll-over at point 3 in Fig. 3.4. Another important parameter for lasers is the wall plug efficiency, defined as [55]

$$\eta_{\text{wp}} = \frac{P_{\text{optical}}}{UI}. \quad (3.5)$$

It relates the optical output power P_{optical} to the electrical input power UI and corresponds to the conversion efficiency of the laser. Usually only the electrical input power of the laser alone is considered. However, for a fair comparison to other systems also the power consumption of the cooling (e.g. Peltier-element, water pump etc.) should be taken into account.

3.3 Materials

For QCLs, alternating material layers with different conduction band offsets are used to build quantum wells and barriers. With the thickness and composition of the materials, the confined energy states and hence the intersubband transitions are engineered. Fig. 3.5 shows a map of commonly used III-V semiconductor material compositions together with their energy bandgaps and lattice constants. For completeness also other selected semiconductors are included in this plot. A comprehensive list of material parameters for III-V

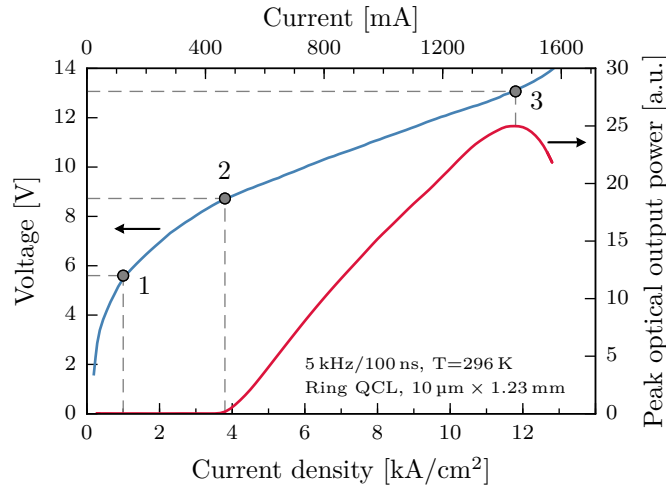


Fig. 3.4: Typical LIV characteristics of a ring QCL. Between the points 1 and 2 the energy levels in the heterostructure start to align and (amplified) spontaneous emission can be observed in the sub-threshold regime. At point 2 lasing threshold is reached, which can be seen in the onset of stimulated emission. At point 3 the external bias voltage is so high that the energy levels start to misalign, which leads to a reduction of the output power. Based on [41].

semiconductors can be found in [117]. To minimize the strain in the epitaxially grown layers, the lattice constants of the material layers need to be similar. For the heterostructure of QCLs, a lattice-matched or strain-compensated growth of the compound materials on a substrate is required. The GaAs/ $\text{Al}_x\text{Ga}_{1-x}\text{As}$ material system for instance is lattice-matched for all Al contents x . Whereas the $\text{In}_x\text{Ga}_{1-x}\text{As}/\text{In}_y\text{Al}_{1-y}\text{As}$ system requires a fixed composition of $x = 0.53$ and $y = 0.52$ for lattice matching. With the method of strain-compensation, e.g. a compressive strain in one layer is compensated by another tensile strained material layer. This results in an overall close to zero accumulated strain, which is mandatory to grow thick heterostructures. However, the strain build-up in unmatched layers can also be used to engineer (increase) the conduction band offset ΔE_c . Effective higher barriers can help to suppress carrier leakage at higher energies and are necessary to realize short-wavelength lasers. On the other hand, higher potential barriers require a thinner material layer to maintain the same tunneling probability. Furthermore, also scattering from the Γ -point to other valleys (e.g. X or L) has to be considered, which can lower the effective barrier height significantly. Besides an appropriate conduction band offset ΔE_c , also the effective electron mass m^* in the well material is important. A lower effective mass leads to a higher optical dipole matrix element and therefore a higher optical gain. Several material compounds with phosphides, arsenides or antimonides have been explored for the growth of QCLs. Some important binary and ternary material systems are listed in Tab. 3.1.

The GaAs/AlGaAs material system has a low barrier height, which is however well suited for long-wavelength THz lasers. The lattice-matched or strain-compensated InGaAs/InAlAs material system grown on InP is preferably used for mid-infrared QCLs. Moreover, the InP can be used as waveguide material, because it has a lower refractive index. The conduction band offset of the InAs/AlSb is effectively reduced by inter-valley scattering

Material system	ΔE_c^Γ	m^*	Substrate
GaAs/AlGaAs	0.3 eV	$0.067m_0$	GaAs
InGaAs/InAlAs	0.52 eV	$0.043m_0$	InP
InAs/AlSb	2.1 eV	$0.023m_0$	InAs

Tab. 3.1: Selected material systems used for quantum cascade lasers with the conduction band offset ΔE_c^Γ at the Γ -point, the effective electron mass m^* and the corresponding substrate material for epitaxial growth.

to around 0.73 eV. Nevertheless, this material system can be used for short-wavelength lasers and it offers a low effective electron mass. In addition, many other material combinations are possible, e.g. InGaAs/GaAsSb or quaternaries such as InGaAs/AlInAsSb or InGaAs/AlInGaAs [101]. A typical mid-IR QCL is composed of roughly 1000 layers and has a total thickness of $\sim 10 \mu\text{m}$, where the thinnest layers are on the order of 0.5 nm. Such precise and stable growth is achievable with MBE or MOCVD systems. The former growth technique is used at the Center for Micro- and Nanostructures at the TU Wien, where the MBE system exhibits a typical growth rate of $\sim 1 \mu\text{m/h}$.

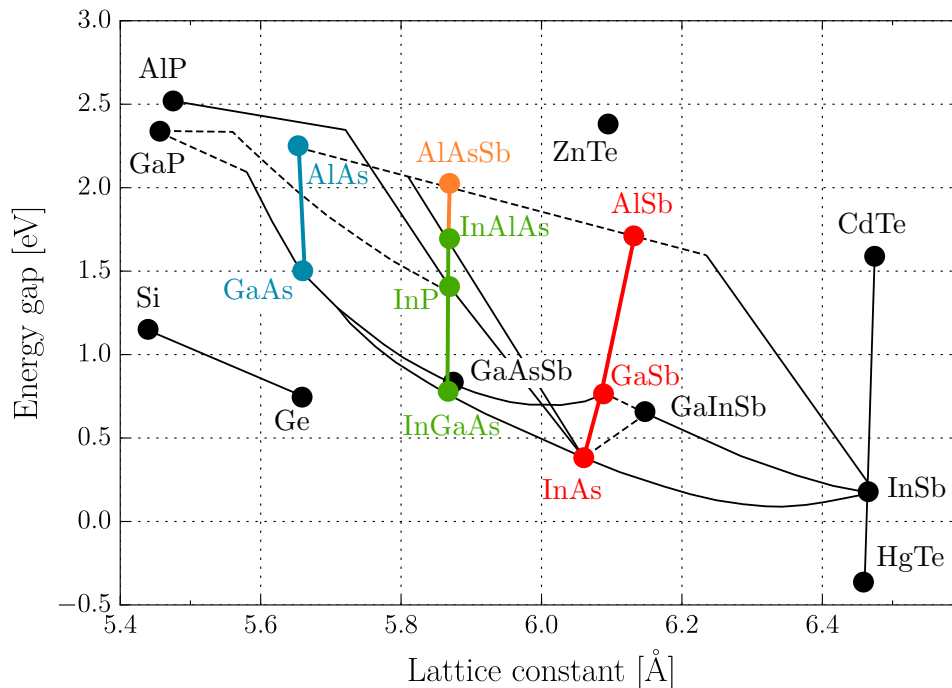


Fig. 3.5: Energy bandgap versus lattice constant for various semiconductor materials. Common material combinations for quantum cascade lasers are highlighted with different colors. To reduce the amount of strain in the heterostructure layers, materials with similar lattice constants are grown epitaxially on top of each other.

3.4 Ring quantum cascade lasers

Most quantum cascade laser devices are fabricated into Fabry-Pérot resonators, as they are simple to manufacture and their properties are well known. Applications such as spectroscopy, chemical sensing or free-space communication may rely on a compact single-mode laser with low divergence of the emitted beam. However, the farfield of an edge-emitting Fabry-Pérot laser is strongly divergent due to the small emission area of the facet. Light emission via the surface/substrate (larger emitting area) would enable to build compact QCL devices with low beam divergence. Furthermore, vertical light emission allows to easily integrate multiple devices on the same chip, which can simultaneously operate at different wavelengths. While the vertical cavity surface emitting laser (VCSEL) is a well established device for interband diode lasers, the concept cannot be directly transferred to the QCL technology. The reason is that QCLs are transverse-magnetic polarized due to the restriction of the gain by the intersubband selection rule. Hence, the electric field points in growth direction and the light propagates in-plane. To couple the light out in vertical direction photonic crystals enhanced QCLs [118] or second-order DFB gratings can be used [119, 120, 121]. Photonic crystals require a rather sophisticated fabrication since holes with high aspect ratios are etched into the waveguide. In the case of a DFB grating, a discrimination of all modes except the one at or close to the Bragg wavelength is achieved by optical feedback.

Circularly-shaped resonators, such as disks [45, 122] or rings, support the propagation of whispering-gallery modes. Especially the ring geometry, shown in Fig. 3.6(a), is highly interesting for the usage as a laser cavity, because the electrically pumped area is much smaller than for disks. Furthermore, due to the reduced width of the waveguide also higher-order lateral modes can be efficiently suppressed. Light is coupled out from the cavity via a second-order DFB grating, as shown in Fig. 3.6(b). The ring resonator has no cleaved facets, which allows a monolithic integration of an array of lasers. In addition, on-chip testing during the fabrication becomes possible. In case of ridge devices, the position of the cleaved facet is subjected to variations, as the cleaving process cannot be controlled on the nanometer scale. As a result, the uncertainty in the cleave position introduces an additional phase-shift with respect to the DFB grating. This in turn influences the mode discrimination and at the end the emitted light. Ring QCLs circumvent these issues and allow to build coherent surface-emitting light sources with collimated emission beams.

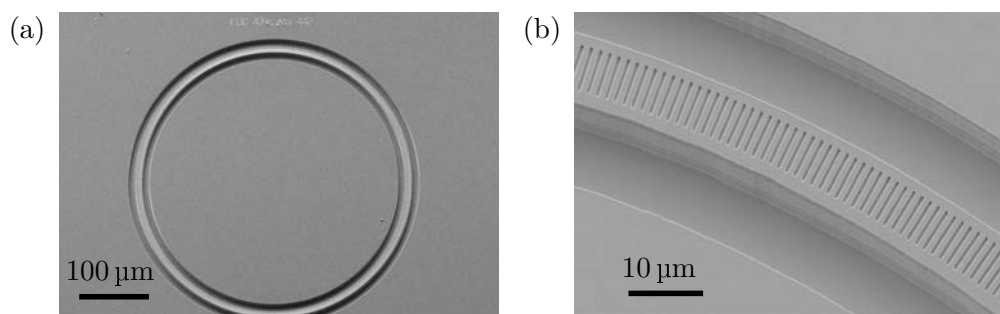


Fig. 3.6: (a) Scanning electron microscope image of a ring QCL. (b) A second-order DFB grating is used for single-mode selection and vertical light emission.

In 2008, Mujagić et al. [123] demonstrated the first ring QCL with light emission via the surface. The combination of a ring-shaped laser cavity with a second-order DFB grating resulted in a multimode emission at a center wavelength around $\lambda \approx 4.11 \mu\text{m}$. In contrast to ridge QCLs with second-order DFB gratings, this device concept features a symmetric farfield pattern. Shortly after, single-mode emission was achieved by using a DFB grating with higher grating duty-cycle and etch depth [124]. The concept of ring lasers was transferred to ring QCLs emitting monomode in the far-infrared region around 3.2 THz [125, 126]. In 2010, the coherent coupling between two surface-emitting ring QCLs at a wavelength of $\sim 8 \mu\text{m}$ was investigated [127]. The closely-spaced ($1 \mu\text{m}$ gap) ring lasers are coupled by the evanescent field. This proof-of-concept work showed the feasibility of coupling several devices to build e.g. phase-locked array of ring lasers. High temperature (380 K) and single-mode operation with a side-mode suppression ratio of 30 dB of mid-IR ring QCLs is reported in [128, 129]. With an array of 16 ring lasers, where each device emits at a different wavelength, a total spectral coverage of $\sim 180 \text{ cm}^{-1}$ is obtained (see Fig. 3.7) [130].

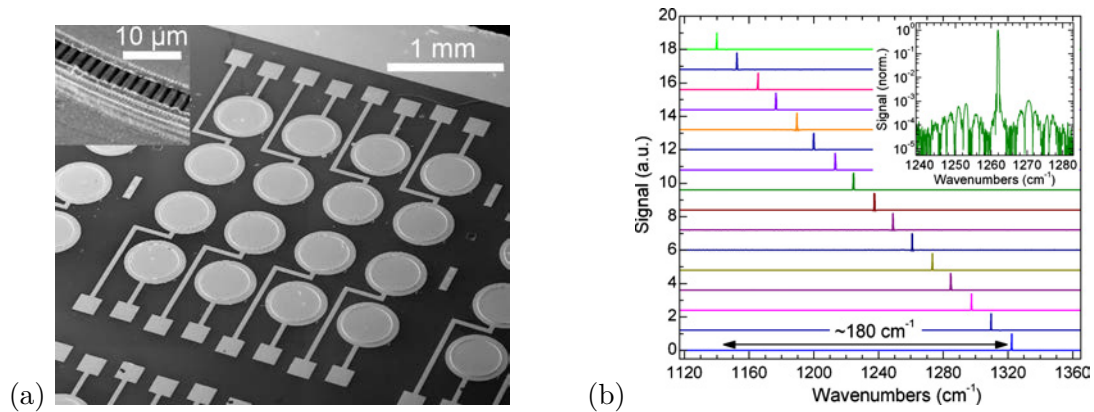


Fig. 3.7: (a) Two-dimensional array of 16 ring QCLs integrated on the same chip. (b) The array covers a spectral region of $\sim 180 \text{ cm}^{-1}$. Reprinted with permission from [130].

High power and continuous-wave operation at room-temperature is achieved with an improved thermal management [131]. The rings are fabricated as a buried heterostructure, where the DFB grating is placed directly above the active region and the whole stack is overgrown with InP. Nearfield measurements confirmed the azimuthal polarization in ring QCLs and from farfield images an operation in a higher-order mode is observed for increasing injection currents. However, the single-mode emission at $5 \mu\text{m}$ reaches an optical output power of 0.4 W. The influence of the grating duty-cycle (GDC) on the emission direction of ring lasers is investigated in [81]. It was found that the maximum output power for substrate emission is obtained at a GDC of 56%, whereas for surface emission this occurs at 72% (narrow slits). It was found that diffraction towards the substrate is the predominant out-coupling mechanism for all GDCs. Modifications of the emitted beam are investigated in [132], where two π -shifts are incorporated in the DFB grating to facilitate a central intensity maximum in the farfield. Furthermore, an on-chip wire-grid polarizer is fabricated on the substrate-side, leading to a linearly polarized emission beam (Fig. 3.8).

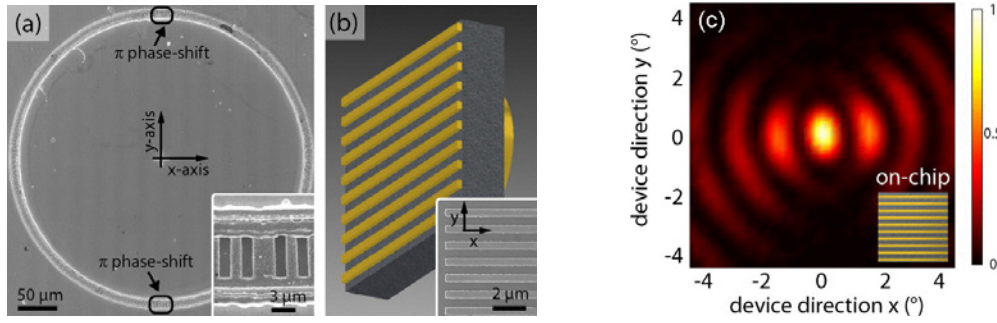


Fig. 3.8: (a) SEM image of a ring laser with two π phase shifts. (b) A wire grid polarizer is fabricated on the substrate with a period of 1 μm and a wire width of 500 nm. (c) Measured farfield pattern of the linearly polarized emission beam. Reprinted with permission from [132].

Although, the divergence angle ($\sim 3^\circ$) of ring lasers is comparable small to edge-emitting ridge lasers ($\sim 60^\circ$), a further reduction of this angle can be achieved with a gradient index metamaterial [133]. Holes with different sizes are etched into the InP substrate of a ring QCL, modifying the local refractive index. This on-chip collimation approach is further discussed in section 3.6.3. Besides the incorporation of two grating π -shifts, an intensity maximum in the farfield center can also be created by shifting the DFB grating relative to the waveguide [134]. This off-center grating similarly breaks the symmetry in the waveguide and leads to constructive interference in the center. Furthermore, by modifying the tilt angle of the centered grating slits it is possible to control the degree of radial polarization. Surface-emitting ring QCLs are highly interesting for spectroscopic applications. In a step-scan assisted time-resolved characterization of rings and ridges [135] it has been found that ring lasers show less mode-hops and an improved current-induced tuning of the wavelength. In 2016, ring QCLs were utilized in gas measurements for process analytics [136]. In an absorption measurement setup, pulsed ring lasers are used as light source for the detection of hydrogen sulfide (H_2S) in a methane (CH_4) matrix. In another study [137], a new sensor concept for multianalyte gas sensing is demonstrated. It combines a surface-emitting ring QCL with a substrate-integrated hollow waveguide. This very compact system allows the detection of gases at two different wavelengths. The monolithic integration of ring laser and detector on the same chip will be further discussed in section 3.7.

3.5 Light propagation and polarization

While the Fresnel diffraction theory describes the wave pattern in close vicinity to the ring (nearfield), Fraunhofer diffraction accounts for the resulting pattern in a distance far away from the source (farfield). There are several definitions at which distances the wave can be considered to be in the nearfield or the farfield regime. Here, the farfield is understood as the wave pattern in the observation plane at a distance much larger than the size D of the object. A possible definition for the Fraunhofer regime can be given by $z \gg D^2/\lambda$, where z is the propagation distance and λ the wavelength of the radiation. But this is a loose definition as there is no abrupt transition between nearfield and farfield.

The farfield can be directly calculated via a 2D Fourier-transformation of the near field distribution. More specifically, the near field is separated into horizontal and vertical polarization. Both are then Fourier-transformed and finally superimposed to get the total farfield pattern. The nearfields can be either obtained by simulating the mode distribution in the ring with e.g. COMSOL or by extracting the data from polarization-sensitive near field measurements with e.g. a wire-grid polarizer. Fig. 3.9 shows the near field patterns of a ring QCL from which the farfield patterns retrieved via Fourier-transformation. Due to destructive interference of the fields, emitted from opposite sides of the circular symmetric ring geometry, an intensity minimum occurs in the center. The ring QCL is azimuthally polarized or in other words the electric field vector points tangential to the ring circumference. The size of the second-order DFB grating determines the emitting area. The farfield is composed of concentric lobes, where most of the intensity is contained in the first lobe. The angular positions of the lobes are directly related to the diffraction order n by the following equation [37]

$$\sin(2\Omega) = 2 \left(n + \frac{1}{2} \right) \frac{\lambda}{D}, \quad (3.6)$$

where Ω is angle between the center and the intensity maxima, λ the free-space wavelength and D the diameter of the ring. This result is similar to the double-slit experiment of Young, if the ring diameter is considered as the distance between the slits. However, in the double-slit experiment an intensity maximum is observed in the center, while for the ring a minimum is obtained. The reason is that in ring lasers the emitted electric fields from opposite sides are rotated by 180° with respect to each other, which leads to the destructive interference in the center of the farfield. Fig. 3.10 shows a comparison between a measured farfield pattern and the corresponding simulation. Very good agreement between theory and experiment are obtained.

The light emission from ring lasers can also be seen as the propagation of a wave through a ring-shaped aperture. As the light travels through the aperture, it will be diffracted. The constructive and destructive interference of waves, emitted from different points on the zero plane, will create a characteristic pattern on another plane in a distance further away. From an application point of view it is important to know how the shape and thus the intensity distribution changes with propagation distance. For the computation of the intensity pattern, various theoretical approaches with certain assumptions and limitations exist [139]. For instance the farfield can be directly calculated via Fourier-transformation of the nearfield pattern. However, everything that happens between nearfield and farfield is hidden. Furthermore, the incorporation of other optical elements, such as e.g. phase plates, lenses or apertures, in the beam path requires to know the field distribution at that intermediate positions. Therefore the propagation of the emitted light is investigated more in detail by simulation.

For the ring lasers, the light propagation is described by the Rayleigh-Sommerfeld model within the scalar diffraction theory. Besides some constraints on the boundary condition, no further approximation is included. The electric field at a point P_1 is calculated by the full Rayleigh-Sommerfeld integral of the first kind [140]

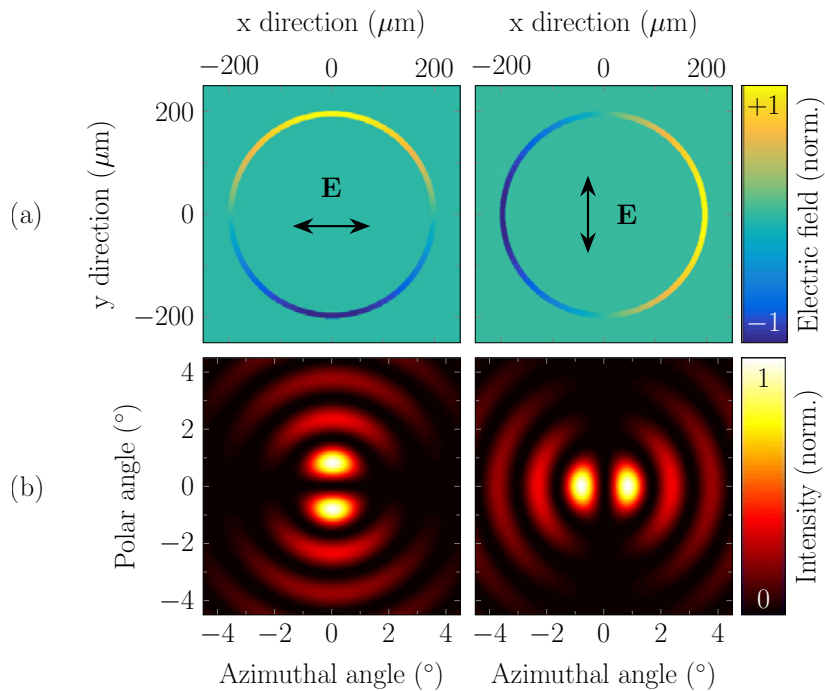


Fig. 3.9: (a) The near field of ring QCLs is azimuthal polarized. The electric field vector points in the direction tangential to the ring circumference. Vertical and horizontal near field components are plotted separately. (b) With a Fourier-transformation the farfield pattern can be calculated from the corresponding near field. The total field is obtained by the superposition of both polarization components. Reprinted with permission from [138].

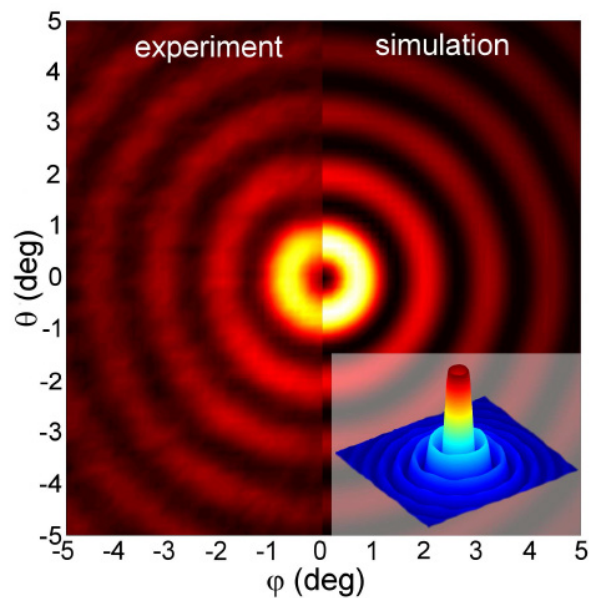


Fig. 3.10: Measured farfield pattern and comparison to the simulation result. Reprinted with permission from [37].

$$E(P_1) = \frac{1}{2\pi} \iint E_{z=0} \frac{\exp(jkr)}{r^3} z_1(jkr - 1) dx_0 dy_0, \quad (3.7)$$

where $E_{z=0}$ is the assumed electric field at the zero plane ($z = 0$), $k = 2\pi n/\lambda$ is the wavevector in the material with refractive index n , z_1 is the propagation distance and $r = \sqrt{(x_1 - x_0)^2 + (y_1 - y_0)^2 + z_1^2}$. Under the assumption $\rho \gg \lambda$ this equation simplifies to the so called Fresnel-Kirchhoff diffraction integral. In the following, simulations of the propagated light (intensity profiles in a plane located at the propagation distance) for a ring laser are presented. The device has a diameter of $400 \mu\text{m}$ and a waveguide width of $10 \mu\text{m}$ and emits light at a wavelength of $8 \mu\text{m}$. The 2D Rayleigh-Sommerfeld scalar diffraction integral is solved numerically with Python. Fig. 3.11(a) shows the source or aperture from which the light is emitted into the free-space. The waist of the beam increases with increasing propagation distance ($d = z_1$). At a travel distance of around $300 \mu\text{m}$ most of the intensity is concentrated in a small spot in the center, as shown in Fig. 3.11(d). In accordance to Huygens principle, every point on the wave front is the source for a new wave. The superposition of all waves results in the observed interference patterns. The beam pattern in Fig. 3.11(f) resembles the farfield and can also be directly calculated via a Fourier-transformation, as will be shown later.

While these beam patterns are simulated for light travelling in free-space, also the propagation in a material is of practical relevance. For the ring QCLs, discussed in section 3.9, the light is emitted through the InP substrate. Therefore, a refractive index of $n = 3.06$ is used for the substrate material at a wavelength of $8 \mu\text{m}$. Fig. 3.12 shows a comparison of the simulated beam pattern evaluated at a travel distance of $350 \mu\text{m}$ in air (a) and in the InP substrate material (b). The propagation distance corresponds to the standard thickness of the InP wafers used for the fabrication of the ring lasers. Due to the higher refractive index of the InP material, the intensity pattern still shows near field character with an increased ring shape. In contrast, for propagation in air the intensity is already concentrated in a small spot, indicating the transition to the concentric interference fringes in the farfield. Knowing the approximate size and shape of the emitted beam is important if one wants to place other optical elements or a detector in the beam path of the ring laser.

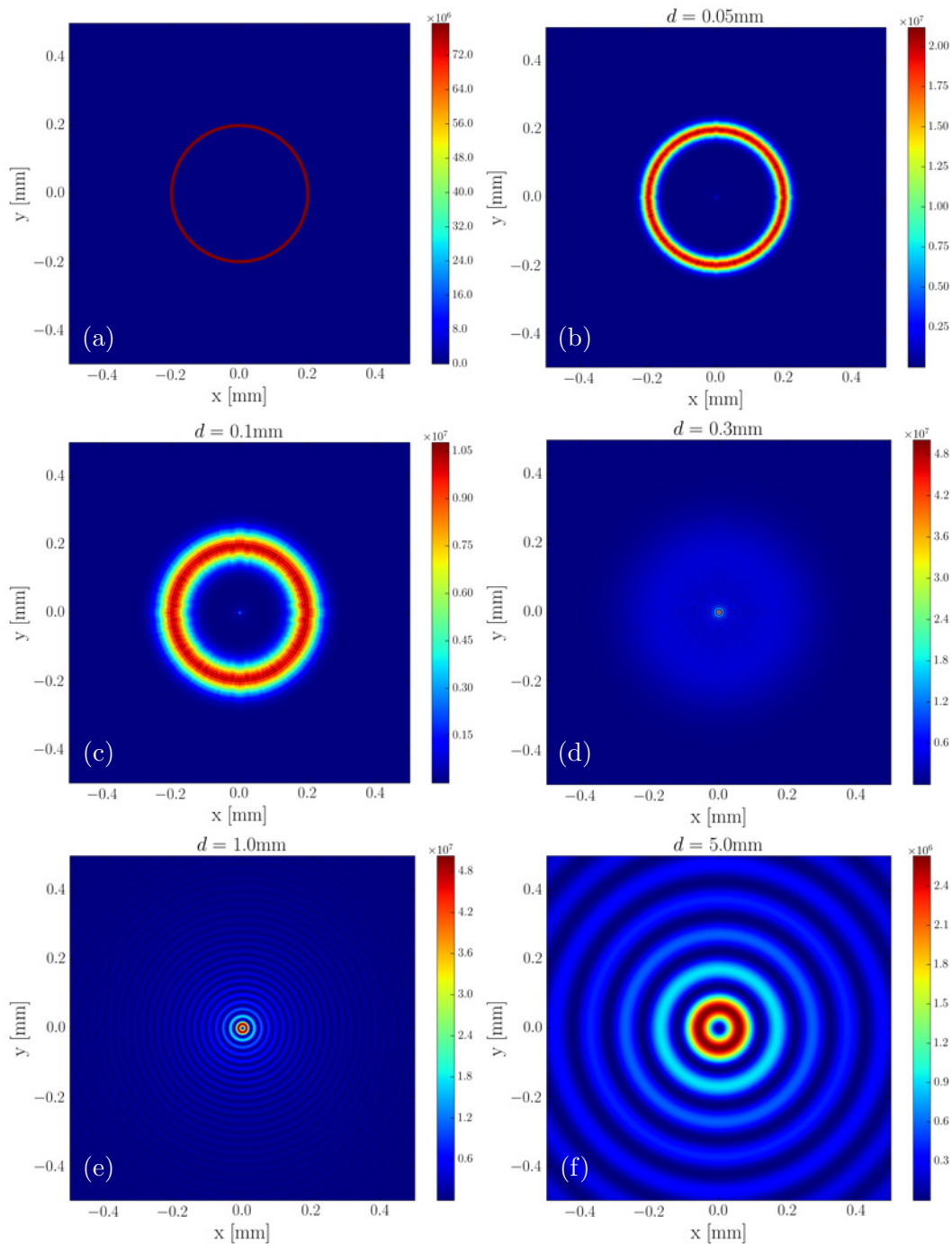


Fig. 3.11: Simulated free-space propagation of a beam emitted from a ring-shaped aperture (a) with 400 μm diameter and an aperture width of 10 μm at a wavelength of 8 μm . Evaluation of the intensity distribution after (b) 50 μm (c) 100 μm (d) 300 μm (e) 1 mm and (f) 5 mm propagation length.

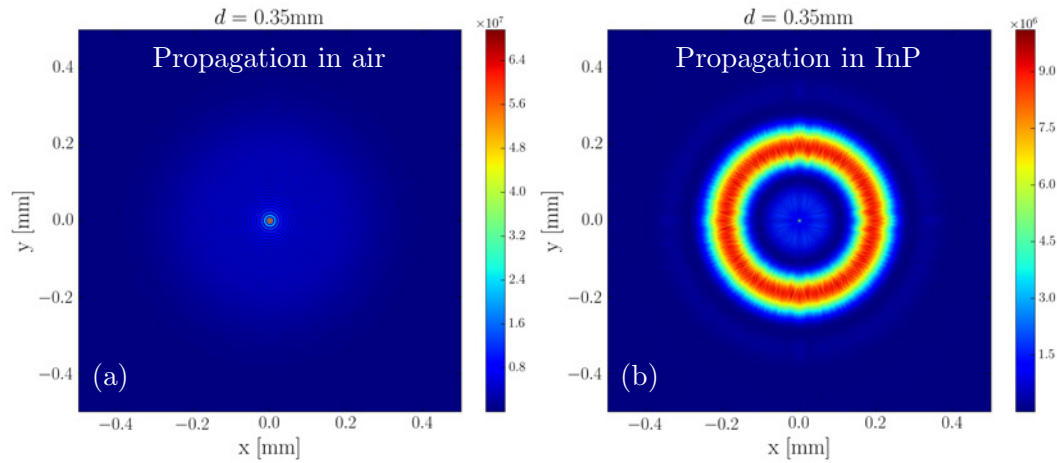


Fig. 3.12: Comparison of the simulated beam pattern after $350\ \mu\text{m}$ propagation in (a) air with the refractive index $n = 1$ and (b) InP with $n = 3.06$ for a wavelength of $8\ \mu\text{m}$. While the typical farfield pattern is observed in the former case, the higher refractive index slows down the propagation in the latter case. Hence, light beam has still nearfield character with the broadened ring-shaped aperture.

3.6 Beam shaping

As described in the previous section, the farfield of ring QCLs exhibits an intensity minimum in the center. However, for certain applications an intensity maximum in the center is desired e.g. to couple as much light as possible into a detector element. Therefore, the anti-parallel orientation of the electric field emitted from opposing sides of the ring has to be changed to a parallel orientation.

3.6.1 Abrupt grating shifts

One way to control the polarization is to incorporate phase-shifts in the second-order DFB grating. The field vectors from opposite sides need to have the same orientation, which can be achieved with two π phase shifts. An ordinary DFB grating consists of an alternating sequence of grating slit and bar. Hence, a π -shift can be generated by replacing a single slit with a grating bar or vice versa e.g. a double-bar or double-slit configuration. With this phase shift the sign of the field vector can be flipped, leading to a constructive interference in the farfield. Two π -shifts are necessary to preserve the periodicity of the phase over the whole ring [41]. The phase shifts are located at opposite sides of the ring (angular distance of 180°). Fig. 3.13 shows an illustration of a ring laser with a π -shift on top and at the bottom of the DFB grating. The farfield exhibits a central intensity maximum, which is exclusively vertically polarized.

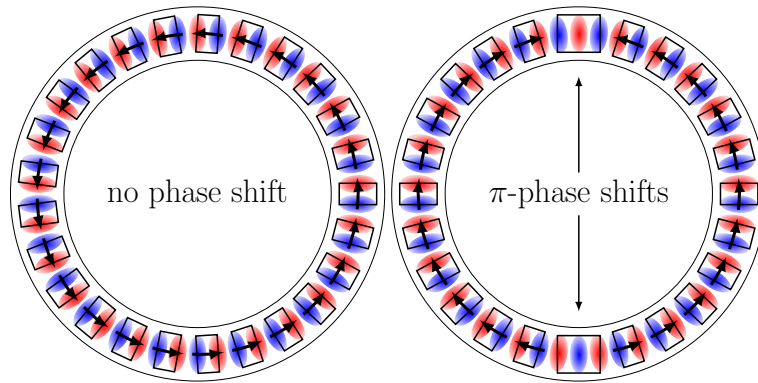


Fig. 3.13: Left: Illustration of a standard ring QCL with a DFB grating. Right: Ring laser with two abrupt π -shifts inserted on top and the bottom of the distributed-feedback grating. Field vectors (indicated by arrows) of opposite sides interfere constructive in the farfield, which leads to an intensity maximum in the center. Reprinted with permission from [141].

3.6.2 Continuous grating shifts

The abrupt π -shifts discussed before create an intensity maximum in the center. Another possibility is to use two continuous π -shifts [41, 134]. With dual DFB gratings the π -shift can be distributed over one half of the ring. Instead of an abrupt phase shift, the phase shift is smeared out over the circumference of the ring. The inner grating has the grating slits at the angular positions, where the outer grating has the grating bars. Fig. 3.14 shows an illustration of a continuous π -shift grating. Since the inner grating emits a different polarization than the outer grating, the total polarization can be adjusted by changing the relative strength of both components. In a first approximation this can be accomplished by varying the emitting area of inner and outer DFB grating. The ratio of the areas is a measure for the degree of polarization. The grating period cannot be changed as it defines the feedback for a certain wavelength and hence it is fixed. But the radial width of the grating slit and thus the emitting area can be chosen arbitrarily. An angle-dependent variation of the emitting areas can be simply utilized by changing the transition point between inner and outer grating according to e.g. a linear or cosine function. For each angle, the ratio of the grating areas then defines the degree of polarization.

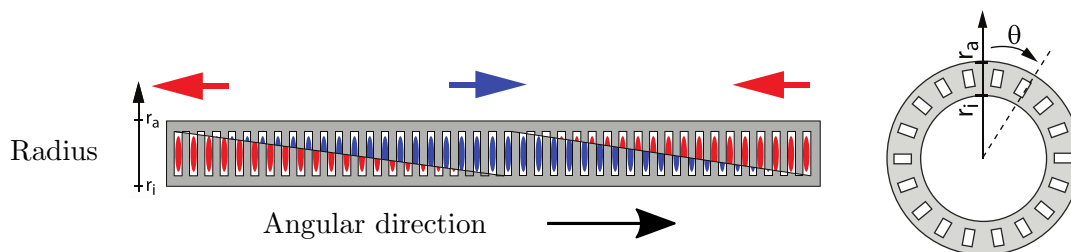


Fig. 3.14: Illustration of a DFB grating with a continuous π -shift. With modifications from [41].

Local light annihilation is expected in the regions where the area ratio between inner and outer grating is 50%. This is only true, if the mode is centered in the middle of

the waveguide. However, the center of mass of whispering-gallery modes is shifted more towards the outer radius of the ring, as can be seen in Fig. 2.16(a) in section 2.3.8. Hence, the emitting areas have to be weighted by the mode overlap. In the farfield regime an intensity maximum is observed in the center. If the dual DFB grating with two continuous π -shifts is designed for a ring QCL in such a way, that the ratio of the emitting slit areas becomes 50% for angles of e.g. 0° and 180° , then the intensity of the farfield becomes not zero for this angles. Instead, one observes a farfield, which seems to be rotated in counter-clockwise direction. Once again, the reason for this behavior is the asymmetric distribution of the whispering-gallery mode (WGM) along the radial direction. In turn, the rotation angle is directly related to the position of the WGM in the ring waveguide. More specifically, the position of the mode's center-of-mass relative to the grating determines the tilt angle in the farfield. This allows to determine the location of the WGM in the waveguide. Typical rotation angles between 8.8° and 19.6° have been extracted from measured farfields [142]. The higher angles occur for larger differences between the mode's center-of-mass and the center of the grating slit center. Some farfields surprisingly showed a rotation in opposite direction. Fig. 3.15 shows the measurement of ring QCLs with two continuous π -shifts, where the farfield is rotated different. This clockwise rotation can be observed if a higher-order radial WGM is excited in the ring laser. Because its center-of-mass is shifted more towards the inner radius of the ring, it changes the angle at which local light annihilation occurs. As a result the farfield is rotated in the clockwise direction.

3.6.3 On-chip collimation

The following section is based on the publication "Ring quantum cascade lasers with grating phase shifts and a light collimating dielectric metamaterial for enhanced infrared spectroscopy" [141].

The demand for compact, powerful and reliable infrared light sources for spectroscopic applications is a strong driving force for new concepts. The emitted light preferably has an intensity maximum in the center and features a small beam diameter. Both requirements can be fulfilled with substrate-emitting ring QCLs [141]. A standard ring laser has a second-order DFB grating, which couples out the light in vertical direction. Without any modifications on the grating, the farfield exhibits an intensity minimum in the center. As discussed in section 3.6.1, the incorporation of two π -phase shifts creates a central intensity maximum. Due to the emission of the light from the large surface area, the divergence angle is rather small as compared to ridge lasers. With an additional collimating lens, fabricated on the substrate side of the laser, an even narrower emission beam can be created [133].

The collimating lens on the substrate-side is fabricated as a dielectric gradient index metamaterial [143, 144] and effectively increases the emitting area. While the ring QCL on the surface has a diameter of $400\ \mu\text{m}$ and a waveguide width of $10\ \mu\text{m}$, the metamaterial on the substrate-side has a width of $80\ \mu\text{m}$. A collimation of the light beam is achieved with a refractive index gradient in radial direction by etching differently sized (sub-wavelength) holes into the InP substrate. The required radial refractive index profile $n_{\text{lens}}(r)$ can be estimated using Fermat's principle and geometric optics. Fig. 3.16(a) shows a sketch of

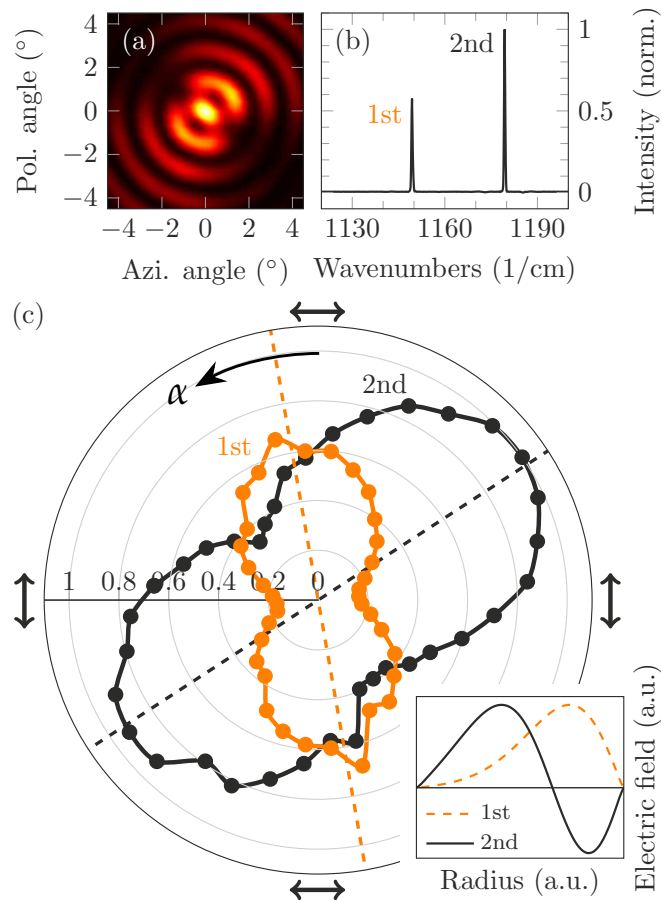


Fig. 3.15: (a) Instead of an expected counter-clockwise rotation, the measured farfield is rotated clockwise. (b) The presence of a second mode in the spectrum changes the emission behavior. (c) Polarization sensitive spectral measurements confirm that the second mode causes a rotation in the other direction. The center-of-mass of this mode is shifted towards the inner ring radius. Reprinted with permission from [142].

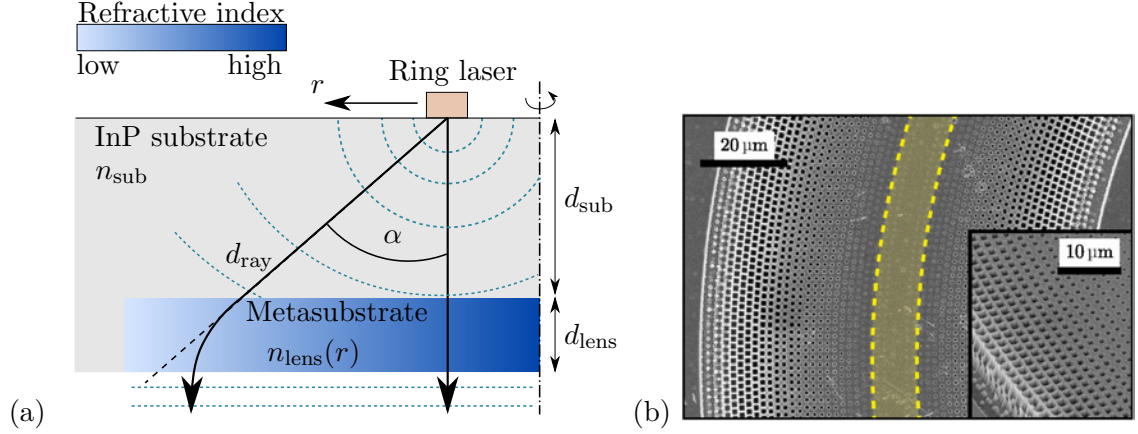


Fig. 3.16: (a) Sketch of the optical ray paths from the half-section of a ring laser. Illustration based on [133]. The lens is a gradient index metamaterial written into the InP substrate. Rays emitted under a larger angle α pass the lens at the radial position with lower refractive index. (b) Scanning electron microscope image of a fabricated metamaterial lens. Reprinted with permission from [141].

the substrate-integrated metamaterial lens. The time needed for a light ray to travel straight through the substrate of thickness d_{sub} and the metamaterial lens section d_{lens} is given by

$$t_{\text{direct}} = \frac{d_{\text{sub}}}{c_0/n_{\text{sub}}} + \frac{d_{\text{lens}}}{c_0/n_{\text{lens}}(r=0)}, \quad (3.8)$$

where the speed of light in the media is slowed down due to the higher refractive index. In a similar manner the time to propagate through substrate and metamaterial can be calculated by

$$t_{\text{indirect}} = \frac{d_{\text{ray}}}{c_0/n_{\text{sub}}} + \frac{d_{\text{lens}}}{c_0/n_{\text{lens}}(r=R)}, \quad (3.9)$$

where d_{ray} is the path length in the substrate for a ray emitted under an angle α . The refractive index at the radial position $R = \tan(\alpha)d_{\text{sub}}$, where the ray enters the metamaterial section, is given by $n_{\text{lens}}(r=R)$. The aim of the metamaterial lens is to equalize the propagation times for rays emitted under different angles. In other words, the spherical wavefronts are planarized in the metamaterial and share the same phase after passing the lens. This is achieved by slowing down the rays at small angles and reducing the effective optical path length for rays emitted under larger angles. With that the light is emitted from a much larger area, which results in a more collimated beam. By equating (3.8) and (3.9) an approximate refractive index profile of the metamaterial lens can be calculated to be

$$n_{\text{lens}}(r) = n_{\text{sub}} \left(1 + \frac{d_{\text{sub}}}{d_{\text{lens}}} - \frac{\sqrt{d_{\text{sub}}^2 + r^2}}{d_{\text{lens}}} \right), \quad (3.10)$$

where $n_{\text{sub}} = 3.06$ is the refractive index of the InP substrate ($n_{\text{lens}}(r = 0) \approx n_{\text{sub}}$) and $d_{\text{ray}} = \sqrt{d_{\text{sub}}^2 + r^2}$ is the geometric length of the ray. The thickness of the lens section d_{lens} is limited by the technological achievable etch depth. Fig. 3.16(b) shows a scanning electron microscope image of a metasubstrate fabricated into the substrate of a ring QCL [133]. Holes with smaller diameters experience a shallower depth due to aspect ratio dependent etching ARDE [145]. The metamaterial lens is written by e-beam lithography and transferred to a SiN etch mask. The etch depth ($= d_{\text{lens}}$) is $4.2 \mu\text{m}$ and reduces for holes below $1.5 \mu\text{m}$ diameter due to the aforementioned ARDE. Fig. 3.17(a) shows the calculated farfield with and without the metamaterial lens. The two π -phase shifts in the DFB grating cause an intensity maximum in the center, as can be seen in the measured farfield in Fig. 3.17(b). With the collimation optic the peak intensity increases to 265%. However, the theoretical value of around 724% is not reached, which is caused by a misalignment of the metamaterial with respect to the ring laser. Nevertheless, this concept shows that the monolithic integration of a lens on the substrate side of the ring laser allows to build very compact optical systems.

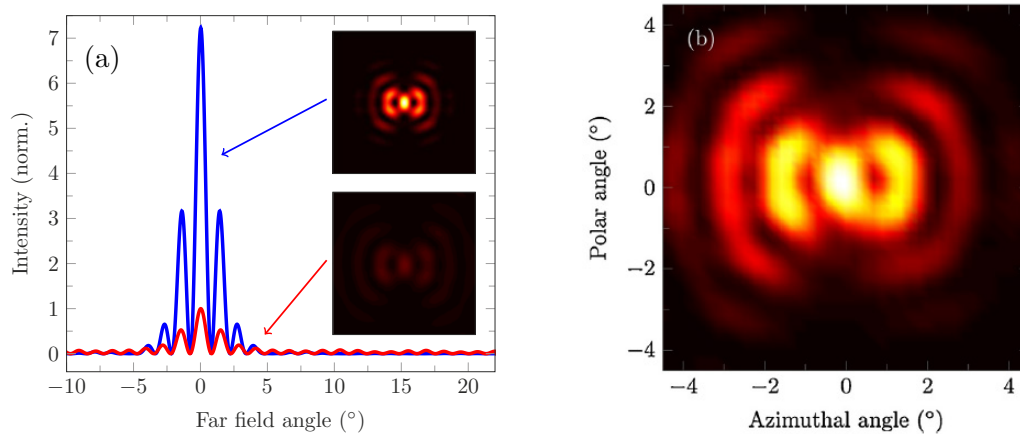


Fig. 3.17: (a) Calculated farfield distributions without collimating metasubstrate (blue line) and with the lens (red line). The insets show the corresponding 2D farfield patterns. (b) The measured farfield pattern shows an peak intensity increase of 265% compared to the ring QCL without lens. Reprinted with permission from [141].

3.7 Remote sensing

The following section is based on the publication "Remote Sensing with Commutable Monolithic Laser and Detector" [146].

Conventional spectroscopic sensing setups typically consist of a light source, a lens, an interaction region with the analyte, another lens and a detector. Every part not only

needs to be adjusted and aligned separately, but also takes up space and makes the whole arrangement bulky and heavy. For field applications, portability is an important selection criteria for a measurement system.

Quantum cascade lasers are powerful and wavelength tunable infrared light sources with a rather small footprint, which makes them very interesting for mobile sensing systems. Moreover, quantum cascade structures can also be used as detectors, as demonstrated first by Hofstetter et al. [147]. These photodetectors are based on intersubband transitions and are also referred as quantum cascade detectors (QCDs) [148]. QCDs are photovoltaic devices, which means that they generate a photocurrent without an external bias voltage. The quantum structures have been optimized for detection over the past years [149, 150, 151]. To build compact optical systems it would be good to have the same heterostructure working as laser and detector. This monolithic integration on the same chip offers new opportunities for mobile sensing systems. However, the transition of the biased heterostructure is red-shifted with respect to the unbiased case. Hence, the emission wavelength does not coincide with the absorption wavelength.

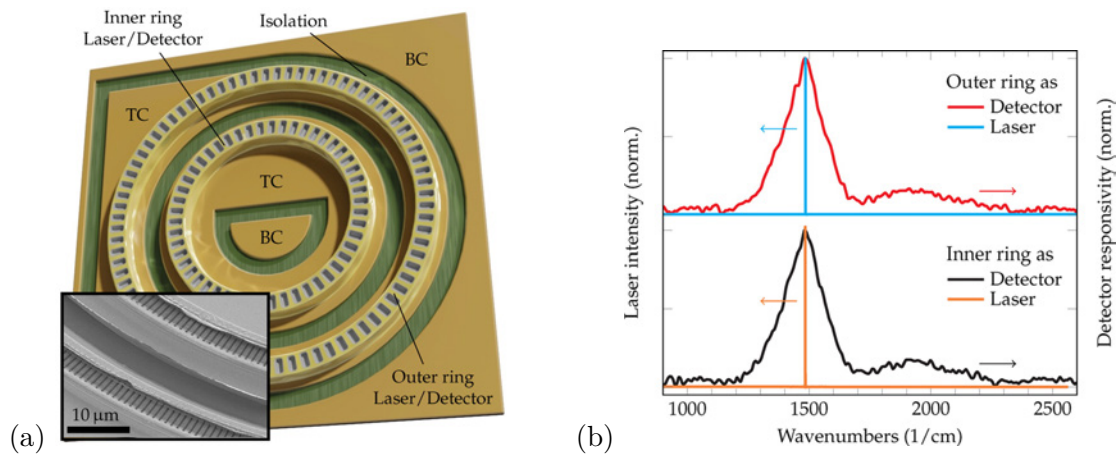


Fig. 3.18: (a) Illustration of the on-chip ring laser/detector system. To reduce the electrical crosstalk, each ring is connected with separate top and bottom contacts. A second-order DFB grating is used for in- and out-coupling of the light. (b) Single-mode spectra and broad absorption spectra of both devices measured with a DTGS detector and a global source. Emission and absorption perfectly overlap in this bi-functional QCLD heterostructure. Reprinted with permission from [146].

This problem can be solved by engineering the confined energy states, i.e. by reducing the coupling between lower laser level and extractor as well by inserting a narrow well between injector and active well. With that modifications, a bi-functional quantum cascade device for lasing and detection at the same-frequency has been demonstrated by Schwarz et al. [152, 153]. An integrated system with a quantum cascade laser and a detector together with a surface plasmon-polariton enhanced waveguide is used to sense liquids [115, 154]. In another concept, a surface-emitting ring laser is combined with a disk-shaped detector to measure gaseous species [155]. However, it turned out that the overlap of the emitted ring-shaped intensity pattern with the disk-shaped detector element is not optimal. Most of the light is lost and only a small amount is coupled into the detector.

A better combination is to use two concentric rings as laser and detector. Ring devices with diameters of 330 μm and 400 μm are fabricated with second-order DFB gratings for in- and out-coupling on the same chip. Fig. 3.18(a) shows an illustration of the miniaturized sensing system. Each ring has its own top- and bottom contacts to reduce the electrical crosstalk. The bi-functional quantum cascade laser detector (QCLD) material [156] is designed for emission and detection at around 6.7 μm . Fig. 3.18(b) shows the measured emission spectra (40 kHz/100 ns) and absorption spectra of both rings. They operate single-mode at 1483.3 cm^{-1} and 1484.3 cm^{-1} with a peak power of 79 mW and 100 mW for the inner and outer ring, respectively. The absorption spectrum covers the range from 1200 cm^{-1} to 1700 cm^{-1} with a peak responsivity of 1.2 mA/W at 1481 cm^{-1} . The chip with the two concentric rings is used in a remote sensing setup, illustrated in Fig. 3.19(a).

One ring is operated as laser and emits light via the second-order DFB grating towards the surface. The beam is collimated with a lens and directed into a 10 cm long gas absorption cell. A flat gold-coated mirror is placed behind the absorption cell to reflect the light back, where it passes the absorption cell once again and is finally focused with the same lens on the detector ring. A chopper wheel is used in combination with a lock-in amplifier to filter the crosstalk between laser and detector. For this proof-of-principle experiment the two gases isobutene (C_4H_8) and isobutane (C_4H_{10}) are used. The absorbance spectra of both gases as well as the emission spectra of the rings are shown in Fig. 3.19(b). While isobutene shows a linear absorbance, isobutane features a quadratic behavior around the emission wavelength of the ring laser.

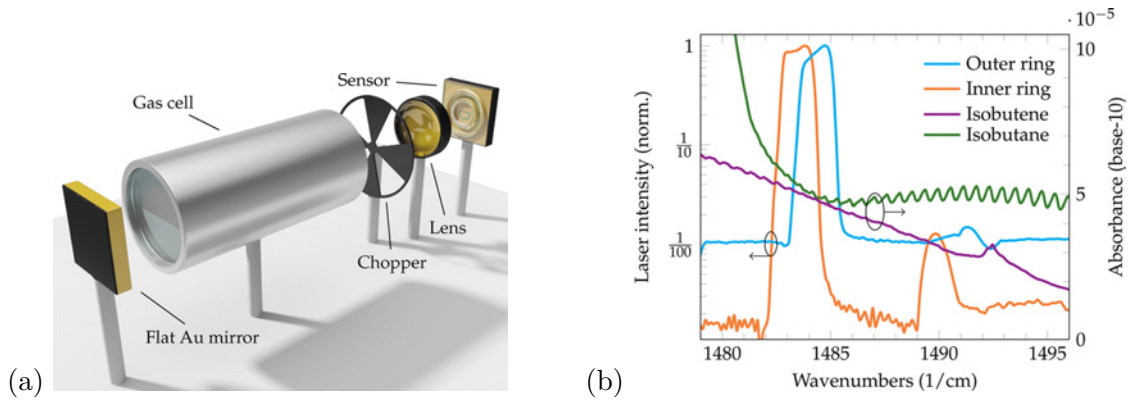


Fig. 3.19: (a) Sketch of the remote sensing setup. (b) Emission spectra of the ring laser together with the absorbance spectra of isobutene (C_4H_8) and isobutane (C_4H_{10}). Absorbance data from the Pacific Northwest National Laboratory infrared database for gas-phase sensing [157]. Reprinted with permission from [146].

The shift of the laser emission line during each 100 ns pulse ($\sim 1.4 \text{ cm}^{-1}$) is used to distinguish the gases in an absorption measurement. The signal of the detector ring is measured with 120 datapoints and a lock-in time constant of 0.5 s. For the detectable gas concentrations between 0–16%, a good agreement with the Beer-Lambert law is achieved. Fig. 3.20 shows the transmittance for the on-chip measurement of isobutane and isobutene. Inner and outer ring are used as commutable laser and detector. In the configuration where the inner ring operates as detector and the outer ring as laser, similar absorbance values are obtained for both gases i.e. $A_{\text{C}_4\text{H}_8} = 4.75 \times 10^{-5}$ (isobutene) and $A_{\text{C}_4\text{H}_{10}} = 4.78 \times 10^{-5}$

(isobutane), respectively. For the inverted configuration, where the inner ring emits the light and the outer ring acts as detector, higher absorbance values of $A_{C_4H_8} = 5.07 \times 10^{-5}$ and $A_{C_4H_{10}} = 5.49 \times 10^{-5}$ are obtained. For the isobutane measurement a 3σ limit of detection (LOD) of 397 ppm is calculated for the configuration with the inner ring as detector and the outer ring as laser. Furthermore, an optimum averaging time of 300 s is estimated from long-term measurements with nitrogen [146, 138].

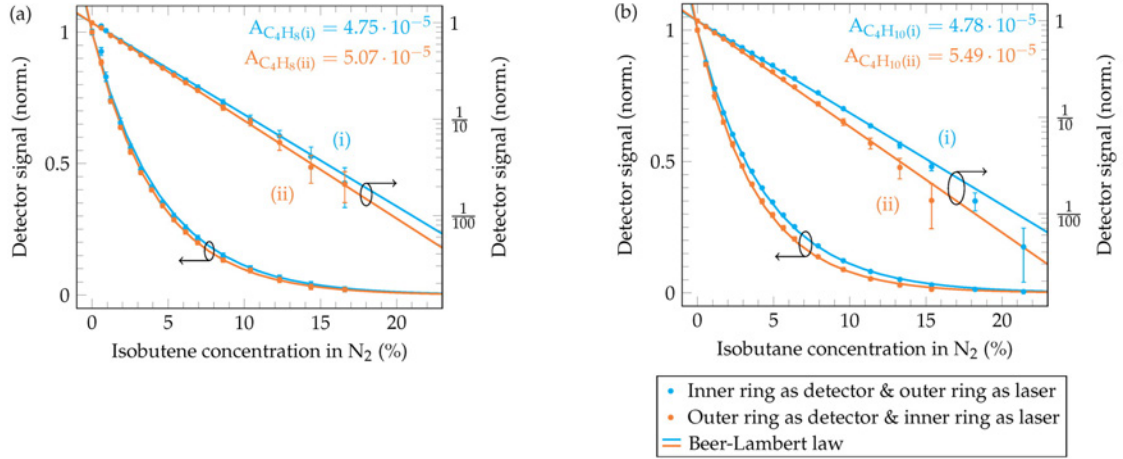


Fig. 3.20: Measured transmittance for isobutene (C_4H_8) and isobutane (C_4H_{10}) as function of the gas concentration. In configuration (i) the outer ring operates as laser and the inner ring as detector. In configuration (ii) the operation is inverted. (a) Isobutene measured in both configurations and plotted in linear and semi-logarithmic scale. Experimental data is represented as dots, while the fit to the Beer-Lambert law is drawn with solid lines. The absorbance fit parameter are provided in the upper right. (b) Same measurement and data fit for isobutane. Reprinted with permission from [146].

3.8 Thermal management

In the active region of QCLs, a substantial amount of heat is generated, which needs to be dissipated. If heat is accumulated, the temperature in the core of the laser rises and due to the exponential dependence $J = J_0 \exp(T/T_0)$, also the current increases. This leads to an increase of the temperature and the current rises again. More specifically, with increasing temperature, the inter- and intrasubband lifetimes are reduced and non-radiative scattering losses, as well as backfilling, are enhanced. This positive feedback loop leads to self-heating of the device and as a result, the performance of the laser is strongly degraded. For QCLs, the dissipated power density is in the range of 20 – 50 kW/cm². In comparison, a hotplate dissipates ~ 6 W/cm² and a computer processor dissipates ~ 50 W/cm². For QCLs, device heating is identified as the major limiting factor for achieving continuous-wave operation at higher operating temperatures [158]. The temperature in the active region T_{act} is directly related to the electrical input power of the device via [17]

$$T_{act} = T_{sub} + R_{thermal}UI, \quad (3.11)$$

where T_{sub} is the submount temperature, R_{thermal} the thermal resistance and U and I the applied voltage and the current through the laser device. The thermal resistance gives a measure for the arising temperature difference across a component due to an energy flow, e.g. an electrical input power. It is defined as

$$R_{\text{thermal}} = \frac{\Delta T}{IU}, \quad (3.12)$$

with the unit in [K/W]. In low pulse duty-cycle operation, e.g. with 5 kHz/100 ns, the active region temperature equals approximately the submount temperature. However, in high duty-cycle or cw mode, T_{act} can be substantially higher than T_{sub} due to heat accumulation in the active region. An estimate for the maximum operating temperature in continuous wave operation can be derived, considering the exponential dependence of the threshold current density on the temperature in the active region [159]. The submount temperature at threshold then reads

$$T_{\text{sub}} = T_{\text{act}} - R_{\text{thermal}} U_{\text{th}} J_{\text{th}} A \quad (3.13)$$

$$= T_{\text{act}} - R_{\text{thermal}} U_{\text{th}} J_0 \exp(T_{\text{act}}/T_0) A, \quad (3.14)$$

where U_{th} is the threshold voltage, J_0 and T_0 are fitting parameters and A is the device area. Taking the derivative of (3.14) with respect to T_{act} and equating to zero delivers $T_{\text{act}} = \ln [T_0 / (R_{\text{thermal}} U_{\text{th}} A J_0)]$ which can be again inserted into (3.13) and an expression for the maximum operating temperature is found with

$$T_{\text{sub,max}} = T_0 \left[\ln \left(\frac{T_0}{R_{\text{thermal}} U_{\text{th}} A J_0} \right) - 1 \right] \quad (3.15)$$

$$= T_0 \left[\ln \left(\frac{G_{\text{thermal}} T_0}{U_{\text{th}} J_0} \right) - 1 \right], \quad (3.16)$$

with the specific thermal conductance $G_{\text{thermal}} = JU/\Delta T$ in units of [W/(K cm²)]. From this analytic expression it is apparent that a higher operating temperature of the laser can be gained if the T_0 value is increased, the specific thermal conductance G_{thermal} is increased and the threshold power $U_{\text{th}} J_0$ is minimized. Therefore, an optimization of active region and waveguide as well as the thermal management are necessary. For instance, alloy scattering strongly reduces the phonon mean free path, which prevents an efficient heat transport. Therefore, ternary materials such as InGaAs or InAlAs have a thermal conductivity, which is around 15 times lower than of the binary InP [17]. Ways to improve the thermal management include an appropriate device geometry, good thermal conducting materials and also the mounting technique.

In the following, different approaches for optimizing the heatsinking in ring QCLs are in-

vestigated by simulation. More specifically, the impact of the waveguide geometry, waveguide materials, substrate thickness, epilayer-down bonding and buried heterostructure configuration on the thermal management are analyzed.

3.8.1 Thermal model

In general, a heat flow is caused by a (negative) temperature gradient between two materials/components and the heat can be transferred via three mechanisms:

1. Conduction
2. Convection
3. Radiation

The heat conduction covers a variety of heat transport mechanisms. In gases, for instance, collisions of molecules are responsible for the heat transport, while in fluids the molecules perform oscillations. For solids, the thermal energy is mainly transferred via electrons and lattice vibrations (phonons). Another possibility to release heat is by natural or forced convection, e.g. cooling of a device with air-flow or water-cooling. For the simulations of the lasers, no convection loss is assumed. The third option is the dissipation of heat via thermal radiation in the surrounding. This process is proportional to $\epsilon\sigma(T^4 - T_{\text{amb.}}^4)$, where ϵ is the emissivity of a surface, σ is the Stefan-Boltzmann constant, T is the temperature and $T_{\text{amb.}}$ is the ambient temperature. In a first order approximation the thermal radiation is neglected and only heat transfer by conduction is considered for the simulation of the structure.

In general, the heat transfer in solids is described by following equation

$$Q = -\vec{\nabla} \cdot (\underline{k} \cdot \vec{\nabla} T) + \rho C_p \frac{\partial T}{\partial t}, \quad (3.17)$$

where Q denotes the heat source density in [W m^{-3}], \underline{k} the thermal conductivity (scalar or tensor), T the temperature, ρ the density and C_p the heat capacity at constant pressure. The dissipated power density in the active region is given by $Q = JE$, where J is the current density and E the electric field in the active region [17]. For the thermal analysis of the ring laser devices a steady-state heat dissipation model is used. Since for a steady-state solution the time dependence of the temperature is zero, the right term on the right hand side of (3.17) vanishes. As a result, the thermal problem is described by following 2D Fourier's heat transfer equation

$$Q = -\vec{\nabla} \cdot \left(\begin{bmatrix} k_{\parallel} & 0 \\ 0 & k_{\perp} \end{bmatrix} \cdot \vec{\nabla} T \right), \quad (3.18)$$

where k_{\parallel} and k_{\perp} are the in-plane and cross-plane (in growth direction) anisotropic thermal conductivities, given in [$\text{W}/(\text{m K})$]. For bulk materials, an isotropic scalar value for the

thermal conductivity can be used, but for semiconductor layers in lasers with their typical much lower thicknesses in growth direction compared to the lateral size, an anisotropic behavior can be expected. The thermal conductivity is lower for heat flowing in growth direction due to scattering of the phonons at the interfaces. The mean free paths of the phonons are reduced and hence the thermal transport is limited. As a result, the thermal conductivity for a heat flow parallel to the layers is approximately 3–10 times higher than perpendicular to the layer plane ($k_{\parallel} > k_{\perp}$) [160]. Furthermore, the thermal conductivities are temperature-dependent and usually decrease with increasing temperature.

To avoid confusion arising from the different usage of terms in the literature, a list of important thermal quantities is given below. The definitions are based on the steady-state temperature difference between two surfaces ΔT in [K], the plane area A in [m²], the heat flow per area q in [W m⁻²] and the thickness L of a material or component given in units of [m].

- Thermal conductivity: $k = qL/\Delta T$ in [W/(K m)]
- Thermal resistance: $R_{\text{thermal}} = L/(kA)$ in [K/W]
- Thermal conductance: $C_{\text{thermal}} = kA/L = 1/R_{\text{thermal}}$ in [W/K]
- Thermal insulance: $R_{\text{in}} = L/k$ in [K m²/W]
- Specific thermal resistance (resistivity): $R_{\lambda} = 1/k$ in [K m/W]
- Specific thermal conductance: $G_{\text{thermal}} = k/L$ in [W/(K m²)]

The heat transfer equation (3.18) is solved by a finite-element method implemented in COMSOL for the P51 QCL material (for the growth sheet see A.3.1). Due to the symmetry of the ring QCL, a 2D axisymmetric model is used for the computation of the temperature distribution. The model geometry as well as the meshed domains of the ring laser are shown in Fig. 3.21. Within the axisymmetric model the conductivity tensor takes the form

$$\underline{\underline{k}} = \begin{pmatrix} k_{rr} & 0 & 0 \\ 0 & k_{\phi\phi} & 0 \\ 0 & 0 & k_{zz} \end{pmatrix}, \quad (3.19)$$

where the in-plane thermal conductivity is $k_{\parallel} = k_{rr} = k_{\phi\phi}$ and the out-of-plane component is $k_{\perp} = k_{zz}$. The standard waveguide width is $w = 10 \mu\text{m}$ and the substrate height is $350 \mu\text{m}$. For electrical isolation, the laser is covered with a 250 nm thin Si₃N₄ passivation layer. The metallization consists of a 10 nm Ti adhesion layer followed by 300 nm of Au. An indium solder with 3 μm thickness is considered between the InP substrate and the copper submount.

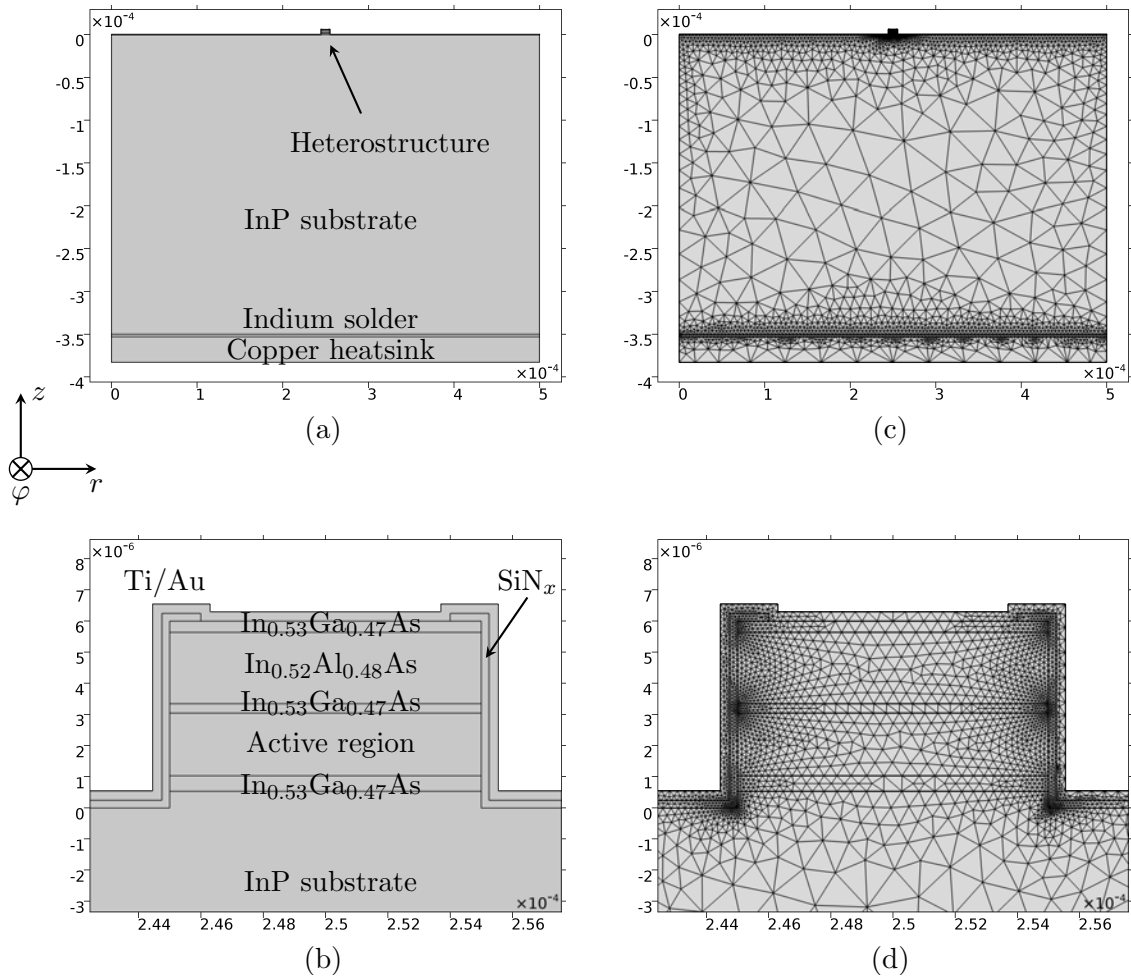


Fig. 3.21: Model geometry (a) and magnified heterostructure (b) as well as the corresponding meshes (c) and (d) used for the thermal simulations in COMSOL. An axisymmetric model is used for the ring laser, where the structure is revolved around the vertical symmetry axis at the origin. The entire simulation geometry consists of ~ 14600 triangular elements and in the region of interest (around the active region) the mesh size has been refined.

3.8.2 Boundary conditions

For the solution of the heat equation, different boundary conditions are used. In particular the thermal simulations include following constraints:

1. Constant temperature, $T = T_{\text{const}}$.
2. Thermal insulation, $\mathbf{e}_n \cdot (k\vec{\nabla}T) = 0$
3. Constant heatsource density, $Q = Q_{\text{source}}$
4. Thin thermally resistive layer, $R = d_s/k_s$

The bottom edge of the copper submount has been set to a constant temperature of $T = 293.15\text{ K}$ and for all other outer boundaries of the simulation domain a thermal insulation boundary condition is set. The latter condition states that there is no heatflux across the boundary, or in other words, the temperature gradient is zero, which means that the temperatures on both sides of the boundary have to be equal. For the active region, a homogeneous heatsource density $Q = U_{\text{th}}J_{\text{th}}/h_{\text{AR}}$ is assumed, where $U_{\text{th}} = 10\text{ V}$ and $J_{\text{th}} = 2.5\text{ kA/cm}^2$ are the threshold voltage and current density, respectively. For the height of the active region in the P51 laser material $h_{\text{AR}} = 2\text{ }\mu\text{m}$ is used. From these values a heatsource density of $Q = 1.25 \times 10^{14}\text{ W/m}^3$ is calculated, which corresponds to a total heat source of $\sim 3\text{ W}$ dissipated in the active region ($= 25\text{ kW/cm}^2$). Since there is no light emission at threshold, all electrical input power is converted to heat. A contribution due to Joule heating via current transport through the contacts and cladding layers can be usually neglected. The gradings between the waveguide sections as well as the Ti adhesion layer for the metallization are modelled as thermal boundary resistance layer. The thicknesses of these layers are on the order of $10 - 25\text{ nm}$, which would require a very fine mesh for a 2D implementation. Instead, a computational more convenient 1D representation as thin thermally resistive layers is used. The heat flux across the thermal boundary resistance layer (TBR) is defined as

$$\mathbf{e}_{n1} \cdot (k_1\vec{\nabla}T_1) = k_s \frac{T_2 - T_1}{d_s} \quad (3.20)$$

$$\mathbf{e}_{n2} \cdot (k_2\vec{\nabla}T_2) = k_s \frac{T_1 - T_2}{d_s}, \quad (3.21)$$

with the unit vectors \mathbf{e}_{n1} and \mathbf{e}_{n2} perpendicular to the layer plane of the boundary, the thermal conductivities k_1 and k_2 and the temperatures T_1 and T_2 in the two domains. The interface thermal resistance is specified by the thickness d_s and the thermal conductivity k_s .

Material (doping)	Thermal conductivity k [W/(Km)]	$k_{293.15\text{K}}$
Au	$337 - 660 \times 10^{-4}T$	318
AuSn solder	$-160 \times 10^{-4}T + 62$	57
AlAs	$22.527 \times 10^4 T^{-1.37}$	94
AlN	$575 \times 10^{-5}T^2 - 6T + 1540$	275
Cu	$349 + 14710T^{-1}$	399
Diamond		1200
GaAs	$7.5 \times 10^4 T^{-1.28}$	52
InAs	$4.5 \times 10^5 T^{-1.73}$	24.3
In solder	$93.9 - 696 \times 10^{-4}T + 986 \times 10^{-7}T^2$	82
InP	$282 \times 10^3 T^{-1.45}$	75
$\text{In}_{0.53}\text{Ga}_{0.47}\text{As}$ ($5 \times 10^{16} \text{ cm}^{-3}$)	$23 - 930 \times 10^{-4}T + 106 \times 10^{-6}T^2$	4.8
$\text{In}_{0.53}\text{Ga}_{0.47}\text{As}$ ($8 \times 10^{18} \text{ cm}^{-3}$)	$0.8(23 - 930 \times 10^{-4}T + 106 \times 10^{-6}T^2)$	3.9
$\text{In}_{0.52}\text{Al}_{0.48}\text{As}$ ($2 \times 10^{17} \text{ cm}^{-3}$)	$20.5 - 840 \times 10^{-4}T + 95 \times 10^{-6}T^2$	4
SiO_2	$974 \times 10^{-4} + 538 \times 10^{-5}T - 469 \times 10^{-8}T^2$	1.3
Ti	$34.88 - 7.34 \times 10^{-2}T + 1.2 \times 10^{-4}T^2 - 6.81 \times 10^{-8}T^3$	22
Si_3N_4	$30 - 140 \times 10^{-4}T$	26

Tab. 3.2: Temperature dependent thermal conductivities for various materials and evaluation at a temperature of $T = 293.15$ K. Data from [161, 162, 163, 17, 160].

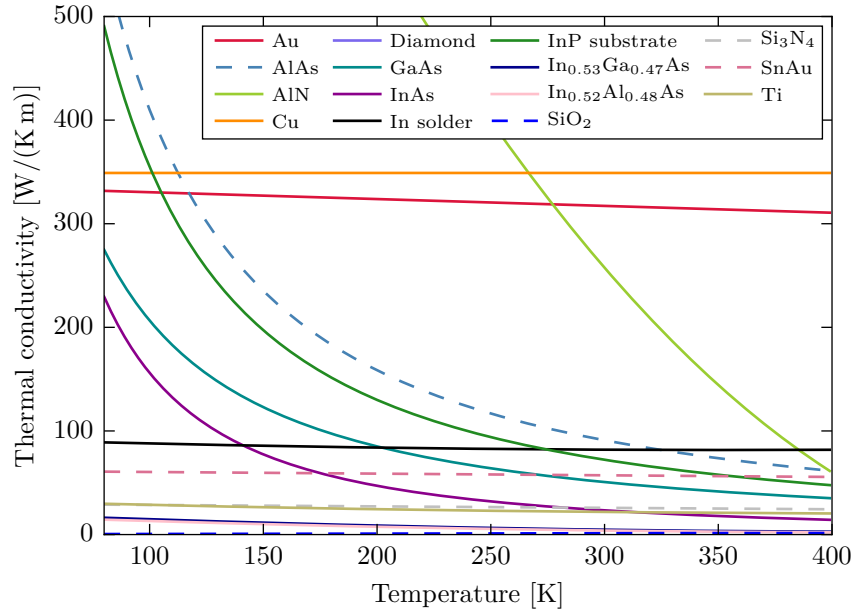


Fig. 3.22: Thermal conductivities of various materials from Tab. 3.2 as function of the temperature.

3.8.3 Materials

In order to reach a high operating temperature of the laser, the total thermal resistance R_{thermal} has to be minimized. This task often leads to a tradeoff between low loss waveguide, good optical confinement and at the same time low thermal resistance. As already mentioned, the in-plane and cross-plane thermal conductivities of superlattices and heterostructures in general are not the same and can differ from the bulk values due to interface scattering [164]. In growth direction (cross-plane), the heat transport is limited due to scattering of the phonons. In the active region a large number of interfaces is present, which requires to consider an anisotropic heat transport. Fig. 3.23 shows a scanning electron microscopy image of such a layer stack together with the in-plane and cross plane directions. Following the approach from [165, 166], the cross-plane thermal conductivity can be calculated from the bulk resistivities via

$$k_{\perp} = 1 / \left(\sum_i \frac{d_i}{d_{\text{total}}} R_i + \frac{N}{d_{\text{total}}} \text{TBR} \right). \quad (3.22)$$

Here, d_i denotes the thickness of a single layer, d_{total} is the total thickness of the whole layer stack and the bulk resistivity ($= 1/k_i$) of each material is given by R_i . For the P51 active region, a total number of interfaces $N \approx 770$ is considered. For each interface, a thermal boundary resistance TBR, also known as Kapitza resistance [167, 168], is applied. An average value of $\text{TBR} = 1.5 \times 10^{-9} \text{ K m}^2/\text{W}$ is used for the $\text{In}_{0.53}\text{Ga}_{0.47}\text{As}/\text{In}_{0.52}\text{Al}_{0.48}\text{As}$ layers lattice matched to InP [169]. The in-plane thermal conductivity is estimated [160] as the weighted average of the bulk values via

$$k_{\parallel} = 0.75 \sum_i \frac{d_i}{d_{\text{total}}} R_i. \quad (3.23)$$

For the simulations, an in-plane thermal conductivity of $k_{\parallel} = 3.2 \text{ W}/(\text{K m})$ and a cross-plane value of $k_{\perp} = 1.2 \text{ W}/(\text{K m})$ are used. The thermal conductivity of a ternary alloy can be calculated from its binary compounds using Abele's interpolation scheme [170]

$$\frac{1}{k_{A_x B_{1-x} C}} = \frac{x}{k_{AC}} + \frac{1-x}{k_{BC}} + \frac{x(1-x)}{C_{AB}}, \quad (3.24)$$

with the composition x , the bowing parameter C_{AB} and the thermal conductivities of the binary materials k_{AC} and k_{BC} [163]. The temperature dependent thermal conductivities of various materials are listed in Tab. 3.2. Experimental values for the thermal conductivities can be obtained e.g. with the 3ω method [171] or by photoluminescence spectroscopy [160, 168]. The consideration of the gradings (see P51 growthsheet in A.3.1) between the waveguide layers has only a marginal effect on the simulation result compared to a simulation without these thin thermally resistive layers with $k_{\text{grading}} \approx 3 \text{ W}/(\text{K m})$ (T_{max} decreases by $\sim 3 \text{ K}$). Nevertheless, the thermal boundary resistances due to the grading layers are included in the simulations, because it does not cause too much effort.

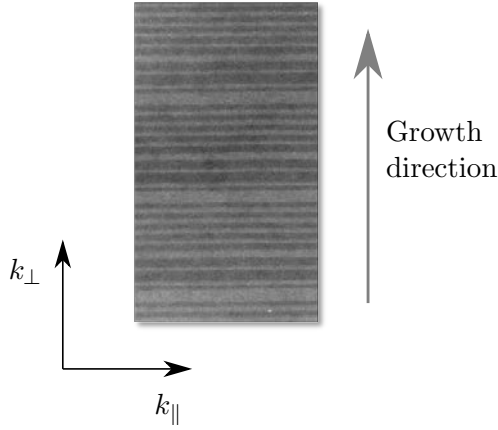


Fig. 3.23: In-plane (k_{\parallel}) and cross-plane (k_{\perp}) thermal conductivities are used to model the anisotropic heat transport in the active region of the ring QCL. The transmission electron micrograph shows the active region of a QCL (courtesy of USTEM, TU Wien).

3.8.4 Simulation results

The temperature in the active region is related to the submount temperature via (3.11), which can be rewritten to following expression

$$T_{\text{act}} = T_{\text{sub}} + \frac{UJ}{G_{\text{thermal}}}. \quad (3.25)$$

Knowing the input power density UJ and the fixed submount temperature T_{sub} , the simulation delivers an active region temperature T_{act} , which can be translated to the specific thermal conductance (conductance per area) G_{thermal} of the laser device. The latter one is explicitly given as

$$G_{\text{thermal}} = \frac{UJ}{T_{\text{act}} - T_{\text{sub}}}. \quad (3.26)$$

In the following, simulations of different ring laser configurations are discussed and compared in terms of G_{thermal} . Hereby, the simulation output $\Delta T_{\text{max}} = \max(T_{\text{act}} - T_{\text{sub}})$ will be used to calculate the specific thermal conductance, where the submount temperature $T_{\text{sub}} = 213.15 \text{ K}$ is kept constant. If nothing else is specified, the colorbars always show the temperature difference $T_{\text{act}} - T_{\text{sub}}$. Fig. 3.24 shows the simulation result for the standard ring configuration with a waveguide width of $w = 10 \mu\text{m}$ and an outer diameter of $400 \mu\text{m}$. Approximately half of the heat generated in the active region is directly transferred via the InP substrate to the heat sink, as indicated by the large arrow. The other half of the heat is dissipated via the upper and the left/right boundary of the active region, as shown in Fig. 3.24(a). Furthermore, the orientation of the heat flow is visualized with small arrows. As expected, the peak temperature occurs in the active region, where a constant heat source density is assumed. A maximum temperature (absolute) of $T_{\text{max}} = 508 \text{ K}$ is extracted, corresponding to a relative temperature increase of $\Delta T_{\text{max}} = 215 \text{ K}$. From this

extracted value a specific thermal conductance of $G_{\text{thermal}} = 116 \text{ W}/(\text{K cm}^2)$ can be calculated for this configuration. The heat transfer equation (3.18) is solved for a 2D simulation area, but due to the axisymmetry a 2.5D solution can be generated via a revolution around the vertical symmetric axis at the origin. An 3D illustration of a slice of the temperature distribution is shown in Fig. 3.24(c).

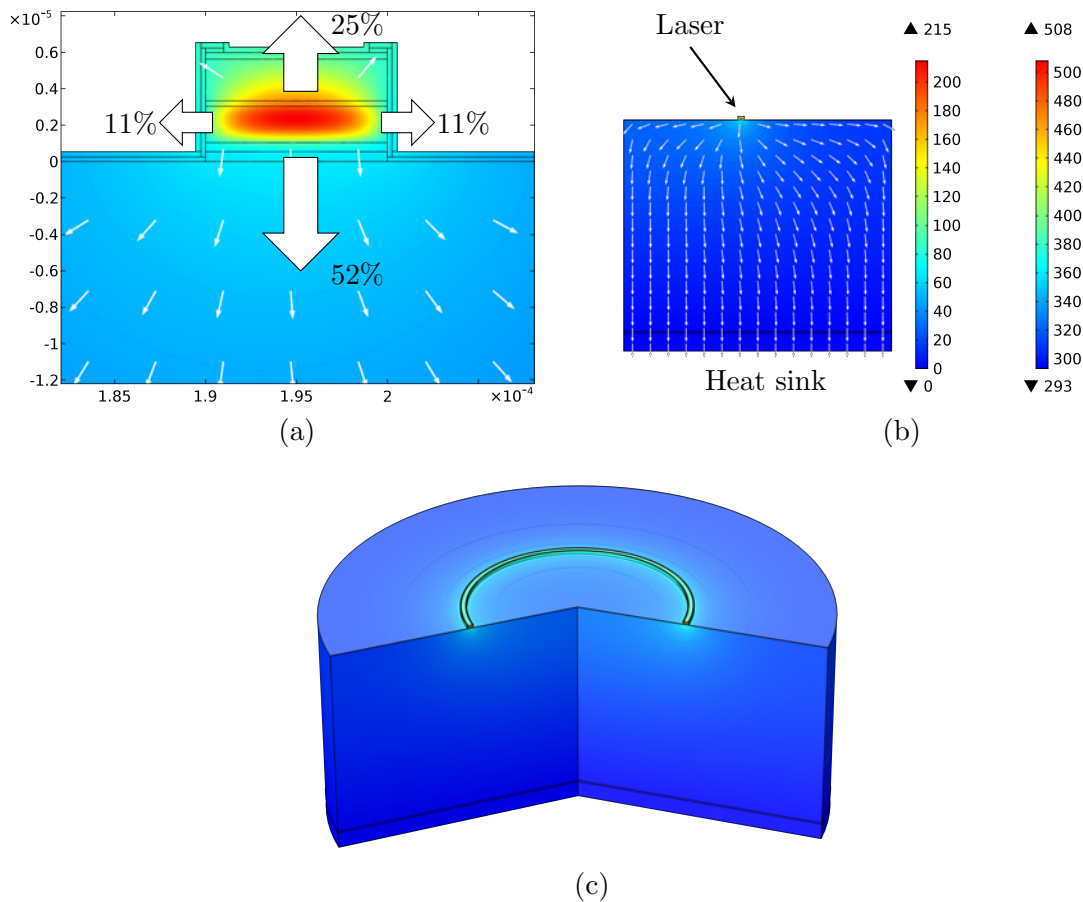


Fig. 3.24: Simulated temperature profile for a standard ring QCL with a waveguide width of $w = 10 \mu\text{m}$. (a) The small arrows visualize the orientation of the heat flux, while the large arrows indicate the amount of heat transferred in the specified direction. (b) Total simulated structure with the temperature color legend. The absolute temperature in [K] is shown in the right colorbar, while the left one shows the relative temperature increase $\Delta T = T - T_{\text{sub}}$ with respect to the submount temperature $T_{\text{sub}} = 293.15 \text{ K}$. The colorbars are valid for all three figures. (c) Slice through simulation domain, which can be constructed by a revolution around the vertical symmetry axis.

Influence of the geometry

In a next step the dependence of the temperature distribution on the waveguide width is investigated. For the $10 \mu\text{m}$ wide standard ring, 52% of the heat is directly transferred through the bottom boundary of the active region to the heat sink on the substrate bottom

side. Only a small fraction of the heat flux passes through the left and right boundaries, as indicated in Fig. 3.24. In contrast, a narrow ring QCL with a waveguide width of only $5\ \mu\text{m}$ has a substantial higher lateral heat transport. The simulated temperature pattern, shown in Fig. 3.25(a), gives a $\Delta T_{\text{max}} = 117\ \text{K}$, corresponding to $G_{\text{thermal}} = 212\ \text{W}/(\text{K cm}^2)$. On the other hand, if the waveguide width is increased to $15\ \mu\text{m}$, most of the heat is again transferred directly downwards, shown in Fig. 3.25(b). The broader waveguide features a $G_{\text{thermal}} = 91\ \text{W}/(\text{K cm}^2)$ and therefore has the poorer thermal performance. A narrow waveguide on one hand allows to reduce the total dissipated power, since the heat source density is proportional to the input current and thus to the device area. Furthermore, the distance to the good thermal conducting metal layer is reduced. The in-plane thermal conductivity in the active region is higher than in the growth-direction, which is also beneficial for the heat dissipation in lateral direction.

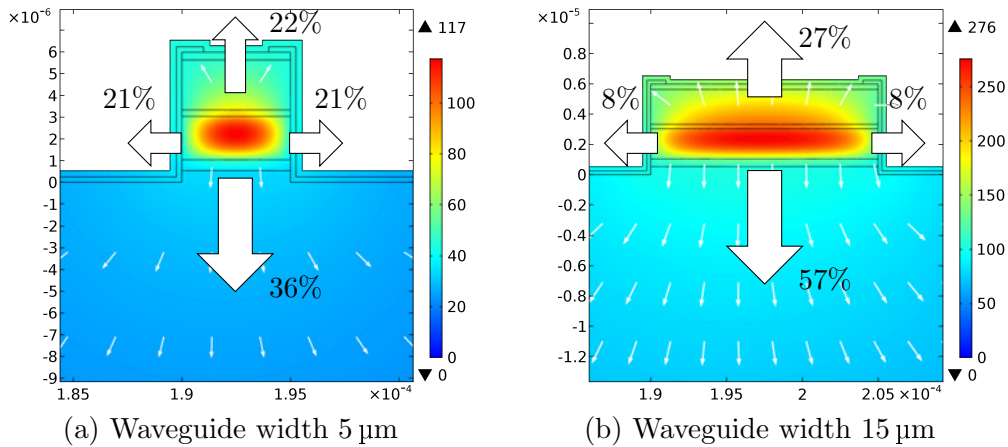


Fig. 3.25: Influence of the waveguide width on the thermal performance. (a) For a narrow waveguide ($5\ \mu\text{m}$), the lateral heat transport is enhanced compared to a broad waveguide (b) with a width of $15\ \mu\text{m}$. The colorbars show the relative temperature increase $\Delta T = T - T_{\text{sub}}$.

The thickness of the InP substrate defines the distance between the heat source (active region) and the heat sink (copper submount). Thinning the substrate should have a positive effect on the thermal management. For the standard ring, a substrate thickness of $350\ \mu\text{m}$ is used, which is the nominal wafer thickness as it is shipped by the supplier. Fig. 3.26 shows the simulation results for a reduced thickness of $200\ \mu\text{m}$ (a) and $100\ \mu\text{m}$ in (b). In the former case, the specific thermal conductance at threshold is calculated to $G_{\text{thermal},200\ \mu\text{m}} = 126\ \text{W}/(\text{K cm}^2)$ and in the latter case to $G_{\text{thermal},100\ \mu\text{m}} = 136\ \text{W}/(\text{K cm}^2)$.

Metallization

In order to enable an efficient heat dissipation from the active core, the thickness of the metallization layer (nominal $300\ \text{nm}$) on top of the laser can be increased. Fig. 3.27(a) to (c) shows the simulated temperature profile for thicknesses of $1\ \mu\text{m}$, $5\ \mu\text{m}$ and $10\ \mu\text{m}$. As expected, the maximum temperature in the active region decreases with increasing metallization. The metal layer acts as heatspreader, which allows a better dissipation

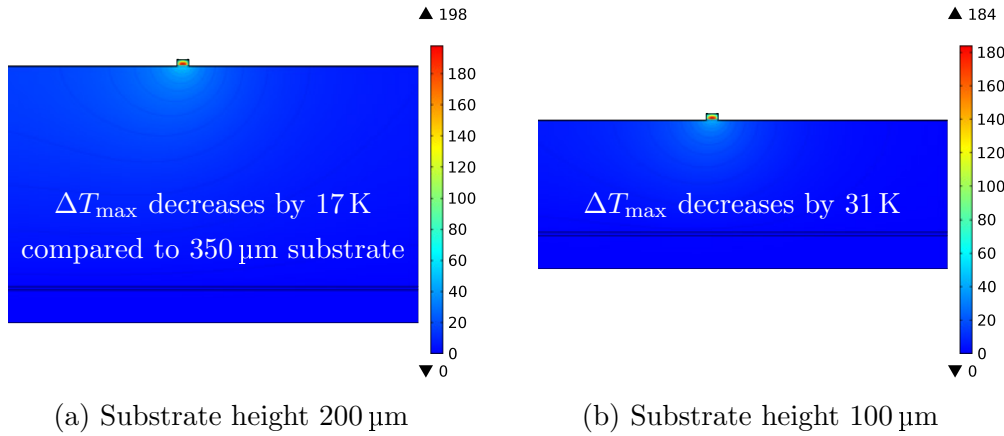


Fig. 3.26: Influence of the substrate thickness on the maximum temperature. The colorbars show the relative temperature $\Delta T = T - T_{\text{sub}}$.

from the core region. The heat flow is distributed more in lateral direction, which gives an effective larger cooling area. However, the benefit of a much thicker layer becomes less and less significant, as shown in Fig. 3.27(d). For a layer thickness larger than $\sim 5 \mu\text{m}$, the impact on the temperature performance is negligible. Hence it is not necessary to sputter/electroplate thicker Au metallization layers.

Lateral regrowth

A common way to improve the thermal management in QCLs is to laterally regrow the etched waveguide with semi-insulating InP material (Fe-doped). Such a process is also known as buried heterostructure [17]. The refractive index of InP is lower than the one of the active region, which is beneficial for waveguiding. Even more important is the much higher thermal conductivity of InP, which helps to enhance the lateral heat dissipation. For the buried heterostructure process, the waveguide of the laser is etched using a SiO_2 or Si_3N_4 mask. This mask can be reused in the following InP:Fe regrowth process using a MOCVD or gas-source MBE system. Hereby, a thin InAlAs spacer layer can be grown first to reduce void defects at the arsenide-phosphide interface between active region and regrown InP [172]. Moreover, leakage currents at the interface can be reduced by using this blocking layer. The regrown InP layers only grow laterally due to the dielectric mask on top of the laser. This mask is removed after the growth and the passivation/metallization layers are then deposited like in a standard process. A slightly modified process was developed at the ETH, which is called the inverted buried heterostructure process [173]. Instead of regrowing the whole laser after the waveguide etch, this process starts with a laser that consists of the lower cladding and the active region but without the upper cladding. In a first step, a mask is used for etching the waveguide, which in this case is only $2 - 3 \mu\text{m}$ instead of $3 - 7 \mu\text{m}$ in the standard process. Afterwards the laser is laterally regrown with semi-insulating InP, the mask is stripped and the whole stack is overgrown with n-doped InP for the upper cladding layer. The advantages of this

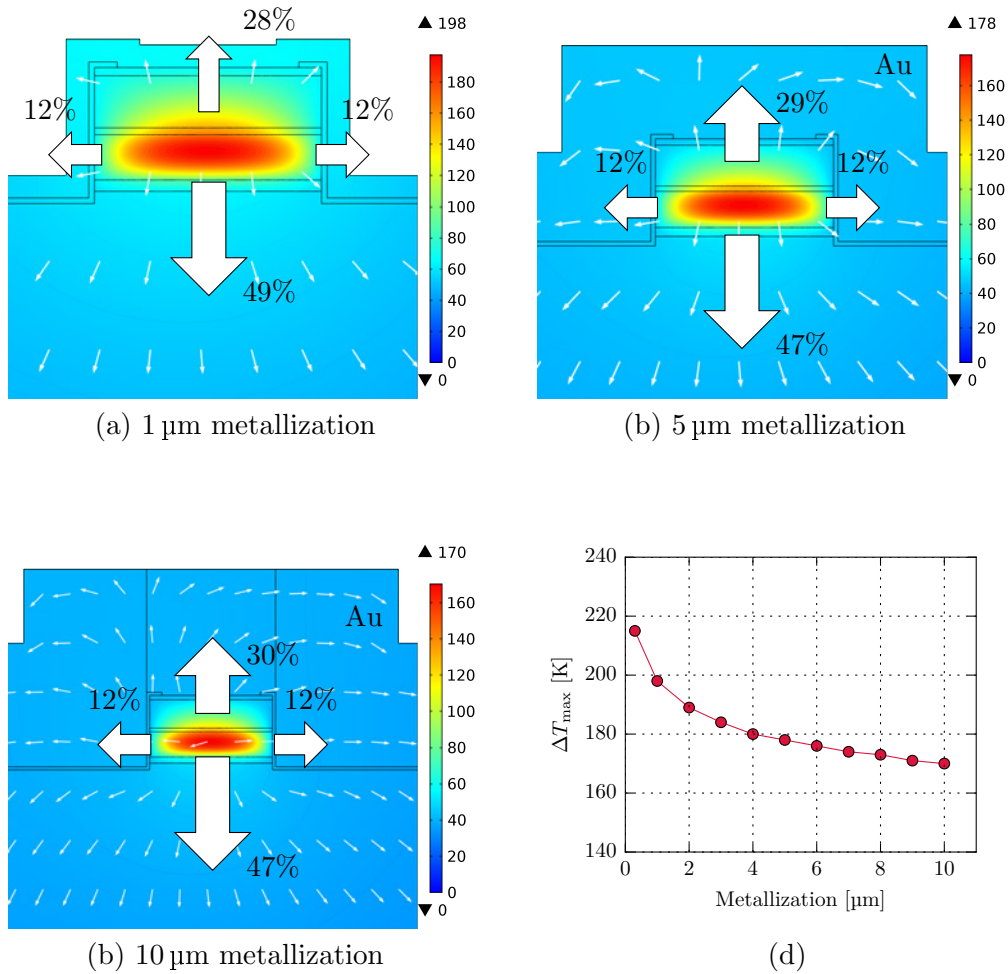


Fig. 3.27: Temperature distributions for different thicknesses of the Au metallization. (a) 1 μm , (b) 5 μm and (c) 10 μm thick metallization layer. (d) Maximum temperature difference as function of the metallization thickness.

approach are the reduced number of process steps, an easier fabrication and a planar surface after the regrowth. Fig. 3.28 shows the simulation result for the lateral regrown ring QCL. Compared to the standard ring, a reduction of the maximum temperature by 21 K is achieved by the regrowth. In combination with a thick metallization ($5\ \mu\text{m}$), the thermal management can be further improved, as shown in Fig. 3.28(b). The specific thermal conductance of the latter configuration is calculated to $G_{\text{thermal}} = 141\ \text{W}/(\text{K cm}^2)$. However, a standard ring without regrowth but also with $5\ \mu\text{m}$ metallization shows a comparable value. Furthermore, most of the heat is still removed in the vertical direction rather than laterally. Comparing the thermal conductivities from Tab. 3.2 shows that gold has a higher value than InP.

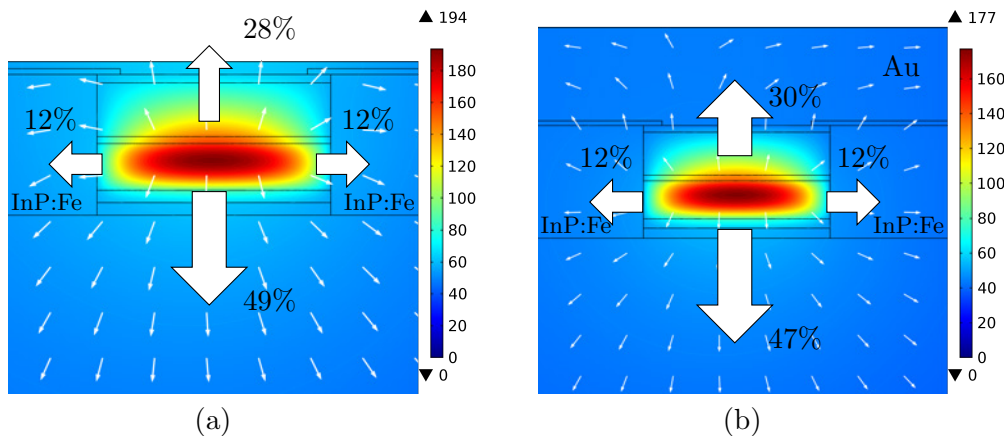


Fig. 3.28: Lateral regrowth with semi-insulating InP:Fe. (a) With the standard metallization thickness of 300 nm and (b) with $5\ \mu\text{m}$ gold.

Cladding material

The P51 QCL heterostructure consists of $\text{In}_{0.52}\text{Al}_{0.48}\text{As}$ cladding layers, whose thermal conductivities are around $4\ \text{W}/(\text{K m})$. In comparison to InP with $k_{\text{InP}} = 75\ \text{W}/(\text{K m})$, the ternary material has much poorer heat dissipation capabilities. To verify this statement, thermal simulations are performed, where $\text{In}_{0.52}\text{Al}_{0.48}\text{As}$ cladding layers are replaced by InP. Fig. 3.29 shows the simulated temperature distribution of the ring laser. Compared to the standard ring configuration, the maximum temperature in the device with InP cladding drops by 45 K ($G_{\text{thermal}} = 147\ \text{W}/(\text{K cm}^2)$). The internal temperature can even be further decreased by combining the InP cladding with a lateral regrowth of semi-insulating InP:Fe. The simulation result, shown in Fig. 3.29(b), gives an even better value of $G_{\text{thermal}} = 168\ \text{W K}^{-1}\ \text{cm}^{-2}$. By incorporating InP in the laser structure, the heat is efficiently dissipated and a thermal performance boost can be gained.

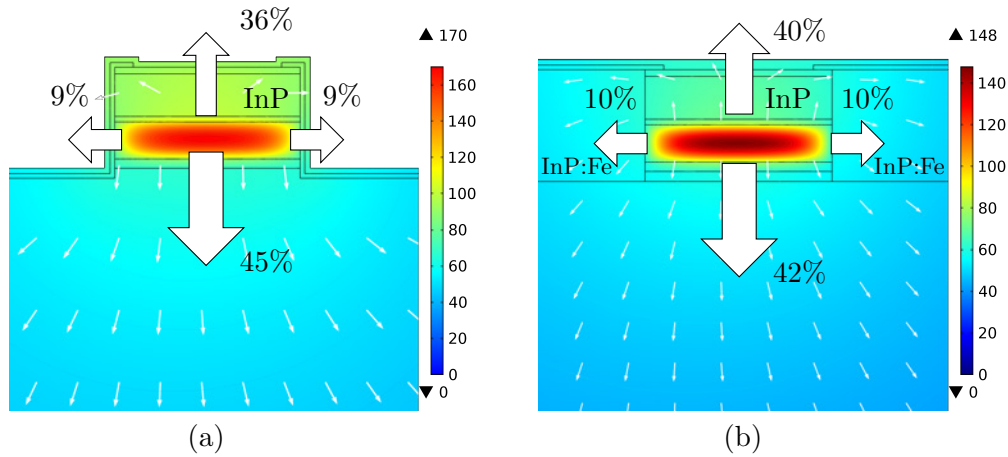


Fig. 3.29: Replacement of the ternary $\text{In}_{0.52}\text{Al}_{0.48}\text{As}$ cladding layers with InP. (a) The higher thermal conductivity of InP helps to remove the heat from the active core. (b) InP cladding in combination with laterally regrown semi-insulating InP:Fe layers.

Mounting technique

For all thermal simulations presented so far, only configurations in which the laser is mounted epitaxial-side up are discussed. However, for an efficient heat removal from the device not only the laser itself but also the mounting has to be considered. Heat accumulation in the active region occurs due to the poor thermal conductivities of the material layers and the long distance between heat source and heat sink. Intuitively, the heat can be better dissipated if the ring laser is bonded directly with the surface to the copper submount. The epilayer-down bonding [174] of the device enables an improved thermal management since the heat transport through the thick InP substrate is not necessary anymore. Fig. 3.30(a) shows the simulated temperature profile for a ring QCL directly bonded with indium to the copper heat sink. The maximum temperature difference is calculated to $\Delta T_{\text{max}} = 169$ K. Further improvement can be achieved by increasing the thickness of the metallization to $5\ \mu\text{m}$, as shown in Fig. 3.30(b). The thicker metallization increases the contact area to the submount and enables also a heat flow from the substrate via the sidewall metallization to the heat sink ($\Delta T_{\text{max}} = 127$ K). A comparable thermal performance as the $5\ \mu\text{m}$ thick metallization can be gained by replacing the InAlAs cladding with InP. The gold metallization layer is still considered to be $300\ \text{nm}$ thick. Due to the high thermal conductivity of InP, a maximum temperature difference of $\Delta T_{\text{max}} = 121$ K can be reached. Most of the heat from the active region ($\sim 47\%$) is removed directly upwards in vertical direction.

An even better thermal performance is obtained if InP is used as the cladding material together with the $5\ \mu\text{m}$ gold and the epi-down bonding scheme. From the simulation, a value of $\Delta T_{\text{max}} = 92$ K is extracted for this configuration, which translates to a specific thermal conductance of $G_{\text{thermal}} = 291\ \text{W}/(\text{K cm}^2)$.

The epi-down mounting is also beneficial for laterally regrown ring QCL. Fig. 3.31(a) shows the simulated temperature profile for such a configuration. The maximum temperature

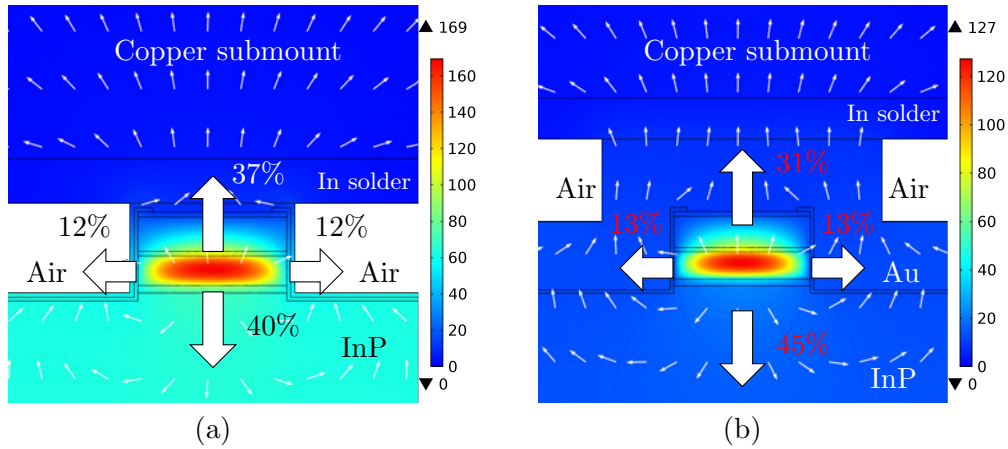


Fig. 3.30: Temperature distributions for epilayer-down bonded ring lasers. (a) The laser with a metallization layer thickness of 300 nm is soldered with indium directly onto the copper heat sink. (b) Simulation result for a device with 5 μm metallization. The small arrows indicate the orientation of the heat flux and the large arrows indicate amount of the total heat flux flowing through the boundary of the active region in the specified direction.

difference is found to be $\Delta T_{\text{max}} = 120 \text{ K}$. Using a thicker metallization with e.g. 5 μm gold, shows no improvement of the maximum temperature. Furthermore, by replacing the ternary InAlAs cladding with InP, the heat is better transferred to the copper heat sink, as shown in Fig. 3.31(b). There, a value of $\Delta T_{\text{max}} = 86 \text{ K}$ can be reached, corresponding to a $G_{\text{thermal}} = 291 \text{ W}/(\text{K cm}^2)$.

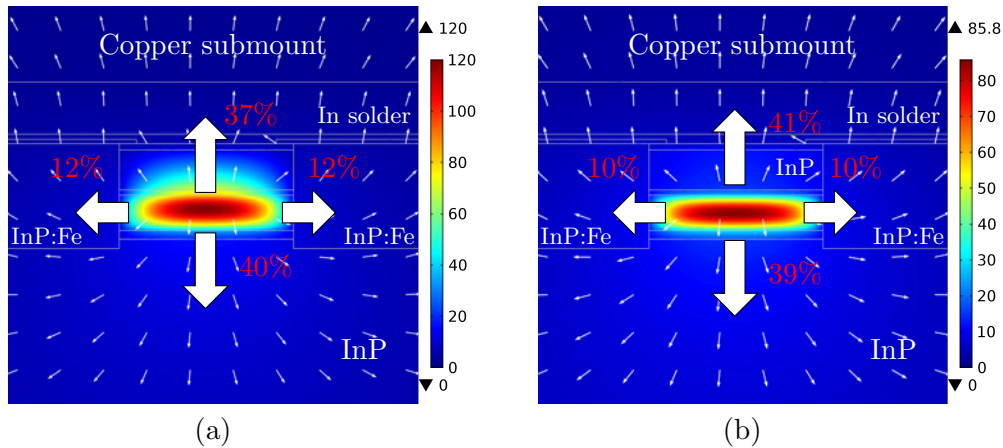


Fig. 3.31: Temperature profiles for laterally regrown (InP:Fe) and epilayer-down bonded ring QCLs. (a) Standard heterostructure layer stack and (b) with InAlAs replaced by InP cladding.

From a technology point of view, the materials used as solder and submount not only need to have a thermal conductivity as high as possible, but also their thermal expansion has to be considered. For instance, the thermal expansion coefficient (CTE) of InP is $\alpha_{\text{InP}} = 4.6 \times 10^{-6} \text{ K}^{-1}$, whereas the oxygen-free copper submount has a value of

$\alpha_{Cu} = 15 \times 10^{-6} \text{ K}^{-1}$. This expansion mismatch needs to be compensated by the indium solder. The indium solder is a "soft solder" that easily diffuses into contacts and in the worst case into the laser if no diffusion barrier is used. A better long-term stability can be gained if AlN is used as the submount material [17]. The AlN has a thermal expansion coefficient of $\alpha_{AlN} = 4.6 \times 10^{-6} \text{ K}^{-1}$, which closely matches the one of InP. Herefore, a fluxless eutectic AuSn solder alloy is used ("hard solder"). For bonding, the whole package has to be heated in nitrogen or forming gas atmosphere to a temperature of $\sim 280 \text{ }^\circ\text{C}$ for a 80%Au/20%Sn solder.

A summary of the simulation results is given in Tab. 3.3. From the thermal simulations point of view, a narrow waveguide with InP as cladding material is beneficial for lowering the maximum temperature in the active region. Furthermore, the performance difference between laterally regrown semi-insulating InP:Fe and a thick ($\sim 5 \mu\text{m}$) metallization layer is not significant. Mounting the laser epilayer-down directly on the submount can improve the thermal management (G_{thermal}) by 30 – 90%, depending on the specific configuration. The highest area-specific thermal conductance with $G_{\text{thermal}} = 291 \text{ W}/(\text{K cm}^2)$ is achieved for a laterally regrown ring laser with InP cladding bonded epi-side down on the copper submount. This corresponds to a thermal resistance of $R_{\text{thermal}} = 1/(G_{\text{thermal}}A) = 28 \text{ K/W}$ for a ring QCL with a diameter of $400 \mu\text{m}$ and a waveguide width of $10 \mu\text{m}$. In comparison, Wittman et al. [175] reported values for ridge lasers ($12.7 \mu\text{m} \times 1.5 \text{ mm}$) of $G_{\text{thermal}} = 400 - 660 \text{ W}/(\text{K cm}^2)$, corresponding to thermal resistances $R_{\text{thermal}} = 7.9 - 12.7 \text{ K/W}$. There, the lower threshold current density and voltage lead to a lower heat source density, which can be easier dissipated. Evans et. al [176] demonstrated ridge QCLs fabricated into buried heterostructure geometries with values of $470 - 1238 \text{ W}/(\text{K cm}^2)$. From a narrow low dissipation ridge DFB laser ($5 \mu\text{m} \times 3 \text{ mm}$), which is mounted epi-down on AlN, an impressive value of $2646 \text{ W}/(\text{K cm}^2)$ is extracted [17, 79]. A similar specific thermal conductance of $\sim 2660 \text{ W}/(\text{K cm}^2)$ is obtained by high-quality strain-balanced interfaces in the laser core ($\lambda \sim 4.7 \mu\text{m}$) of narrow ridges ($6 \mu\text{m}$), which are epi-down bonded on diamond submounts [177].

Configuration	Mounting	ΔT_{\max} [K]	G_{thermal} [W/(K cm ²)]
Standard ring ($w = 10 \mu\text{m}$)	epi-up	215	116
Ring ($w = 5 \mu\text{m}$)	epi-up	118	212
Ring ($w = 15 \mu\text{m}$)	epi-up	276	91
Standard Ring with 100 μm substrate	epi-up	184	136
Standard Ring with 200 μm substrate	epi-up	198	126
Standard Ring with 1 μm gold	epi-up	198	126
Standard Ring with 5 μm gold	epi-up	178	140
Standard Ring with 10 μm gold	epi-up	170	147
Ring with lateral InP regrowth	epi-up	194	129
Ring with lateral InP regrowth (5 μm gold)	epi-up	177	141
Ring with InP cladding	epi-up	170	147
Ring with InP cladding and regrowth	epi-up	148	169
Standard ring	epi-down	169	148
Standard Ring with 5 μm gold	epi-down	127	197
Ring with InP cladding	epi-down	121	207
Ring with InP cladding + 5 μm gold	epi-down	92	272
Ring with lateral InP regrowth	epi-down	120	208
Ring with lateral InP regrowth (5 μm gold)	epi-down	120	208
Ring with InP cladding and regrowth	epi-down	86	291

Tab. 3.3: Summary of the results from the thermal simulations.

3.9 Metal-covered ring quantum cascade lasers

To improve the thermal management in ring QCLs, different strategies with better heat sinking capabilities have been investigated in the previous section. From the results of the thermal simulations, various device configurations are selected for further feasibility studies. With the standard processing of ring lasers [130, 81, 134], the light is diffracted via a second-order distributed feedback grating towards the surface/substrate. There, the refractive index contrast between air and metal/semiconductor is responsible for the feedback mechanism. In most experiments, light emission through the surface is utilized, while the ring lasers are operated in pulsed mode. To enable high duty-cycle or cw operation at room temperature and above, the fabrication of the ring lasers has to be changed. There are several reasons: First of all, the heat in the laser can only be extracted through the substrate and the sidewalls since the standard fabrication is optimized for emission through the surface. Moreover, an epilayer-down bonding of the rings is not feasible as it would block the light emission through the surface. On the other hand, emission through the substrate can be engineered with an appropriate grating design [81]. However, for epilayer-down bonding, the chip is pressed into a film of e.g. Indium or AuSn to guarantee a good thermal contact to the submount material. Most likely, the film then also covers parts of the grating grooves, which leads to a modification of the feedback mechanism due to a refractive index change. Furthermore, air chambers between film and etched grating grooves will increase the thermal resistance. Hence, for a better thermal management the standard ring configuration has to be modified/replaced by another more

suitable device architecture. Bai et al.[131] presented high power ring quantum cascade lasers, which are processed into buried-heterostructures. The second-order DFB grating is etched directly in the layers above the active region before the whole laser is overgrown with InP. Afterwards a thick gold layer (3 μm) is electroplated and the chip is bonded epilayer-down to AlN submounts. Measurements revealed a maximum output power of 0.51 W with a wallplug efficiency of 6.25% at room temperature. However, the device operated not in the fundamental mode but a extremely higher order mode ($m = 61$). The close vicinity of the grating above the active region leads to an increased coupling strength and the ring laser easily becomes overcoupled. Furthermore, the buried heterostructure process has the disadvantage that the DFB grating needs to be written for all devices before the whole chip is overgrown. Thus, once the grating is defined, the wavelength cannot be easily adjusted post-growth. On the other hand, a surface grating gives the design freedom to modify the grating shape and parameters without to grow a new laser material.

In the following, an approach based on the complete coverage of the laser including the DFB surface grating slits with metal is discussed. At first sight this strategy seems counter-productive since metals cause optical losses for the waveguide mode. Therefore, it would be better to keep those lossy materials far away from the grating, where the mode is strongly interacting. However, due to the strong refractive index contrast between semiconductor and metal, a high coupling strength can be achieved without etching the grating grooves too deep. Of course some trade-off between coupling strength and induced losses has to be made. But once this issue is solved satisfactory, the filling of the grating grooves with metallization offers several advantages. First of all the thermal management can be optimized, since the heat generated in the active region can be now also dissipated efficiently upwards in vertical direction. The grating grooves are filled with good thermal conducting Au and the metallization acts like a heatspreader. Furthermore, epilayer-down bonding becomes possible without altering the feedback mechanism of the grating. This should enable the fabrication of high power ring quantum cascade lasers. Fig. 3.32 shows an illustration of the metal-covered ring QCL, where the light is out-coupled via the substrate.

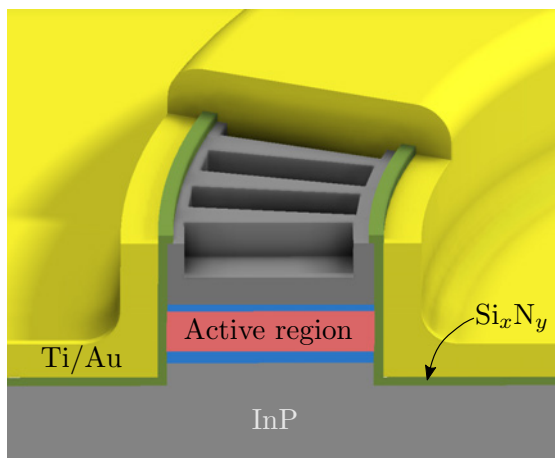


Fig. 3.32: Illustration of the metal-covered ring QCL with a second-order DFB grating. The etched slits are filled with gold and in this configuration the generated light is emitted through the substrate.

3.9.1 Lateral regrowth

To improve the thermal management in ring QCLs, first the feasibility of a lateral regrowth with InP:Fe is investigated. However, the standard fabrication process [132] used for ring QCLs is not compatible with this approach. The reason for this is the top contact metallization, which is used in the standard procedure as the etch mask for the waveguide. For the regrowth however, the sample needs to be re-inserted into the MBE/MOCVD chamber after the waveguide etch. A gold metallization or any other contamination is strictly forbidden in the growth chamber. Therefore, the fabrication of the ring QCLs has to be modified. Fig. 3.33 shows the process steps for the laterally regrown ring laser. Instead of gold, a layer of silicon nitride serves as etch mask for the waveguide definition. Ring waveguides with (outer) diameters of 400 μm and waveguide widths of 10 μm , 15 μm and 20 μm are etched into the QCL material (H977_B4_MH, P51 regrowth). The laser heterostructure was grown by MBE on a low n-doped InP substrate. Afterwards, the sample is sent to our collaborators at the Humboldt University Berlin, where it is laterally regrown with semi-insulating InP:Fe. A short wet chemical etch is used to smooth the sidewalls and support a better growth. However, this isotropic etch also reduces the width of the waveguides symmetrical by approximately 5 μm .

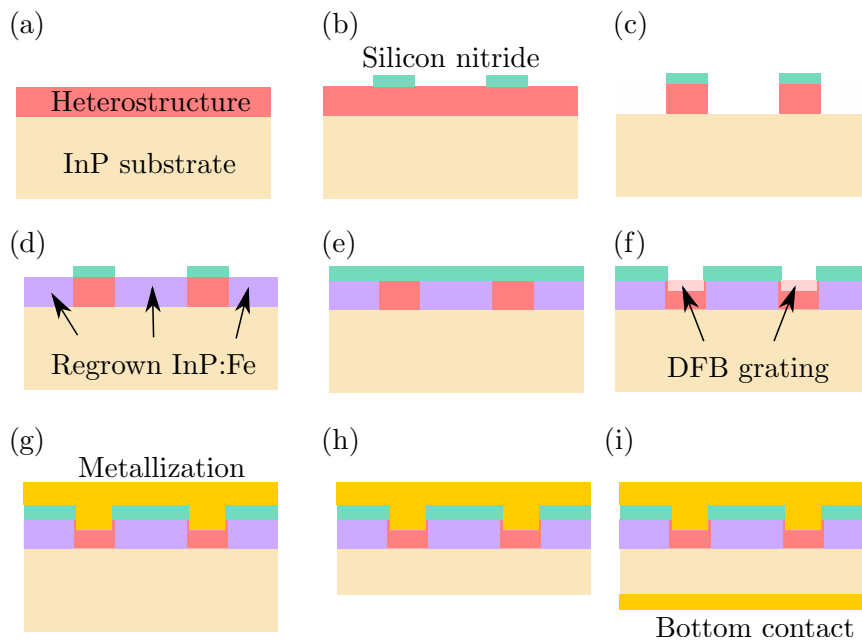


Fig. 3.33: Process steps for the lateral regrowth of ring QCLs. (a) Heterostructure grown on a low n-doped InP substrate. (b) Deposition and patterning of silicon nitride as etch mask. (c) Reactive ion etching of the ring waveguide. (d) Selective regrowth with semi-insulating InP:Fe. (e) Removal of the residual SiN and deposition of a new layer. (f) E-beam lithography and etching of second-order DFB grating. (g) Sputtern of top metallization. Optional: (h) Lapping and polishing of the substrate. (i) Deposition of the bottom contact metallization.

The regrowth process itself is done at a temperature of $\sim 500^\circ\text{C}$ in a gas-source MBE [172]. The SiN mask layer is removed and a new passivation layer is deposited. The second-

order DFB grating ($\lambda \approx 8.6 \mu\text{m}$) is written with e-beam lithography and transferred to the passivation layer, which acts as the etch mask for the subsequent grating etch. Finally, the Ti/Au top metallization is sputtered ($10 \text{ nm}/4.5 \mu\text{m}$).

For the bottom contact lithography an alignment between the ring structure on the surface and the contact mask on the substrate side is necessary. Therefore, an optical alignment with immediate visible feedback would be beneficial. The InP substrate has a bandgap of $E_g \approx 1.3 \text{ eV}$, corresponding to a wavelength of about 950 nm . Hence, with a light source and a near-infrared detector above this wavelength it is possible to see through the substrate. The mask aligner (Süss MJB3) is equipped with a Thorlabs CCD camera, which can be utilized for the exposure of the bottom side. The detector array of the CCD camera is sensitive also to near-infrared radiation. However, an additional filter in the camera cuts off the wavelengths above $\sim 650 \text{ nm}$. By removing the filter and re-adjusting the focus of camera it is possible to capture not only visible, but also infrared light. Furthermore, a double-side polished silicon wafer is inserted in the path between the light source of the mask aligner and the camera. This is necessary to block the visible part of the spectrum, because otherwise the camera signal would overshoot. Within the camera software, settings like gain boost, low frames per second and long exposure time improve the contrast of the image. With this slight modification it is possible to see the rings through the InP substrate and align the bottom contact with the existing structure on the surface. Fig. 3.34 shows a camera image of the alignment between rings on the surface and the mask on the substrate side. For a certain focus the rings appear sharp, while the bottom contact mask is slightly blurred. But nevertheless a good alignment can be achieved with this approach.

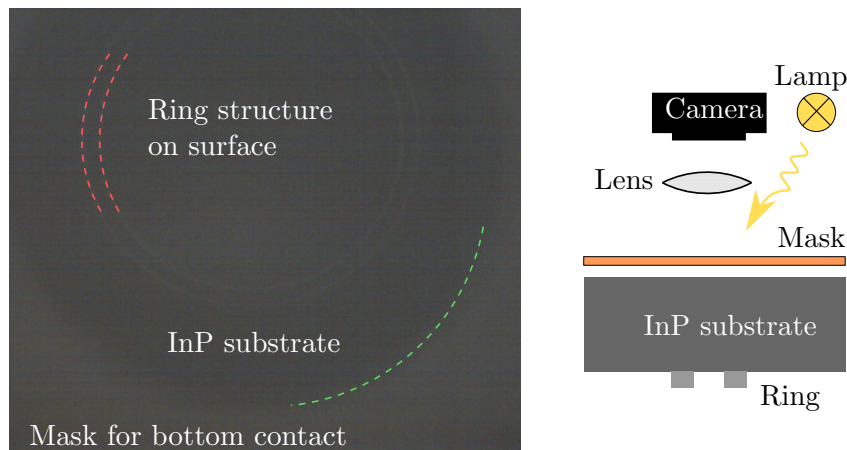


Fig. 3.34: Alignment for the bottomsides exposure. Left: Camera image of the alignment between already processed rings on the surface and the mask for the bottom side exposure. Right: Schematic illustration of the sideview for this setup.

To test the laterally regrown and metal-covered second-order DFB lasers, the sample is mounted with silver paste on a copper plate. The copper plate serves as submount and has a drilled hole to allow for substrate emission. Fig. 3.35 shows a microscope image of

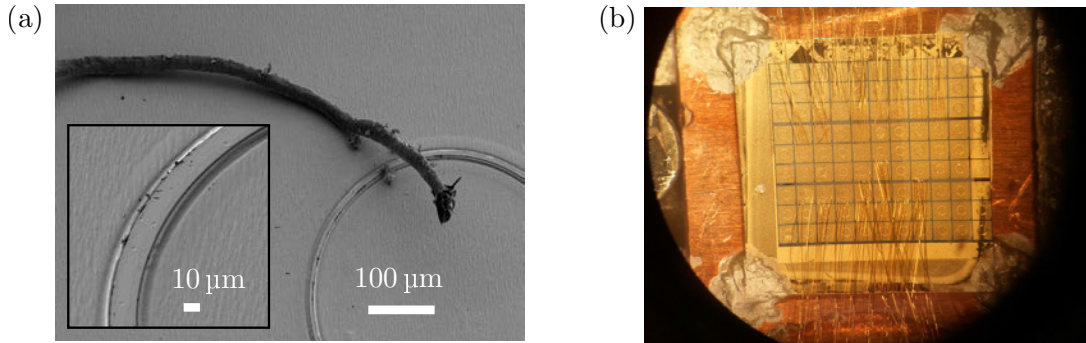


Fig. 3.35: (a) Scanning electron microscope image of a laterally regrown ring laser. A textile fiber found its way on the chip during sample transfer. The inset shows a magnified section of the laser before the grating is fabricated. (b) Image of the fabricated sample with an array of metal-covered substrate-emitting ring QCLs.

the mounted sample (H977_B4_MH, see A.3.1) with the array of ring lasers. For electrical and optical characterization the sample is mounted in a liquid nitrogen cooled cryostat and the light is measured with the internal DTGS detector of the FTIR spectrometer. The devices are operated in pulsed mode (5 kHz/100 ns) and the LIV is recorded for different submount temperatures. Fig. 3.36 shows the measurement results of a ring QCL with an outer diameter of 400 μm and a waveguide width of 15 μm .

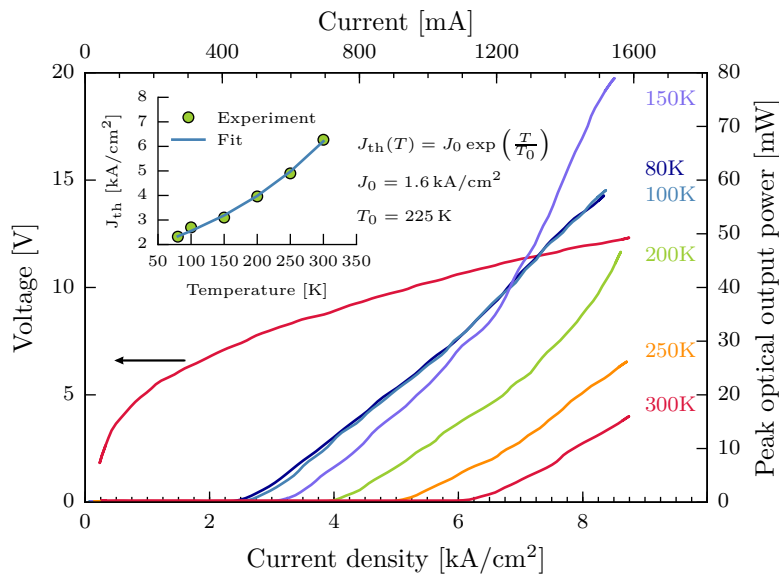


Fig. 3.36: Measured LIV characteristics of a laterally regrown ring QCL mounted in a cryostat. The device has a diameter of 400 μm and a waveguide width of 15 μm and is operated with 5 kHz/100 ns pulses. The inset shows the extracted threshold current densities for different submount temperatures.

At room temperature a relatively high threshold current density of $J_{\text{th}} = 6.3 \text{ kA/cm}^2$ is obtained. Measurements of narrower devices showed an even higher value. In comparison,

typical thresholds of surface-emitting rings from this material are on the order of 4 kA/cm^2 . This increase can partly be attributed to a known non-ideal InP:Fe regrowth process for this sample. Furthermore, there is room for optimizing the parameters of the metal-covered grating. As expected, the light output through the substrate increases with decreasing submount temperature. Unfortunately, the power dissipation is still too high to operate these devices in continuous wave mode - even at low temperatures. At the submount temperature of 150 K the optical signal increases due to the emission from multiple modes, which is confirmed in spectral measurements. However, the ring laser features single-mode operation at room temperature, as shown in Fig. 3.37. At a drive current of 1.6 A the substrate-emitting device features a side-mode suppression ratio (SMSR) greater than 25 dB. The concept of using a metal-covered second-order DFB grating to emit the light through the substrate in principle works, but the whole process including the design of the grating needs to be refined. An optimized ring laser is presented in section 3.9.3.

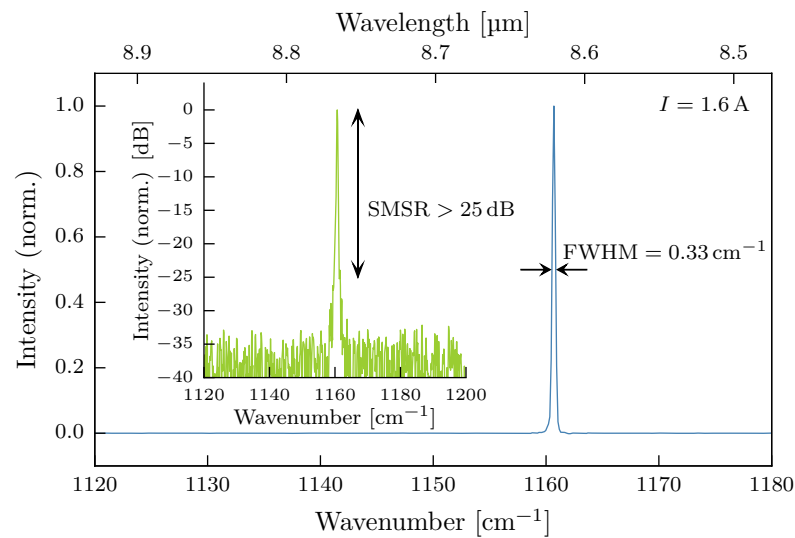


Fig. 3.37: Spectral measurements of a substrate-emitting ring QCL with $15 \mu\text{m}$ waveguide width. At room temperature single-mode emission with a side-mode suppression ratio of $\text{SMSR} > 25 \text{ dB}$ is observed for a pulsed current of 1.6 A (80 kHz/30 ns).

3.9.2 Direct wafer bonding

Due to the long distance between the heat source (active region) and the heat sink (copper submount), heat is accumulated in the laser core and leads to a rise of the temperature. For an efficient dissipation, QCLs are commonly mounted epilayer-down on an AlN or diamond submounts, which have superior thermal conductivities compared to the InP substrate. Here, the feasibility of another approach with direct wafer bonding of the sample epilayer-down on a copper submount is investigated. Such direct wafer bonding process would allow to get the heat source very close to the heatsink without any thermal interface material, such as indium. For this, a copper plate is coated with gold ($\sim 1 \mu\text{m}$) and joined with a processed array of ring lasers via an Au-Au thermo-compression bonding

at 330 °C (EVG501 Wafer Bonding System). The sample H975_MH_megA is a regrowth of the P51 QCL material (see the growth sheet in A.3.1). After this process step all rings are connected electrically in parallel, thus the devices need to be separated. This is done in a dicing process with a mechanical saw. For this, the copper plate with the chip is put on a sticky dicing tape and individual devices are manufactured by removing the bars between them. Fig. 3.38(a) shows the diced sample as it is mounted on the dicing tape. Straight cut lines from the mechanical saw blade are visible as well as many dicing residuals. Unfortunately, these residuals are actually ring laser devices, which were destroyed during the sawing process. Possible reasons can be a too weak bond between submount and device, a too high mechanical stress during sawing or temperature induced stress. Fig. 3.38(b) shows the separated devices bonded epilayer-down on the copper submount. Measurements of single devices before (epi-up) and after the saw dicing (epi-down) show that the electrical characteristics are not altered by the process. However, the process yield is not satisfying, because many devices are lost during the sawing step.

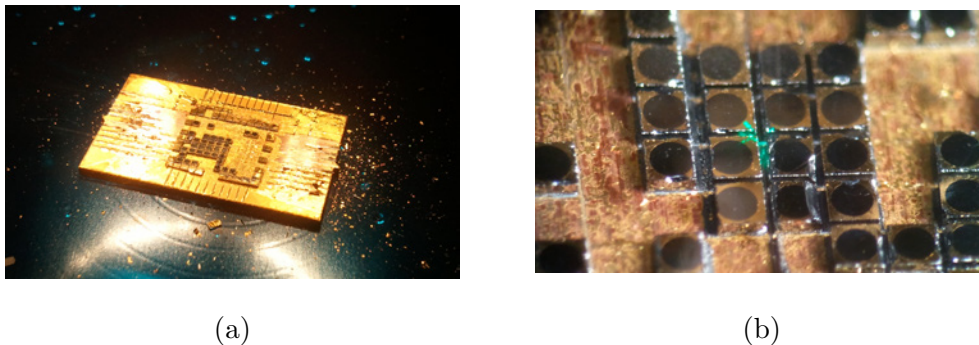


Fig. 3.38: Diced array of ring QCLs. (a) The sample is wafer bonded epilayer-down on an Au-coated copper submount and individual devices are separated with a mechanical saw. (b) Single devices of substrate-emitting ring lasers. The green spot in the center is the alignment laser of the bonding machine.

3.9.3 Optimized grating design

The laterally regrown ring lasers presented in section 3.9.1 confirmed that the approach of metal-covered gratings in principle works, but at the expense of relatively high threshold currents. One possible reason is that the grating parameters are not optimal adjusted for the specific heterostructure. Therefore, the DFB grating is investigated more in detail and optimized with respect to substrate out-coupling efficiency.

On the surface, a second-order DFB grating is used to diffract the light in vertical direction towards the substrate. An illustration of the DFB grating together with the important grating parameters is shown in Fig. 3.39. Here, the grating duty-cycle σ (GDC) is defined as the ratio between etched groove and grating period Λ_g . As the grating is completely covered with metal, σ corresponds to the amount of gold in the grooves per grating period. A duty-cycle of $\sigma = 0\%$ corresponds to a structure without etched grooves and thus no gold in the slits; $\sigma = 60\%$: $0.4\Lambda_g$ are unetched and the remaining $0.6\Lambda_g$ are etched and filled

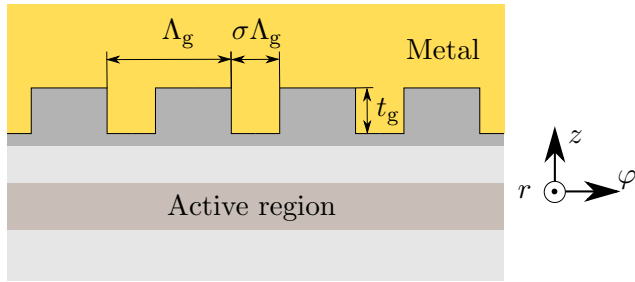


Fig. 3.39: Metal-covered distributed-feedback grating with the grating period Λ_g , the grating duty-cycle σ and the etch depth of the grating groove t_g .

with gold; $\sigma = 100\%$: everything is etched and fully covered with metal. The influence of the grating etch depth t_g and duty-cycle σ , on the coupling and loss coefficients are investigated by simulation. As pointed out in section 2.4.5 the coupled-mode theory is not appropriate to describe DFB gratings with large refractive index contrasts. Hence, the following simulations are based on the more general Floquet-Bloch approach [86].

Material	Thickness [nm]	Doping [cm^{-3}]	Refractive index
Air	1000		$1.0000 + j0.0000$
Gold	700		$5.8093 + j61.9945$
InGaAs	10	1×10^{20}	$0.3024 + j12.1313$
InGaAs	350	8×10^{18}	$0.2821 + j1.0401$
InAlAs	800	2×10^{17}	$3.1291 + j0.0010$
InAlAs	1500	1×10^{17}	$3.1399 + j0.0005$
InGaAs	300	5×10^{16}	$3.4089 + j0.0005$
Active region	2089		$3.3281 + j0.0000$
InGaAs	500	5×10^{16}	$3.4089 + j0.0005$
InP	10000	1×10^{17}	$3.0546 + j0.0013$

Tab. 3.4: Layer sequence and corresponding complex refractive indices used for simulating the properties of the DFB grating. The material parameters are evaluated for a target wavelength of $\lambda = 8.7 \mu\text{m}$.

The P51 quantum cascade laser material (see growthsheet in the appendix A.3.1) is designed for an emission wavelength around $8 - 9 \mu\text{m}$. To enable substrate emission at a target wavelength of $\lambda = 8.7 \mu\text{m}$, a second-order DFB grating is etched into the upper InAlAs cladding layers with a grating period of $\Lambda_g = 2.74 \mu\text{m}$. This corresponds to 447 grating slits over the 1.23 mm ring circumference, assuming a ring with $400 \mu\text{m}$ diameter and a waveguide width of $10 \mu\text{m}$. The simulated layer sequence and corresponding refractive indices are listed in Tab. 3.4. Etched grating grooves are subsequently filled with gold. In order to investigate the influence of the grating etch depth t_g on various DFB parameters, t_g is swept in steps of 100 nm for a fixed grating duty-cycle of $\text{GDC} = 50\%$.

Fig. 3.40 shows the results of the waveguide/grating simulations. The magnitude of the coupling constant $|\kappa|$ indicates a strong feedback of the DFB grating for an etch depth between 400 and 1200 nm (red curve). The grating is complex-coupled, with non-negligible real and imaginary parts in the coupling constant. Due to the fact that the surface is fully covered with metal, also the surface radiation loss α_{surf} is zero. In contrast to that, the emission towards the substrate α_{sub} shows a maximum at an grating etch depth around

700 – 800 nm. Moreover, the absorption loss α_{abs} has a local minima at $t_g \approx 800$ nm (black curve). At this depth, the total losses α_{total} (orange curve) are dominated by the radiation loss and an out-coupling efficiency of $\eta_{\text{sub}} \approx 80\%$ is achieved into the InP substrate. From this simulation, a grating etch depth of around 800 nm seems to be very promising. Fig. 3.41 shows the vertical mode profile of the TM-polarized wave for GDC = 50% and $t_g = 800$ nm. The overlap of the mode with the active region is calculated to $\Gamma = 67\%$.

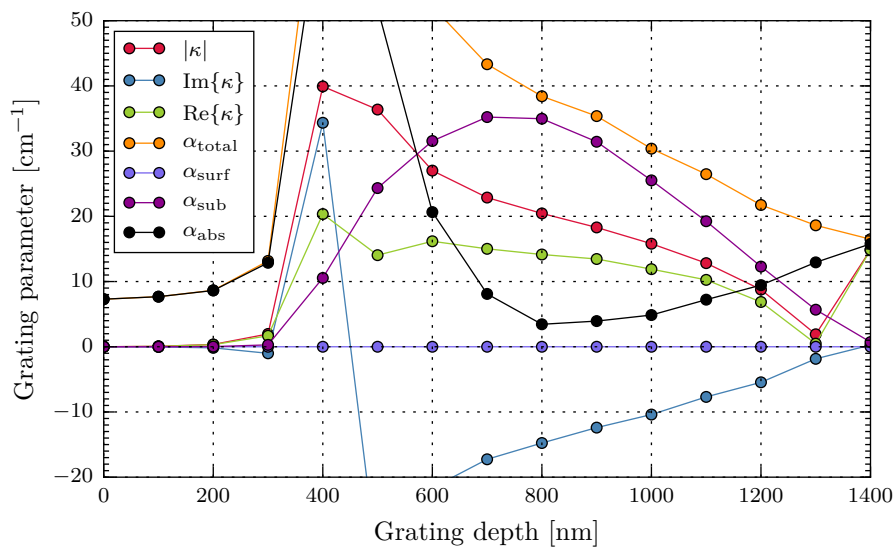


Fig. 3.40: Waveguide simulations reveal an absorption minimum for a grating etch depth around 800 nm for a grating duty-cycle of 50%. At this etch depth, the radiation loss through the substrate is high and translates into an out-coupling efficiency around 80%.

For completeness, the partial waves for the Floquet-Bloch approach are plotted in Fig. 3.42. In total, 41 partialwaves are considered for the waveguide/grating simulation. The most important resonant partial waves are the right- and left-going waves $|H_0|$ and $|H_{-2}|$, as well as the radiating wave $|H_{-1}|$. Fig. 3.43 shows the results of the eigenfrequency calculation for the waveguide/grating problem with $t_g = 800$ nm and GDC = 50%. The simulation is performed with COMSOL for a wavelength of $\lambda = 8.7 \mu\text{m}$. Periodic boundary conditions are used on the left and right boundaries, respectively. Mode 1, shown in Fig. 3.43(b), is identified as the symmetric (radiating) waveguide mode with an effective refractive index $n_{\text{eff},1} = 3.2196 - j6.3803 \times 10^{-4}$. The second mode is the antisymmetric solution for the infinite grating/waveguide problem with $n_{\text{eff},2} = 3.2255 - j8.3854 \times 10^{-4}$. An engineered incorporation of metal in the DFB grating allows to achieve a strong feedback, while keeping the losses on a moderate level. In another approach [88, 178] the metallized DFB grating is used to suppress the antisymmetric mode by coupling it resonantly to a surface plasmon mode. The grating etch depth and duty-cycle is chosen in such a way that the antisymmetric mode experiences higher losses and is strongly absorbed. In turn, the second-order DFB grating couples out the symmetric mode, which has negligible absorption loss and creates a single-lobed farfield [179].

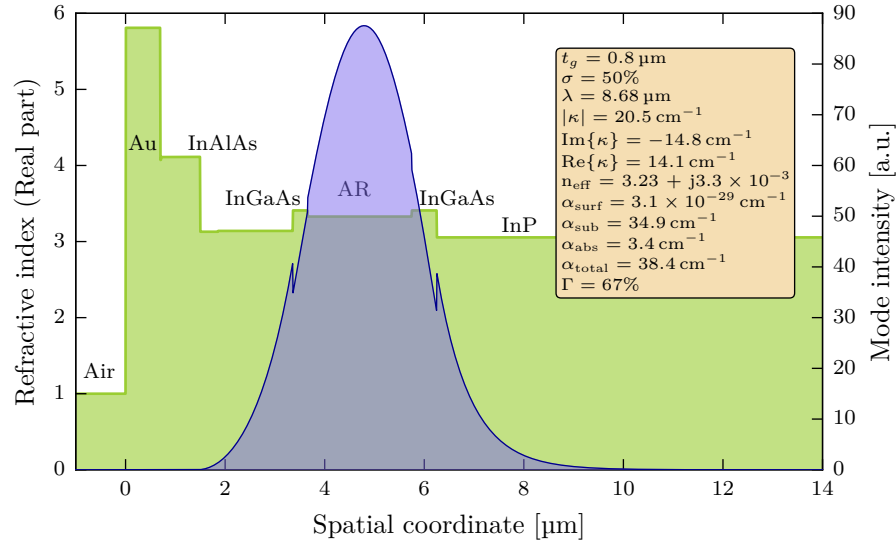


Fig. 3.41: Vertical mode profile in the heterostructure for a grating duty-cycle of 50% and an etch depth of $t_g = 800$ nm. Important properties for the second-order DFB grating are given in the inset.

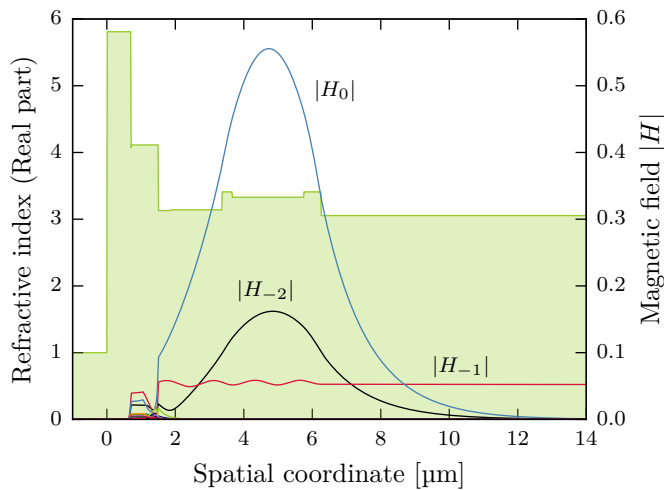


Fig. 3.42: Right- and left-going resonant partial waves $|H_0|$ and $|H_{-2}|$, respectively. The radiating wave $|H_{-1}|$ is responsible for the light out-coupling via the second-order DFB grating. The refractive index profile in the heterostructure is indicated in green.

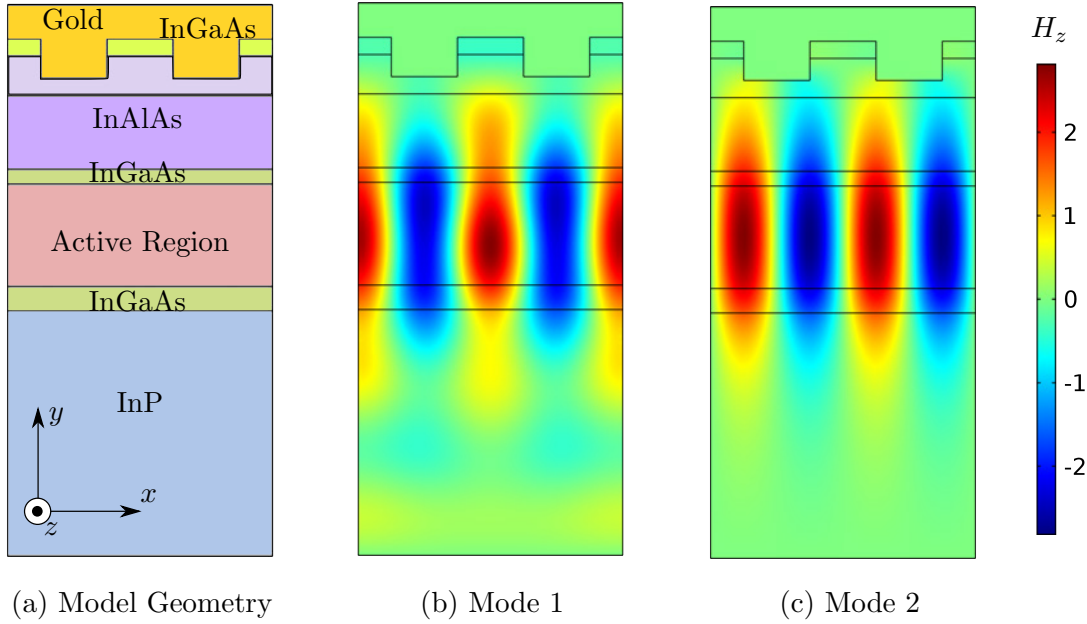


Fig. 3.43: Simulation of the waveguide modes in a metal-covered 2nd-order DFB grating for a wavelength of $\lambda = 8.7 \mu\text{m}$. (a) Simulated layer structure of the infinite grating/waveguide problem. (b) Magnetic field distribution (H_z -component) of mode 1. This waveguide mode represents the symmetric (radiating) solution with an eigenfrequency of $3.4557 \times 10^{13} + j6.8481 \times 10^9 \text{Hz}$ and a complex effective refractive index $n_{\text{eff},1} = 3.2196 - j6.3803 \times 10^{-4}$. (c) Mode 2 is the antisymmetric solution at an eigenfrequency of $3.4495 \times 10^{13} + j8.9677 \times 10^9 \text{Hz}$ with $n_{\text{eff},2} = 3.2255 - j8.3854 \times 10^{-4}$.

Fabrication

The QCL material H860 (P51 regrowth) is based on a $\text{In}_{0.53}\text{Ga}_{0.47}\text{As}/\text{In}_{0.52}\text{Al}_{0.48}\text{As}$ two-phonon active region design [180], which is grown by molecular beam epitaxy (MBE) on a low-doped ($2 \times 10^{17} \text{cm}^{-3}$) double-side polished InP wafer. The fabrication starts with the deposition of a $1.5 \mu\text{m}$ thick Si_xN_y hardmask via plasma enhanced chemical vapor deposition. This layer is then structured with conventional optical lithography into ring-shaped cavities with a diameter of $400 \mu\text{m}$ and a waveguide width of $10 \mu\text{m}$. An anisotropic reactive ion etching (RIE) process with SiCl_4/Ar at 25°C is then used to etch the waveguide. After removal of the hardmask a new layer of Si_xN_y is deposited and the second-order DFB grating is written by e-beam lithography. The grating period of $\Lambda_g = 2.741 \mu\text{m}$ is chosen for light emission at $\lambda \sim 8.7 \mu\text{m}$. Three different grating duty-cycles (45%, 65% and 85%) are realized on the chip. The grating slits are etched into the upper waveguide layers with the same anisotropic process as before. The fabrication steps for the grating increase the grating duty-cycle by around 15%, which has been already taken into account in the design of the grating mask. Different grating etching depths in the range of $t_g \sim 300 - 1400 \text{nm}$ are realized on the same chip. A 450nm thick Si_xN_y passivation layer is deposited and opened on top with an O_2/CHF_3 based RIE recipe. In a next step, a thick Ti/Au metallization ($\sim 10 \text{nm}/700 \text{nm}$) is sputtered over the whole sample. Finally, the ring lasers are electrically separated by a selective removal of the

metallization between the devices with a $KI:I_2$ wet etch solution. A detailed process description is given in the appendix A.4.1. Fig. 3.44 shows microscope images of the fabricated metal-covered ring QCLs. For testing, the chip is mounted epilayer-up on a copper-plate (with a drilled hole) and the light is emitted through the substrate.

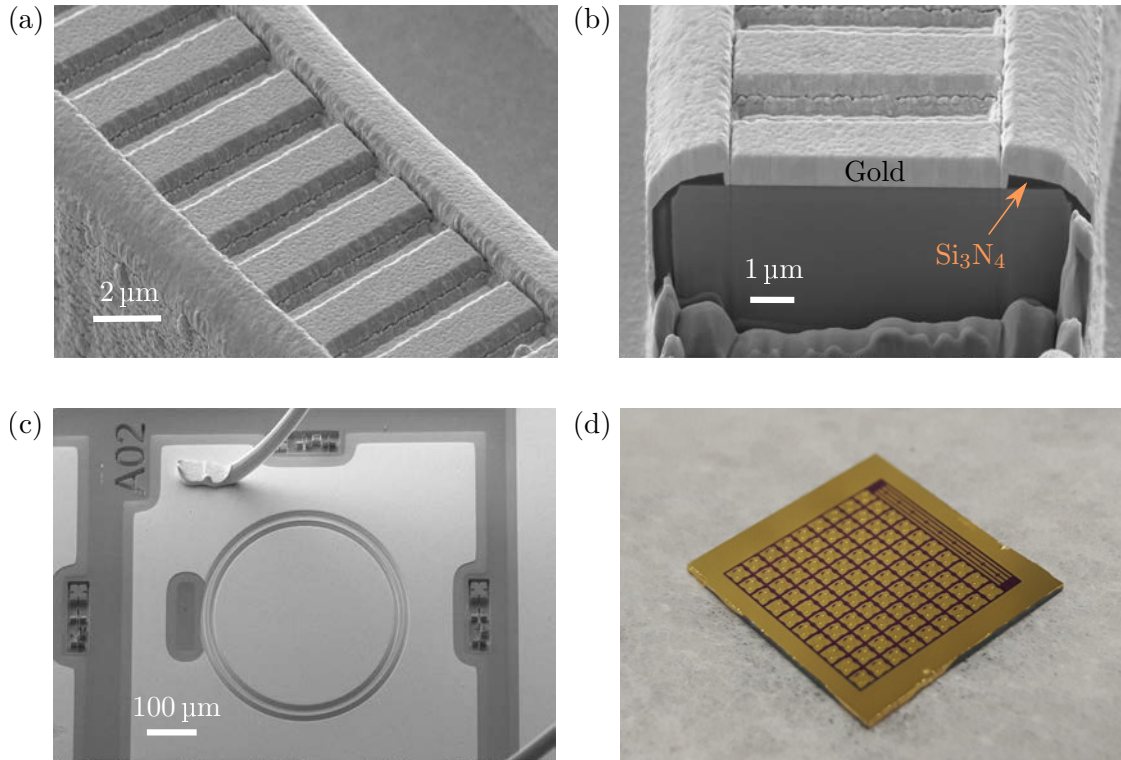


Fig. 3.44: (a) Scanning electron microscope image of the metal-covered second-order DFB grating. (b) Focused ion beam cut through a ring laser. (c) Wire-bonded substrate-emitting ring QCL. (d) Fabricated chip with an array of devices.

Results

For characterization the sample is mounted in a temperature controlled cryoflow cryostat. The radiation emitted through the ZnSe window of the cryostat is collected with a 1.5'' ZnSe lens and focused on the deuterated triglycine sulfate (DTGS) detector of a Bruker Vertex 70v Fourier transform infrared (FTIR) spectrometer. The peak optical output power is measured with 5 kHz/100 ns pulses and rescaled by a reference measurement with a calibrated thermal detector (Thorlabs S401C), which is placed directly in front of the substrate-emitting device. Fig. 3.45 shows the measured LIV characteristics of devices with different grating duty-cycles but the same etch depth of $t_g = 790$ nm. Almost the same maximum optical output power is achieved with all three grating types. However, for the ring laser with a grating duty-cycle of 45% the lowest threshold current density is obtained.

In Fig. 3.46, devices with different grating duty-cycles and etch depths are compared in terms of threshold current density J_{th} . A significant dependence of the laser threshold on

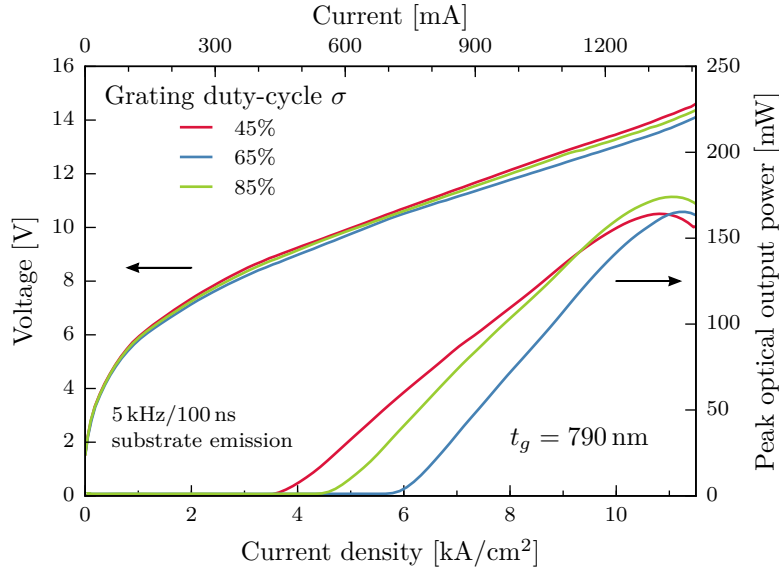


Fig. 3.45: Measured LIV characteristics of metal-covered ring QCLs for different grating duty-cycles. All devices have the same grating etch depth of $t_g = 790$ nm.

the set of grating parameters (σ, t_g) can be seen. The general trend shows that devices with a duty-cycle of $\sigma = 45\%$ experience a lower threshold, which is beneficial for a reduced power consumption. For a shallow grating ($t_g = 260$ nm) the highest threshold is measured, which is not surprising, because the etching stopped in the highly doped ($8 \times 10^{18} \text{ cm}^{-3}$) plasmon layer (see growth sheet appendix A.3.1). On the other hand, the lowest losses are observed for very deep etched gratings of $t_g = 1425$ nm together with a grating duty-cycle of $\sigma = 45\%$. However, a direct comparison to devices with $t_g = 790$ nm at the same duty-cycle shows that the output power is much lower for the deep etched gratings. In the intermediate region of $t_g = 540$ nm no great influence of the grating duty-cycle is observed. For the following discussions, ring laser devices with the grating parameter set ($\sigma = 45\%, t_g = 790$ nm) are used. The extracted threshold current density of 3.7 kA cm^{-2} is comparable to the values ($\sim 3 - 4 \text{ kA/cm}^2$) obtained with standard surface-emitting rings or Fabry-Perot devices from the same material.

Figure 3.47 shows the pulsed power-current-voltage characteristics of the device at different heatsink temperatures. At room temperature a maximum peak output power of 160 mW is obtained. From measurements of the threshold current density J_{th} as a function of heat sink temperature T and an exponential fit with $J_{\text{th}}(T) = J_0 \exp(T/T_0)$, a characteristic temperature $T_0 = 210$ K together with $J_0 = 0.84 \text{ kA cm}^{-2}$ is extracted.

Lasering spectra are measured with the FTIR spectrometer in rapid-scan mode with a resolution of 0.21 cm^{-1} while the devices are operated at a drive current of 1 A at 80 kHz/30 ns. For measurements of the farfield, a liquid nitrogen cooled mercury-cadmium-telluride detector with a pixel size of 1 mm^2 is placed on a two-dimensional linear translational stage at a distance of ~ 16 cm without any optics in the beam path. Figure 3.48(a) shows the lasing spectra of the ring device with ($t_g = 790$ nm, $\sigma = 45\%$) at different heat sink tem-

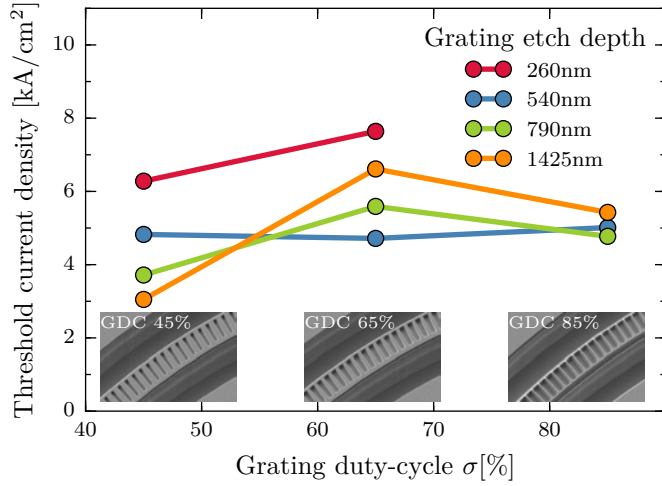


Fig. 3.46: Comparison of the threshold current densities for different grating duty-cycles and etch depths. The insets show SEM images made during fabrication of the ring waveguides. Second-order DFB gratings with 45%, 65% and 85% duty-cycle are then finally covered with metal.

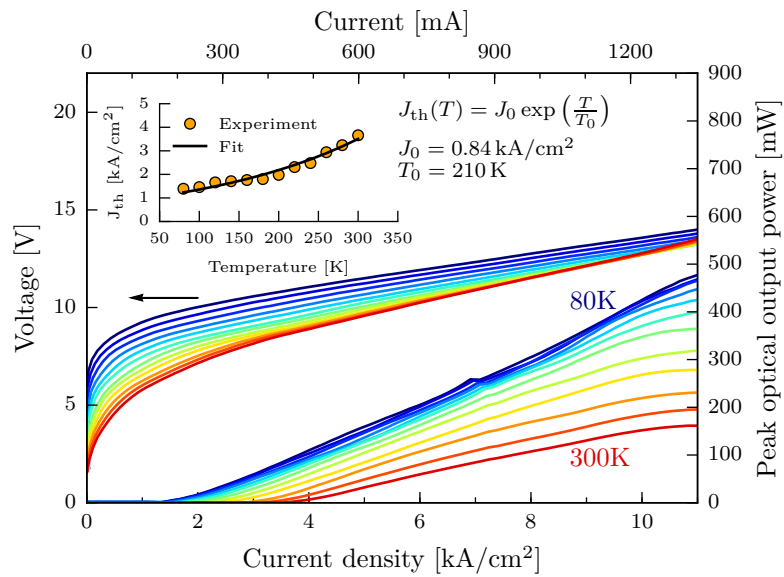


Fig. 3.47: LIV as function of different submount temperatures in steps of 20 K. The substrate-emitting ring laser has a second-order DFB grating with an etch depth of $t_g = 790$ nm and a grating duty-cycle of 45%. The inset shows the threshold current density extracted for every submount temperature. From the fit to an exponential function a characteristic temperature of $T_0 = 210$ K and $J_0 = 0.84$ kA/cm².

peratures. Single-mode emission is observed in the whole temperature range from 80 K to 300 K. The wavelength of the emitted light changes with temperature, which can be understood considering the temperature-dependence in the Bragg condition (2.82). For second-order DFB lasers ($m = 2$) this Bragg condition reads

$$\lambda_B(T) = n_{\text{eff}}(T)\Lambda_g(T), \quad (3.27)$$

with the effective refractive index $n_{\text{eff}}(T)$ and the grating period $\Lambda_g(T)$. Taking the derivative of this equation with respect to the temperature and normalizing by the wavelength, one arrives at the spectral tuning coefficient [17]

$$\frac{1}{\lambda_B} \frac{d\lambda_B}{dT} = \frac{1}{n_{\text{eff}}} \frac{dn_{\text{eff}}}{dT} + \frac{1}{\Lambda} \frac{d\Lambda}{dT} \quad (3.28)$$

The second term describes the thermal expansion of the cavity, whose materials (e.g. InP or InGaAs) have expansion coefficients of $\sim 5 - 6 \times 10^{-6} \text{ K}^{-1}$. In contrast to that, the first term corresponds to the temperature tuning of the refractive index. This tuning is typically one order of magnitude larger than the cavity expansion and therefore determines the overall wavelength tuning [181, 17]. From the shift of the emission peak a temperature tuning coefficient of $\Delta\nu/\Delta T = -0.0674 \text{ cm}^{-1}/\text{K}$ can be calculated. A side-mode suppression ratio of 24 dB is obtained at room-temperature, as shown in Fig. 3.48(b).

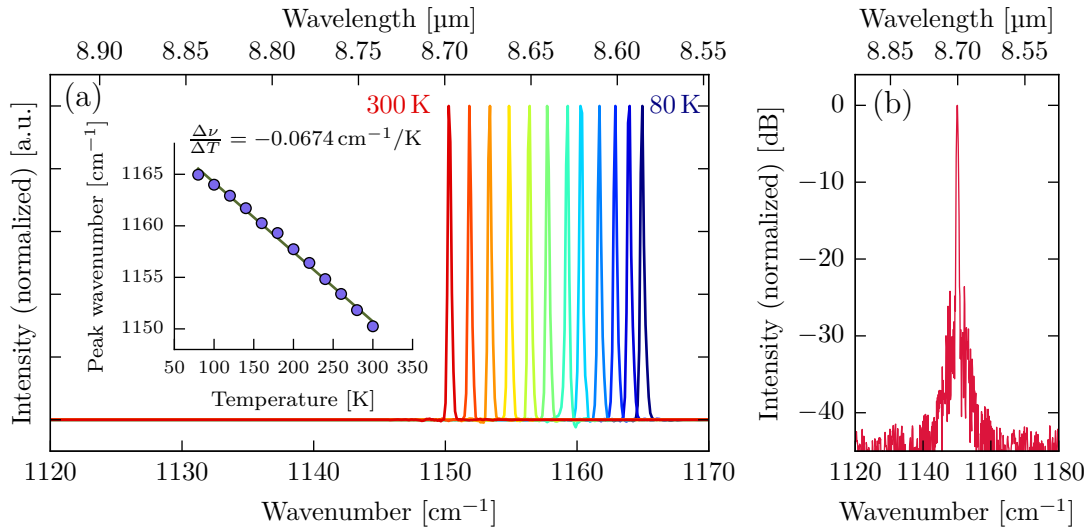


Fig. 3.48: (a) Temperature-dependent spectrum measured at a drive current of 1.2 A with 80 kHz/100 ns pulses. The inset shows the shift of the emission peak as function of the submount temperature. (b) Semi-logarithmic plot of the spectrum at 300 K. A side-mode suppression ratio of 24 dB is obtained.

While a distributed-feedback laser emits in a single-mode above lasing threshold, the device shows a fairly different behavior in the sub-threshold regime. There, a broad multi-mode spectrum can be observed, as several modes are amplified within the gain spectrum.

Fig. 3.49 shows an example for a sub-threshold amplified spontaneous emission spectrum of a, in this case, standard surface-emitting ring QCL. To increase the optical output power, the device is liquid-nitrogen cooled and operated with long pulses (67 kHz/7.46 μ s). The light is focused with a 1.5" ZnSe lens into a FTIR spectrometer, which is equipped with an external MCT detector. The spectrometer is operated in step-scan mode with a resolution of 0.21 cm^{-1} . The spacing between individual peaks $\Delta\nu = 2.41 \text{ cm}^{-1}$ is the free spectral range (FSR), which is determined by the length of the cavity (see section 2.3.7). Below lasing threshold, many longitudinal whispering-gallery modes (WGMs) are present in the ring cavity. The spontaneous emission peaks at around 8.4 μm , where the WGM experiences the lowest losses.

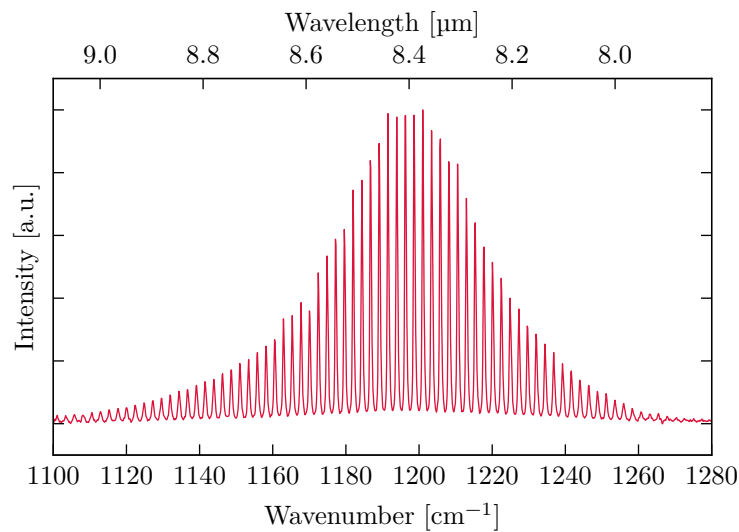


Fig. 3.49: Sub-threshold measurement of the emission spectrum of a surface-emitting ring QCL (sample C0038_RS2). The device is mounted in a liquid-nitrogen cooled cryostat ($T = 77 \text{ K}$) and operated with 67 kHz/7.46 μs pulses at a drive current of 120 mA. The spacing between the peaks $\Delta\nu = 2.41 \text{ cm}^{-1}$ is determined by the cavity length $L = 1.23 \text{ mm}$.

A technique to actually measure the sub-threshold gain was developed by Hakki and Paoli [182]. This method has the advantage that only one single device needs to be measured, which avoids problems with performance fluctuations between multiple devices (caused by growth, fabrication, measurement setup, etc.). The method of gain estimation is fairly simple, because it relies only on the measurement of the emission spectrum below threshold. The depth of modulation, which is introduced by Fabry-Pérot resonances into the spontaneous emission spectrum, is used for the computation of the gain. For a reliable estimation, the sub-threshold spectrum needs to be relatively "clean". This means that there should not be any other (transverse) mode contributing minima and maxima in the spectrum [183]. The net modal gain is calculated from the fringe contrast $P_{\text{max}}/P_{\text{min}}$ with the following equation [182]

$$g(\lambda) = -\frac{1}{L} \left[\ln \left(\frac{\sqrt{P_{\text{max}}/P_{\text{min}}} + 1}{\sqrt{P_{\text{max}}/P_{\text{min}}} - 1} \right) + \ln(R) \right], \quad (3.29)$$

where L denotes the length of the cavity and R is the facet reflectivity. Fig. 3.50(a) shows the LIV characteristics of a metal-covered substrate-emitting ring QCL. Amplified spontaneous emission is observed below lasing threshold. The light signal rapidly increases if the lasing threshold is reached at around 86 mA. Fig. 3.50(b) shows the extracted net modal gain measured at different drive currents. The ring laser ($L = 1.23$ mm) is pulsed with 67 kHz/40% duty-cycle and operated at 77 K.

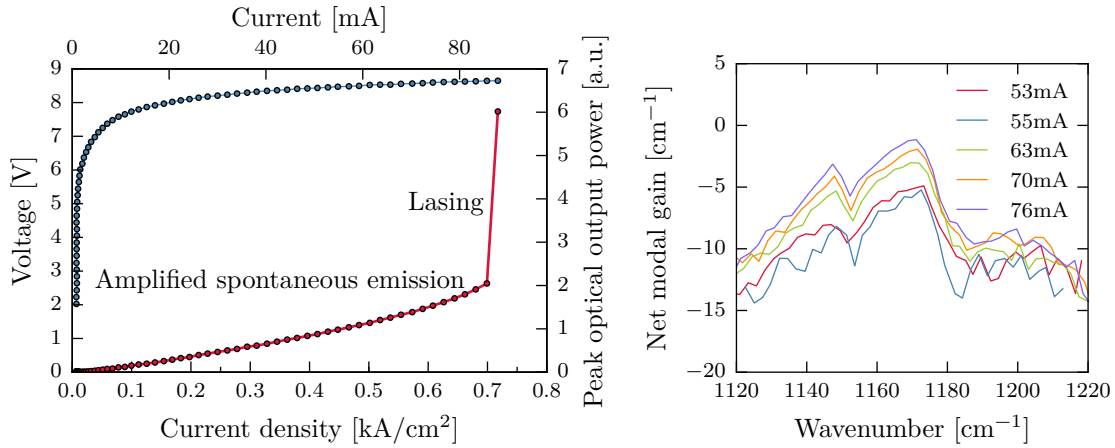


Fig. 3.50: (a) LIV characteristics of a substrate-emitting metal-covered ring QCL operated with 67 kHz/40% duty-cycle pulses at $T = 77$ K. Below threshold amplified spontaneous emission is observed from the 1.23 mm long ring device. (b) The net modal gain can be extracted from the fringe contrasts in the emission spectra via the Hakki-Paoli method [182].

To investigate the beam shape of the emitted light, the farfield is measured with an MCT detector mounted on a translational stage. Fig. 3.51 shows the farfield profile and its projection of the substrate-emitting ring laser at room-temperature for a drive current of 1.2 A (5 kHz/100 ns). The farfield exhibits an intensity minimum in the center, which has been also observed for surface-emitting ring lasers with second-order semiconductor/air DFB gratings [128]. Hence, the ring laser operates in a symmetric lasing mode. For some applications, a central intensity maximum may be required, which can be achieved by an off-center grating [134], two π -shifts [132] or a continuous π -shift [142] incorporated into the DFB grating. It has to be noted that for some lasers a central intensity maximum is observed, which is most probably caused by a shift of the grating with respect to the waveguide. This shift can be introduced by a slight misalignment (off-center grating) during the e-beam lithography. The farfield in Fig. 3.51 shows that most of the light intensity is concentrated in the inner fringe around $\pm 1^\circ$ full-width at half maximum (FWHM). Compared to a edge-emitting ridge lasers, the farfield of rings has a lower beam divergence, e.g. a Fabry-Perot laser typically has a FWHM of around $\pm 30^\circ$. In addition, the effective refractive index n_{eff} of the mode can be also estimated from the measured farfield with the relation

$$n_{\text{eff}} = \sin(\alpha) + \frac{\lambda}{\Lambda_g}, \quad (3.30)$$

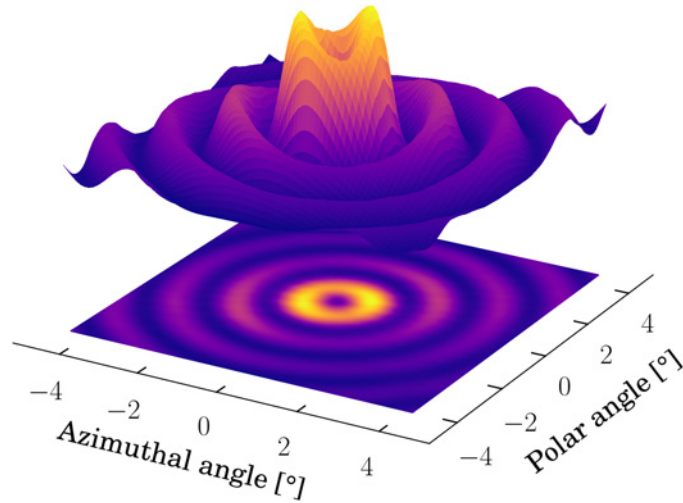


Fig. 3.51: Measured farfield profile and its projection on the emission plane of a substrate-emitting ring laser with a metal-covered second-order DFB grating. The substrate material is double-side polished InP.

where λ is the free-space emission wavelength and Λ_g is the fabricated grating period. For $\alpha \approx 1^\circ$, $\lambda = 8.7 \mu\text{m}$ and $\Lambda_g = 2.741 \mu\text{m}$, a refractive index of $n_{\text{eff}} = 3.19$ is estimated. This value is close to the effective index value of $n_{\text{eff,spec}} = 3.17$ that is retrieved from measurements of the spectrum.

Fig. 3.52 shows images of the projected nearfields of the metal-covered laser. The light emitted from the substrate is collimated with a lens and captured with a bolometer camera. A wiregrid polarizer is inserted in the beam path to examine the polarization of the nearfield, shown in Fig. 3.52(b) and (c). The electric field parallel to the wires of the polarizer is absorbed and only the perpendicular component is transmitted. From these measurements an azimuthal (tangential) orientation of the electric nearfield is found. This polarization orientation has been also observed for other ring quantum cascade lasers [134, 131]. With an optimized metal-covered DFB grating, lasers can be fabricated with thick top metalization layers that act as heatspreader. Thermal simulations, discussed in section 3.8, suggest that a good thermal conducting gold layer can out-perform a lateral regrowth with InP. In combination with epi-side down bonding techniques, the metallized grating allows to fabricate regrowth-free high-performance DFB lasers.

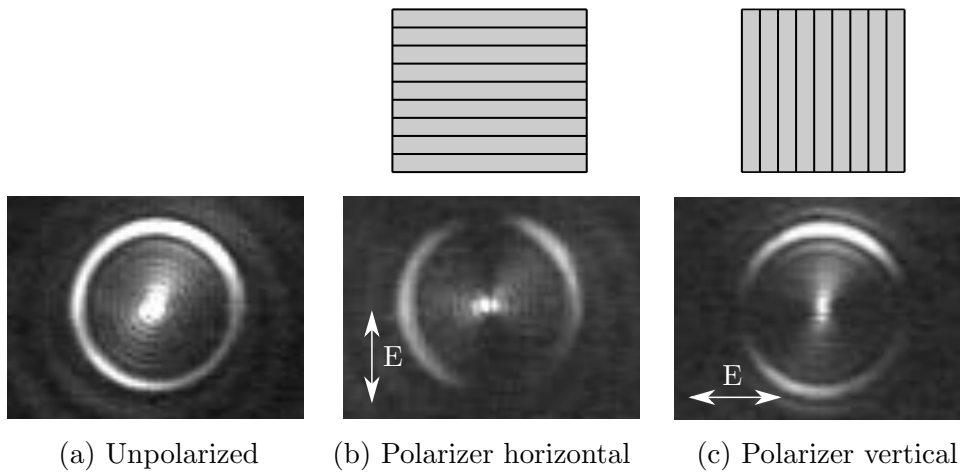


Fig. 3.52: Projected nearfield images of the metal-covered ring QCL, recorded with a bolometer camera. (a) Bright emission over the full circumference is observed. (b) A wiregrid polarizer is placed in the beam path and the wires are oriented parallel in horizontal direction. (c) The polarizer is rotated by 90 degree and the wires are oriented vertical. From these measurements an azimuthal (tangential) polarization of the electric field in ring QCLs is confirmed.

Interband cascade lasers

The spectral region between 2 and 4 μm is highly interesting for gas sensing applications, as strong absorption lines for CH_4 , CO_2 , SO_2 , O_3 and many other gases are absorbing in this range. Several semiconductor laser concepts are covering these wavelengths, such as type-I GaSb-based quantum well lasers with quinternary barriers (3.7 μm) [7], quantum cascade lasers with large conduction band offsets (2.6–3.3 μm) [111, 33], strain-compensated QCLs [184, 185] or injectorless QCLs with intracavity second-harmonic generation at 2.7 μm [112]. For QCLs, the largest conduction band offset that has been realized to date is $\Delta E_c = 2.1 \text{ eV}$ in the InAs/AlSb material system. Compared to typical alloys grown on InP substrates, the direct-indirect valley separation in InAs is higher. However, QCLs suffer from electron scattering from the Γ -minimum into other valleys (X or L), which reduces the population inversion at short wavelengths [186].

Semiconductor based diode lasers are limited by several physical mechanisms to wavelengths below $\sim 3 \mu\text{m}$. First, only poor carrier confinement is possible due to small conduction and/or valence band offsets in narrow-gap group III-V semiconductors. This leads to high threshold carrier densities. Another limiting factor is Auger recombination [187], mainly via the conduction band-to-heavy-hole recombination processes together with heavy-to-split-off-hole transitions (CHHS Auger process). The probability for this non-radiative energy relaxation path increases with temperature and bandgap lowering. Due to the fact that the bandgap energy E_g in InAs-rich alloys is comparable to the split-off gap Δ_{SO} , such processes are more likely to occur within those materials. Fig. 4.1 illustrates a basic bandstructure including relevant conduction and valence bands. An overview of absorption and recombination mechanisms in semiconductors is given in the appendix A.2 on page 173. Furthermore, free-carrier absorption as well as intervalence band absorption increase with wavelength [188]. Despite their rapid progress, the realization of long wavelength mid-infrared laser diodes remains very challenging.

By switching to quantum well heterostructures with type-II band alignment the CHHS Auger processes are suppressed due to a mismatch between E_g and Δ_{SO} . In such structures, the valence band edge of one QW lies energetically higher than the conduction band edge of the adjacent QW. Furthermore, the confinement is also improved due to larger band offsets in the nearly lattice matched InAs-GaSb-AlSb material system. Together

with the good control of crystal quality the development of a new class of coherent light sources for the mid-IR spectral region became possible.

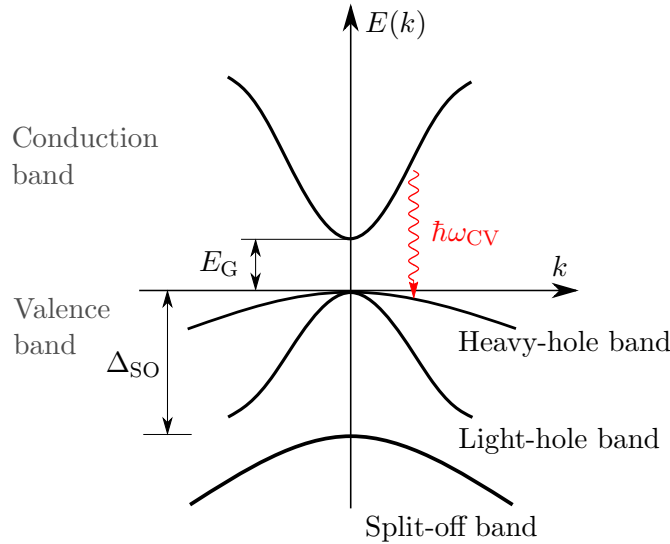


Fig. 4.1: Schematic illustration of a semiconductor bandstructure including conduction and valence band together with an optical interband transition of energy $\hbar\omega_{CV}$. The spin-orbit coupling between p -orbitals and the spin angular momentum of the electron leads to the formation of a split-off band. The probability for non-radiative transitions increases if the bandgap energy E_G is comparable to the split-off gap Δ_{SO} .

The so-called interband cascade laser is a combination of the conduction-to-valence band optical transitions in diode lasers with the electron recycling feature of cascading quantum structures like in quantum cascade lasers [189]. This hybrid concept competes with two other device architectures in the mid-IR spectral range, namely the conventional type-I diode laser and the QCL.

While the diode lasers technology is used to access the spectral region between $3 - 6 \mu\text{m}$ from the short wavelength side, the QCL approaches it from longer wavelengths. A sketch of the heterostructures and transitions for the different device concepts are shown in Fig. 4.2. Although the ICL shares some features with the QCL, they differ fundamentally in terms of involved physical processes. While the former deals with electrons in the conduction band and holes in the valence band ("bipolar"), the latter relies on electron transitions within the conduction band only ("unipolar"). As an important consequence, the carrier lifetimes are fundamentally different for interband and intersubband cascade lasers. Long upper state lifetimes on the order of $\sim 1 \text{ ns}$ are possible for interband transitions [190], whereas the intersubband lifetimes in quantum cascade lasers [10] are on the order of $\sim 1 \text{ ps}$. This results in an approximately two orders of magnitude higher modal gain per stage in an ICL compared to a QCL device [191]. In addition, the low power consumption of ICLs makes them ideal candidates for mobile (e.g. battery powered) applications.

The concept of cascading (see section 2.2 on page 11) allows the realization of differential quantum efficiencies above 100% by connecting multiple active regions in series [192]. In

other words, each injected electron/hole can emit as many photons as there are available stages. This is in contrast to conventional diode lasers where only one photon can be generated per injected electron. Early simulations suggested that the cascaded geometry enables a lower threshold current density and a higher differential slope efficiency than conventional interband quantum well lasers [193].

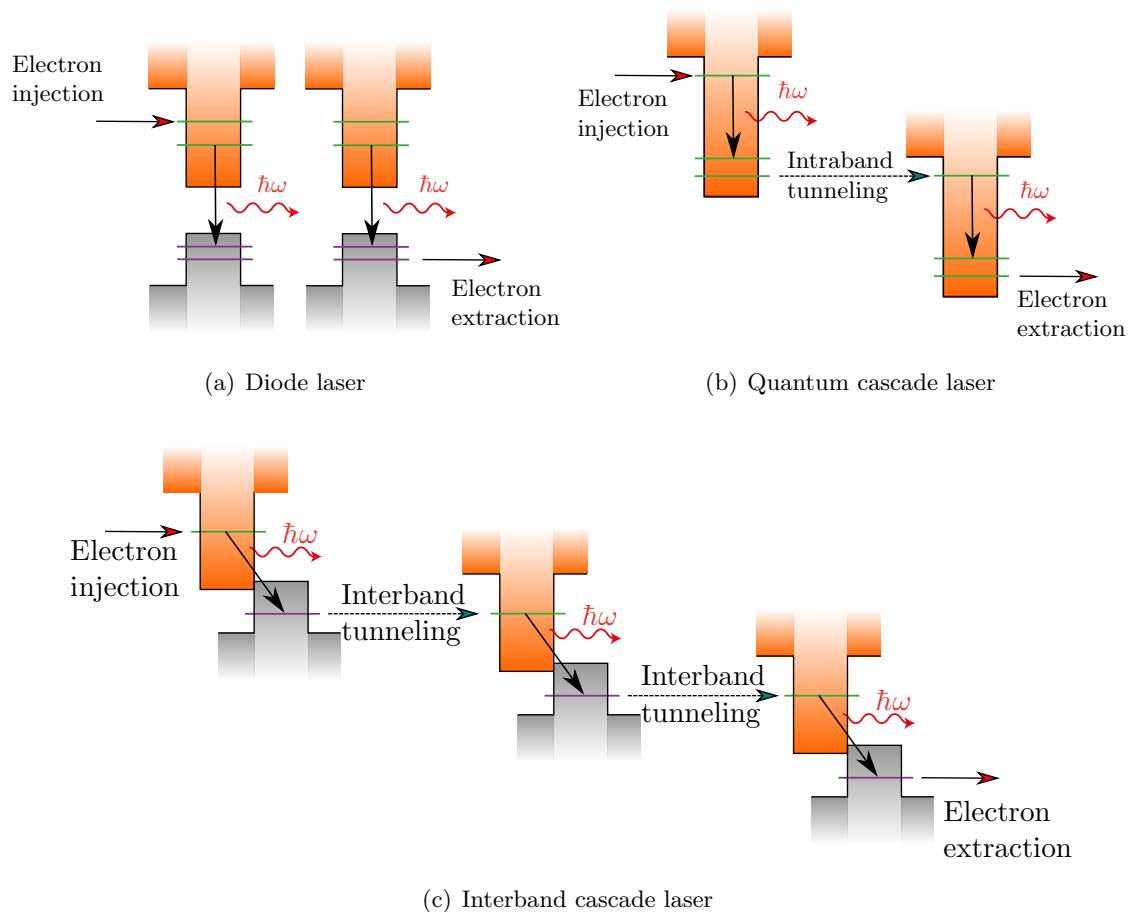


Fig. 4.2: Comparison of different device concepts for mid-IR semiconductor lasers. (a) The conventional diode laser relies on the radiative recombination of electrons in the conduction band with holes in the valence band. Multiple QWs are connected in parallel to increase the optical gain. (b) The quantum cascade laser on the other hand is a unipolar device, where electrons undergo transitions between states in the conduction band only. (c) Both concepts are combined in the interband cascade laser, where the radiative transitions occur between states in the conduction and valence band. Carriers from the valence band are recycled via interband tunneling and injected into the next stage.

4.1 A short historical review

In 1995, Rui Q. Yang proposed¹ an infrared laser based on resonant *interband tunneling* [194] in a leaky quantum well structure [14]. The concept allowed to create population inversion between subbands and also helped to suppress nonradiative losses (e.g. optical phonon relaxation), which have been the major obstacles in achieving stimulated photon emission in intersubband devices. Just as a side note, the QCL was realized one year earlier, anyway. In 1996, Jerry R. Meyer, Igor Vurgaftman, Rui Q. Yang and L. Ramdas Ram-Mohan proposed the first heterostructure designs for interband cascade lasers (ICLs) based on type-I and type-II band alignments [189]. An illustration of these designs is shown in Fig. 4.3. In case of a type-I band alignment, the optical transition takes place in an $\text{InAs}_{0.64}\text{Sb}_{0.36}$ QW with a design wavelength of $\lambda = 3.2\ \mu\text{m}$. In the design for a type-II alignment an InAs (electrons) and a $\text{Ga}_{0.7}\text{In}_{0.3}\text{Sb}$ (holes) QW are used for emission at $\lambda = 3.4\ \mu\text{m}$.

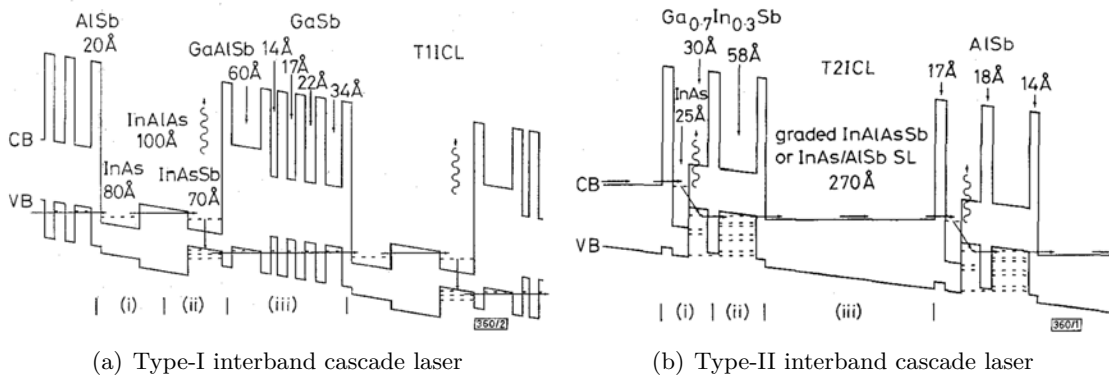


Fig. 4.3: First heterostructure design proposals named as *interband cascade laser*. Conduction and valence band profiles for the (a) type-I (T1ICL) and (b) type-II interband cascade laser (T2ICL). Reprinted with permission from [189] © 2011 IEEE.

After the electrons make an optical transition from the conduction to the valence band, a fast tunneling process ($< 100\ \text{ps}$) into a $\text{Ga}_{0.7}\text{In}_{0.3}\text{Sb}$ QW extracts the carriers from the active region. Electrons from the valence band of the first stage are then transferred via elastic interband tunneling into the conduction band of the next stage. A key building block is the broken bandgap alignment in type-II quantum wells, which enables carrier recycling via interband tunneling. This transition from the valence to the conduction band is of type-II in both design schemes (type-I and type-II ICL) as illustrated in Fig. 4.3.

Based on theoretical predictions [24], the first electroluminescence measurements of type-II IC light emitting diodes were presented in 1996 [195]. The device showed light emission around $3.64\ \mu\text{m}$ with a FWHM of $54\ \text{meV}$. In 1997, stimulated emission was observed for the first time from a 20-stages type-II Sb-based ICL at $3.8\ \mu\text{m}$ up to temperatures of $170\ \text{K}$ [196]. A light-emitting diode, fabricated from the same InAs/(In)GaSb/(In)AlSb laser material, showed an improvement in the output power by three orders of magnitude,

¹The manuscript was submitted to the journal in August 1994. In the same year the first QCL was demonstrated experimentally [10].

compared to the previously mentioned electroluminescence measurements [195]. Encouraged by these promising results, research focused on type-II ICLs and in the same year external quantum efficiencies (EDQE) above unity (1.3 photons per injected electron) were achieved with a "W" configuration [187] of the active region [197]. In such a "W" structure the $\text{Ga}_{0.7}\text{In}_{0.3}\text{Sb}$ hole QW is sandwiched between two InAs electron QWs, which enhances the gain due to a better wavefunction overlap [198]. Shortly afterwards, lasing in pulsed mode near room-temperature ($T_{\text{max}} = 286 \text{ K}$) was achieved with a 25-stage ICL at $\lambda \sim 3.5 \mu\text{m}$ [199]. Slope efficiencies of $dP/dI = 735 \text{ mW/A}$ corresponding to an EDQE of 456 % were reported [200], exceeding the limit (1 photon per electron) of conventional diode lasers significantly. Although the material quality of the grown crystals was not optimal, the emission wavelength could be extended up to $15 \mu\text{m}$ with Sb-based type-II IC LEDs [201]. By improving the device fabrication cw-operation up to 142 K together with high wall-plug efficiencies of $\sim 18 \%$ (at 60 K) was achieved [202]. High slope efficiencies $> 1000 \text{ mW/A}$ corresponding to an EDQE of 620 % have been reported in 2002 [192].

The first DFB ICL emitted in a single-longitudinal mode at $\lambda \sim 3.1 \mu\text{m}$ up to temperatures of 80 K [203]. The grating was formed by interference of two third harmonic beams from a yttrium-aluminium-garnet (YAG) laser under an angle of 45° . With this standing wave pattern a photoresist was exposed, giving a grating period of 465 nm. Later on, by lowering the lasing threshold currents, the maximum temperature for cw-operation was increased up to 200 K, which was already close to the minimum accessible temperature for thermoelectric coolers ($T > 230 \text{ K}$) [204]. An important milestone was the demonstration of the first ICL operating in cw-mode above room-temperature in 2008 by Kim et al. [205]. The laser was based on a 5-stage design with an emission wavelength of $3.75 \mu\text{m}$ and could be operated up to a temperature of 319 K. The optical losses have been reduced by lowering the doping levels in the claddings and separate-confinement layers. An important discovery has been made in 2011, by revealing an imbalance between electron and hole densities in the active wells [23]. Subsequent carrier re-balancing with heavy n-doping of the electron injector lead to a performance boost of ICL devices.

State of the art interband cascade lasers reach threshold current densities as low as 98 A/cm^2 in pulsed operation (1 kHz/350 ns) at 300 K (10-stages, $\lambda \approx 3.65 \mu\text{m}$) [15]. They operate in cw-mode at room-temperature with threshold input powers of 29 mW [23], provide single-mode optical output powers of 55 mW and show wall-plug efficiencies of up to 18 % [191, 206]. This value is close to the cw wall-plug efficiency of 21 % reported for QCLs [113]. Output powers as high as 464 mW ($T = 25^\circ\text{C}$) and lasing up to a temperature of 118°C [206, 207] have been demonstrated. ICLs nowadays cover the wavelength region between $2.8 - 7 \mu\text{m}$ [208, 209, 210]. To date, the longest emission wavelength reported for an InAs-based ICL is $11 \mu\text{m}$ [16].

4.2 Operation principles

Interband cascade lasers consist of a light generating core with typically 5 to 12 stages, which is sandwiched between waveguide layers, the optical claddings and contact layers. Each stage contains an injector for electrons and another one for holes as well as the the

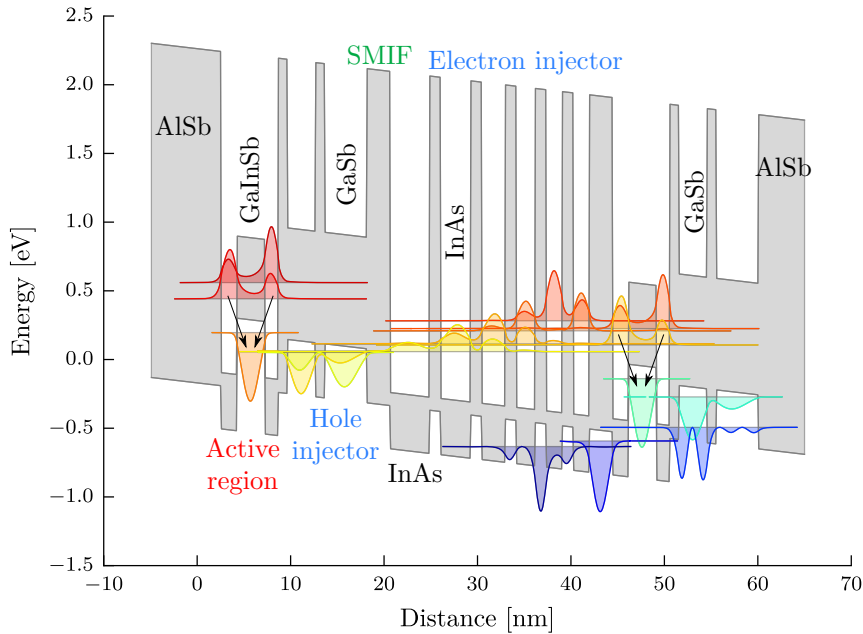


Fig. 4.4: Band diagram of a typical type-II ICL design for emission at $\lambda = 3.7 \mu\text{m}$. Conduction and valence band profiles as well as the squared moduli of some relevant wavefunctions are plotted. Each stage consists of the "W" active region (InAs/GaInSb/InAs), an electron and a hole injector. The electrons and holes are generated internally at the semimetallic interface (SMIF). Heterostructure design from [13].

active QWs, where the carriers recombine. Fig. 4.4 shows the band diagram of a typical ICL design.

The active QWs can have either a type-I or type-II band alignment. In this case it is a state-of-the-art "W" active region with a type-II alignment designed for an emission wavelength of $\lambda = 3.7 \mu\text{m}$. By applying an external bias, electrons are injected from the left n-contact into the first stage, where they tunnel into the active QWs. A quasi-thermal equilibrium is established on a sub-picosecond time scale and recombinations (radiative/non-radiative) with free states in the valence band take place [22]. Ideally only optical transitions occur, where each electron emits a photon. But there are always concurring non-radiative processes limiting the quantum efficiency. The recombination mechanisms are discussed more in detail in section A.2.4. Once the electrons reach the valence band, they travel through the hole injector and the so called semimetallic interface (SMIF). This interface plays an important role for the ICL as it enables the "recycling" of electrons from the valence to the conduction band via interband tunneling. Furthermore, electrons and holes are generated internally at the SMIF. Consequently, the CB-VB transition the charge carrier can be re-used in the electron injector of the next stage and the cycle starts all over again. Subsequently, when the electrons passed all stages, they are collected at the positive p-contact on the right side. In the following, the basic building blocks are discussed in detail.

4.2.1 Semimetallic interface

In order to benefit from a cascaded arrangement, a carrier recycling mechanism has to be incorporated between individual stages. For instance in quantum cascade lasers, the extractor level in one stage is aligned with the injector level of the next stage. This rather simple approach is possible, because only electrons in the conduction band are required for the laser operation. For interband devices the carrier recycling has to transfer electrons between valence and conduction band, which demands for a more sophisticated approach. One possible solution are Esaki or tunnel diodes, where a forward-biased heavily-doped pn-diode allows tunneling from the CB to the VB. Such a configuration is used in bipolar cascade lasers, where vertically stacked diodes are coupled by Esaki junctions [211]. Unfortunately, optical losses due to absorption in the highly doped tunnel junctions and also increased series resistances limits this approach [23].

However, there is another option utilizing the rather "strange" band alignment of GaSb (or GaInSb) and InAs, also known as type-II broken gap alignment. Fig. 4.5 illustrates the heterostructure comprised of a GaSb QW for holes and an InAs QW for electrons.

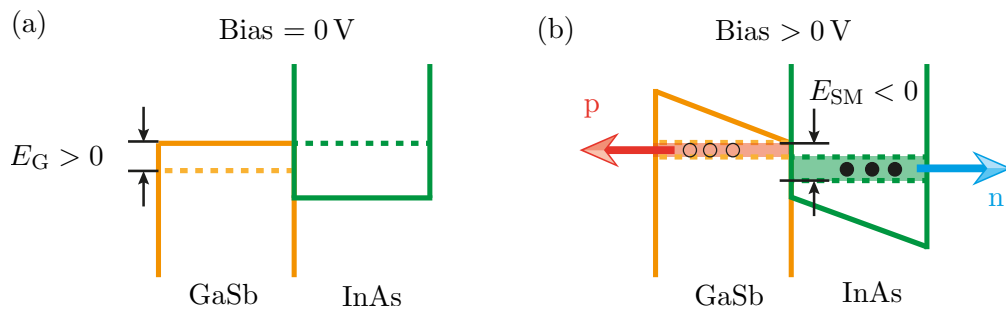


Fig. 4.5: The semimetallic interface (SMIF) between GaSb and InAs plays a crucial role in the operation of ICLs. The solid lines represent the valence/conduction band-edges, while the dashed lines correspond to a confined energy state. (a) Without an external bias a bandgap is created due to quantum confinement. (b) If a bias voltage is applied, the band alignment can be tuned from a semiconducting to a semimetallic behavior. An equal number of holes in the GaSb and electrons in the InAs layer is generated internally. Based on [23].

At room temperature the conduction band minimum of InAs is around 0.21 eV below the valence band maximum of GaSb [117]. Due to quantum confinement, carriers in the hole and electron quantum well have non-zero eigenenergies, which forms an energy gap $E_g > 0$ eV, as shown in Fig. 4.5(a). The band alignment in this case leads to a semiconducting behavior. By decreasing the layer thicknesses the gap can be further increased because states in the CB of InAs are shifted up in energy, while hole levels in GaSb move downwards. On the other hand, by applying an external bias voltage the system can be tuned from a semiconducting to a semimetallic behavior², as shown in

²A semimetallic band alignment can also be achieved by increasing the thicknesses of the layers to such extend that no quantization of the eigenenergies takes place. Valence electrons will move from the GaSb layer to the conduction band states in the InAs.

Fig. 4.5(b). The material is then neither a metal nor a semiconductor. The classification as semimetal (SM) indicates that just a small overlap between subbands in the conduction and valence band exists, which leads to a vanishing band gap. It is true that metals also have a zero bandgap, but there the density of states at the Fermi energy is not negligible. In a SM, a small number of electrons (in InAs) and holes (in GaSb) coexist spatially separated even without doping [23, 212]. Furthermore, semimetals are conductors at $T = 0$ K, while pure semiconductors are insulators [213]. Sometimes they are also referred to as semiconductors with a negative indirect band gap, because the minimum of the CB lies energetically below the maximum of the VB and these extrema occur at different wavevectors in the momentum space [214]. The number of electrons and holes at the semimetallic interface (SMIF) is determined by the population required for a thermal quasi-equilibrium. However, in presence of an external electric field charge carriers are separated and holes move to the left, while electrons are forced to the right in Fig. 4.5(b). To preserve a quasi-equilibrium, an equal number of additional holes and electrons is generated again at the SMIF [23]. Thus, the amount of carriers can be controlled with an external bias voltage, where the band overlap energy E_{SM} is given by [22]

$$E_{SM}(V) = E_{\text{field}}(d_e + d_h)q - E_G, \quad (4.1)$$

with the applied electric field E_{field} , the center-of-mass distances d_e and d_h from the SMIF of the electron and the hole probability densities, respectively, and E_G is the energy gap due to carrier confinement. On the other hand an approximation for the common quasi-Fermi level E_F across the SMIF can be expressed by [22]

$$E_F \approx E_{SM} \frac{m_r^*}{m_e^*} + E_c, \quad (4.2)$$

where E_c is the conduction band minimum and the electron mass m_e^* and the hole mass m_h^* are included in the reduced density-of-states mass $m_r^* = m_e^* m_h^* / (m_e^* + m_h^*)$. For a two-dimensional system with a parabolic dispersion relation, the density-of-states is defined as

$$\rho_{2D} = \frac{m_e^*}{\pi \hbar^2}. \quad (4.3)$$

Carrier densities of electrons/holes can be evaluated by integrating the density-of-states and the Fermi-function $f(E)$ over a given energy interval. Assuming zero temperature (and hence $f(E) = 1$), the electron density induced by the semimetallic band overlap in the InAs QW can be calculated as

$$n = p = \int_{E_c}^{E_F} \rho_{2D}(E) f(E) dE \quad (4.4)$$

$$= \int_{E_c}^{E_F} \frac{m_e^*}{\pi \hbar^2} dE = \frac{m_e^*}{\pi \hbar^2} \left(E_{SM} \frac{m_r^*}{m_e^*} + E_c - E_c \right) \quad (4.5)$$

$$= \frac{m_r^*}{\pi \hbar^2} E_{SM} \quad (4.6)$$

The same result can also be derived for holes by replacing m_e^* with m_h^* and integrating from E_F to the valence band edge E_v in the GaSb QW. Equation (4.6) shows the important result that the number of charge carriers generated at the SMIF depends on the band overlap energy. Furthermore, holes and electrons are generated with equal densities. An estimation of the required band overlap energy for creating a typical threshold carrier density of $n_{th} = 2 \times 10^{12} \text{ cm}^{-2}$ with $m_e^* = 0.004m_0$ and $m_h^* = 0.009m_0$ (at $T = 300 \text{ K}$) gives a value of $E_{SM} \approx 173 \text{ meV}$. In ICL heterostructure designs, as shown exemplary in Fig.4.4, the SMIF is placed between electron and hole injector.

Using the unique semimetallic type-II band alignment the charge carriers are generated internally. However, carefully designed layer thicknesses are necessary in order to generate just the right amount of carriers. A too high population would increase the free-carrier absorption, while a too low value increases the lasing threshold current.

4.2.2 Active region

Instead of a single type-II interface, state-of-the-art ICL active regions feature a "W"-arrangement, where a GaInSb hole QW is sandwiched between two InAs electron QWs. This configuration is known to increase the interband optical matrix element [22] compared to a design with a single InAs and a GaInSb QW. It is worth to mention that the spatial wavefunction overlap for a type-I QW design (electron/hole located in same well) is commonly better than for a type-II transition, but the latter can effectively suppress Auger scattering processes [215]. Fig. 4.6(a) shows the simulated bandprofiles and squared wavefunctions for an unbiased active region. The wavelength of the emitted photon is determined by the energy separation $E_{E1} - E_{H1} = hc/\lambda$ between the electron state E1 in the InAs QW and the hole state H1 in the GaInSb QW. The diagonal lasing transition between conduction and valence band is indicated by black arrows. In such a configuration, the emission wavelength can be tailored from $\sim 2 \mu\text{m}$ up to around $100 \mu\text{m}$. However, non-radiative Auger recombination processes as well as free-carrier absorption also increase at longer emission wavelengths. Furthermore, the wavefunction overlap decreases and lowers the gain [22].

An important design aspect is to maximize the interband optical matrix element, which determines the gain. Fig. 4.6(b) shows the biased heterostructure ($E_{field} = 80 \text{ kV}$), where

the electron probability density becomes larger in the right InAs QW compared to the left well. To compensate this imbalance, an asymmetric design with a slightly thinner InAs electron QW on the right side is used. Besides increasing the optical gain, also resonances between valence intersubband splittings and the energy gap have to be considered, which contribute to the losses via Auger recombination and free carrier absorption processes [193]. The indium content in the $\text{Ga}_{1-x}\text{In}_x\text{Sb}$ hole QW introduces a compressive strain in the structure, with $x = 30\%$ to 35% . As a result, the topmost heavy-hole subband rises in energy and thinner InAs QWs can be used which reduces the hole effective mass [22].

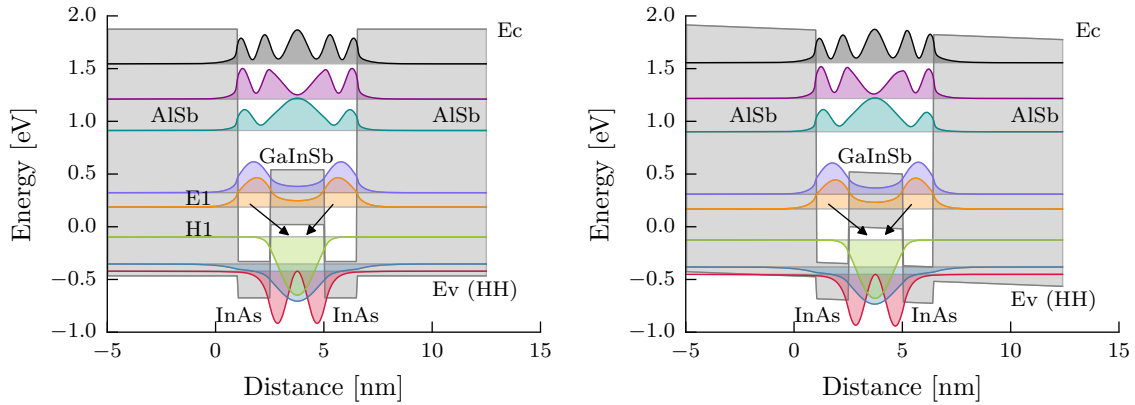


Fig. 4.6: Left: Typical "W"-shaped active region of an unbiased ICL. Electrons are injected into the upper laser level (orange) via tunneling and the optical transitions from the InAs to the GaInSb QWs are marked with arrows. Right: Under an external electrical field of 80 kV/cm the center-of-mass positions of the wavefunctions change. To compensate this shift, the thickness of the right InAs QW is typically slightly reduced.

4.2.3 Hole injector

As discussed before, both carriers (electrons/holes) for the optical interband transition in the active region are supplied by the SMIF. The purpose of the hole injector is to transfer the generated holes to the GaInSb QW. As can be seen in Fig. 4.4, the hole injector is composed of AlSb barriers and GaSb wells.

From empirical studies it is concluded that the position of the injector state is less critical. But the injected electrical threshold power can be minimized if the hole injector state is located not more than 80–100 meV ($\approx 4k_{\text{B}}T$) below the topmost hole subband energy in the active GaInSb QW [13]. This ensures that the holes, which are generated at the SMIF, are then efficiently transferred to the active region rather than residing in the injector. Furthermore, the hole injector serves as a barrier between the InAs QW in the active region and the electron injector. Otherwise, tunneling of electrons from the upper laser state to states in the electron injector via midgap defects would be enhanced, leading to higher lasing thresholds [23]. To prevent electron escape from the active region an AlSb barrier is placed between InAs electron QW and hole injector. Another concern is interband absorption at the SMIF between electron and hole injector. To suppress

parasitic absorption processes, an AlSb barrier is inserted between the GaSb and InAs QWs.

4.2.4 Electron injector

The counterpart to the hole injector is the electron injector, which transfers electrons from the SMIF to the InAs QWs in the active region. To ensure stimulated light generation, the separation between the quasi-Fermi levels of electrons and holes must be greater than the photon energy $E_{\text{Fn}} - E_{\text{Fp}} > \hbar\omega$. Because of a fast energy exchange rate across the semimetallic interface, holes in stage i and electrons in the next stage $i+1$ share a common quasi-Fermi level $E_{\text{Fp},i} = E_{\text{Fn},i+1}$. Or in other words, the carrier transport is fast compared to the carrier lifetime (≈ 0.5 ns) and therefore a thermal equilibrium is established across the QWs. Thus, the transparency condition from before can be rewritten to

$$E_{\text{Fn},i} - E_{\text{Fn},i+1} = \hbar\omega + \Delta E, \quad (4.7)$$

where $E_{\text{Fn},i}$ denotes the quasi-Fermi level of electrons in stage i and $E_{\text{Fn},i+1}$ in the next stage $i+1$, respectively. All kinds of additional losses are included via ΔE , which is typically on the order of the thermal energy $k_{\text{B}}T$ [13]. From (4.7) follows that the minimum voltage drop per stage is given by $V_{\text{th}} = (\hbar\omega + \Delta E)/q$. If properly designed, V_{th} equals the voltage needed at the SMIF to generate just enough electrons/holes. The corresponding threshold electric field is found to be

$$E_{\text{field,th}} = \frac{\hbar\omega + \Delta E}{d_{\text{stage}}q} = \frac{E_{\text{SM}} + E_{\text{G}}}{(d_{\text{e}} + d_{\text{h}})q}, \quad (4.8)$$

where d_{stage} is the total stage thickness and the term on the right hand side is obtained by inserting E_{field} from (4.1). A direct relation between the band overlap energy E_{SM} and the carrier density generated at the SMIF was found in (4.6). Thus, the quasi-equilibrium carrier density has to be consistent with the voltage drop across the stage, which implies a proper adjustment of the thicknesses of the GaSb and InAs layers.

A critical design parameter is the thickness of the first InAs QW of the electron injector (see Fig. 4.4). If the QW is too wide, more electrons and holes will be generated than needed, leading to an accumulation in the injector wells. As a result, free-carrier absorption as well as Auger recombination will increase the lasing threshold. On the other hand, if the InAs QW is too thin, generated electron and hole populations are not sufficient to produce enough optical gain. Consequently, a higher bias voltage is necessary to increase the band overlap at the SMIF and hence to produce more carriers.

The band diagram with relevant states of an electron injector is shown in Fig. 4.4. It consists of alternating layers of InAs/Al(In)Sb wells and barriers. As can be seen, the thicknesses of the layers are chirped to ensure good coupling between the QWs and "funneling" the electrons to the upper laser state. The last AlSb barrier on the right hand side is slightly thicker to prevent hybridization of an injector state and the active region

subband [13]. However, self-consistent simulations showed that most of the electrons stay in the injector rather than move to the active region. In contrast to that, nearly all holes transfer to the active GaInSb QW. Due to the fact, that the same number of electrons and holes are generated at the SMIF, the threshold hole population in the active QWs is far higher than the electron density ($p_{\text{th}} \gg n_{\text{th}}$) [23]. To compensate this imbalance additional carriers have to be injected, which results in an increased threshold current. One may assume that the ideal operating point is reached when $p_{\text{th}} = n_{\text{th}}$. But in fact the density of states is larger in the valence band and also free-carrier absorption cross-sections and Auger coefficients are not the same for electrons and holes. Although doping experiments revealed comparable Auger coefficients, a slightly higher electron density is preferable [23]. Rebalancing the carrier densities by increasing the doping in the electron injector QWs from $4 \times 10^{17} \text{ cm}^{-3}$ to $5 \times 10^{18} \text{ cm}^{-3}$ led to a calculated ratio of $n_{\text{th}}/p_{\text{th}} \approx 1.19$. As a result, the threshold current density was lowered from $J_{\text{th}} \sim 400 \text{ A cm}^{-2}$ to 167 A cm^{-2} [23].

4.3 Materials

The operation of interband cascade laser relies on a broken gap band alignment in type-II quantum wells. Such an exotic arrangement, where the valence band edge of one material lies energetically above the conduction band edge of another material, cannot e.g. be created with GaAs/AlGaAs or InGaAs/InAlAs, which are used for quantum cascade lasers. However, type-II alignment is observed in layers composed of InAs and GaSb. There, energy gaps of 0.354 eV (InAs) and 0.73 eV (GaSb) are measured at room temperature. A map of the most important III-V and also II-VI semiconductor materials is shown in Fig. 4.7. Materials commonly used for ICLs are marked with red dots.

For the barrier material AlSb is used, which has an energy gap of 1.615 eV. The hetero-junction GaSb/AlSb has a type-I band alignment, which is also present in GaAs/AlGaAs heterostructures. Fig. 4.8 shows a comparison between type-I and type-II band alignments in semiconductor heterostructures. All three semiconductors, InAs, GaSb and AlSb, correspond to the so called 6.1 Å family [216], as their lattice constants are very similar. In addition, they share the same Zincblende (cubic) crystal lattice. A lattice matched growth of the heterostructure can be accomplished by using either GaSb or InAs as substrate. Some properties of the materials are listed in Tab. 4.1. The valence band offset at the interface InAs/GaSb is $VBO \sim 0.56 \text{ eV}$. According to [117] this guide value corresponds to an averaged VBO that needs to be adjusted to the interface bond type. For the hetero-junction GaSb/AlSb, a $VBO \sim 0.38 \text{ eV}$ is recommended, which leads to a VBO of 0.18 eV for the staggered InAs/AlSb interface. For bandstructure simulations (e.g. with the $\mathbf{k} \cdot \mathbf{p}$ method) the parameters from [117] can be used, which are a good starting point. Fig. 4.9 shows an illustration of the band lineups for the 6.1 Å family.

An important property of semiconductors is the adjustment of the electronic behavior via the incorporation of dopands in the crystal lattice. In arsenide-based heterostructures commonly Si or Sn are used as donors. Si has the advantage of a low vapor pressure, which corresponds to an evaporation at higher temperatures. This in turn allows faster

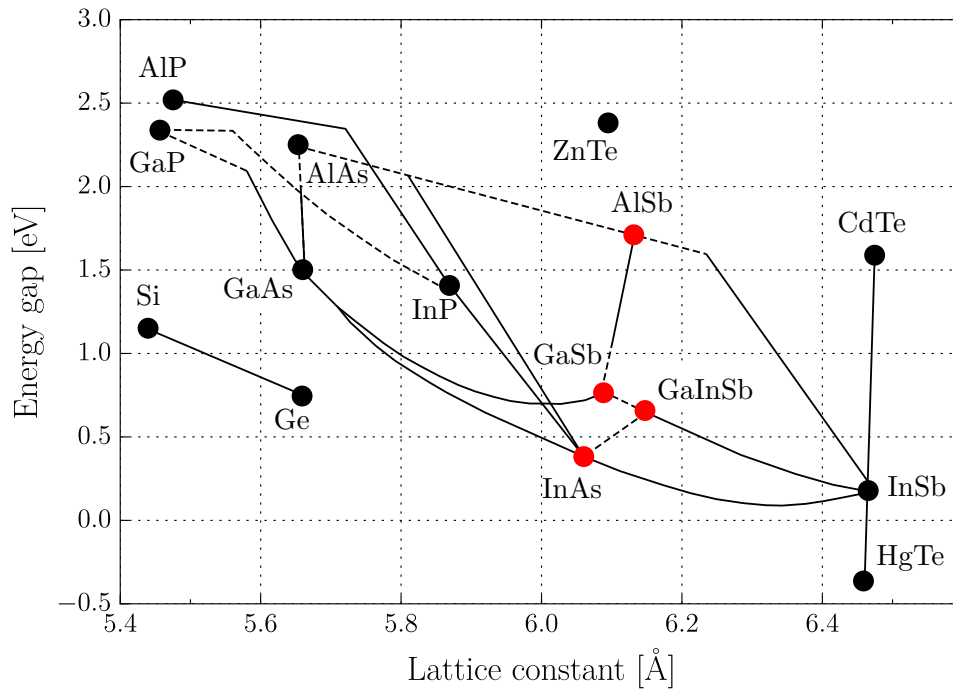


Fig. 4.7: Important group III-V and II-VI (HgTe and CdTe) semiconductor materials (energy gap vs. lattice constant). The solid/dashed lines correspond to direct/indirect energy bandgaps. For interband cascade lasers, material combinations of InAs, Ga(In)Sb and AlSb are typically used.

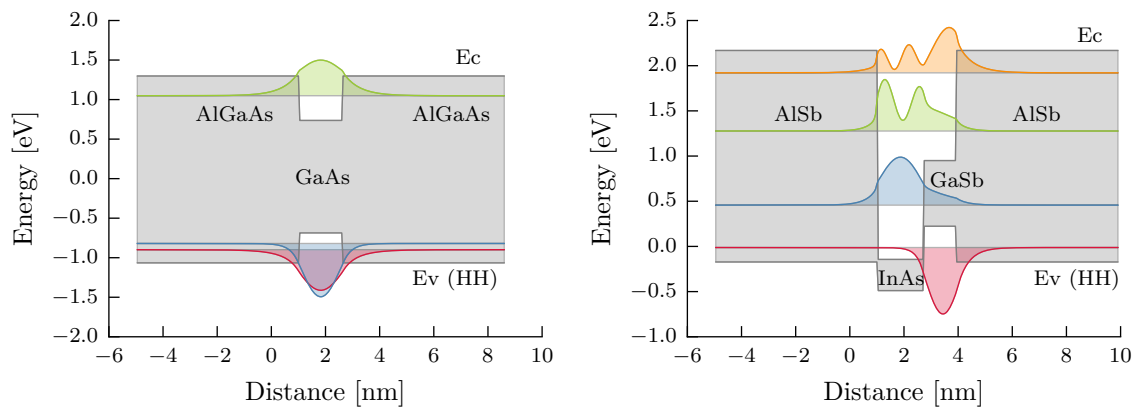


Fig. 4.8: Band alignment in type-I (left) and type-II (right) heterostructures. The plots show the simulated conduction and heavy-hole valence bands together with the squared moduli of the wavefunctions. The type-I QW is made of AlGaAs/GaAs/AlGaAs with layer thicknesses of 1/1.6/1nm. For simulations of the type-II band alignment between InAs/GaSb, a AlSb/InAs/GaSb/AlSb heterostructure with 1/1.7/1.2/1nm is used. States in the conduction band correspond to electrons, while heavy-holes are present in the valence band.

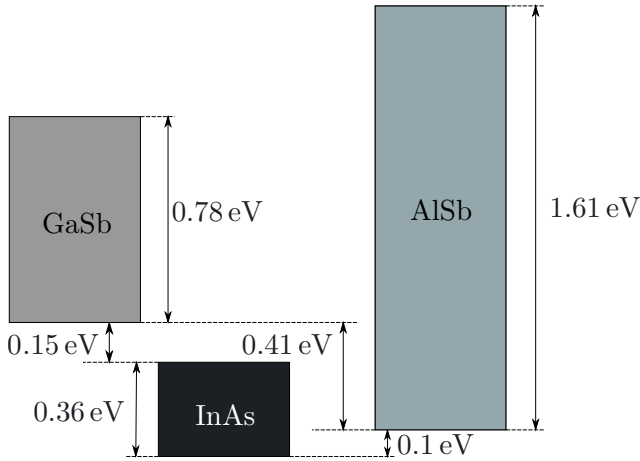


Fig. 4.9: Energy band gaps (shaded areas) and band alignments of the binary semiconductors from the 6.1 Å family. The conduction band maximum of InAs lies energetically below the valence band minimum of GaSb. Such an arrangement is called a type-II band alignment.

	InAs	GaSb	AlSb
Lattice constant [Å]	6.058	6.096	6.136
Bandgap [eV]	0.354 (d)	0.73 (d)	1.615 (id)
Electron effective mass	0.024	0.042	0.14
Hole effective mass	0.025 (LH), 0.37 (HH)	0.4	0.98
Electron mobility [cm ² /(V s)]	3×10^4	5000	200
Hole mobility [cm ² /(V s)]	450	1600	420
Thermal conductivity [W/(K m)]	27	40	70
Thermal expansion coefficient [1/K]	4.52×10^{-6}	6.7×10^{-6}	4×10^{-6}
Substrate	InAs/GaSb	InAs/GaSb	InAs/GaSb

Tab. 4.1: Selected properties of III-V materials, which are important for the fabrication of interband cascade lasers [217, 218]. The acronym (d) stands for direct bandgap and (id) for an indirect bandgap.

cooling rates of the cell temperature. Furthermore, the material is well-studied, non-toxic and cheap, which makes it very popular as a dopant. However, for GaSb and AlSb grown layers Si and Sn are acceptors, instead of donors [216]. Therefore, elements from the group VI, such as Te, are used for n-doping.

GaSb

The binary compound GaSb forms a Zincblende (cubic) crystal structure with a direct bandgap. With increasing temperature, the interatomic spacings increase, which in turn leads to a reduction of the energy bandgap. The relation between bandgap and lattice temperature is modelled with the empirical Varshni equation [219]:

$$E_g(T) = E_g(T = 0\text{K}) - \frac{\alpha T^2}{T + \beta}, \quad (4.9)$$

with the bandgap at zero temperature $E_g(T = 0\text{K}) = 0.812\text{ eV}$ and the fitting parameters

$\alpha = 0.417 \text{ meV K}^{-1}$ and $\beta = 140 \text{ K}$. The temperature dependence is plotted in Fig. 4.10. For GaSb the energy separation of the spin-orbit split off band is $\Delta_{\text{SO}} = 0.76 \text{ eV}$. Commonly, interband cascade lasers are grown on GaSb wafers. However, as-grown undoped GaSb is always p-type regardless of the growth conditions [220]. Typical concentrations of the residual acceptors are in the order of 10^{17} cm^{-3} . State-of-the-art ICLs incorporate some indium content ($\sim 30 - 35\%$) in the GaSb QW for the holes in the active region. As a result a large compressive strain is induced in the $\text{Ga}_{1-x}\text{In}_x\text{Sb}$ layer, which pushes the heavy-hole subband to higher energies [221]. This allows to reach a certain design wavelength without increasing the width of the InAs electron QWs. Moreover, the hole effective mass close to the top of the valence band is also reduced.

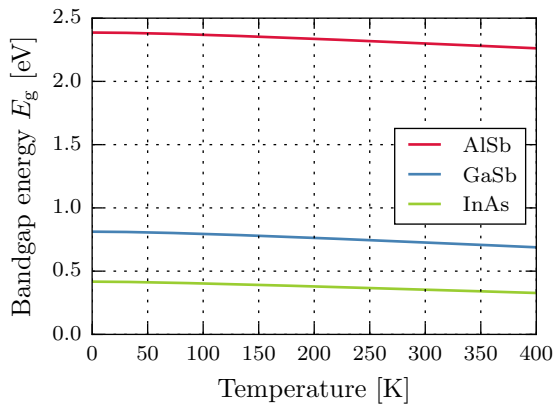


Fig. 4.10: Bandgap energy in dependence of the lattice temperature for materials from the 6.1 Å family.

InAs

A comparison of the lattice constants from Tab. 4.1 shows, that InAs will grow under tensile strain on GaSb. The lattice constant of InAs is slightly smaller than that of GaSb. Layers of InAs are used in ICLs as the QWs for electrons. An important property of InAs is that it does not create a rectifying Schottky contact with a metal. The Fermi level at the interface of Au/InAs is pinned at around 130 meV above the conduction band edge of InAs [222]. As a result, the electron transport is not blocked by Schottky barriers and a good ohmic behavior can be expected. The fitting parameters for InAs in the Varshni equation (4.9) are $\alpha = 0.276 \text{ meV K}^{-1}$ and $\beta = 93 \text{ K}$ and the energy bandgap at zero temperature is $E_g(T = 0 \text{ K}) = 0.417 \text{ eV}$. For wavelengths above $\sim 5 \mu\text{m}$, InAs is used as substrate material instead of GaSb. Si is commonly used as a donor material in InAs layers, which is prohibited in AlSb or GaSb [13].

AlSb

In contrast to InAs, AlSb has a larger lattice constant than GaSb. Consequently, a film of AlSb on a GaSb substrate will grow under compressive strain. By growing alternating layers of InAs and AlSb it is possible to compensate the lattice mismatch. The resulting layer stack then has an averaged lattice constant, which is closely matched to the GaSb

substrate. This allows to grow thick (several μm) heterostructures with a low defect density. The fitting parameters for the Varshni equation (4.9) are $\alpha = 0.42 \text{ meV K}^{-1}$ and $\beta = 140 \text{ K}$ and the energy bandgap at the Γ -point is $E_g(T = 0 \text{ K}) = 2.386 \text{ eV}$. The spin-orbit split off band is $\Delta_{\text{SO}} = 0.39 \text{ eV}$.

4.4 Waveguides

The design of the laser core is driven by optimization of optical transitions and reduction of unwanted non-radiative scattering processes. Hence, the efficient generation of light is the main concern. The waveguide design focuses on issues and tradeoffs concerning optical, electrical and thermal properties of the laser. First of all a good optical overlap of the generated light field with the active core is required, which can be achieved by dielectric and/or metallic waveguides. Preferably, dielectric waveguides are used, since they feature low absorption losses. GaSb is a common material used for optical confinement in ICLs. These waveguide layers sandwich the active region and are often referred to as separate-confinement layers (SCL). Since the refractive index of the substrate, either GaSb ($n_{\text{GaSb}} \approx 3.78$) or InAs ($n_{\text{InAs}} \approx 3.49$), is higher than the averaged refractive index of the active region ($n_{\text{AR}} \approx 3.45$), the mode would leak into the substrate [223]. Therefore, optical cladding layers are grown on top and below of the waveguide layers, which have lower refractive indices and thus guide the light (index-guiding). In ICLs, several micrometer-thick superlattices of InAs/AlSb are commonly used. Alternatively, a quaternary alloy, such as bulk AlGaAsSb, is also possible [224]. The upper cladding layer also spatially separates the active region from the highly n-doped InAs cap layer ($N \sim 10^{19} \text{ cm}^{-3}$) to reduce the free-carrier absorption. In a similar way the lower cladding layer prevents the mode overlap with a highly doped substrate. Fig. 4.11 shows a schematic of the complete material stack. The doping in the claddings is not uniform over all layers. More specifically, the layers close to the active region are lower doped ($N \sim 10^{16} \text{ cm}^{-3}$) and the concentration is gradually increased so that the regions further away typically are doped in the order of 10^{17} cm^{-3} . This is a tradeoff between low optical absorption losses due to free-carrier absorption and a good electrical contact with a low series resistances [13]. The thicknesses for the cladding layers are typically in the range between $1.5 - 3.5 \mu\text{m}$, where the lower cladding is normally thicker to reduce a mode leakage into the substrate. Fig. 4.12 shows the calculated optical mode profile in a typical waveguide of a six-stage ICL emitting at $\lambda = 3.6 \mu\text{m}$.

4.4.1 Plasmon-enhanced waveguide

For ICLs operating at longer wavelengths much thicker cladding layers would be necessary, as the mode extends more into the surrounding materials. However, growing thicker InAs/AlSb superlattices is time consuming and requires careful calibration and monitoring of the system, which makes the process technologically difficult and economically disadvantageous [225]. Furthermore, the poor thermal conductivity with $\kappa \sim 3 \text{ W}/(\text{K m})$ of the superlattice prevents efficient heat dissipation from the laser core. Instead of the

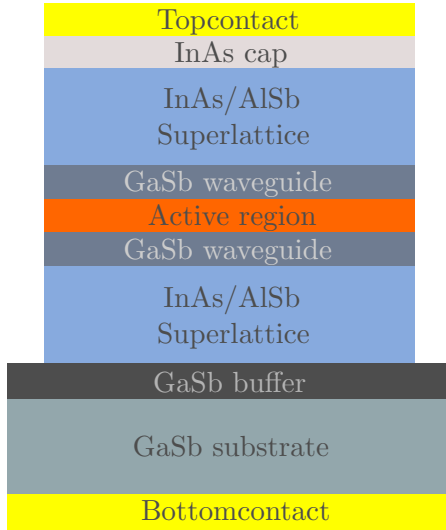


Fig. 4.11: Schematic of a typical waveguide for a GaSb-based ICLs. For a good mode confinement the active laser core is surrounded by GaSb waveguide layers, which are also known as separate-confinement layers. InAs/AlSb superlattices are used as optical cladding layers, which separate the active region from the highly doped InAs cap layer and the substrate. The doping in the cladding layers is gradually increased for larger distance from the active region ($N \sim 10^{16} \rightarrow 10^{17} \text{ cm}^{-3}$).

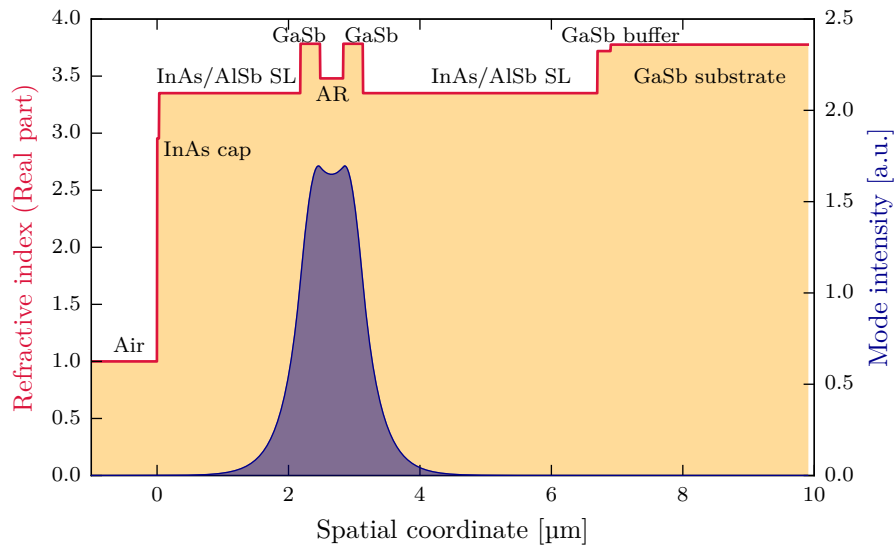


Fig. 4.12: Calculated optical mode intensity (blue) in a typical ICL waveguide at a wavelength of $\lambda = 3.6 \mu\text{m}$. The mode is confined by GaSb waveguide layers (= separate confinement layers) to enhance the overlap with the active region (AR). Top and bottom claddings consist of InAs/AlSb (2.43 nm/2.3 nm) superlattices (SL). The refractive index of the layers is indicated by the red line.

InAs/AlSb cladding, a plasmon-enhanced waveguide can be used [225, 226]. Such waveguide configuration is often called shortly a plasmon waveguide and was first experimentally demonstrated with QCLs [31, 227]. For plasmon-enhanced ICLs the InAs cladding layers are doped heavily ($\sim 5 \times 10^{18} \text{ cm}^{-3}$) and consequently the plasma frequency comes close to the laser frequency. The refractive index is lowered and hence also the mode confinement in the active region is enhanced. Despite the easier growth of the InAs layer also the thermal dissipation capabilities are improved. The material stack of a plasmon-enhanced waveguide is shown in Fig.4.13. Of course, the optical losses in the highly-doped cladding layers are also increased, but with a proper design the total waveguide losses can be reduced. By engineering the penetration depth of the optical mode into the cladding layers via a high refractive index contrast, the losses are kept at a moderate level. The plasmon-enhanced InAs waveguide has been successfully applied to long wavelength ICLs emitting up to $\lambda \sim 10.4 \mu\text{m}$ [226, 228]. In addition, the plasma effect is not restricted to InAs cladding layers. It can also be utilized for GaSb-based ICLs [229]. There, standard n-doped InAs/AlSb top and bottom superlattices are used, but the bottom layer is followed by an $4 \times 10^{18} \text{ cm}^{-3}$ doped $\text{InAs}_{0.91}\text{Sb}_{0.09}$ layer. The purpose of this is the same as in the case of InAs, the reduction of the refractive index via the plasma effect.

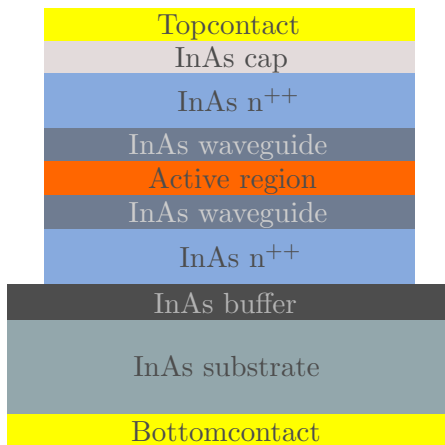


Fig. 4.13: Plasmon-enhanced waveguide using highly doped InAs optical cladding layers. The refractive index in the InAs n^{++} layers (Si doped, e.g. $5 \times 10^{18} \text{ cm}^{-3}$) is lowered, which leads to a better mode confinement. A typical thickness of the plasmon layers is on the order of $1.6 \mu\text{m}$.

4.4.2 Dielectric-metal hybrid cladding

An alternative to the plasmon-enhanced InAs waveguide is the insertion of a thin dielectric layer between semiconductor and metal. The so-called dielectric-metal hybrid cladding has been successfully applied to lasers emitting around $5.3 \mu\text{m}$, which showed comparable or slightly better performance than the plasmon-enhanced waveguide [230]. For the dielectric layer simply the passivation material (Si_3N_4 or SiO_2) can be used. It has low optical absorption losses together with a low refractive index and features a high index contrast to the active region. Hence, the penetration depth of the waveguide mode into the lossy metal is suppressed. Fig. 4.14 shows a schematic of the material stack. The advantage of this approach is that no thick plasmon-enhanced top cladding layer needs to be grown. This fact becomes even more important at longer wavelengths, where the thickness of the cladding layer needs to be increased. Compared to a quantum cascade laser with a dielectric-metal hybrid cladding, the ICL can have, if designed well, lower absorption losses

in the metal. The reason for this lies in the different polarization of the generated light. Since ICLs mainly generate TE-polarized light, the coupling to a lossy surface-plasmon mode is prohibited. In contrast to that, QCLs are TM-polarized and the mode leakage into the metal can be substantially.

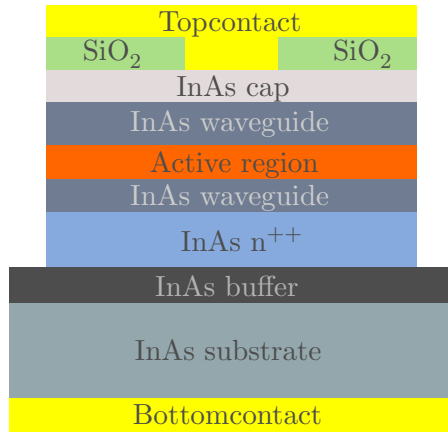


Fig. 4.14: Dielectric-metal hybrid cladding, where the top cladding layer is omitted and the metallization is in direct contact with InAs contact layer (~ 30 nm). The upper waveguide layer (= separate confinement layer) is made thicker to reduce free-carrier absorption losses introduced by the topcontact metallization.

4.5 Substrate-emitting ring interband cascade lasers

Ring quantum cascade lasers with second-order DFB-gratings have been proven to be well suited light sources for spectroscopic and sensing applications. Outcoupling of the light via the surface/substrate, rather than a cleaved facet, enables the generation of collimated emission beams due to the large emitting area. However, the high threshold currents also lead to a higher power consumption, which has several drawbacks for in-field applications. First of all, the power supply has to be designed for the higher demand, which makes the system more costly. Another important point is thermal management, as the lasers typically generate a lot of heat. A good control of the laser's temperature is mandatory to obtain a stabilized and reproducible emission behavior. This demands for an adequate cooling system with e.g. Peltier-elements, appropriate packaging/housing, heat-spreader, fans, water-cooling etc. As a result the overall system becomes heavier and bulkier, which disqualifies it for some mobile applications. Therefore it is very interesting to transfer the concept of ring lasers also to other semiconductor laser technologies with lower power consumption.

So far there have been no attempts to combine ring lasers with the emerging concept of interband cascade lasers. However, this combination is very promising for battery-powered applications, since ICLs have in general lower threshold current densities and voltages compared to QCLs. The light emitted from ring lasers is in general better collimated than from a typical edge emitting device due to the larger aperture. Another point is the absence of cleave facets, whose position strongly influence the performance of DFB devices. In contrast to VCSELs [75, 54], the output power of ring ICLs can be scaled by simply increasing the ring diameter and/or the waveguide width. Furthermore, new device concepts may be possible due to the TE-polarized nature of the emitted light, whereas QCLs are restricted by the intersubband selection rule to TM polarization only.

The following section is based on the publication "Substrate-emitting ring interband cascade lasers" [231].

4.5.1 Basic considerations

The ICL wafers, supplied by *nanoplus* and the *University of Würzburg*, are designed for emission wavelengths roughly between 3.5 and 4.5 μm . The emission wavelengths of the ring QCLs, which have been processed so far, were mostly around 9 μm . Hence, a much shorter grating period of the 2nd-order DFB grating is necessary for the ICL, which also increases the requirements for a reliable, reproducible and robust process technology. In particular, the process parameters for the e-line lithography, which is used for the grating definition, have to be optimized to meet the required precision.

Another issue concerns the TE-polarized nature of the generated light. For a surface emitting ring laser, the DFB-grating consists of etched grooves and unetched bars with metal on top. However, for ICLs the metal could act as a wire grid polarizer for the light emitted towards the surface. Fig. 4.15 illustrates the polarization of the waveguide modes for QCL and ICL. A second-order DFB-grating rotates the propagation direction of the waveguide mode (= direction of the Poynting vector \mathbf{S}) by 90° and vertical light emission is possible. The out-coupled light is p-polarized for the QCL and s-polarized for the ICL. For the latter case, the electric field vector points in the same radial direction as the metallized grating bar. Huge transmission losses and hence strongly suppressed light emission towards the surface can be expected for this configuration. To avoid such possible "polarizing filter effect" with surface emission, a metal-covered grating is used instead, where the etched grooves and the also the surface are coated with metallization. The basic idea is to diffract the generated light towards the substrate. For this scenario the absorption losses in the GaSb substrate have to be low enough. The refractive index of the substrate (doped $5 \times 10^{17} \text{ cm}^{-3}$) at the wavelength of $\lambda \approx 3.7 \mu\text{m}$ is $n_{\text{GaSb}} = 3.775 + j6 \times 10^{-4}$ (using the parameters from Tab. 4.2). This translates to an absorption loss of $\alpha = 4\pi \text{Im}\{n_{\text{GaSb}}\}/\lambda \approx 21 \text{ cm}^{-1}$. A more intuitive interpretation for this value can be gained if the propagation through the GaSb substrate is considered. The transmission is proportional to $\exp(-\alpha L)$, where L denotes the propagation length. A transmission value of 30% is calculated for the $L \sim 550 \mu\text{m}$ thick GaSb substrate. However, Fresnel reflections at the GaSb/air interface as well as diffraction losses have been neglected in this first estimation. Under the assumption of a normally incident beam at the interface, the reflectivity is given by

$$R = \left(\frac{n_{\text{sub}} - n_{\text{air}}}{n_{\text{sub}} + n_{\text{air}}} \right)^2, \quad (4.10)$$

with the refractive index of the substrate $n_{\text{sub}} = n_{\text{GaSb}}$ and of air $n_{\text{air}} = 1$. This gives a reflectivity value of $R \approx 34\%$, which is only caused by the mismatch of the refractive indices. The transmission through a parallel-sided plate including multiple reflections inside the sample then reads

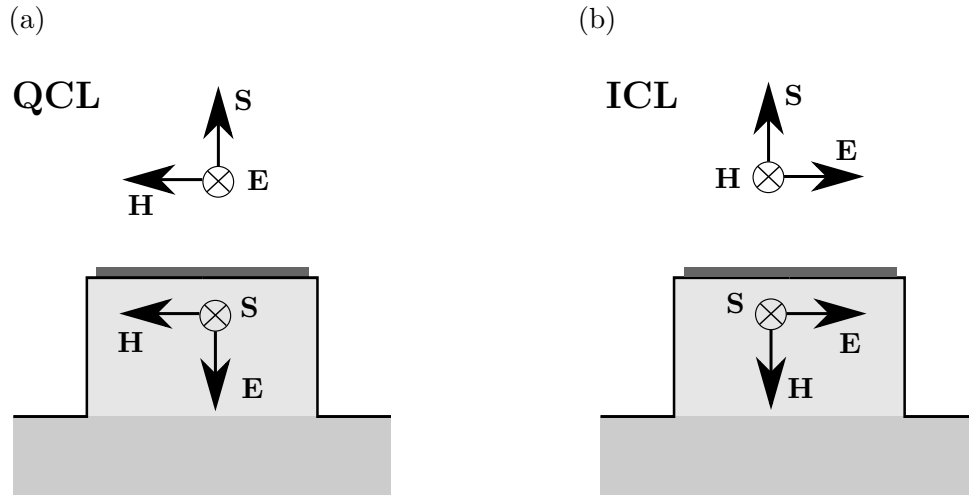


Fig. 4.15: Comparison of the polarization of the generated light in QCLs (a) and ICLs (b). For a QCL, the waveguide mode is TM-polarized, which means that there is no component of the magnetic field \mathbf{H} in propagation direction. Here, the propagation direction coincides with the direction of the Poynting vector \mathbf{S} . A second-order DFB-grating on the surface, illustrated by the dark shaded area on top of the waveguide, out-couples the light in vertical direction. Hence it rotates the Poynting vector by 90° and the free-space propagating wave is in a p-polarized state. On the other hand, the waveguide mode in the ICL is dominantly TE-polarized with the electric field perpendicular to the propagation direction. The waveguide mode is out-coupled by a second-order DFB-grating and the free-space propagating wave is in a s-polarized state.

$$T = \frac{(1 - R_1)(1 - R_2)e^{-\alpha L}}{1 - R_1 R_2 e^{-2\alpha L}}, \quad (4.11)$$

where R_1 and R_2 are the reflectivities of the front and the back surfaces respectively. In absence of absorption in the substrate ($\alpha = 0$), a maximum transmission of $T \approx 50\%$ is obtained. Experimentally determined absorption coefficients of tellurium doped GaSb wafers suggest that free carrier absorption by free electrons (FCA) is only one mechanism out of several others [220]. For short wavelengths, inter-valley conduction band absorption (CBV) has been identified as the dominant absorption mechanism. Hence, the absorption losses in the substrate of the ring ICL device may still be underestimated, as only FCA is considered in the calculation of the refractive index. However, designing the laser for substrate emission has some distinct advantages compared to surface emitting devices. First of all, epi-side down bonding is possible, which helps significantly to remove the heat generated in the active region of the laser. Higher operating temperatures in continuous-wave mode can be expected. Second, the substrate-side can still be used to fabricate/integrate other functional elements like e.g. polarizer, lenses, fluidic channels and many others. Compact optical systems, as well as combinations with mechatronic systems, are possible. Moreover, chemical analytes can be used in direct contact with the laser without altering its performance, which enables a higher degree of freedom in the design of functional devices.

4.5.2 Grating design

For light emission through the substrate, a metallized second-order DFB-grating is fabricated into the upper cladding layers of the ICL. An illustration of the grating is shown in Fig. 4.16. The important design parameters are the grating duty-cycle σ as well as the etch depth t_g , as indicated in Fig. 4.16(a). A Ti/Au metallization covers the entire surface of the laser (also the isolated sidewalls) and hence diffracts the light generated in the active region towards the substrate. In the following the design process for the DFB-grating is described in more detail.

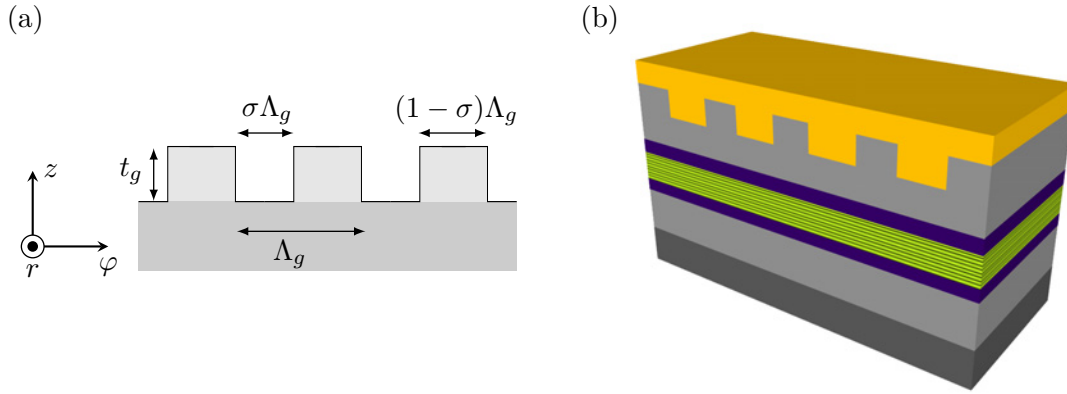


Fig. 4.16: (a) Illustration of the metal-covered DFB-grating, where the grating duty-cycle σ defines the lateral size of the etched grooves ($\sigma\Lambda_g$) and corresponds to the amount of metallization per grating period Λ_g . The important design parameters are the grating duty-cycle σ and the etch depth t_g . Depending on these parameters, the coupling strength as well as the losses can be controlled. (b) The DFB-grating is etched into the surface layers and subsequently coated with Ti/Au. In this configuration the light is only emitted towards the substrate.

Once the target wavelength λ for the emitted light is fixed and the modal effective refractive index n_{eff} is estimated, the grating period Λ_g can be calculated using the Bragg-condition (2.82)

$$\Lambda_g = \frac{\lambda}{n_{\text{eff}}} \frac{m}{2}, \quad (4.12)$$

where m denotes the order of the grating ($m = 1, 2, 3, \dots$). For a target wavelength of $\lambda = 3.77 \mu\text{m}$ and an estimated effective refractive index of $n_{\text{eff}} = 3.42$ the second-order DFB-grating ($m = 2$) requires a grating period of $\Lambda_g = 1.103 \mu\text{m}$. The modal effective refractive index n_{eff} can be obtained by the following procedure: Fabricate a standard Fabry-Perot ridge laser without a grating and measure the spectrum. A wavelength around the emission maximum should be considered as target wavelength for the subsequent grating design. In the next step a laser with a DFB-grating is fabricated. Therefore, a good guess for the effective refractive index is a reliable starting point. For ICLs it is typically in the range of $n_{\text{eff}} \sim 3.4 - 3.5$. A spectral measurement of the processed device typically shows an emission at a different wavelength. Hence, the guessed effective refractive index

does not exactly match the one of the real device. However, a back-calculation with the known fabricated grating period gives the modal effective refractive index $n_{\text{eff}} = \lambda/\Lambda_g$ of the real device (assuming a second-order grating with $m = 2$). Alternatively, the effective refractive index can also be estimated via simulations of the waveguide.

Material parameters

The complex refractive indices for InAs, AlSb and GaSb are calculated using the Lorentz-Drude model explained in section 2.3.2. Tab. 4.2 summarizes the model parameters for calculating the refractive indices. Fig. 4.17(a) shows the calculated permittivity of InAs in dependence of the input parameters i.e. the wavelength λ and the doping density N . Below the plasma wavelength (= above the plasma frequency) the free carriers are too slow to follow the oscillations of the incident wave and therefore the wave can penetrate with low losses through the material. The real part of the permittivity is negative, which indicates a metal-like behavior. Above this edge (at longer wavelengths), losses are increasing due to free carrier absorption (FCA). Fig. 4.17(b) shows the refractive index and corresponding FCA for InAs, (c) AlSb and (d) GaSb.

Material	ϵ_∞	m^* [kg]	μ_{min} [cm ² /Vs]	μ_{max} [cm ² /Vs]	N_{ref} [cm ⁻³]	α
InAs	12.25	$0.066m_0$	0	30000	8×10^{17}	0.75
AlSb	10.24	$0.12m_0$	30	200	4×10^{17}	3.25
GaSb	14.4	$0.041m_0$	1050	5650	2.8×10^{17}	1.05

Tab. 4.2: Material parameters used for the simulations: InAs [223], AlSb [232, 233, 234] and GaSb [102, 235]).

The complex refractive indices are calculated for a wavelength of $\lambda = 3.73 \mu\text{m}$ and the layers given by the ICL3 heterostructure (growthsheet in appendix A.3.2). These values together with the layer thicknesses are summarized in Tab. 4.3.

Simulations

The coupling coefficient, as well as the induced losses are calculated using a modified version of a MATLAB program originally written by N. Finger [86]. The program searches for Floquet-Bloch solutions of an infinite-length grating-waveguide problem and calculates the grating parameters within the framework of the coupled-mode theory [71]. The code has been modified within this thesis for the calculation of TE-polarized ICL structures. For the initial grating design, different combinations of grating duty-cycle and etch depth are investigated. From the simulations, a grating duty-cycle of around 50% seems to be a reasonable starting point. For the actual processed devices, a duty-cycle of $\sigma = 59\%$ is measured using a scanning electron microscope. This value is also used for the simulations discussed in the following. In a next step the right grating etch depth needs to be determined. Fig. 4.18 shows the dependence of various grating parameters on the grating etch depth. First of all the surface losses are zero, because the grating is fully covered

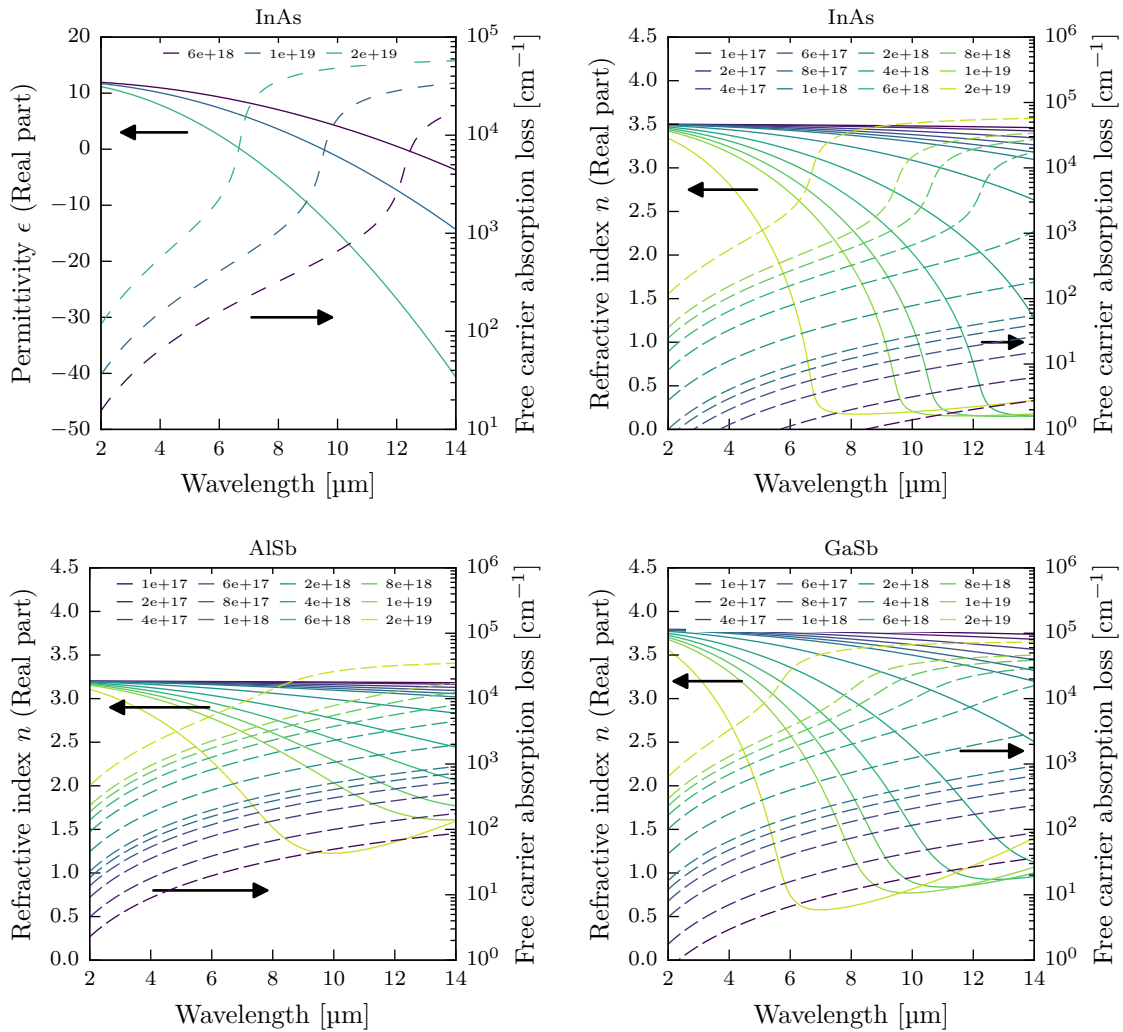


Fig. 4.17: (a) Permittivity of InAs in dependence of the wavelength λ and doping concentration. The solid lines correspond to the real part of the permittivity ϵ and the dashed lines show the imaginary part rewritten as a free carrier absorption coefficient $\alpha = 4\pi \text{Im}\{n\}/\lambda$. (b) Refractive index and FCA of InAs, (c) AlSb and (d) GaSb. The solid lines correspond to the real part of the complex refractive index $n \approx \sqrt{\epsilon}$.

Material	Thickness [nm]	Doping [cm^{-3}]	Refractive index
Air	1000		1.0000 + j0.0
Gold	500		1.0772 + j27.4654
InAs	25	2×10^{19}	2.9104 + j0.0139
InAs/AlSb SL	2120	8×10^{17} to 2×10^{17}	$3.3502 + j2.2 \times 10^{-5}$
GaSb	200	3×10^{17}	$3.7827 + j3.2 \times 10^{-4}$
Active region	350		3.4800 + j0.0
GaSb	200	3×10^{17}	$3.7827 + j3.2 \times 10^{-4}$
InAs/AlSb SL	3570	2×10^{17} to 8×10^{17}	$3.3502 + j2.2 \times 10^{-5}$
GaSb	200	2×10^{18}	3.7137 + j0.0045
GaSb	3000	5×10^{17}	$3.7746 + j6.5 \times 10^{-4}$

Tab. 4.3: Layer sequence for the simulated DFB grating design of the ICL3 material and corresponding complex refractive indices at a wavelength of $\lambda = 3.73 \mu\text{m}$. The doping in the superlattice (SL) is linearly increased from 8×10^{17} to 2×10^{17} in the upper cladding and vice versa in the lower cladding. Note that COMSOL uses a different sign convention, where the sign of the imaginary part of the refractive index is inverted.

with gold. The substrate radiation losses increase with increasing etch depth and show a local maximum around $t_g = 1.1 \mu\text{m}$. The out-coupling efficiency reaches at this point values of $\eta_{\text{sub}} = \alpha_{\text{sub}}/\alpha_{\text{total}} \approx 90\%$. Furthermore, the coupling coefficient $|\kappa|$ is estimated to be around 8 cm^{-1} , which should be sufficient to achieve single-mode operation for this ring geometry.

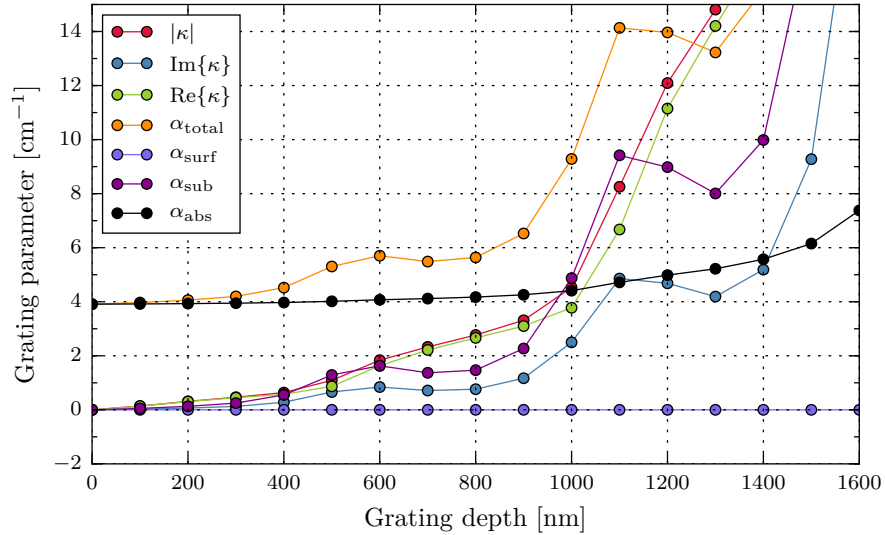


Fig. 4.18: Simulations of the second-order DFB grating for various etch depths at a fixed grating duty-cycle of $\sigma = 59\%$. For an etch depth of $\sim 1.1 \mu\text{m}$ the coupling coefficient κ should be high enough to achieve a good mode discrimination together with moderate absorption losses α_{abs} .

Simulations of the second-order DFB grating for an etch depth of $1.1 \mu\text{m}$ and a duty-cycle of 59% are shown in Fig. 4.19. For this parameter set (t_g, σ) a complex coupling coefficient of

$\kappa = 4.9 + j6.7 \text{ cm}^{-1}$ is calculated. For the ring waveguide with an outer diameter of $400 \mu\text{m}$ and a waveguide width of $10 \mu\text{m}$ ($L_{\text{ring}} = 2\pi \times 195 \mu\text{m} = 1.23 \text{ mm}$) a coupling strength of $|\kappa|L_{\text{ring}} \sim 1$ is found. Compared to other fabricated interband cascade lasers [236, 237], this DFB grating is moderately coupled. The substrate emission loss $\alpha_{\text{sub}} = 9.4 \text{ cm}^{-1}$ reaches a high value, while the free-carrier absorption loss $\alpha_{\text{abs}} = 4.72 \text{ cm}^{-1}$ remains moderate. The latter one is caused by the overlap of the waveguide mode with lossy materials (non-zero imaginary part of the refractive index). The overlap of the mode with the active region is quantified with the confinement factor $\Gamma = 30\%$, which is a typical value for ICLs [13].

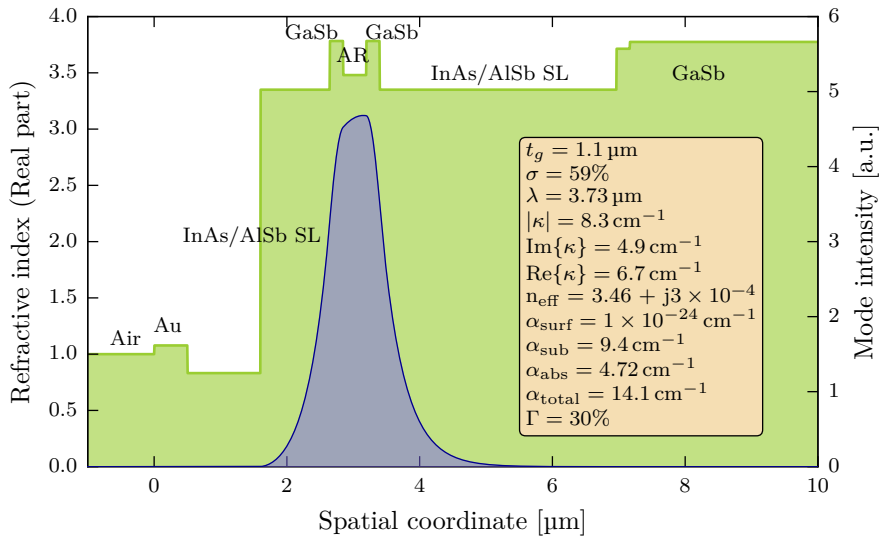


Fig. 4.19: Simulation of the waveguide/grating problem for a grating etch depth of $1.1 \mu\text{m}$ and a duty-cycle of 59% . The green curve shows the real part of the complex refractive index and the blue curve the mode intensity. The coupling strength is calculated to be $|\kappa|L_{\text{ring}} \sim 1$, with the complex coupling coefficient κ and the length of the ring waveguide $L_{\text{ring}} = 1.23 \text{ mm}$. Since the surface is covered with metal, the surface emission loss $\alpha_{\text{surf}} \approx 0 \text{ cm}^{-1}$. However, a high value of α_{sub} is obtained for substrate emission, while the absorption losses α_{abs} are kept low.

For the DFB-grating an eigenfrequency calculation has been carried out using COMSOL. Fig. 4.20(a) shows the simulation region, which consists of two grating periods with a grating duty-cycle of 59% and an etch depth of $1.1 \mu\text{m}$. The grating period of the second-order DFB grating is $1.1 \mu\text{m}$. Periodic boundary conditions are used at the left and right boundaries to calculate the eigenfrequencies of the infinite-length DFB grating. The first mode in Fig. 4.20(b) has an eigenfrequency of $7.852 \times 10^{13} + j2.4 \times 10^9 \text{ Hz}$ and features a maximum of the electric field (E_z -component) in the center of the etched groove. On the other hand, the second solution has a field minimum in the center and the eigenfrequency reads $7.849 \times 10^{13} + j1.07 \times 10^9 \text{ Hz}$.

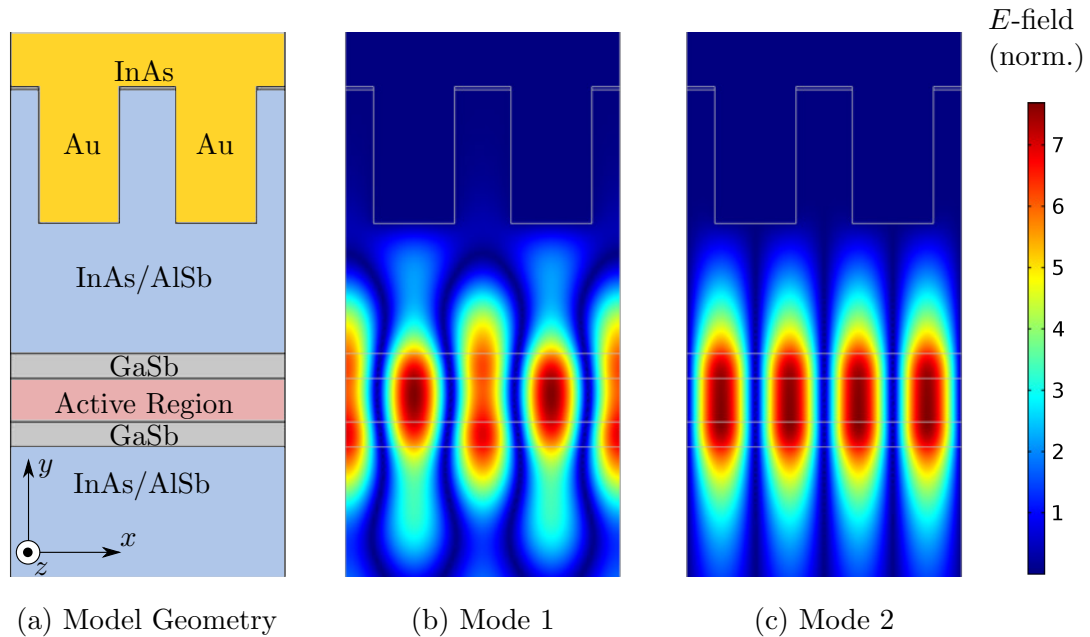


Fig. 4.20: Simulation of the infinite-length DFB grating for an etch depth of $1.1\ \mu\text{m}$ and a duty-cycle of 59%. (a) Model geometry and assigned materials for two grating periods. At the boundaries on the left and right hand side periodic boundary conditions are set. (b) Simulated mode profile (normalized electric field E) corresponding to the first waveguide mode. (c) The other waveguide mode has a minimum of the electric field in the center of the etched grating groove.

4.5.3 Fabrication

The ring-ICLs are fabricated from the ICL3 wafer, which is supplied by *nanoplus* and the *University of Würzburg*. The structure itself is based on a 6-stage active region design and grown by MBE on a single-side polished $2 \times 10^{18}\ \text{cm}^{-3}$ n-doped GaSb (100) substrate. A description of the heterostructure can be found in the appendix A.3.2. The processing of the ring ICLs is similar to the fabrication steps used for ring QCLs, with slight modifications. A step-by-step recipe for the processing can be found in appendix A.4.2.

First, a Si_xN_y hardmask is deposited with PECVD and structured into ring shaped waveguides (double-channel geometry) by optical lithography. The rings have an outer diameter of $400\ \mu\text{m}$ and a waveguide width of $10\ \mu\text{m}$. The pattern is transferred to the hardmask via a RIE etching-step in an O_2/CHF_3 chemistry. After removal of the photoresist by an O_2 plasma oxidizer and cleaning in NEP/Isopropanol the sample is dry-etched with SiCl_4/Ar . To prevent current spreading, the lasers are etched through the active region and the process is stopped when reaching the lower cladding layers. The RIE process leads to vertical sidewalls due to the mainly physical etching component caused by Ar ions. However, it allows a precise definition of the waveguide size. As a drawback of the anisotropic etching recipe, additional losses due to surface-damage at the sidewalls are introduced (surface roughness). However, a subsequent wet chemical etch can be used to smooth the surface. After removal of the Si_xN_y hardmask with SF_6 a new Si_xN_y layer is deposited by PECVD again.

The second-order DFB grating is then written by e-beam lithography with a grating period of $\Lambda = 1.104 \mu\text{m}$ and a grating duty-cycle of 30% over the full width of the waveguide. For "standard" ring lasers [142, 132] the grating has a width of $\sim 6 \mu\text{m}$ ($10 \mu\text{m}$ waveguide width minus a border of $2 \mu\text{m}$ at each side). There, the metal-covered border regions are mandatory as they serve as the etch mask for the subsequent waveguide etch. Processing a grating that extends over the full waveguide width would require a more sophisticated approach. The fundamental whispering gallery mode in the ring waveguide is located closer to the outer sidewall, which is confirmed by simulations with COMSOL. In the standard grating configuration, as shown in 4.21(a), a poor overlap with the waveguide mode is observed, which reduces the coupling. To enhance the overlap with the surface grating the mode should also extend into the border regions, as indicated in 4.21(b).

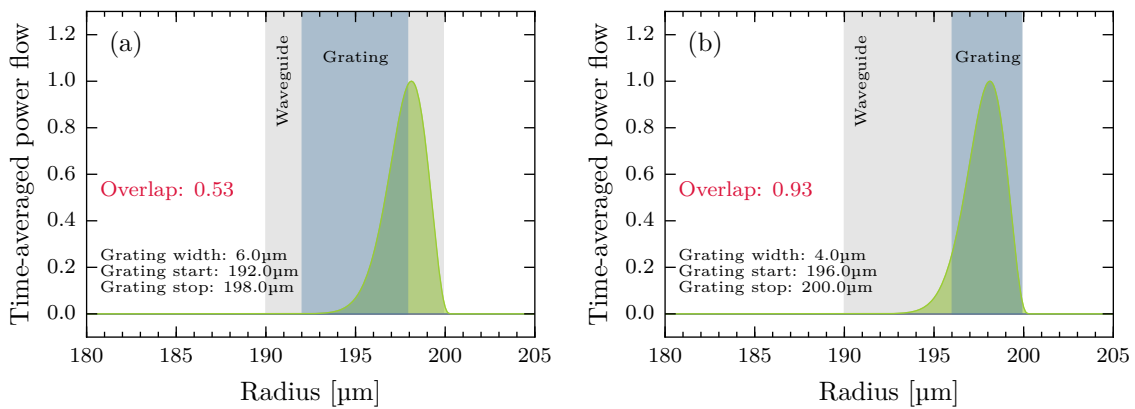


Fig. 4.21: Overlap between the fundamental waveguide mode (normalized time-averaged power flow, green curve) and the grating in the ring ICL. The grey-shaded area marks the $10 \mu\text{m}$ wide ring waveguide and the blue-shaded area highlights the position of the grating on top of the waveguide. (a) For a standard grating ($6 \mu\text{m}$ width) the overlap between the whispering gallery mode and the grating region is only 53%, assuming margins of $2 \mu\text{m}$ on both sides. (b) Even if the grating width is reduced to only $4 \mu\text{m}$, a better overlap (93%) can still be obtained by shifting the grating towards the outer sidewall.

Therefore, a new process has been developed for the metal-covered DFB-grating extending over the full width of the ring lasers. But as usual this results in a trade-off: the advantage of a self-aligned waveguide etch is exchanged with the possibility of fabricating arbitrary shaped gratings. As a consequence more effort was invested into optimizing the alignment between the etched waveguide and the DFB-grating, written by e-beam lithography. More specifically, it is the alignment between optical lithography mask and the e-beam lithography. The optical mask is written in-house by a Heidelberg DWL 66 fs laser lithography system, which has a specified positioning tolerance of around 200 nm . However, this value is not reached in a real exposure, because of variations in focus, photoresist thickness and uneven samples. Hence, the exact position of the lasers on the chip can vary randomly from device to device. Furthermore, also the Raith e-beam machine (e-Line) drifts over time (at a specified rate of around 300 nm/h) and causes deviations from the designed mask. So even if sample and e-Line mask are perfectly aligned with the 3-point and write-field alignment procedures (provided by the software) before the start of the exposure, the exposed structure can be misaligned. One possibility to overcome the positioning in-

accuracy of the laserwriter could be to scan the optical mask once with the e-Line and save the real positions of the devices. However, this is not possible due to the large size of the optical mask (soda lime glass with $3'' \times 3''$), which cannot be easily introduced into the vacuum chamber of the e-Line system. Instead, an automated dynamic alignment procedure is used prior to the exposure of every ring structure, with the following steps:

1. Drive to the center position of the corresponding marker (e-Line mask coordinates)
2. Take an image of the marker (optional)
3. Perform a linescan in x- and y-direction
4. Start an automatic writefield alignment, which only shifts the coordinate system (no rotation correction!)
5. Take an image of the marker (optional)
6. Drive to the center of the ring
7. Expose grating structure

For the overall alignment of the sample coordinate system (X, Y, Z) to the mask coordinate system (U, V, W), a 3-point alignment is performed. Therefore 3 arbitrary markers are used from the sample, where every ring has its own marker. Afterwards, the beam coordinate system is aligned with the mask coordinate system via a writefield alignment. At this stage all 3 markers are very well aligned, but all other markers (from the other rings) are most probably slightly misaligned. For these markers an automatic-alignment is mandatory to write the DFB-grating with high precision. In Fig. 4.22 images of a marker before and after the auto-alignment procedure are shown. The automatic algorithm detects the edges of the marker bars in x and y direction and shifts the coordinate system to match the center of the marker. Although the center of the marker was detected correctly by the algorithm, a shift of around 250 nm in x- and y-direction still remained. The origin for this offset is unclear, but it can be easily corrected by an additional (automatic) shift of the coordinate system. The shift is already corrected in Fig. 4.22(b). With this procedure a reproducible good alignment for every exposure of a DFB-grating on the ring waveguides is possible. The drift of the e-Line is then negligible, since the writing time for a single ring is on the order of 10 min (depending on the grating geometry) and before the exposure of the next ring the writefield is again automatically adjusted.

After the grating has been exposed, the pattern is transferred into the underlying Si_xN_y hardmask via an anisotropic dry-etch process (RIE) with O_2/CHF_3 . The grating grooves are then etched 1.1 μm deep into the upper cladding layers with the same SiCl_4/Ar RIE process used for the waveguide fabrication. Due to variations in the development of the e-Line photoresist and also the etch process, the realized grating duty-cycle is about 15 to 30% larger than the size specified on the mask. However, this increase is already taken into account during the mask design process. The hardmask is removed and a 450 nm thick Si_xN_y passivation layer is deposited to protect the laser from short-circuiting. For electrical connection, the isolation layer is selectively removed on top with window opening widths of $\sim 9.4 \mu\text{m}$. The small overhangs of Si_xN_y ensure a proper isolation of the sidewalls.

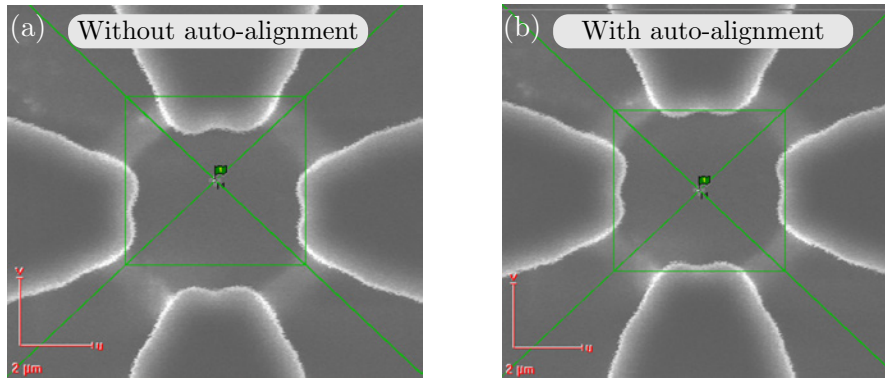


Fig. 4.22: SEM images of an alignment marker (a) without automatic alignment and (b) after execution of the procedure for the e-beam lithography. With the automatic writefield alignment, the coordinate system, indicated by the green cross, is perfectly centered for each ring.

Afterwards the whole laser, including the grating grooves, is covered with 10 nm/500 nm thick Ti/Au layers. Since many ring lasers are processed on a single chip, all devices are now electrical connected, which is not desired. Thus, the metallization has to be selectively removed between the devices. This is done with a wet chemical etch based on potassium iodide ($\text{KI}:\text{I}_2:\text{H}_2\text{O}$). Fig. 4.23 shows the substrate-emitting ring ICLs at different stages of the fabrication. The final chip is mounted epitaxial-side up with silver paste on a copper plate. To allow light emission through the substrate of the laser, the copper plate has a 8 mm hole. It has to be noted that the GaSb substrate has been neither thinned nor polished. Measurements with atomic force microscopy (AFM) on the substrate delivered a root mean squared roughness of ~ 133 nm for a scan field of $30 \mu\text{m} \times 30 \mu\text{m}$.

4.5.4 Results

The ring ICLs are characterized on a self-made laser stage with active temperature stabilization via a 2-stage Peltier element including water-cooling. The emitted light is collected from the substrate-side with a 1.5" focal-length ZnSe lens and focused on a wide-range deuterated triglycine sulfate (DTGS) detector of a Burkert Vertex 70v Fourier transform infrared (FTIR) spectrometer. The sample is mounted on a copper submount, which has a hole in the center that enables substrate emission.

For the characterization, the devices are operated in pulsed mode (5 kHz/100 ns). Fig. 4.24 shows the measured LIV characteristics for different heatsink temperatures. A typical threshold current density of $J_{\text{th}} = 0.75 \text{ kA/cm}^2$ ($I_{\text{th}} = 92 \text{ mA}$) is measured for ring lasers with 400 μm diameter and a waveguide width of 10 μm (20 °C heatsink temperature).

Encouraged by the low threshold current densities of the devices, the operation at higher pulse duty-cycles was investigated. However, cw operation of the ring ICLs has not been achieved. This is simply due to the heat dissipation limitations of the mounting. The hole in the copper submount is necessary to enable substrate emission, but it also prevents heat extraction from the laser to the heatsink in vertical direction. Thus, the generated heat has to flow a relatively long distance in the horizontal direction before it reaches the cool copper

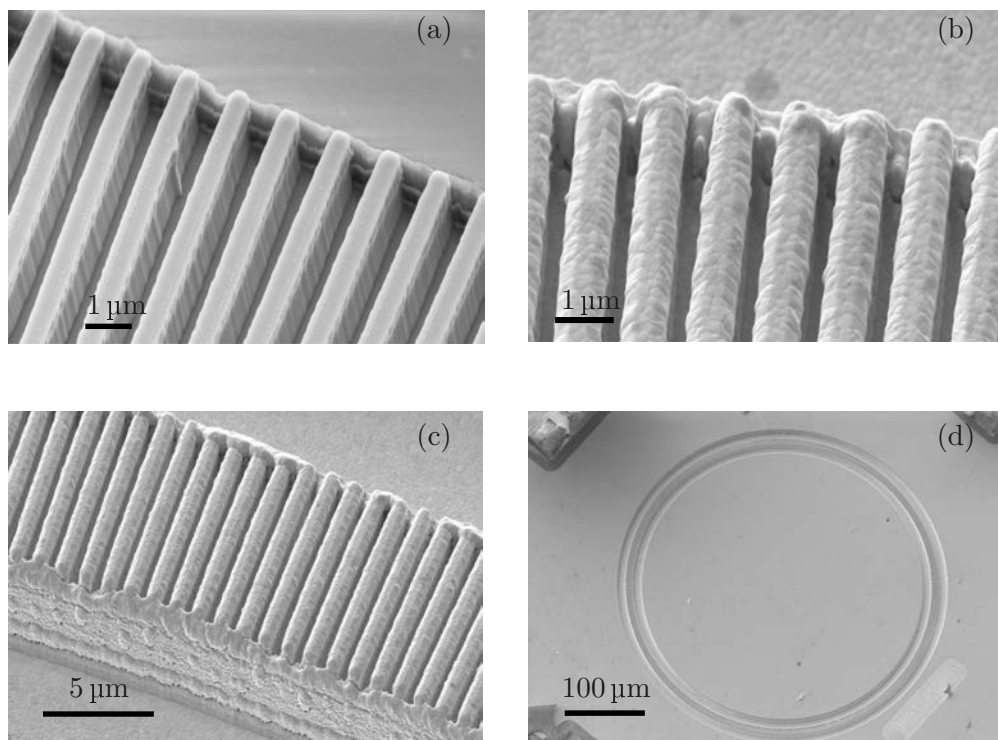


Fig. 4.23: SEM images of a fabricated substrate-emitting ring-ICL. (a) The anisotropically etched 2nd-order DFB grating covers almost the entire width of the ring waveguide and the grating is etched to a depth of 1.1 μm. (b) Subsequently the laser is covered with a 10 nm/500 nm Ti/Au metallization. (c) The sputtered metallization covers the steep sidewalls, which is necessary for a good electrical connection. Furthermore, the metal also serves as a heatspreader. (d) Final ring ICL device with an outer diameter of 400 μm and a waveguide width of 10 μm.

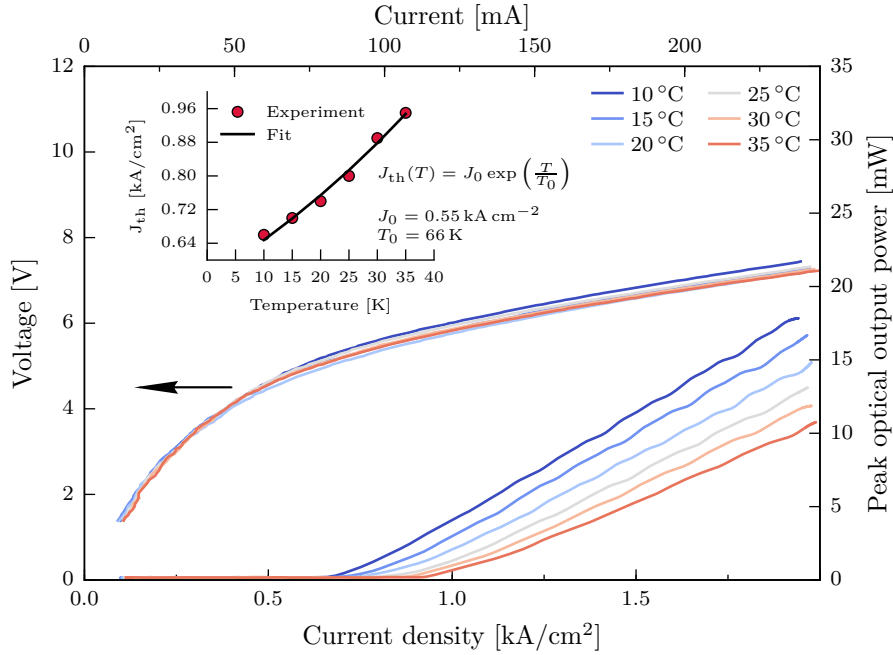


Fig. 4.24: Light-current-voltage characteristics of the ring ICL at different heatsink temperature. The device has an outer diameter of $400\ \mu\text{m}$ and a waveguide width of $10\ \mu\text{m}$. It is operated in pulsed mode with $5\ \text{kHz}/100\ \text{ns}$ and the light is diffracted with a second-order DFB grating towards the GaSb substrate. The inset shows the measured threshold current densities together with an exponential fit [231].

plate. As a result, heat is accumulated in the device, which leads to a temperature rise and a subsequent shutdown of the laser (thermal roll-over). Continuous-wave operation should be feasible with an epi-side down mounting of the devices, which reduces the distance between heatsource and heatsink. By sweeping the submount temperature from $10\ ^\circ\text{C}$ to $35\ ^\circ\text{C}$ and fitting the measured threshold current density to the empirical law:

$$J_{\text{th}}(T) = J_0 \exp\left(\frac{T}{T_0}\right), \quad (4.13)$$

a characteristic temperature of $T_0 = 66\ \text{K}$ together with $J_0 = 0.55\ \text{kA}/\text{cm}^2$ is extracted. In general, a small value of T_0 indicates a strong temperature dependence of the current, since $dJ_{\text{th}}/dT = J_{\text{th}}/T_0$ is inversely proportional to T_0 . Similar values of around $45 - 60\ \text{K}$ are obtained with other ICL devices [13]. However, in direct comparison to QCLs, where values in the range of around $100 - 400\ \text{K}$ [238, 185, 113] are reported, the T_0 value for ICLs appear rather low. Besides the different physics of interband processes, there is also no comparable overgrowth technology available for GaSb-based devices [191, 239]. High-power QCLs mostly rely on InP-based buried-heterostructures [105, 240]. Another interesting quantity is the voltage efficiency of the device, which is given by

$$\eta_{\text{voltage}} = \frac{N\hbar\omega}{V_{\text{th}}}, \quad (4.14)$$

where N is the number of stages, $\hbar\omega$ the energy of the emitted photons in [eV] and V_{th} the measured lasing threshold voltage. For the 6-stage ring device, a threshold voltage of 5.2 V is measured at an emission wavelength of $\lambda \sim 3.77 \mu\text{m}$. This corresponds to a voltage efficiency of $\eta_{\text{voltage}} \approx 38 \%$. In comparison to other ICL devices, where values in the range of 70 – 90% are obtained [241, 226, 228], the threshold voltage seems to be higher than necessary. The theoretical lower limit for the threshold voltage can be estimated by

$$V_{\text{th,min}} \approx N(\hbar\omega + 2k_{\text{B}}T) + \rho_{\text{s}}J_{\text{th}}, \quad (4.15)$$

where T is the temperature, ρ_{s} the series resistivity and J_{th} the threshold current density. For a differential series resistivity of $0.2 \text{ m}\Omega \text{ cm}^2$ and a threshold current density of 0.75 kA cm^{-2} , the minimum threshold voltage is only $\sim 2.4 \text{ V}$. Compared to this value, the ring ICL device shows a rather high excess voltage, which may come from a voltage drop at the electrical contacts. In general, the threshold voltage can be lowered by decreasing the number of cascades and reducing the differential series resistance.

At the submount temperature of $20 \text{ }^\circ\text{C}$, a differential slope efficiency of $dP/dI = 104 \text{ mW/A}$ is extracted. In comparison, measurements of a single-stage vertical-cavity surface-emitting laser (VCSEL) with a buried tunnel junction [54], where the aperture is $12 \mu\text{m}$ wide, revealed a maximum slope efficiency of 26 mW/A at a temperature of $-40 \text{ }^\circ\text{C}$. Furthermore, a 15-stages interband cascade VCSEL with $60 \mu\text{m}$ mesa size and $40 \mu\text{m}$ aperture diameter reached $\sim 52 \text{ mW/A}$ at $20 \text{ }^\circ\text{C}$ [75]. The ring ICL device shows the highest slope efficiency of surface-emitting interband cascade lasers. However, in comparison to facet-emitting ridge devices [206] these values are still considerably low, suggesting that there is room for improvements. The external differential quantum efficiency

$$\eta_{\text{ext}} = \frac{dI}{dP} \frac{q\lambda}{hc_0}, \quad (4.16)$$

is calculated to $\eta_{\text{ext}} \approx 31\%$ for an emission wavelength of $\lambda = 3.7 \mu\text{m}$. For spectral characterization the ring laser is pulsed with $80 \text{ kHz}/30 \text{ ns}$ and the FTIR is operated in rapid-scan mode. Fig. 4.25 shows the collected spectra at a drive current of $I = 130 \text{ mA}$ and different heatsink temperatures. For temperatures up to $20 \text{ }^\circ\text{C}$ an emission peak at $\lambda = 3.73 \mu\text{m}$ is observed, whereas another peak at $3.77 \mu\text{m}$ appears at higher temperatures. With the known fabricated grating period of $\Lambda_{\text{g}} = 1.104 \mu\text{m}$, the effective index

$$n_{\text{eff}} = \frac{\lambda}{\Lambda_{\text{g}}}, \quad (4.17)$$

can be calculated to be $n_{\text{eff}} = 3.38$ for the emission at $3.73 \mu\text{m}$. The peak at the longer wavelength of $3.77 \mu\text{m}$ corresponds to $n_{\text{eff}} = 3.418$. Fig. 4.26 shows simulations of sev-

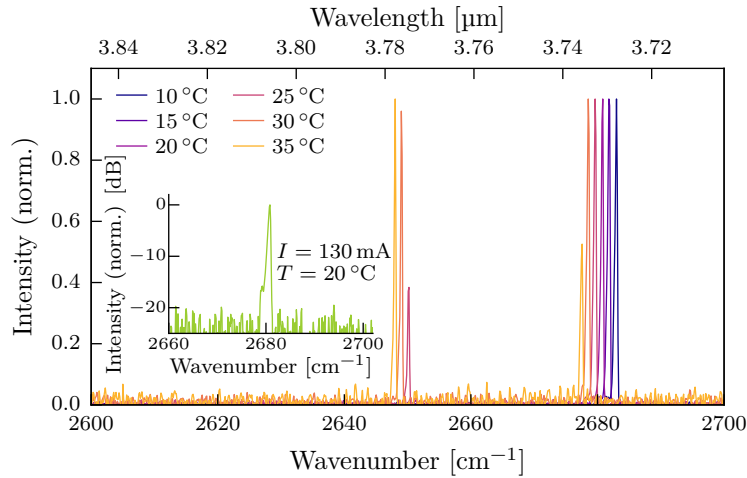


Fig. 4.25: Measured emission spectra at different heatsink temperatures (drive current 130 mA, 80 kHz/30 ns). The inset shows the emission spectrum at 20 °C in a semi-logarithmic scale with a side-mode suppression ratio > 15 dB [231].

eral whispering gallery modes, which are supported by the waveguide. Comparing the waveguide simulations with the measured spectra, suggests that the ring ICL lases at the fundamental radial mode (3.77 μm) at temperatures beginning from 25 °C and above, but exclusively emits in a higher-order mode at 3.73 μm from 10 °C to 20 °C. Furthermore, the shift of the emission wavelength as a function of heatsink temperature is investigated. As the laser is operated in pulsed mode at a low duty-cycle (80 kHz/30 ns) a heating of the active region can be neglected. The temperature in the active region can be assumed to equal the submount temperature i.e. $T_{\text{AR}} \approx T_{\text{heatsink}}$. Therefore, a shift of the emission wavelength can be related to a temperature-induced change of the refractive index. Fig. 4.27 shows the temperature tuning characteristics at $I = 130 \text{ mA}$. The emission peak shifts linearly with a temperature tuning coefficient of $\Delta\lambda/\Delta T = 0.3 \text{ nm}/^\circ\text{C}$ or $\Delta\nu/\Delta T = -0.21 \text{ cm}^{-1}/^\circ\text{C}$. Similar values of $\Delta\lambda/\Delta T = 0.31 - 0.35 \text{ nm}/^\circ\text{C}$ have been obtained for DFB ridge laser [242, 237].

Finally, the polarization of the projected nearfields for ring lasers are investigated. Depending on the character of the optical transition from conduction to valence band, the contributions of transverse magnetic (TM) or transverse electric (TE) polarizations are determined. The character of optical transitions in quantum well structures is dictated by the polarization selection rules [243], which has been discussed in section 2.1.2. The radiative recombination of an electron with a light-hole favors TM waveguide modes, while an electron to heavy-hole recombination supports TE modes. For standard ICL devices, the compressive strain in the GaInSb layer favors electron to heavy-hole optical transitions and therefore waveguide modes that are TE polarized. Recently, a design for a mid-infrared interband cascade laser with polarization-independent gain has been proposed [243]. With the help of strain and confinement engineering it should be possible to change the character of the optical transition to an electron to light-hole type. The TM/TE ratio can be controlled by adjusting the thickness or composition of the GaAsSb layer in type-II W-shaped quantum wells. The intersubband selection rule states that only components

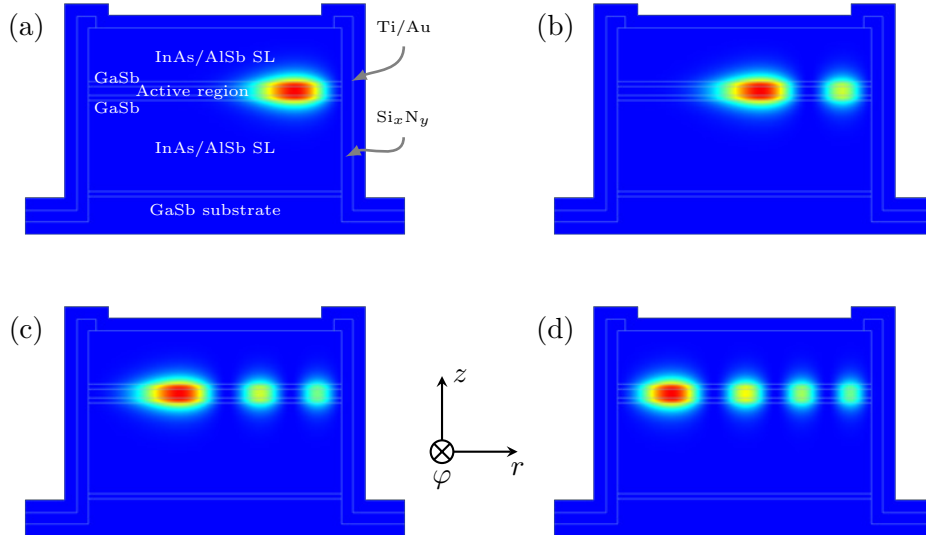


Fig. 4.26: Normalized time-averaged power-flow of the first four radial modes in φ -direction (into the plane of the paper). (a) Fundamental transversal-electric mode (TE1) in the ring waveguide. The active region is sandwiched between two GaSb waveguide layers, which ensure a high modal gain due to confinement. The cladding materials on top and the bottom consist of InAs/AlSb superlattices, which are grown on a n-doped GaSb substrate. (b) Second-order (TE2), (c) third-order (TE3) and (d) fourth-order (TE4) radial waveguide mode.

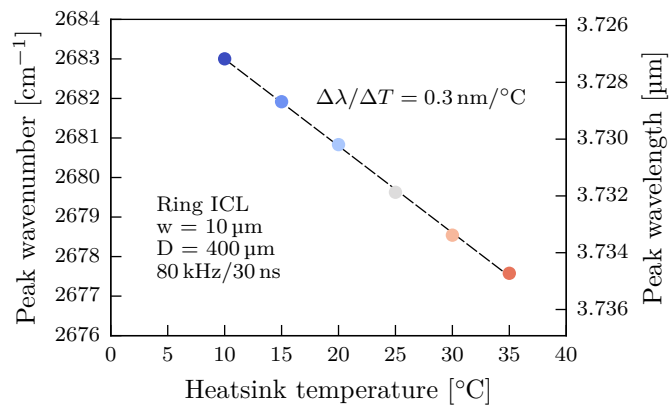


Fig. 4.27: Shift of the emission wavelength around $3.73\ \mu\text{m}$ with the heat sink temperature. A linear temperature tuning coefficient of $\Delta\nu/\Delta T = -0.21\ \text{cm}^{-1}/^\circ\text{C}$ is extracted [231].

of the electric field in the growth direction can create a non-zero dipole matrix element. Or in other words, only the electric field perpendicular to the layer plane couples to inter-subband transitions. As a result, the waveguide modes in QCLs are restricted to favor a TM polarization. The waveguide modes of interband (TM) and intersubband (TE) lasers have different polarizations of the electric field (see Fig. 4.15). Therefore, the out-coupled light from ring ICLs should also have a different orientation compared to QCLs. To verify this fact, projected nearfield images of both device types are captured with a bolometer camera. The ring QCL device has the same geometrical dimensions and also features substrate-emission via a metal-grating at a wavelength of $\lambda \sim 8.7 \mu\text{m}$. It is one of the optimized laser devices, which have been discussed in 3.9.3. Since the longer wavelength is not affecting the polarization a comparison is possible. Images of the projected nearfields are shown in Fig. 4.28.

While the QCL shows bright emission over the full circumference, an inhomogeneous emission pattern is observed for the ICL. The reason for this non-ideal behavior of the ring ICLs is attributed to technological reasons. The grating etch depth is relatively deep ($1.1 \mu\text{m}$) and together with the small size of the grooves it is challenging to completely remove the Si_xN_y from the bottom of the DFB grating (passivation opening). A longer overetch also increases the risk to remove Si_xN_y from the sidewalls, which can cause shortcuts of the active region in the subsequent metallization step. Therefore, some residuals of Si_xN_y can still be left in the grating grooves, influencing the emission pattern. Nevertheless, the light intensity is strong enough to investigate the polarization of the nearfields.

A polarizer is inserted in the beam path to examine the orientation of the electric field. For a horizontal orientation (0°) of the polarizer, shown in Fig. 4.28(b), the electric field is also blocked in the horizontal direction. In this case, bright emission is observed for the upper and lower part of the ICL device. While for the QCL device, emission from the left and right regions are observed. Rotating the polarizer to 45° (Fig. 4.28(c)) shows a similar, but complementary behavior, where the emission patterns are rotated by 90° with respect to each other. A further rotation of the polarizer to 90° (Fig. 4.28(d)) blocks the electric field in vertical direction and the ICL shows vanishing intensity in the upper and lower regions, while the QCL displays high intensities there. From these measurements, a radial polarization of the emitted light for ring ICL is strongly suggested. On the other hand, for the ring QCL, we find an azimuthal orientation of the electric field, which has been also observed in previous studies [131, 132]. The resulting orientation of the electric field is sketched in Fig. 4.29 for both device types. These experimental results underline the different nature of light generation in ring interband and intersubband cascade lasers, owing to the character of the optical transitions.

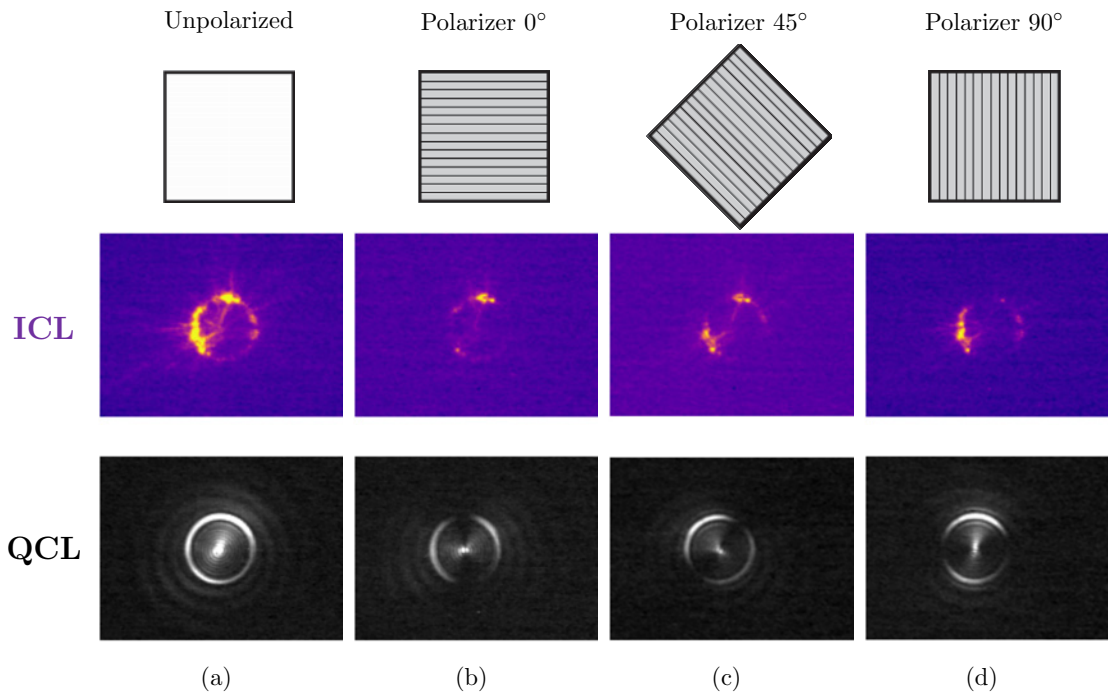


Fig. 4.28: Measurements of the projected nearfields of interband ($\lambda \sim 3.7 \mu\text{m}$) and intersubband ($\lambda \sim 8.7 \mu\text{m}$) ring lasers. Images from the bolometer camera of both device types are compared: (a) Without polarizer, (b) horizontal polarization, (c) 45° orientation of the polarizer and (d) for vertical polarization.

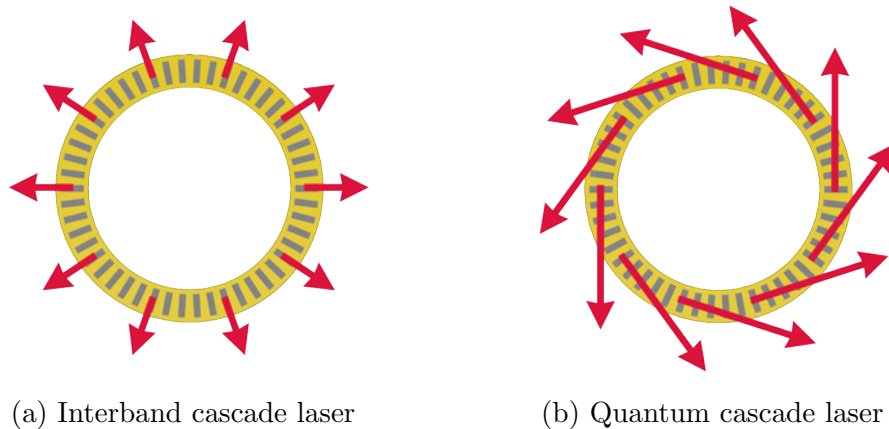


Fig. 4.29: Illustration of the projected nearfield polarizations. From measurements of interband and intersubband devices a radial polarization is observed for the ring ICL (a), while an azimuthal orientation of the electric field is observed for the ring QCL (b).

Summary and Outlook

The motivation for this thesis is driven by the demand for compact, coherent and power-efficient infrared light sources. Ring quantum cascade lasers have proven to be well suited for spectroscopic measurements. In this work the beam shaping with dual DFB gratings and the influence of the whispering gallery mode on the far field rotation is investigated. It could be shown that ring QCLs allow to determine the position of the whispering-gallery mode inside the cavity. Therefore, a second-order distributed feedback grating is fabricated with two continuous π phase-shifts. Normally, the far fields are rotated counter-clockwise due to the lateral asymmetry of the waveguide mode, where the mode's center-of-mass is shifted towards the outer sidewall. However, a clockwise orientation can be observed if a higher-order lateral mode is excited. Then the center-of-mass of the mode is closer to the inner sidewall, which results in a change of the overlap with the grating. The fraction of out-coupled light changes with the angular position (along the ring circumference), which leads to the far field rotation in the opposite direction.

A metamaterial lens, fabricated into the substrate, together with phase-shift DFB gratings allowed to collimate the emitted light and to create a central intensity maximum in the far field center. Compared to an ordinary ring laser, the device with the metasubstrate lens showed an increase of 265% of the peak intensity. The combination of a ring laser with a lens on the same chip allows to shrink the size of optical systems.

In addition, a compact laser/detector system with two commutable rings, fabricated in the same bi-functional QCLD material, is developed. The bi-functional material allows lasing and detection at the same wavelength with the same device. A sensing chip for infrared radiation at $\lambda = 6.5\ \mu\text{m}$ with two concentric rings is utilized in gas absorption measurements of isobutene and isobutane. For the configuration, where the outer ring operates as laser and the inner ring as detector, a 3σ limit of detection of 397 ppm is found for the isobutane measurement. With the demand for optimizing the performance of ring QCLs, a detailed investigation of the thermal management is conducted by finite-element simulations.

With an axisymmetric anisotropic thermal transport model the influence of various parameters on the active region temperature is systematically studied. Significant improvements of the heat dissipation can be achieved by using narrow waveguides with InP clad-

ding material together with a lateral regrowth with semi-insulating InP. Alternatively, a thick metallization layer of $\sim 5 \mu\text{m}$ can be used to efficiently remove the heat from the active region. Stimulated by these results, several methods for optimizing the heat sinking are tested experimentally. This finally lead to the development of new ring devices with metallized second-order DFB gratings. Hereby, the surface and also the grating slits are completely covered with a thick gold layer. With an optimized grating design, ring QCLs are fabricated that emit single-mode light at $8.7 \mu\text{m}$ through the substrate. With this approach, an improved thermal management with e.g. epi-side down bonding of the ring lasers becomes possible. While the laser benefits from the close distance to the sub mount heat sink, the substrate-side still can be used for other purposes. For instance, a compact, high-performance sensing platform can be realized.

Interband cascade lasers are very power-efficient devices, which feature threshold current densities well below $1 \text{ kA}/\text{cm}^2$. Hence, these devices are highly interesting for mobile applications. The concept of ring lasers is transferred from the intersubband cascade lasers to the emerging field of interband cascade lasers. With a ring device of $400 \mu\text{m}$ diameter and a waveguide width of $10 \mu\text{m}$, a threshold current of 92 mA is achieved. This first ring interband cascade laser features light emission towards the GaSb substrate. In measurements of the projected near fields of interband and intersubband cascade lasers the different nature of the optical transitions is obtained. While the ring quantum cascade laser features an azimuthal orientation, the interband cascade laser shows a radial polarization of the electric near field. The interband transitions occur between electrons in the conduction band and heavy-holes in the valence band, which are commonly TE polarized. On the other hand, intersubband transitions are subjected to the intersubband selection rule, which allows only TM polarized light to couple to these transitions.

Outlook

The bi-functional QCLD design allows to develop compact sensing platforms. Surface-emitting/detecting sensors enable a two-dimensional array integration on the same chip, which can enhance the spectral coverage and increase the flexibility for sensing applications. A highly integrated sensing platform with laser, detector, lens and other optical elements on the same chip would allow to shrink the size of such complex systems drastically. Substrate-emitting ring lasers/detectors with on-chip lenses and polarizers are perfect candidates for a new class of miniaturized optical systems.

Fig. 5.1 shows a comparison between the number of publications for quantum cascade lasers and interband cascade lasers. Obviously, the development of the QCL received much more attention than its interband counterpart. Although the interband cascade laser was invented only shortly after the QCL, the progress in design and modelling, growth and fabrication was slowed down due to several issues. Nevertheless, the interband cascade laser is an interesting device since it combines transitions between conduction and valence band and the unique type-II band alignment. This makes the heterostructure design more complicated, but maybe also offers new possibilities. Optimizations of the quantum design, waveguide structures, growth and fabrication are necessary to unfold the full potential of interband cascade lasers. Furthermore, concepts which have already been developed for diode lasers or quantum cascade lasers can be transferred directly or with some modifications to the interband cascade laser. Due to their low power consumption,

these devices are very interesting for mobile applications. For ring ICLs, the combination of a first-order lateral grating and a second-order surface grating may improve the feedback mechanism and allows to shape the emission beam.

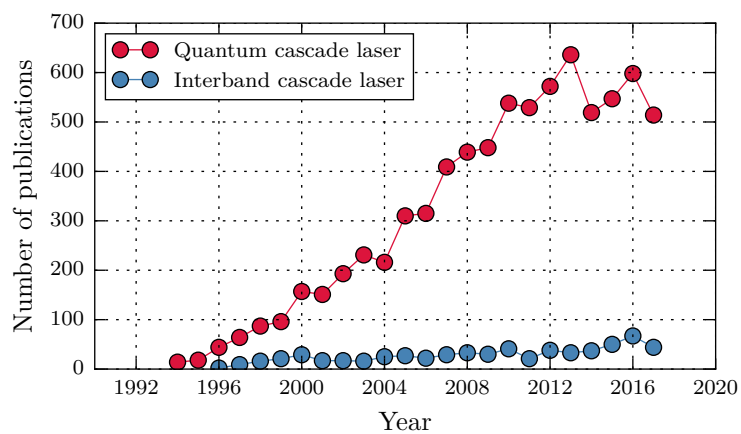


Fig. 5.1: Number of publications using the terms "quantum cascade laser" or "interband cascade laser" over the years from 1994 to 2017. The source data is obtained from Web of Science [244].

Appendix

A.1 Fundamentals

A.1.1 Electromagnetic fields

Starting point for the analytical calculation of the electromagnetic field distributions are Maxwell's equations [245]

$$\vec{\nabla} \cdot \mathbf{B}(\mathbf{r}, t) = 0 \quad (\text{A.1})$$

$$\vec{\nabla} \cdot \mathbf{D}(\mathbf{r}, t) = \rho(\mathbf{r}, t) \quad (\text{A.2})$$

$$\vec{\nabla} \times \mathbf{E}(\mathbf{r}, t) = -\frac{\partial \mathbf{B}(\mathbf{r}, t)}{\partial t} \quad (\text{A.3})$$

$$\vec{\nabla} \times \mathbf{H}(\mathbf{r}, t) = \mathbf{J}(\mathbf{r}, t) + \frac{\partial \mathbf{D}(\mathbf{r}, t)}{\partial t}, \quad (\text{A.4})$$

where the time and space dependent vectors \mathbf{B} , \mathbf{D} , \mathbf{E} and \mathbf{H} represent the magnetic flux density in $[\text{Vs/m}^2]$, the electric flux density in $[\text{As/m}^2]$, the electric field strength in $[\text{V/m}]$ and the magnetic field strength in $[\text{A/m}]$. The quantity ρ corresponds to the free electric charge carrier density in $[\text{As/m}^3]$, \mathbf{r} is the coordinate vector and \mathbf{J} is the current density in $[\text{A/m}^2]$. The Nabla symbol $\vec{\nabla}$ denotes the gradient operator, which reads in a three dimensional cartesian coordinate system

$$\vec{\nabla} = \mathbf{e}_x \frac{\partial}{\partial x} + \mathbf{e}_y \frac{\partial}{\partial y} + \mathbf{e}_z \frac{\partial}{\partial z}, \quad (\text{A.5})$$

with the unit vectors in x , y and z direction \mathbf{e}_x , \mathbf{e}_y and \mathbf{e}_z , respectively. The local connection between flux densities and field strengths is expressed in the material equations

$$\mathbf{D}(\mathbf{r}, t) = \underline{\epsilon}(\mathbf{r}, t, \mathbf{E}) \cdot \mathbf{E}(\mathbf{r}, t) \quad \text{and} \quad \mathbf{B}(\mathbf{r}, t) = \underline{\mu}(\mathbf{r}, t, \mathbf{H}) \cdot \mathbf{H}(\mathbf{r}, t), \quad (\text{A.6})$$

with the tensors of the permittivity $\underline{\epsilon}$ and the permeability $\underline{\mu}$. In general, the properties of a material can be inhomogeneous, anisotropic, time-dependent and nonlinear. To simplify the following derivation it is assumed that the material parameters are linear, isotropic and time-independent and hence can be represented by a scalar. For convenience, the permittivity ϵ is then written as the product of the permittivity in vacuum $\epsilon_0 \approx 8.854 \times 10^{-12}$ F/m and a material dependent relative dielectric constant ϵ_r . In a similar manner the permeability μ is expressed as the product of the permeability of vacuum $\mu_0 = 4\pi \times 10^{-7}$ H/m and the relative permeability μ_r . Therefore (A.6) can be written as

$$\mathbf{D} = \epsilon_0 \epsilon_r \mathbf{E} \quad \text{and} \quad \mathbf{B} = \mu_0 \mu_r \mathbf{H}. \quad (\text{A.7})$$

At optical frequencies the relative permeability can be set to $\mu_r = 1$, because the magnetization is in most cases negligible. For completeness, the boundary conditions for the electromagnetic field components are given by

$$\begin{aligned} \mathbf{n} \times \llbracket \mathbf{E} \rrbracket &= \mathbf{E}_t^{(2)} - \mathbf{E}_t^{(1)} = \mathbf{0} & \mathbf{n} \cdot \llbracket \mathbf{B} \rrbracket &= \mathbf{B}_n^{(2)} - \mathbf{B}_n^{(1)} = 0, \\ \mathbf{n} \times \llbracket \mathbf{H} \rrbracket &= \mathbf{H}_t^{(2)} - \mathbf{H}_t^{(1)} = \mathbf{K} & \mathbf{n} \cdot \llbracket \mathbf{D} \rrbracket &= \mathbf{D}_n^{(2)} - \mathbf{D}_n^{(1)} = \sigma, \end{aligned} \quad (\text{A.8})$$

with \mathbf{n} as the unit vector normal to the surface and the symbol $\llbracket \cdot \rrbracket$ denotes the change of the field component across the interface between region 1 and region 2. Such change of the tangential component of the magnetic field strength \mathbf{H}_t is caused by a surface current density \mathbf{K} . On the other hand, the normal component of the electric flux density \mathbf{D} changes due to surface charges σ at the interface. The tangential component of the electric field strength \mathbf{E}_t and the normal component of the magnetic flux density \mathbf{B}_n are continuous across the interface.

A.1.2 Wave propagation

In the following, the transition from electromagnetic fields to propagating waves is discussed. For simplicity, it is assumed that no charges and also no currents are present in the region of interest ($\rho = 0$ and $\mathbf{J} = \mathbf{0}$). Taking the curl of (A.3) and eliminating $\vec{\nabla} \times \mathbf{H}$ with (A.4)

$$\vec{\nabla} \times (\vec{\nabla} \times \mathbf{E}) = \vec{\nabla} \times \left(-\mu \frac{\partial \mathbf{H}}{\partial t} \right) \quad (\text{A.9})$$

$$= -\mu \frac{\partial}{\partial t} \left(\epsilon \frac{\partial \mathbf{E}}{\partial t} \right). \quad (\text{A.10})$$

The left-hand side of (A.9) can be expressed as

$$\vec{\nabla} \times (\vec{\nabla} \times \mathbf{E}) = \vec{\nabla}(\vec{\nabla} \cdot \mathbf{E}) - \vec{\nabla}^2 \mathbf{E}. \quad (\text{A.11})$$

Since there are no free charges, the term $\vec{\nabla} \cdot \mathbf{E} = \rho/\epsilon = 0$ vanishes and one arrives at the Helmholtz equation

$$\vec{\nabla}^2 \mathbf{E}(\mathbf{r}, t) = \mu\epsilon \frac{\partial^2 \mathbf{E}(\mathbf{r}, t)}{\partial t^2}, \quad (\text{A.12})$$

where $\vec{\nabla}^2 = \mathbf{e}_x \frac{\partial^2}{\partial x^2} + \mathbf{e}_y \frac{\partial^2}{\partial y^2} + \mathbf{e}_z \frac{\partial^2}{\partial z^2}$ is the vector Laplace operator. The Helmholtz equation looks very similar to the well-known wave equation $\frac{\partial^2 \psi}{\partial x^2} = \frac{1}{v^2} \frac{\partial^2 \psi}{\partial t^2}$ with the velocity v corresponding to

$$v = \frac{1}{\sqrt{\mu\epsilon}} = \frac{1}{\sqrt{\mu_0 \mu_r \epsilon_0 \epsilon_r}} = \frac{c_0}{\sqrt{\mu_r \epsilon_r}}. \quad (\text{A.13})$$

Hence, the description of the propagation of electromagnetic waves follows directly from Maxwell's equations. For convenience, the material parameters are condensed into the refractive index $n = c_0/v = \sqrt{\mu_r \epsilon_r}$, which is given by the ratio of the speed of light in free space and the propagation velocity of the electromagnetic wave in the medium. Possible solutions to (A.12) can be obtained with a plane wave ansatz

$$\mathbf{E}(\mathbf{r}, t) = \mathbf{E}_0 e^{j(\mathbf{k} \cdot \mathbf{r} - \omega t)}, \quad (\text{A.14})$$

with the wave amplitude \mathbf{E}_0 , the angular frequency $\omega = 2\pi f$ and the wave vector $\mathbf{k} = (2\pi/\lambda)\mathbf{e}_k$, which points in the propagation direction \mathbf{e}_k of the electromagnetic wave. It has to be noted that also other types of waves like cylindrical, spherical, Gaussian and many others are solutions of the Helmholtz equation (A.12). Inserting (A.14) into (A.12) gives the fundamental connection between ω and k , which is known as the dispersion relation

$$|\mathbf{k}| = k = \frac{\omega}{v} = \frac{n\omega}{c_0}. \quad (\text{A.15})$$

For monochromatic waves, $\mathbf{E}(\mathbf{r}, t)$ in (A.14) can be written as

$$\mathbf{E}(\mathbf{r}, t) = \text{Re} \left[\tilde{\mathbf{E}}(\mathbf{r}, \omega) e^{j\omega t} \right], \quad (\text{A.16})$$

with the complex amplitude $\tilde{\mathbf{E}}(\mathbf{r}, \omega)$, which has to fulfill the Helmholtz equation in the frequency domain

$$\vec{\nabla}^2 \tilde{\mathbf{E}}(\mathbf{r}, \omega) + \mu \epsilon \omega^2 \tilde{\mathbf{E}}(\mathbf{r}, \omega) = 0. \quad (\text{A.17})$$

A.1.3 Energy transport

An expression for the energy flux density associated with the propagating electromagnetic wave can be derived by taking the dot-product of \mathbf{H} with (A.3) and \mathbf{E} with (A.4), and building the difference

$$\mathbf{H} \cdot (\vec{\nabla} \times \mathbf{E}) - \mathbf{E} \cdot (\vec{\nabla} \times \mathbf{H}) = -\mathbf{H} \cdot \frac{\partial \mathbf{B}}{\partial t} - \left(\mathbf{E} \cdot \mathbf{J} + \mathbf{E} \cdot \frac{\partial \mathbf{D}}{\partial t} \right) \quad (\text{A.18})$$

$$= \vec{\nabla} \cdot (\mathbf{E} \times \mathbf{H}), \quad (\text{A.19})$$

where the term $\mathbf{S} = \mathbf{E} \times \mathbf{H}$ is the so-called Poynting vector in [W/m²]. In isotropic media, the energy flow is parallel to the propagation direction \mathbf{k} , thus the material equations from (A.7) with $\mathbf{D} = \epsilon \mathbf{E}$ and $\mathbf{B} = \mu \mathbf{H}$ can be used. In anisotropic media, such as birefringent crystals, the energy flow is not necessarily in the same direction as the wave propagation. By using the product rule $\frac{1}{2} \frac{\partial}{\partial t} (\mathbf{y} \cdot \mathbf{y}) = \mathbf{y} \cdot \frac{\partial}{\partial t} \mathbf{y}$, the Poynting theorem [246] then reads

$$\vec{\nabla} \cdot \mathbf{S} = -\frac{\partial}{\partial t} \left(\frac{\mu_0 \mu_r}{2} \mathbf{H} \cdot \mathbf{H} + \frac{\epsilon_0 \epsilon_r}{2} \mathbf{E} \cdot \mathbf{E} \right) - \mathbf{E} \cdot \mathbf{J} \quad (\text{A.20})$$

$$= -\frac{\partial}{\partial t} (w_m + w_e) - \mathbf{E} \cdot \mathbf{J}, \quad (\text{A.21})$$

with the the magnetic and electric energy densities w_m and w_e , respectively. The term $\mathbf{E} \cdot \mathbf{J} = \mathbf{E} \cdot \gamma (\mathbf{E} + \mathbf{v} \times \mathbf{B})$ corresponds to the exchange between different types of energies via currents. In the simple case of a material with an electrical conductivity γ and zero velocity ($\mathbf{v} = \mathbf{0}$) it describes the energy transferred from the electromagnetic field into Joule heating. In the integral form the Poynting theorem (A.20) describes the energy flow through a surface (left hand side), leading to a change of the energy stored in the volume (right hand side).

A.1.4 Polarization

The orientation of the electromagnetic field vectors \mathbf{E} and \mathbf{H} relative to each other and also with respect to the propagation direction \mathbf{k} plays a significant role in the description of optical phenomena. Hereby, the polarization state of an electromagnetic wave is usually referred as the orientation of the electric field strength \mathbf{E} . Under the assumption of a linear, homogeneous, isotropic and charge free region ($\vec{\nabla} \cdot \mathbf{D} = 0$), the plane wave cannot

have an electric field component in the propagation direction ($\mathbf{k} \cdot \mathbf{E} = 0$). This can be seen by taking the divergence of (A.14), which gives $\vec{\nabla} \cdot \mathbf{E} = \mathbf{j}\mathbf{k} \cdot \mathbf{E}$ and

$$\vec{\nabla} \cdot \mathbf{D} = \epsilon \vec{\nabla} \cdot \mathbf{E} = \mathbf{j}\epsilon \mathbf{k} \cdot \mathbf{E} = 0. \quad (\text{A.22})$$

Just for completeness, the presence of free charges also allows plane waves with field components in propagation direction. Such waves are then longitudinal polarized and referred as plasma waves [247]. In a similar way as before the divergence $\vec{\nabla} \cdot \mathbf{H}$ of the magnetic field $\mathbf{H}(\mathbf{r}, t) = \mathbf{H}_0 e^{i(\mathbf{k} \cdot \mathbf{r} - \omega t)}$, together with the lack of magnetic monopoles ($\vec{\nabla} \cdot \mathbf{B} = 0$), leads to

$$\vec{\nabla} \cdot \mathbf{B} = \mu \vec{\nabla} \cdot \mathbf{H} = \mathbf{j}\mu \mathbf{k} \cdot \mathbf{H} = 0. \quad (\text{A.23})$$

Hence, it immediately follows that the electromagnetic wave is transversal oriented, or in other words \mathbf{E} and \mathbf{H} are perpendicular to the propagation direction ($\mathbf{k} \cdot \mathbf{E} = \mathbf{k} \cdot \mathbf{H} = 0$). Furthermore, electric and magnetic fields are orthogonal to each other, which is a direct consequence of the plane wave ansatz inserted into the Maxwell equations (A.3) and (A.4). For convenience, the spatial derivative of plane waves is represented by $\vec{\nabla} \rightarrow \mathbf{j}\mathbf{k}$ and the time derivative $\frac{\partial}{\partial t}$ corresponds to a multiplication with $-j\omega$. Faraday's law of induction then reads

$$\vec{\nabla} \times \mathbf{E} = -\frac{\partial \mathbf{B}}{\partial t} \quad (\text{A.24})$$

$$\mathbf{j}\mathbf{k} \times \mathbf{E} = j\omega \mu \mathbf{H}, \quad (\text{A.25})$$

and with the assumption of a current free region ($\mathbf{J} = \mathbf{0}$) the Ampere-Maxwell law can be written as

$$\vec{\nabla} \times \mathbf{H} = \frac{\partial \mathbf{D}}{\partial t} \quad (\text{A.26})$$

$$\mathbf{j}\mathbf{k} \times \mathbf{H} = -j\omega \epsilon \mathbf{E}. \quad (\text{A.27})$$

Electric and magnetic fields are oriented perpendicular to the propagation direction of the plane wave and the vectors \mathbf{E} , \mathbf{H} and \mathbf{k} build an orthogonal system. A plane wave impinging on a surface can be classified by its polarization state. Hereby, the orientation of the electric field \mathbf{E} with respect to the so-called plane of incidence determines the polarization state. Fig. A.1 shows an illustration of the two possible polarization states for a plane wave impinging on a surface. The plane of incidence is created by the surface normal vector \mathbf{e}_n and the propagation direction \mathbf{k} . In the case where \mathbf{E} is perpendicular to the plane of incidence, the plane wave is referred to be in a s-polarized or σ -polarized

state. On the other hand, if \mathbf{E} lies in the plane of incidence (parallel), the plane wave is in a p-polarized or π -polarized state. Generally, this classification can be applied to waves propagating in free space or in a medium. Sometimes s- and p-polarization are also referred as TE and TM polarized waves to indicate that the electric/magnetic field is perpendicular to the plane of incidence. However, the latter notation is normally used for labeling the polarization state of waveguide modes, which easily creates confusion.

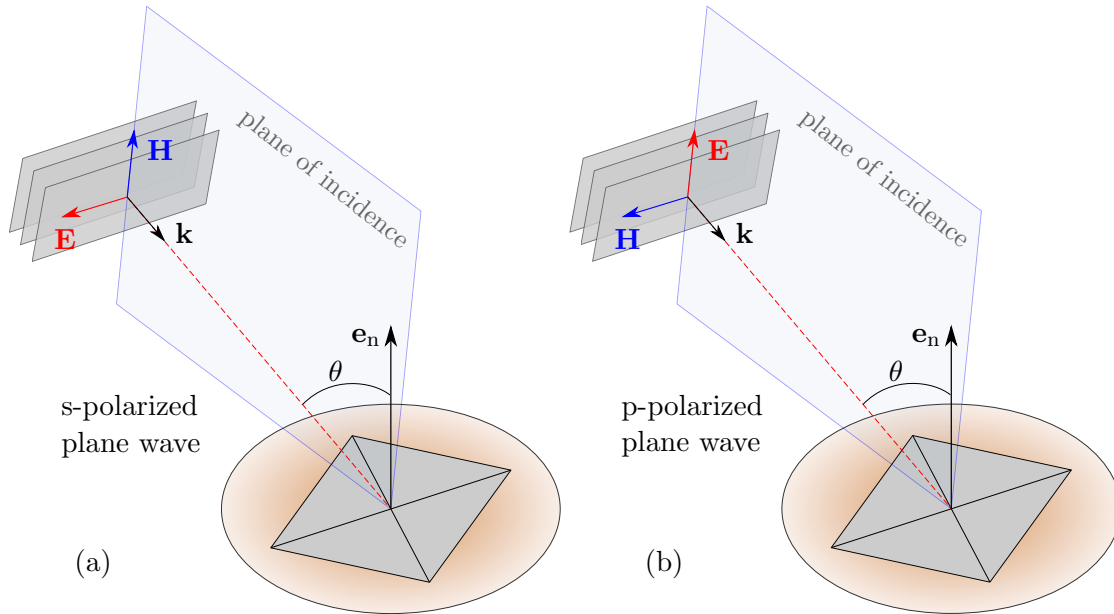


Fig. A.1: Polarization state of a plane wave impinging on a surface. The plane of incidence serves as the reference plane. It is spanned by the propagation vector \mathbf{k} and the normal vector \mathbf{e}_n of the surface. (a) The electric field vector \mathbf{E} is oriented perpendicular to the plane of incidence. The plane wave is in a s-polarized or σ -polarized state. (b) The electric field is parallel to the plane of incidence, which corresponds to a p-polarized or π -polarized state.

Waveguide modes

The distribution of the electromagnetic field in a waveguide can be constructed by the superposition of plane waves. The resulting waveguide modes are classified into different types: transversal electric (TE), transversal magnetic (TM) and transversal electromagnetic (TEM) modes. Fig. A.2 shows an illustration of the associated orientations of the electric and magnetic fields. The TE-polarized wave has no electric field component in propagation direction \mathbf{k} (in the coordinate system use in Fig. A.2 this corresponds to $E_z = 0$). However, a magnetic field in propagation direction is allowed ($H_z \neq 0$). On the other hand, the magnetic field components of a TM-polarized wave are all transversal, while H_z vanishes ($E_z \neq 0$). In waveguides with two or more conductors, such as coaxial cables or striplines, the excitation of a TEM mode is possible. All electric and magnetic field components vanish in propagation direction ($E_z = H_z = 0$) and only components in the plane perpendicular are allowed. For completeness, it has to be mentioned that also modes exist, which have non-negligible field components ($E_z \neq 0, H_z \neq 0$) in propagation

direction. These modes can be observed in e.g. optical fibers or dielectric waveguides and also called hybrid modes.

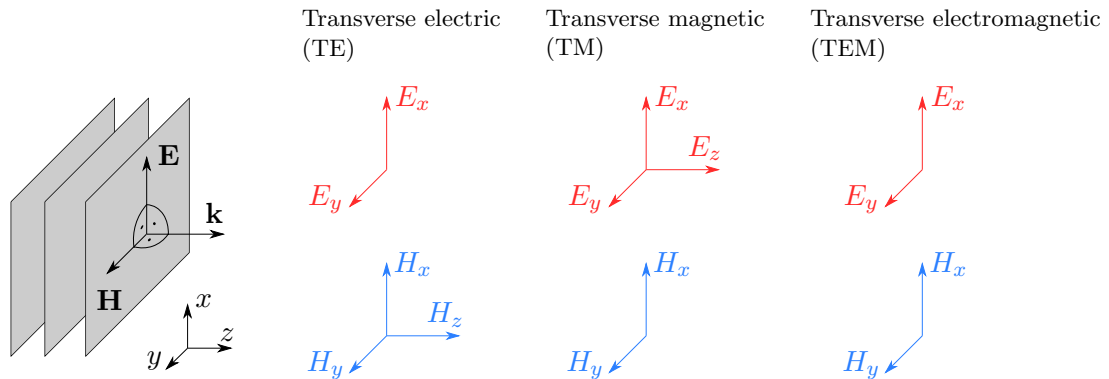


Fig. A.2: Plane wave propagating in positive z -direction. Electric and magnetic fields are perpendicular oriented with respect to each other and may vary in the x - y -plane perpendicular to the propagation direction \mathbf{k} . In waveguides, basically three types of modes can be distinguished: TE, TM and TEM. The electric/magnetic field component in z -direction vanishes for the TE/TM wave. The TEM waves can only be excited with two or more conductors, such as coaxial cables or striplines.

A.2 Absorption and recombination in semiconductors

The main optical absorption mechanisms in semiconductors at room temperature are [220]:

1. Free carrier absorption by electrons/holes
2. Inter-valley conduction band absorption by electrons
3. Inter-valence band absorption by holes

The strength of each contribution depends on the material, doping, wavelength, temperature and the carrier concentrations (electrons and holes). In the following, these absorption mechanisms are discussed more in detail.

A.2.1 Free carrier absorption

The free carrier absorption describes the absorption of a photon by an electron/hole, leading to a subsequent transition to a higher energy state within the same band [248]. Thus, the carrier is already in an excited state, e.g. an electron in the conduction band, and moves to an unoccupied higher state, which most likely requires a change in momentum. For completeness, interband absorption is not the same process, because there the carrier

makes a transition from a non-conducting to a conducting state (valence to conduction band). For the free carrier absorption process the momentum conservation has to be fulfilled. As the momentum of the photon $\hbar k$ is negligible, the transition relies on another interaction partner. This can be a scattering process with ionized impurities or the lattice via acoustical or optical phonons. In general, contributions from all three scattering mechanisms are present, but with different wavelength dependencies. The free carrier absorption coefficient then reads [220]:

$$\alpha_{\text{FCA}} = \underbrace{sA\lambda^{1.5}}_{\text{acoustic phonons}} + \underbrace{sB\lambda^{2.5}}_{\text{optical phonons}} + \underbrace{sC\lambda^3}_{\text{ionized impurities}}, \quad (\text{A.28})$$

where A, B and C are fitting parameters and s is a constant prefactor. The latter one is calculated within the classical Drude-Zener theory [220] to equal

$$s = \frac{e^3}{4\pi^2 c^3 m_0^2 \epsilon_0} \frac{1}{n\mu(m^*/m_0)^2}, \quad (\text{A.29})$$

with the refractive index n , the mobility μ and the effective mass m^* of the free carrier. For practical purposes, the number of fitting parameters in (A.28) is reduced to only two by using following relation [220],

$$\alpha_{\text{FCA}} = K_{\text{FCA}}\lambda^p, \quad (\text{A.30})$$

with the doping-dependent constant K_{FCA} and the fit parameter p for the wavelength dependence.

A.2.2 Inter-valley conduction band absorption

An electron in a subband of the conduction band can make a transition to another minima in the same subband, which is situated at a different k value. The carrier can scatter from one band minimum to another valley at the zone edge, e.g. a transition between Γ and X or as well Γ and L valley. This interaction between an electron and a (near) zone-edge phonon can be very fast (scattering times on the order of 30 fs) [249]. The wavelength dependence of the absorption can be approximated by [250]

$$\alpha \sim (\hbar\omega - E_0)^{1/2}, \quad (\text{A.31})$$

where $\hbar\omega$ is the energy of the incident photon and E_0 a threshold energy for the transition. The latter one can be written as

$$E_0 = \Delta E + E_{\text{phonon}} - E_{\text{F,n}}, \quad (\text{A.32})$$

with the energy separation ΔE between the conduction band valleys, the large wavevector phonon energy E_{phonon} and the Fermi energy for electrons $E_{F,n}$. From (A.31) and (A.32) it also follows that the absorption is proportional to the carrier concentration and decreases with increasing wavelength.

A.2.3 Inter-valence band absorption

Transitions between states in the heavy-hole (HH), light-hole (LH) and split-off (SO) band can be initiated by absorption of a photon. In particular, the absorption coefficients for the transitions $\text{LH} \rightarrow \text{HH}$, $\text{SO} \rightarrow \text{LH}$ and $\text{SO} \rightarrow \text{HH}$ are distinguished in a three band Kane model [251]. For GaSb, the energy of the split-off band at the Γ -point ($k = 0$) is $\Delta_{\text{SO}} = 0.8 \text{ eV}$ [252]. On the other hand, the bandgap (heavy-hole to conduction band) energy is only 0.725 eV , thus smaller as Δ_{SO} . As a result, direct transitions from the split-off band to the heavy-hole band are only possible for energies larger than the bandgap. In other words, for incident radiation with photon energies below the bandgap, the transition $\text{SO} \rightarrow \text{HH}$ is not possible. Furthermore, it is found that for GaSb the absorption coefficient $\alpha_{\text{LH} \rightarrow \text{HH}} \gg \alpha_{\text{SO} \rightarrow \text{LH}}$, which implies that the inter-valence band absorption is caused mainly by light-hole to heavy-hole transitions [220].

A.2.4 Recombination mechanisms

In semiconductors, thermal equilibrium can be established mainly by three recombination mechanisms [253]:

- Spontaneous/stimulated radiative emission
- Shockley-Read-Hall non-radiative recombination
- Auger non-radiative recombination

An illustration of these processes is shown in Fig. A.3.

The radiative recombination Fig. A.3(a) can be either a spontaneous or stimulated emission of an electron from the conduction to the valence band. Since the momentum associated with the generated photon is very small, such band-to-band transitions are important for direct bandgap materials. In indirect materials, the momentum difference between initial and final state has to be supplied by another scattering partner, e.g. a phonon. Shockley-Read-Hall recombination is caused by traps, which are energetically located between conduction and valence band. The recombination rate depends on the material quality and thus represents no fundamental physical limitation. Shockley-Read-Hall recombination can be controlled by engineering the crystal growth quality. In contrast to that, Auger recombination can be a severe problem in narrow gap materials. The non-radiative processes are discussed later more in detail.

In general, the total recombination rate [254] can be written as a sum over all contributions

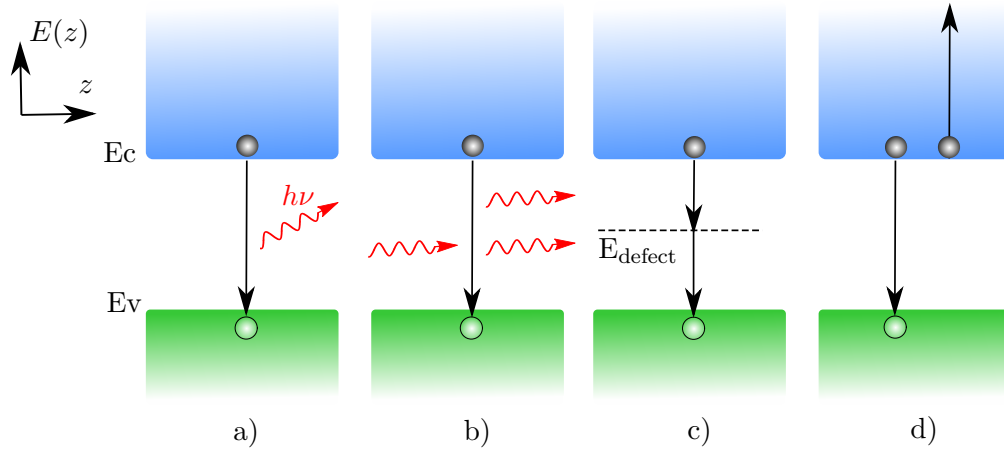


Fig. A.3: Radiative and non-radiative recombination paths in interband cascade lasers: (a) Spontaneous emission, (b) stimulated emission, (c) Shockley-Read-Hall recombination and (d) Auger recombination.

$$R = R_{\text{spon}} + R_{\text{stim}} + R_{\text{non-rad}} + R_{\text{leak}}, \quad (\text{A.33})$$

where R_{spon} and R_{stim} correspond to the spontaneous and stimulated emission rates, respectively. Auger and Shockley-Read-Hall non-radiative recombination processes are subsumed in $R_{\text{non-rad}}$. The last term R_{leak} refers to carrier leakage above a semiconductor barrier, such as AlSb. Carriers in the high-energy tail of the carrier distribution reach energies higher than the bandoffset of the barrier material and can escape from the active region. This situation is illustrated in Fig. A.4.

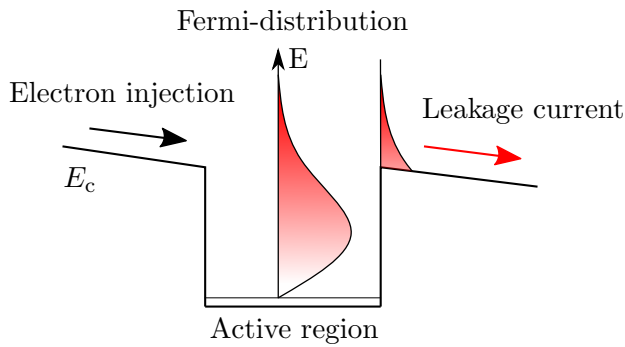


Fig. A.4: Carrier leakage is caused by electrons (or holes) in the high-energy tail of the Fermi-distribution. Electrons with energies larger than the barrier band-offset can escape from the active region. The leakage rate R_{leak} increases significantly with temperature.

While the stimulated emission requires at least one additional photon, the remaining recombination processes represent natural carrier decays. Thus, the recombination rate can also be expressed as the inverse of a carrier lifetime τ ,

$$R = \frac{n}{\tau(n)} + R_{\text{stim}}, \quad (\text{A.34})$$

where n denotes the carrier concentration. The carrier concentration dependent lifetime in (A.34) can be written phenomenologically [246] as

$$\tau(n) = \frac{1}{A + Bn + Cn^2}, \quad (\text{A.35})$$

where A denotes the monomolecular (defect-related) recombination coefficient, B stands for bimolecular recombination (spontaneous emission) and C for Auger recombination. Combining (A.34) and (A.35), the total recombination rate can be expressed as

$$R = (An + Cn^3) + Bn^2 + R_{\text{stim}}. \quad (\text{A.36})$$

Here, the first term corresponds to non-radiative recombinations and the second term to radiative recombinations by emission of photons. It is useful to define separate lifetimes for radiative and non-radiative processes:

$$\tau_{\text{rad}} = \frac{1}{Bn} \quad \text{and} \quad \tau_{\text{non-rad}} = \frac{1}{A + Cn^2}. \quad (\text{A.37})$$

The internal quantum efficiency η_i can be calculated by setting the radiative recombination rate in relation to the total recombination rate:

$$\eta_i = \frac{1/\tau_{\text{rad}}}{1/\tau_{\text{rad}} + 1/\tau_{\text{non-rad}}} = \frac{\tau_{\text{non-rad}}}{\tau_{\text{rad}} + \tau_{\text{non-rad}}}. \quad (\text{A.38})$$

In a simple carrier rate equation model [254] the net generation rate can be written as

$$\frac{dn}{dt} = G - R \quad (\text{A.39})$$

$$\Rightarrow \frac{dn}{dt} = \frac{\eta_i I}{qV} - \frac{n}{\tau(n)} - R_{\text{stim}}, \quad (\text{A.40})$$

where the generation rate G is determined by the injected carrier concentration I/qV and the internal quantum efficiency η_i (V is the volume of the active region). The recombination rate R is inserted from (A.34). Under steady-state conditions $dn/dt = 0$, generation and recombination balance each other. At threshold the stimulated emission rate is $R_{\text{stim}} \approx 0$ and from (A.40) the threshold current is expressed as

$$I_{\text{th}} = \frac{qV}{\eta_i} \frac{n}{\tau(n)}. \quad (\text{A.41})$$

By inserting (A.35) for $\tau(n)$, an expression for the threshold current density is found:

$$J_{\text{th}} = \frac{q}{\eta_i} (An_{\text{th}} + Bn_{\text{th}}^2 + Cn_{\text{th}}^3), \quad (\text{A.42})$$

with the threshold carrier density n_{th} .

Shockley-Read-Hall recombination

Shockley-Read-Hall (SRH) recombination [255, 256] is caused by lattice defects or impurities, which create a trap level within the bandgap, as shown in Fig. A.3(b). In principle, there are four transition paths for the carriers: electron capture/emission from the conduction band to the trap level and hole capture/emission from the valence band to the trap level. An illustration of these transitions is illustrated in Fig. A.5. In the case of a recombination process, an electron in the conduction band is temporarily captured by the trap before it is re-emitted to the valence band. Hence, the SRH process is also known as a trap-assisted recombination path. The recombination rate for SRH recombination [254] is given by

$$R^{\text{SRH}} = \frac{np - n_i^2}{(n_1 + n)\tau_h + (p_1 + p)\tau_e}, \quad (\text{A.43})$$

with the electron, hole and intrinsic carrier concentrations n , p and n_i , respectively. Assuming empty trap states, τ_e gives the time required to capture an electron from the conduction band. On the other hand, τ_h is the time to emit an electron from the full trap level into the valence band. This is analogue to a capture of a hole from the valence band to the trap level. The parameters n_1 and p_1 correspond to the carrier concentrations that would be apparent if the Fermi-level equals the trap level E_t . These carrier concentrations are given by

$$n_1 = n_i \exp\left(\frac{E_t - E_i}{k_B T}\right), \quad (\text{A.44})$$

$$p_1 = n_i \exp\left(\frac{E_i - E_t}{k_B T}\right), \quad (\text{A.45})$$

where E_i denotes the middle of the bandgap. The recombination rate in (A.43) increases for trap levels with energies close to the middle of the bandgap ($E_g \approx E_i$), which are also known as deep-level traps. SRH recombination can become a problem in materials with high defect and impurity densities. In contrast to that, modern MBE and MOCVD systems allow to grow high-quality crystals with low trap densities. Hence, SRH recombination rates in state-of-the-art semiconductor materials are typically negligible. Finally, it has to be mentioned that this recombination mechanism represents no fundamental limiting physical mechanism, since it can be controlled by the quality of the grown material [253].

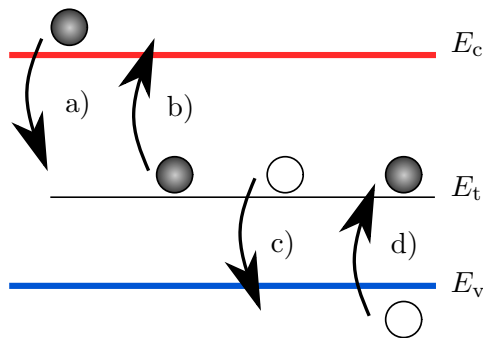


Fig. A.5: Carrier transitions associated with trap centers. (a) Capture of an electron from the conduction band by the trap. (b) Emission of an electron from a trap state to the conduction band. (c) Hole emission and (d) hole capture.

Auger recombination

Auger recombination is a non-radiative three-particle process in which energy and momentum are conserved. An electron recombines with a hole across the bandgap (band-to-band recombination) and the energy difference is given to another (third) carrier (electron or hole), rather than a photon. The inverse of the Auger process occurs under high electric fields (several hundred kV cm^{-1}) and is also known as impact ionization. Depending on which energy bands (conduction, valence or split-off band) are involved, different types of Auger processes can be distinguished. A common way to describe these processes is to abbreviate the conduction band to the heavy-hole valence band transition with "CH", and in a similar manner for split-off and light-hole valence band. The three-particle process is then written as the following: The first two letters correspond to the transition through which the carriers recombine. The energy is given to the third charge carrier. The last two letters indicate the transition of this particle from the initial state to the final state. Thus, a CHSH process corresponds to the recombination of an electron in the conduction band with a heavy-hole in the valence band. The energy difference is given to an electron in the split-off band, which is then excited into an empty state of the heavy-hole valence band. Consequently, there are a variety of Auger processes that are important for III-V semiconductors:

1. CHCC (conduction to heavy-hole band \Rightarrow conduction to conduction band)
2. CHSH (conduction to heavy-hole band \Rightarrow split-off to heavy-hole band)
3. CHLH (conduction to heavy-hole band \Rightarrow light-hole to heavy-hole band)

In general, Auger processes depend on the scattering between charge carriers, thus the recombination rate R increases with higher carrier densities. For an intrinsic (undoped) semiconductor, the density of electrons n equals the density of holes p . The recombination rate is then proportional to $R = Cn^2p = Cn^3$, with the Auger coefficient C . Hence, the recombination rate depends on the cubed carrier density. A low threshold carrier density n_{th} therefore is also beneficial for a reduction of Auger processes. Fig. A.6 illustrates some important Auger recombination mechanisms.

In the CHCC process, an electron in the conduction band recombines with a heavy-hole in the valence band. The excess free energy is given to another electron in the conduction band, which is then excited into a higher unoccupied state within the conduction

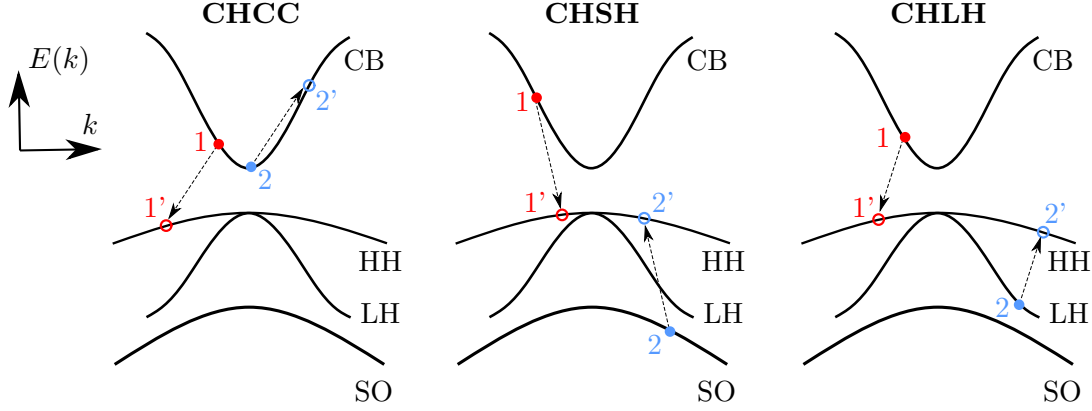


Fig. A.6: Auger recombination processes in III-V semiconductors. CB denotes the conduction band, HH the heavy-hole band, LH the light-hole band and SO the spin-orbit split-off valence band.

band. The recombination rate for this process, assuming parabolic bands and low carrier populations (Boltzmann statistics) is given by [18]

$$R = C_0^{\text{CHCC}} n^2 p e^{-E_a^{\text{CHCC}}/k_B T}, \quad (\text{A.46})$$

with the activation energy for the CHCC process

$$E_a^{\text{CHCC}} = E_g \frac{m_{\text{CB}}}{m_{\text{CB}} + m_{\text{HH}}}. \quad (\text{A.47})$$

The activation energy is determined by the bandgap E_g of the material and the in-plane effective masses in the conduction and heavy-hole valence band m_{CB} and m_{HH} , respectively. As the probability for the CHCC process scales approximately exponentially with the wavelength [257, 229], this Auger recombination mechanism becomes very important in narrow bandgap materials, such as InSb or InAs. Furthermore, the small electron mass of antimonides lowers the activation energy, which rises the probability for Auger scattering processes. Big hope has been put into lead salts alloys, which also feature a narrow bandgap. In contrast to III-V semiconductors, they have mirror conduction and valence bands, which should effectively suppress Auger recombination. However, it turned out that if inter-valley processes are also included in the description, Auger scattering becomes important again [253]. In the case of a CHSH process the recombination rate becomes [18]

$$R = C_0^{\text{CHSH}} n p^2 e^{-E_a^{\text{CHSH}}/k_B T}, \quad (\text{A.48})$$

with the activation energy for the CHSH process (assuming $E_g \geq \Delta_{\text{SO}}$) [257]

$$E_a^{\text{CHSH}} = (E_g - \Delta_{\text{SO}}) \frac{m_{\text{SO}}}{2m_{\text{HH}} + m_{\text{CB}} - m_{\text{SO}}}, \quad (\text{A.49})$$

where Δ_{SO} is the spin-orbit split-off energy and m_{SO} the in-plane effective mass of the charge carrier in the split-off band. From (A.48) it follows that the Auger recombination rate not only scales with the carrier density, but also increases exponentially with temperature. Strong CHSH Auger contributions can be expected for wavelengths at which the bandgap approximately matches the split-off energy Δ_{SO} [258]. However, for GaSb the spin-orbit split-off energy Δ_{SO} is larger than the bandgap energy (~ 0.725 eV), which suppresses the CHSH Auger scattering rate efficiently.

In the CHLH process, a conduction band electron recombines with a heavy-hole and the energy is transferred to a particle in the light-hole band, which is excited to the heavy-hole band. The recombination rate is similar to the CHSH process, but with a different activation energy [257]

$$E_a^{\text{CHLH}} = E_g \frac{m_{\text{LH}}}{2m_{\text{HH}} + m_{\text{CB}} - m_{\text{LH}}}, \quad (\text{A.50})$$

where m_{LH} is the in-plane effective mass in the light-hole valence band. An estimation of the Auger activation energies in GaSb can be derived by using $m_{\text{CB}} = 0.042m_0$, $m_{\text{HH}} = 0.4m_0$, $m_{\text{LH}} = 0.045m_0$, $m_{\text{SO}} = 0.14m_0$, $E_G = 0.73$ eV and $\Delta_{\text{SO}} = 0.8$ eV. As stated before, the CHSH process is effectively suppressed, because the bandgap energy is smaller than the spin-orbit split-off energy ($E_G < \Delta_{\text{SO}}$). For the CHCC process an activation energy of $E_a^{\text{CHCC}} = 69$ meV is calculated, while for the CHLH process $E_a^{\text{CHLH}} = 41$ meV is found. Finally, the total Auger coefficient [217] can be written as the sum of the individual contributions:

$$C_{\text{Auger}} = C_0^{\text{CHCC}} \exp\left(-\frac{E_a^{\text{CHCC}}}{k_B T}\right) + C_0^{\text{CHSH}} \exp\left(-\frac{E_a^{\text{CHSH}}}{k_B T}\right) + C_0^{\text{CHLH}} \exp\left(-\frac{E_a^{\text{CHLH}}}{k_B T}\right). \quad (\text{A.51})$$

The calculation of the discussed recombination rates assumed parabolic conduction and valence bands together with the Boltzmann statistics for the carrier distribution. These assumptions seem to simplify the situation too much, because semiconductor lasers have typical carrier densities in the 10^{18} cm^{-3} range. In a more sophisticated approach one should also consider the non-parabolicity of the bands and the Fermi-Dirac statistics of the electrons/holes [259]. To include the non-parabolicity of the bands, an accurate model of the material's bandstructure is essential, which may not always be known. However, non-parabolicity is only important for transitions far away from the band edge. Furthermore, the simplification in using a Boltzmann statistics for the carriers allows to derive analytical expressions for the Auger rates. The estimated error of the Auger rate is hence expected in the order of 20% [260, 261]. Theories about Auger scattering can describe the effects of temperature, bandgap and material composition in a good way. However, the Auger recombination rate is predicted to an accuracy of only within one order of magnitude [254].

Grein et al. pointed out that the Auger coefficient is not a good benchmark parameter when lasers with different optical designs are compared [262]. The problem is that the Auger coefficient increases squared with the total thickness of the heterostructure, which consists of wells and barriers. Consequently, the Auger coefficient increases also if only the barriers thickness is increased, but with the same active well. Yet, the net material gain per unit recombination current is unchanged.

Strategies to reduce the overall Auger recombination rate include a lowering of the threshold carrier density and/or strain engineering in the heterostructure. In type-II structures, such as the ICL, the spatial separated wells for electrons and holes in the active region reduce the electron-hole overlap. Therefore it can be expected that the Auger recombination rate is also lowered. On the other hand, the spatial separation also decreases the radiative recombination. According to [263], the threshold current density in ICLs (at room-temperature) mostly depends on the Auger recombination rate. Typical values for the 3D (bulk) Auger coefficient of ICLs in the wavelength range of $2.9 - 5.5 \mu\text{m}$ are $2 - 3 \times 10^{-28} \text{ cm}^6/\text{s}$ [191]. Fig. A.7 shows the Auger coefficients for various ICLs together with those of some III-V and II-VI bulk materials. While Auger recombination is the major contribution for narrow-gap materials, it plays only a minor role in e.g. GaAs-based lasers. There, the bandgap is $\sim 1 \text{ eV}$ larger than the spin-orbit splitting energy Δ_{SO} . Typical values for the Auger recombination coefficient in GaAs are in the order of $10^{-31} \text{ cm}^6/\text{s}$ [18].

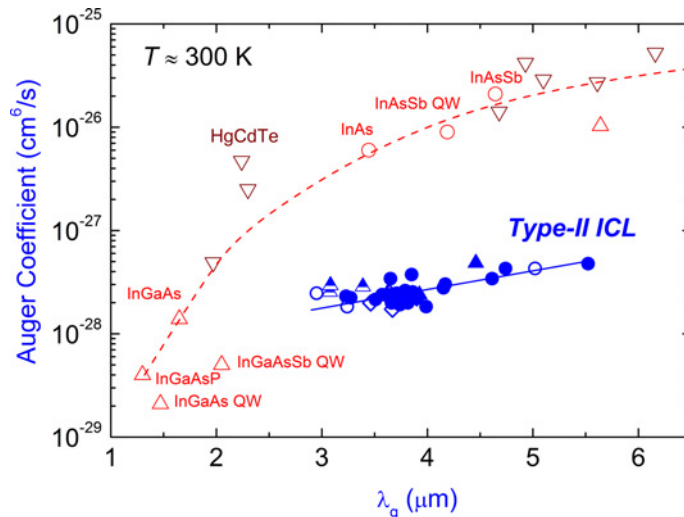


Fig. A.7: Auger coefficients for type-II ICL as well as III-V and II-VI materials extracted from measured data at different wavelengths. Reprinted with permission from [191] © 2013 IEEE.

A.3 Growth sheets

A.3.1 Quantum cascade laser P51

	Material	Thickness [nm]	Doping [cm^{-3}]	Description
	Si:InGaAs	10	1×10^{20}	Contact layer
	Si:InGaAs	350	8×10^{18}	Spacer
	$\text{Ga}_{0.5x}\text{Al}_{0.5(1-x)}\text{InAs}$	25	2×10^{17}	Grading V
	InAlAs	800	2×10^{17}	Cladding
	InAlAs	1500	1×10^{17}	Cladding
	$\text{Ga}_{0.5x}\text{Al}_{0.5(1-x)}\text{InAs}$	25	1×10^{17}	Grading IV
	Si:InGaAs	300	5×10^{16}	Waveguide
	$\text{Ga}_{0.5x}\text{Al}_{0.5(1-x)}\text{InAs}$	13.9	1×10^{17}	Grading VI
35x	$\text{Ga}_{0.5x}\text{Al}_{0.5(1-x)}\text{InAs}$	32.2	2×10^{17}	Grading II
	Active region	27.5		Active region
	$\text{Ga}_{0.5x}\text{Al}_{0.5(1-x)}\text{InAs}$	13.7	1×10^{17}	Grading III
	Si:InGaAs	500	5×10^{16}	Waveguide
	$\text{Ga}_{0.5x}\text{Al}_{0.5(1-x)}\text{InAs}$	25	1×10^{17}	Grading I
	InP	$350 \pm 25 \mu\text{m}$	$1-4 \times 10^{17}$	Substrate

Tab. A.1: Growth sheet of P51 quantum cascade laser design.

The original two-phonon resonance laser is designed by Z. Liu et al. [180]. The active region of P51 consists of a sequence of alternating layers of InAlAs/InGaAs with the layer thicknesses of 4.4/**1.8**/0.9/**5.7**/1.1/**5.4**/1.2/**4.5**/2.5 nm, where the InGaAs layers are written bold. The total thickness of the heterostructure is 5652.1 nm. In the following, the layer sequences for the intermediate grading regions are described. Again, bold numbers correspond to an InGaAs layer and doped layers are underlined.

Grading I: 0.5/**4.5**/1.0/**4.0**/1.5/**3.5**/2.0/3.0/2.5/2.5 nm, where the underlined layers are doped with $1 \times 10^{17} \text{ cm}^{-3}$.

Grading II: **3.4**/1.4/**3.3**/1.3/**3.2**/1.5/3.1/1.9/2.9/2.3/**2.7**/2.5/**2.7**.

Grading III: **2.6**/1.9/3.1/1.8/2.6/1.7 nm, where the underlined layers are doped with $1 \times 10^{17} \text{ cm}^{-3}$.

Grading IV: **0.8**/4.2/**1.6**/3.4/**2.5**/2.5/**3.4**/1.6/**4.2**/0.8 nm. All layers are doped with $1 \times 10^{17} \text{ cm}^{-3}$.

Grading V: 0.8/**4.2**/1.6/**3.4**/2.5/**2.5**/3.4/**1.6**/4.2/**0.8** nm. All layers are doped with $2 \times 10^{17} \text{ cm}^{-3}$.

Grading VI: 0.5/**3.6**/0.8/**3.3**/1.2/**2.9**/1.6 nm. All layers are doped with $1 \times 10^{17} \text{ cm}^{-3}$.

A.3.2 Interband cascade laser ICL3

	Material	Thickness [nm]	Doping [cm^{-3}]	Description
	InAs	25	2×10^{19}	Contact layer
	InAs (2.43 nm)/AlSb (2.3 nm)	2120	$8 \times 10^{17} \rightarrow 2 \times 10^{17}$ in InAs	Cladding
	GaSb	200	3×10^{17}	Waveguide
6x	active region	350		Active region
	GaSb	200	3×10^{17}	Waveguide
	InAs (2.43 nm)/AlSb (2.3 nm)	2120	$2 \times 10^{17} \rightarrow 8 \times 10^{17}$ in InAs	Cladding
	GaSb	200	2×10^{18}	Buffer
	GaSb	550 μm	5×10^{17}	Substrate

Tab. A.2: Growth sheet of ICL3.

A.4 Device fabrication

A.4.1 Ring quantum cascade laser

Cleaning of the sample

- An approximately $10 \times 10 \text{ mm}^2$ sample is cleaved from the wafer.
- Cleaning with Aceton (30 s) and Isopropanol, drying with N_2 .

Hard mask deposition

- Deposition of 1.4–1.7 μm Si_xN_y with Plasma enhanced chemical vapor deposition (PECVD) with the Oxford Systems PlasmaLab 80. Process temperature 300 $^\circ\text{C}$, work pressure 1 torr, base pressure 0.06 torr with the process gases silane (4% SiH_4 & 96% N_2) 700 sccm, NH_3 18 sccm, RF power 12 W (corresponds to ≈ 10 W effective power), steptime 140 min. Typical deposition rates are in the range of 10 – 12 nm/min.
- Check deposited film thickness with Filmetrics tool.

Optical lithography for the waveguides

- Spin coat positive photoresist AZ 5214 1:0 for 35 s at 4000 rpm (ramp 1 s)
- 60 s bake at 100 $^\circ\text{C}$
- 25 s rim exposure (Karl Suss MJB3 mask aligner)
- 25 s development in AZ 726 MIF + cleaning $2 \times \text{H}_2\text{O}$
- 12 s exposure of the waveguides
- 10 s development in AZ 726 MIF + cleaning $2 \times \text{H}_2\text{O}$

Hard mask etch

- Step time 10 min, CM pressure 0.055 torr, penning pressure 8×10^{-5} mbar, 2 sccm O_2 , 20 sccm CHF_3 , RF 120 W, Bias 430 V (Oxford Systems PlasmaLab 80)
- Removing of photoresist and residuals with plasma oxidation (TePla 100-E) for 10 min, 300 W and 0.7 torr O_2 .
- Removing of residuals with NEP and cleaning with Isopropanol.

Waveguide etch

- Reactive ion etch (RIE) preconditioning (Oxford Systems PlasmaLab 100)
- Step time 30 min, set pressure 2 mtorr, strike pressure 40 mtorr, temperature 250 °C, 5 sccm $SiCl_4$, 40 sccm Ar, 200 W RF power, carrier wafer Si
- ~60 min waveguide etch → etch depth $\sim 7.4 \mu m$ (Dektak Profilometer)
- Cleaning 15 s with H_2O

Hard mask removal

- Step time 10 min with SF_6 (Oxford Systems PlasmaLab 80)

Hard mask deposition

- Deposition of Si_xN_y with PECVD (Oxford Systems PlasmaLab 80). Process temperature 300 °C, work pressure 1 torr, base pressure 0.06 torr with the process gases silane (4% SiH_4 & 96% N_2) 700 sccm, NH_3 18 sccm, RF power 12 W (≈ 10 W effective power), step time 45 min.

E-beam lithography of the gratings

- Spin coat photoresist PMMA ARP 627.08 for 35 s at 4000 rpm (ramp 1 s)
- 5 min bake at 170 °C (resist thickness ~ 800 nm)
- Grating exposure, writefield $500 \times 500 \mu m^2$, step size 15.6 nm, dwell time 1.95 μs , nominal dose 133 $\mu C cm^{-2}$ (Raith e-LiNE system)
- 15 s development in AR 600-56 + cleaning Isopropanol

Hard mask etch

- Step time ~ 7 min, CM pressure 0.05 torr, penning pressure 8×10^{-5} mbar, 2 sccm O_2 , 20 sccm CHF_3 , RF 120 W, Bias 430 V (Oxford Systems PlasmaLab 80).
- Removing of photoresist and residuals with plasma oxidation (TePla 100) for 15 min, 300 W and 0.7 torr O_2 .
- Removing of residuals with NEP and cleaning with Isopropanol

Grating etch

- Step time $\sim 4 - 20$ min, set pressure 2 mtorr, strike pressure 40 mtorr, temperature 250°C , 5 sccm SiCl_4 , 40 sccm Ar, 200 W RF power, carrier wafer Si (Oxford Systems PlasmaLab 100)
- Cleaning in Acetone and cleaning with Isopropanol

Hard mask removal

- Step time 7 min with SF_6 (Oxford Systems PlasmaLab 100)

Passivation deposition

- Deposition of Si_xN_y with PECVD (Oxford Systems PlasmaLab 80). Process temperature 300°C , work pressure 1 torr, base pressure 0.06 torr with the process gases silane (4% SiH_4 & 96% N_2) 700 sccm, NH_3 18 sccm, RF power 12 W (≈ 10 W effective power), step time 40 min.

E-beam lithography for passivation open

- Spin coat photoresist PMMA ARP 627.08 for 35 s at 4000 rpm (ramp 1 s)
- 5 min bake at 170°C (resist thickness ~ 800 nm)
- Grating exposure, writefield $500 \times 500 \mu\text{m}^2$, step size 15.6 nm, dwell time 1.95 μs , nominal dose $133 \mu\text{C cm}^{-2}$ (Raith e-LiNE system)
- 10 s development in AR 600-56 + cleaning Isopropanol

Hard mask etch

- Step time ~ 5 min, CM pressure 0.05 torr, penning pressure 8×10^{-5} mbar, 2 sccm O_2 , 20 sccm CHF_3 , RF 120 W, Bias 430 V (Oxford Systems PlasmaLab 80).
- Removing of photoresist and residuals with plasma oxidation (TePla 100) for 10 min, 300 W and 0.7 torr O_2 .
- Removing of residuals with NEP and cleaning with Isopropanol

Sputtern of metallization

- $p_{\text{base}} = 2 \times 10^{-5}$ mbar, $p_{\text{work}} = 8 \times 10^{-3}$ mbar (von Ardenne LS320S)
- Titan cleaning: 2×60 s with 100 W RF power
- Sample cleaning (Ar sputtern): 4×30 s with 25 W RF power
- Titan: 2×30 s with 50 W RF power (~ 5 nm/min)
- Gold: 30×40 s with 25 W RF power (~ 30 nm/min)

Optical lithography for the back etch

- Spin coat positive photoresist maP-1275 for 35 s at 8000 rpm (ramp 1 s)
- 5 min bake at 100 °C
- 60 s exposure of the backetch mask (Karl Suess MJB3 mask aligner)
- 20 s development in ma-D331 + cleaning 2× H₂O

Top metallization back etch

- KI:I₂:H₂O = 4 g:1 g:40 mL + stir bar (etch rate ~ 1 μm/min)
- 20 min etch at room-temperature + cleaning 2× H₂O
- 10 min plasma oxidation (TePla 100), 300 W and 0.7 torr O₂.
- Removing of residuals with NEP and cleaning with Isopropanol

A.4.2 Ring interband cascade laser

Cleaning of the sample

- An approximately 10 × 10 mm² sample is cleaved from the wafer.
- Cleaning with Aceton (30 s) and Isopropanol, drying with N₂.

Hard mask deposition

- Deposition of 1.5 μm Si_xN_y with Plasma enhanced chemical vapor deposition (PECVD) with the Oxford Systems PlasmaLab 80. Process temperature 300 °C, work pressure 1 torr, base pressure 0.06 torr with the process gases silane (4% SiH₄ & 96% N₂) 700 sccm, NH₃ 18 sccm, RF power 12 W (corresponds to ≈ 10 W effective power), steptime 120 min. Typical deposition rates are in the range of 10–12 nm/min.
- Check deposited film thickness with Filmetrics tool

Optical lithography for the waveguides

- Spin coat positive photoresist AZ 5214 1:0 for 35 s at 4000 rpm (ramp 1 s)
- 60 s bake at 100 °C
- 25 s rim exposure (Karl Suess MJB3 mask aligner)
- 25 s development in AZ 726 MIF + cleaning 2× H₂O
- 12 s exposure of the waveguides
- 13 s development in AZ 726 MIF + cleaning 2× H₂O

Hard mask etch

- Step time 11.5 min, CM pressure 0.055 torr, penning pressure 8 × 10⁻⁵ mbar, 2 sccm O₂, 20 sccm CHF₃, RF 120 W, Bias 430 V (Oxford Systems PlasmaLab 80)

- Removing of photoresist and residuals with plasma oxidation (TePla 100-E) for 10 min, 300 W and 0.7 torr O₂.
- Removing of residuals with NEP and cleaning with Isopropanol

Waveguide etch

- Reactive ion etch (RIE) preconditioning (Oxford Systems PlasmaLab 100)
- Step time 45 min, set pressure 2 mtorr, strike pressure 40 mtorr, temperature 250 °C, 5 sccm SiCl₄, 40 sccm Ar, 200 W RF power, carrier wafer Si
- ~65 min waveguide etch → etch depth ~ 4.6 μm (Dektak Profilometer)
- Cleaning 60 s with H₂O + 20 s with Acetone + Isopropanol

Hard mask removal

- Step time 3 min with SF₆ (Oxford Systems PlasmaLab 80)

Hard mask deposition

- Deposition of Si_xN_y with PECVD (Oxford Systems PlasmaLab 80). Process temperature 300 °C, work pressure 1 torr, base pressure 0.06 torr with the process gases silane (4% SiH₄ & 96% N₂) 700 sccm, NH₃ 18 sccm, RF power 12 W (≈ 10 W effective power), steptime 60 min.

E-beam lithography of the gratings

- Spin coat photoresist PMMA ARP 627.08 for 35 s at 4000 rpm (ramp 1 s)
- 5 min bake at 170 °C (resist thickness ~800 nm)
- Grating exposure, writefield 500 × 500 μm², step size 15.6 nm, dwell time 1.95 μs, nominal dose 133 μC cm⁻² (Raith e-LiNE system)
- 12 s development in AR 600-56 + cleaning Isopropanol

Hard mask etch

- Step time ~ 7 min, CM pressure 0.05 torr, penning pressure 8 × 10⁻⁵ mbar, 2 sccm O₂, 20 sccm CHF₃, RF 120 W, Bias 430 V (Oxford Systems PlasmaLab 80).
- Removing of photoresist and residuals with plasma oxidation (TePla 100) for 10 min, 300 W and 0.7 torr O₂.
- Removing of residuals with NEP and cleaning with Isopropanol

Grating etch

- 30 min preconditioning

- Step time 19 min, set pressure 2 mtorr, strike pressure 40 mtorr, temperature 250 °C, 5 sccm SiCl₄, 40 sccm Ar, 200 W RF power, carrier wafer Si (Oxford Systems PlasmaLab 100)
- Cleaning 60 s with H₂O + 10 s with Acetone + Isopropanol

Hard mask removal

- Step time 4 min with SF₆ (Oxford Systems PlasmaLab 100)

Passivation deposition

- Deposition of Si_xN_y with PECVD (Oxford Systems PlasmaLab 80). Process temperature 300 °C, work pressure 1 torr, base pressure 0.06 torr with the process gases silane (4% SiH₄ & 96% N₂) 700 sccm, NH₃ 18 sccm, RF power 12 W (≈ 10 W effective power), steptime 45 min.

E-beam lithography for passivation open

- Spin coat photoresist PMMA ARP 627.08 for 35 s at 4000 rpm (ramp 1 s)
- 5 min bake at 170 °C (resist thickness ~800 nm)
- Grating exposure, writefield 500 × 500 μm², step size 15.6 nm, dwell time 1.95 μs, nominal dose 133 μC cm⁻² (Raith e-LiNE system)
- 13 s development in AR 600-56 + cleaning Isopropanol

Hard mask etch

- Step time ~ 3 min, CM pressure 0.015 torr, penning pressure 8 × 10⁻⁵ mbar, 40 sccm SF₆, RF 50 W (Oxford Systems PlasmaLab 80).
- ~ 1 min, CM pressure 0.050 torr
- Removing of photoresist and residuals with plasma oxidation (TePla 100) for 10 min, 300 W and 0.7 torr O₂.
- Cleaning with Acetone and Isopropanol
- Removing of residuals with NEP and cleaning with Isopropanol

Sputtern of metallization

- $p_{\text{base}} = 2 \times 10^{-5}$ mbar, $p_{\text{work}} = 8 \times 10^{-3}$ mbar (von Ardenne LS320S)
- Titan cleaning: 4 × 60 s with 100 W RF power
- Sample cleaning (Ar sputtern): 2 × 60 s with 25 W RF power
- Titan: 2 × 30 s with 50 W RF power (~ 5 nm/min)
- Gold: 25 × 40 s with 25 W RF power (~ 30 nm/min)

Optical lithography for the back etch

- Spin coat positive photoresist maP-1275 for 35 s at 4000 rpm (ramp 1 s)
- 5 min bake at 100 °C
- 60 s exposure of the backetch mask (Karl Suss MJB3 mask aligner)
- 25 s development in ma-D333 + cleaning 2× H₂O

Top metallization back etch

- Glue sample with AZ5214 onto glas carrier + 20 min on hotplate at 100 °C
- KI:I₂:H₂O = 4 g:1 g:40 mL + stir bar (etch rate ~ 1 μm/min)
- 8 min etch at room-temperature + cleaning 2× H₂O
- 10 min Ar sputtern: CM pressure 0.055 torr, penning pressure 5×10^{-5} mbar, 10 sccm Ar, RF 100 W (Oxford Systems PlasmaLab 80).
- 10 min plasma oxidation (TePla 100), 300 W and 0.7 torr O₂.
- Removing of residuals with NEP and cleaning with Isopropanol

Abbreviations and Acronyms

AFM	Atomic force microscope
AlN	Aluminium nitride
AlAs	Aluminium arsenide
AlGaAs	Aluminium gallium arsenide
AlSb	Aluminium antimonide
Ar	Argon
ARDE	Aspect ratio dependent etching
Au	Gold
AuSn	Gold tin
AZ 5214	Image-reversal photoresist
AZ 726 MIF	Developer for AZ 5214 photoresist
CB	Conduction band
CHHS	Conduction to heavy-hole and heavy-hole to split-off-hole Auger process
COMSOL	COMSOL Multiphysics® modeling software
CBV	Inter-valley conduction band absorption
CCD	Charge-coupled device
CHCC	Conduction to heavy-hole band and conduction to conduction band Auger process
CHLH	Conduction to heavy-hole band and light-hole to heavy-hole band Auger process
CHSH	Conduction to heavy-hole band and split-off to heavy-hole band Auger process
CHF₃	Fluoroform
CTE	Coefficient of thermal expansion
Cu	Copper
cw	Continuous-wave

DC	Direct current
DBR	Distributed Bragg reflector
DFB	Distributed feedback
DTGS	Deuterated triglycine sulfate
DUT	Device under test
EDQE	External differential quantum efficiency
e-Line	E-beam lithography
FCA	Free carrier absorption by free electrons
Fe	Iron
FSR	Free spectral range
FTIR	Fourier-Transform infrared
FWHM	Full width at half maximum
GaAs	Gallium arsenide
GaAsSb	Gallium arsenide antimonide
GaInSb	Gallium indium antimonide
GaSb	Gallium antimonide
GDC	Grating duty-cycle
GPIB	General Purpose Interface Bus
H₂O	Distilled water
HDPE	High density polyethylene
HH	Heavy-hole
HITRAN	High-resolution transmission molecular absorption
N₂	Nitrogen
I₂	Iodine
IC	Interband cascade
ICL	Interband cascade laser
ICL3	Interband cascade laser design 3
InAs	Indium arsenide
InAlAs	Indium aluminium arsenide
InGaAs	Indium gallium arsenide
InP	Indium phosphide
InSb	Indium antimonide
IV	Current-voltage
KBr	Potassium bromide

KI	Potassium iodide
LED	Light-emitting diode
LOD	Limit of detection
LH	Light-hole
LO	Longitudinal optical
LIV	Light-current-voltage
ma-D331	Photoresist developer
ma-D333	Photoresist developer
MATLAB	Commercial software for solving mathematical problems
maP-1275	Positive photoresist
MBE	Molecular beam epitaxy
MCT	Mercury cadmium telluride
MEMS	Microelectromechanical System
MIR	Mid-infrared
mid-IR	Mid-infrared
MOCVD	Metal organic chemical vapor deposition
NEP	N-Ethylpyrrolidone
P51	Quantum cascade laser design
PECVD	Plasma enhanced chemical vapor deposition
PMMA	Polymethylmethacrylate
QCD	Quantum cascade detector
QCL	Quantum cascade laser
QCLD	Quantum cascade laser detector
QW	Quantum well
QWIP	Quantum well infrared photodetector
RIE	Reactive ion etching
RT	Room-temperature
SCL	Separate-confinement layers
Sn	Tin
SEM	Scanning electron microscope
Si	Silicon
SiCl₄	Silicon tetrachloride
SiO₂	Silicon oxide
SiN	Silicon nitride

SL	Superlattice
SM	Semimetal
SMA	SubMiniature version A coaxial connector
SMIF	Semimetallic interface
SMSR	Side mode suppression ratio
SO	Split-off
SRH	Shockley-Read-Hall
TBR	Thermal boundary resistance
TE	Transverse electric
Te	Tellurium
TEM	Transverse electromagnetic
THz	Tera Hertz = 10^{12} Hz
TM	Transverse magnetic
Ti	Titanium
USB	Universal Serial Bus
VB	Valence band
VBO	Valence band offset
VCSEL	Vertical-cavity surface-emitting laser
WGM	Whispering-gallery mode
YAG	Yttrium-aluminium-garnet
ZnSe	Zinc Selenide

List of Symbols

A	Area	ϵ_0	Electric permittivity of free space $8.854 \times 10^{-12} \text{ F m}^{-1}$
α	Absorption coefficient	ϵ_r	Relative permittivity
α_m	Mirror losses	e	Elementary charge $1.6022 \times 10^{-19} \text{ C}$
α_w	Waveguide losses	F	Force
α_{tot}	Total losses	Γ	Confinement factor
β	Propagation constant	H	Magnetic field
c	Speed of light	h	Planck's constant $6.626 \times 10^{-34} \text{ J s}$
c_0	Speed of light in free space $299\,792\,458 \text{ m s}^{-1}$	\hbar	Reduced Planck's constant $h/2\pi = 1.0546 \times 10^{-34} \text{ J s}$
Δ_0	Split-off gap energy	I	Current
D	Electric displacement	I_{th}	Threshold current
$\partial_t, \frac{d}{dt}$	Time derivative	J	Current density
$\partial_x, \frac{d}{dx}$	Spatial derivative	J_{th}	Threshold current density
d	Distance	k	Wave vector
E	Energy	κ	Coupling constant, imaginary part of the complex refractive index
E_F	Fermi energy	k_B	Boltzmann constant $1.3807 \times 10^{-23} \text{ J K}^{-1}$
E_c	Conduction-band edge energy	Λ	Grating period
E_g	Band gap energy	λ	Wavelength
E_{ij}	Transition energy $E_i - E_j$	λ_0	Free-space wavelength
E_v	Valence-band edge energy		
E	Electric field		
ϵ	Permittivity		

λ_B	Bragg wavelength	\mathbf{q}	Plasmon wave vector
l	Length	q	Electric charge
μ	Permeability	R	Electrical resistance, reflectivity
μ_0	Magnetic permeability of free space $4\pi \times 10^{-7} \text{ H m}^{-1}$	\mathbf{r}	Position vector
μ_r	Relative permeability	r	Radius
m^*	Effective mass	σ	Duty-cycle, electrical conductivity
m_0	Electron rest mass $9.109 \times 10^{-31} \text{ kg}$	T	Temperature, transmissivity
ν	Frequency	T_0	Characteristic temperature
$\bar{\nu}$	Wave number	τ	Lifetime
\tilde{n}	Complex refractive index	τ_{nr}	Non-radiative lifetime
n	Refractive index	τ_r	Radiative lifetime
n_{eff}	Effective refractive index	t	Time
ω	Angular frequency	v	Velocity
ω_c	Cyclotron frequency	v_g	Group velocity
ω_p	Plasma frequency	x	Position coordinate
P	Optical power	y	Position coordinate
		z	Position coordinate

References

- [1] <http://hitran.org/>
- [2] D. Jung, S. Bank, M. L. Lee and D. Wasserman. *Next-generation mid-infrared sources*. Journal of Optics 19 (12): 123001 (2017). doi:10.1088/2040-8986/aa939b
- [3] R. N. Hall, G. E. Fenner, J. D. Kingsley, T. J. Soltys and R. O. Carlson. *Coherent Light Emission From GaAs Junctions*. Phys Rev Lett 9: 366–368 (1962). doi:10.1103/PhysRevLett.9.366
- [4] R. J. Phelan, A. R. Calawa, R. H. Rediker, R. J. Keyes and B. Lax. *INFRARED InSb LASER DIODE IN HIGH MAGNETIC FIELDS*. Applied Physics Letters 3 (9): 143–145 (1963). doi:10.1063/1.1753905
- [5] H. Kroemer. *A proposed class of hetero-junction injection lasers*. Proceedings of the IEEE 51 (12): 1782–1783 (1963). doi:10.1109/PROC.1963.2706
- [6] Z. Alferov. *Double heterostructure lasers: early days and future perspectives*. IEEE Journal of Selected Topics in Quantum Electronics 6 (6): 832–840 (2000). doi:10.1109/2944.902131
- [7] K. Vizbaras and M.-C. Amann. *Room-temperature 3.73 μ m GaSb-based type-I quantum-well lasers with quaternary barriers*. Semiconductor Science and Technology 27 (3): 032001 (2012). doi:10.1088/0268-1242/27/3/032001
- [8] H. Preier. *Recent advances in lead-chalcogenide diode lasers*. Applied physics 20 (3): 189–206 (1979). doi:10.1007/BF00886018
- [9] M. Tacke. *New developments and applications of tunable IR lead salt lasers*. Infrared Physics & Technology 36 (1): 447 – 463 (1995). doi:https://doi.org/10.1016/1350-4495(94)00101-P. Proceedings of the Sixth International Conference on Infrared Physics
- [10] J. Faist, F. Capasso, D. L. Sivco, C. Sirtori, A. L. Hutchinson and A. Y. Cho. *Quantum Cascade Laser*. Science 264 (5158): 553–556 (1994). doi:10.1126/science.264.5158.553
- [11] Y. Yao, A. J. Hoffman and C. F. Gmachl. *Mid-infrared quantum cascade lasers*. Nat Photon 6 (7): 432–439 (2012). doi:10.1038/nphoton.2012.143

- [12] B. S. Williams. *Terahertz quantum-cascade lasers*. Nature Photonics 1: 517– (2007)
- [13] I. Vurgaftman, R. Weih, M. Kamp, J. R. Meyer, C. L. Canedy, C. S. Kim, M. Kim, W. W. Bewley, C. D. Merritt, J. Abell and S. Höfling. *Interband cascade lasers*. Journal of Physics D: Applied Physics 48 (12): 123001 (2015). doi:10.1088/0022-3727/48/12/123001
- [14] R. Q. Yang. *Infrared laser based on intersubband transitions in quantum wells*. Superlattices and Microstructures 17 (1): 77 – 83 (1995). doi:10.1006/spmi.1995.1017
- [15] R. Weih, M. Kamp and S. Höfling. *Interband cascade lasers with room temperature threshold current densities below 100 A/cm²*. Applied Physics Letters 102 (23): 231123 (2013). doi:10.1063/1.4811133
- [16] L. Li, H. Ye, Y. Jiang, R. Q. Yang, J. C. Keay, T. D. Mishima, M. B. Santos and M. B. Johnson. *MBE-grown long-wavelength interband cascade lasers on InAs substrates*. Journal of Crystal Growth 425: 369 – 372 (2015). doi:10.1016/j.jcrysgro.2015.02.016
- [17] J. Faist. *Quantum Cascade Lasers*. Oxford Univ. Press, Oxford, UK (2013)
- [18] P. Zory. *Quantum Well Lasers*. OPTICS AND PHOTONICS SERIES. Academic Press (1993)
- [19] J. H. Smet, C. G. Fonstad and Q. Hu. *Intrawell and interwell intersubband transitions in multiple quantum wells for far-infrared sources*. Journal of Applied Physics 79 (12): 9305–9320 (1996). doi:10.1063/1.362607
- [20] G. Bastard. *Wave Mechanics Applied to Semiconductor Heterostructures*. John Wiley and Sons Inc., New York, NY (USA) (1990)
- [21] H. C. Liu, M. Buchanan and Z. R. Wasilewski. *How good is the polarization selection rule for intersubband transitions?* Applied Physics Letters 72 (14): 1682–1684 (1998). doi:10.1063/1.121151
- [22] I. Vurgaftman, W. W. Bewley, C. L. Canedy, C. S. Kim, M. Kim, J. R. Lindle, C. D. Merritt, J. Abell and J. R. Meyer. *Mid-IR Type-II Interband Cascade Lasers*. IEEE Journal of Selected Topics in Quantum Electronics 17 (5): 1435–1444 (2011). doi:10.1109/JSTQE.2011.2114331
- [23] I. Vurgaftman, W. Bewley, C. Canedy, C. Kim, M. Kim, C. Merritt, J. Abell, J. Lindle and J. Meyer. *Rebalancing of internally generated carriers for mid-infrared interband cascade lasers with very low power consumption*. Nature Communications 2: 585– (2011). doi:10.1038/ncomms1595
- [24] R. Q. Yang and S. S. Pei. *Novel type-II quantum cascade lasers*. Journal of Applied Physics 79 (11): 8197–8203 (1996). doi:10.1063/1.362554
- [25] G. Reider. *Photonik: Eine Einführung in die Grundlagen* (2004)

- [26] B. Saleh and M. Teich. *Fundamentals of photonics*. Wiley series in pure and applied optics. Wiley (1991)
- [27] D. M. Caughey and R. E. Thomas. *Carrier mobilities in silicon empirically related to doping and field*. Proceedings of the IEEE 55 (12): 2192–2193 (1967). doi:10.1109/PROC.1967.6123
- [28] C. Hilsum. *Simple empirical relationship between mobility and carrier concentration*. Electronics Letters 10 (13): 259–260 (1974). doi:10.1049/el:19740205
- [29] J. B. Khurgin. *Prospects and merits of metal-clad semiconductor lasers from nearly UV to far IR*. Opt Express 23 (4): 4186–4194 (2015). doi:10.1364/OE.23.004186
- [30] M. Brandstetter, C. Deutsch, M. Krall, H. Detz, D. C. MacFarland, T. Zederbauer, A. M. Andrews, W. Schrenk, G. Strasser and K. Unterrainer. *High power terahertz quantum cascade lasers with symmetric wafer bonded active regions*. Applied Physics Letters 103 (17): 171113 (2013). doi:10.1063/1.4826943
- [31] C. Sirtori, J. Faist, F. Capasso, D. L. Sivco, A. L. Hutchinson and A. Y. Cho. *Quantum cascade laser with plasmon-enhanced waveguide operating at 8.4 μm wavelength*. Applied Physics Letters 66 (24): 3242–3244 (1995). doi:10.1063/1.113391
- [32] C. Sirtori, P. Kruck, S. Barbieri, H. Page, J. Nagle, M. Beck, J. Faist and U. Oesterle. *Low-loss Al-free waveguides for unipolar semiconductor lasers*. Applied Physics Letters 75 (25): 3911–3913 (1999). doi:10.1063/1.125491
- [33] J. Devenson, D. Barate, O. Cathabard, R. Teissier and A. N. Baranov. *Very short wavelength ($\lambda = 3.1 - 3.3\mu\text{m}$) quantum cascade lasers*. Applied Physics Letters 89 (19): 191115 (2006). doi:10.1063/1.2387473
- [34] C. Gmachl, F. Capasso, D. L. Sivco and A. Y. Cho. *Recent progress in quantum cascade lasers and applications*. Reports on Progress in Physics 64 (11): 1533 (2001). doi:10.1088/0034-4885/64/11/204
- [35] M. Brandstetter, M. Krall, C. Deutsch, H. Detz, A. M. Andrews, W. Schrenk, G. Strasser and K. Unterrainer. *Influence of the facet type on the performance of terahertz quantum cascade lasers with double-metal waveguides*. Applied Physics Letters 102 (23): 231121 (2013). doi:10.1063/1.4811124
- [36] S. Fatholouloumi, E. Dupont, C. Chan, Z. Wasilewski, S. Laframboise, D. Ban, A. Mátyás, C. Jirauschek, Q. Hu and H. C. Liu. *Terahertz quantum cascade lasers operating up to ~ 200 K with optimized oscillator strength and improved injection tunneling*. Opt Express 20 (4): 3866–3876 (2012). doi:10.1364/OE.20.003866
- [37] E. Mujagić. *Ring Cavity Surface Emitting Semiconductor Lasers*. Ph.D. thesis, TU Wien (2010)
- [38] T. Ikegami. *Reflectivity of mode at facet and oscillation mode in double-*

- heterostructure injection lasers*. IEEE Journal of Quantum Electronics 8 (6): 470–476 (1972). doi:10.1109/JQE.1972.1077091
- [39] S. Ahn, C. Schwarzer, T. Zederbauer, D. C. MacFarland, H. Detz, A. M. Andrews, W. Schrenk and G. Strasser. *High-power, low-lateral divergence broad area quantum cascade lasers with a tilted front facet*. Applied Physics Letters 104 (5): 051101 (2014). doi:10.1063/1.4863504
- [40] F. Jerome, V. Gustavo, S. Giacomo, R. Markus, B. Christopher, H. Andreas and B. Mattias. *Quantum Cascade Laser Frequency Combs* (2016). doi:10.1515/nanoph-2016-0015
- [41] C. Schwarzer. *Advanced Quantum Cascade Ring Lasers*. Ph.D. thesis, TU Wien (2014)
- [42] L. R. O. F.R.S. *CXII. The problem of the whispering gallery*. The London, Edinburgh, and Dublin Philosophical Magazine and Journal of Science 20 (120): 1001–1004 (1910). doi:10.1080/14786441008636993
- [43] A. Baranov and E. Tournie. *Semiconductor Lasers: Fundamentals and Applications*. Woodhead Publishing Series in. Woodhead Publishing (2013)
- [44] J. Breeze. *Modelling Dielectric Resonators*, 13–41. Springer International Publishing, Cham (2016). doi:10.1007/978-3-319-44547-2_2
- [45] J. Faist, C. Gmachl, M. Striccoli, C. Sirtori, F. Capasso, D. L. Sivco and A. Y. Cho. *Quantum cascade disk lasers*. Applied Physics Letters 69 (17): 2456–2458 (1996). doi:10.1063/1.117496
- [46] L. Mahler, A. Tredicucci, F. Beltram, C. Walther, J. Faist, B. Witzigmann, H. E. Beere and D. A. Ritchie. *Vertically emitting microdisk lasers*. Nat Photon 3 (1): 46–49 (2009). doi:10.1038/nphoton.2008.248
- [47] M. Brandstetter, M. Liertzer, C. Deutsch, P. Klang, J. Schöberl, H. E. Türeci, G. Strasser, K. Unterrainer and S. Rotter. *Reversing the pump dependence of a laser at an exceptional point*. Nat Commun 5: – (2014). doi:10.1038/ncomms5034
- [48] M. R. Foreman, J. D. Swaim and F. Vollmer. *Whispering gallery mode sensors*. Adv Opt Photon 7 (2): 168–240 (2015). doi:10.1364/AOP.7.000168
- [49] M. Heiblum and J. Harris. *Analysis of curved optical waveguides by conformal transformation*. Quantum Electronics, IEEE Journal of 11 (2): 75–83 (1975). doi:10.1109/JQE.1975.1068563
- [50] T. J. Johnson. *Silicon microdisk resonators for nonlinear optics and dynamics*. Ph.D. thesis, California Institute of Technology (2009)
- [51] D. Rabus. *Integrated Ring Resonators: The Compendium*. Springer Series in Optical Sciences. Springer Berlin Heidelberg (2007)

- [52] T.-P. Lee, C. Burrus, J. Copeland, A. Dentai and D. Marcuse. *Short-cavity InGaAsP injection lasers: Dependence of mode spectra and single-longitudinal-mode power on cavity length*. IEEE Journal of Quantum Electronics 18 (7): 1101–1113 (1982). doi:10.1109/JQE.1982.1071656
- [53] K. Iga. *Surface-emitting laser-its birth and generation of new optoelectronics field*. IEEE Journal of Selected Topics in Quantum Electronics 6 (6): 1201–1215 (2000). doi:10.1109/2944.902168
- [54] G. K. Veerabathran, S. Sprengel, A. Andrejew and M.-C. Amann. *Room-temperature vertical-cavity surface-emitting lasers at 4 μm with GaSb-based type-II quantum wells*. Applied Physics Letters 110 (7): 071104 (2017). doi:10.1063/1.4975813
- [55] M. Razeghi. *High-Performance InP-Based Mid-IR Quantum Cascade Lasers*. Selected Topics in Quantum Electronics, IEEE Journal of 15 (3): 941–951 (2009). doi:10.1109/JSTQE.2008.2006764
- [56] B. Mroziowicz, M. Bugajski and W. Nakwaski. *Physics of Semiconductor Lasers*. Elsevier Science (2017)
- [57] V. Jayaraman, Z. M. Chuang and L. A. Coldren. *Theory, design, and performance of extended tuning range semiconductor lasers with sampled gratings*. IEEE Journal of Quantum Electronics 29 (6): 1824–1834 (1993). doi:10.1109/3.234440
- [58] R. Blanchard, S. Menzel, C. Pflügl, L. Diehl, C. Wang, Y. Huang, J.-H. Ryou, R. D. Dupuis, L. D. Negro and F. Capasso. *Gratings with an aperiodic basis: single-mode emission in multi-wavelength lasers*. New Journal of Physics 13 (11): 113023 (2011). doi:10.1088/1367-2630/13/11/113023
- [59] I. A. Avrutsky, D. S. Ellis, A. Tager, H. Anis and J. M. Xu. *Design of widely tunable semiconductor lasers and the concept of binary superimposed gratings (BSG's)*. IEEE Journal of Quantum Electronics 34 (4): 729–741 (1998). doi:10.1109/3.663458
- [60] M. von Edlinger, R. Weih, J. Scheuermann, L. Nähle, M. Fischer, J. Koeth, M. Kamp and S. Höfling. *Monolithic single mode interband cascade lasers with wide wavelength tunability*. Applied Physics Letters 109 (20): 201109 (2016). doi:10.1063/1.4968535
- [61] B. Mroziowicz. *External cavity wavelength tunable semiconductor lasers - A review* 16: 347–366 (2008). doi:10.2478/s11772-008-0045-9
- [62] I. Bayrakli. *Breath analysis using external cavity diode lasers: a review*. Journal of Biomedical Optics 22: 22 – 22 – 15 (2017). doi:10.1117/1.JBO.22.4.040901
- [63] M. G. Littman and H. J. Metcalf. *Spectrally narrow pulsed dye laser without beam expander*. Appl Opt 17 (14): 2224–2227 (1978). doi:10.1364/AO.17.002224
- [64] https://www.rp-photonics.com/external_cavity_diode_lasers.html
- [65] B. Hinkov, F. Fuchs, Q. K. Yang, J. M. Kaster, W. Bronner, R. Aidam, K. Köhler and J. Wagner. *Time-resolved spectral characteristics of external-cavity quantum*

- cascade lasers and their application to stand-off detection of explosives*. Applied Physics B 100 (2): 253–260 (2010). doi:10.1007/s00340-009-3863-7
- [66] A. Hugi, R. Terazzi, Y. Bonetti, A. Wittmann, M. Fischer, M. Beck, J. Faist and E. Gini. *External cavity quantum cascade laser tunable from 7.6 to 11.4 μ m*. Applied Physics Letters 95 (6): 061103 (2009). doi:10.1063/1.3193539
- [67] D. Zhang, J. Zhao, Q. Yang, W. Liu, Y. Fu, C. Li, M. Luo, S. Hu, Q. Hu and L. Wang. *Compact MEMS external cavity tunable laser with ultra-narrow linewidth for coherent detection*. Opt Express 20 (18): 19670–19682 (2012). doi:10.1364/OE.20.019670
- [68] O. Ambacher, R. Ostendorf, D. Bleh, A. Merten, J. Grahmann, R. Schmidt, M. Kunzer, S. Hugger and J. Wagner. *Combining external cavity quantum cascade lasers and MOEMS technology: An approach for miniaturization and fast wavelength scanning*. 2014 International Conference on Optical MEMS and Nanophotonics, 91–92 (2014). doi:10.1109/OMN.2014.6924608
- [69] J. Wagner, R. Ostendorf, J. Grahmann, A. Merten, S. Hugger, J. P. Jarvis, F. Fuchs, D. Boskovic and H. Schenk. *Widely tunable quantum cascade lasers for spectroscopic sensing* (2015). doi:10.1117/12.2082794
- [70] P. Blood. *Quantum Confined Laser Devices: Optical Gain and Recombination in Semiconductors*. Oxford Master Series in Condensed Matter Physics Series. Oxford University Press (2015)
- [71] H. Kogelnik and C. V. Shank. *Coupled-Wave Theory of Distributed Feedback Lasers*. Journal of Applied Physics 43 (5): 2327–2335 (1972). doi:http://dx.doi.org/10.1063/1.1661499
- [72] T. Numai. *Fundamentals of Semiconductor Lasers*. Springer Series in Optical Sciences. Springer Japan (2014)
- [73] <http://www.photodigm.com/difference-between-dbr-and-dfb-lasers>
- [74] D. I. Babic and S. W. Corzine. *Analytic expressions for the reflection delay, penetration depth, and absorptance of quarter-wave dielectric mirrors*. IEEE Journal of Quantum Electronics 28 (2): 514–524 (1992). doi:10.1109/3.123281
- [75] W. W. Bewley, C. L. Canedy, C. S. Kim, C. D. Merritt, M. V. Warren, I. Vurgaftman, J. R. Meyer and M. Kim. *Room-temperature mid-infrared interband cascade vertical-cavity surface-emitting lasers*. Applied Physics Letters 109 (15): 151108 (2016). doi:10.1063/1.4964840
- [76] M. Miller, M. Grabherr, R. Jager and K. J. Ebeling. *High-power VCSEL arrays for emission in the watt regime at room temperature*. IEEE Photonics Technology Letters 13 (3): 173–175 (2001). doi:10.1109/68.914311
- [77] R. Safaisini, J. R. Joseph and K. L. Lear. *Scalable High-CW-Power High-Speed 980-nm VCSEL Arrays*. IEEE Journal of Quantum Electronics 46 (11): 1590–1596 (2010). doi:10.1109/JQE.2010.2053917

- [78] J. Joannopoulos, S. Johnson, J. Winn and R. Meade. *Photonic Crystals: Molding the Flow of Light, Second Edition*. Princeton University Press (2011)
- [79] B. Hinkov. *Radio-Frequency Modulation of Low-Dissipation Distributed-Feedback Quantum Cascade Lasers*. Ph.D. thesis, ETH (2015)
- [80] M. I. Amanti, M. Fischer, G. Scalari, M. Beck and J. Faist. *Low-divergence single-mode terahertz quantum cascade laser*. *Nature Photonics* 3: 586– (2009). doi:10.1038/nphoton.2009.168
- [81] C. Schwarzer, E. Mujagić, S. I. Ahn, A. M. Andrews, W. Schrenk, W. Charles, C. Gmachl and G. Strasser. *Grating duty-cycle induced enhancement of substrate emission from ring cavity quantum cascade lasers*. *Applied Physics Letters* 100 (19): 191103 (2012). doi:10.1063/1.4712127
- [82] F. Kneubühl and M. Sigrist. *Laser*. Teubner Studienbücher Physik. Vieweg+Teubner Verlag (2015)
- [83] N. Finger. *Grating-Coupled Semiconductor Structures*. Ph.D. thesis (2000)
- [84] R. Noll and S. Macomber. *Analysis of grating surface emitting lasers*. *Quantum Electronics, IEEE Journal of* 26 (3): 456–466 (1990). doi:10.1109/3.52121
- [85] H. Maier. *Rote oberflächenemittierende DFB-Laserdioden*. Master’s thesis (2001)
- [86] N. Finger, W. Schrenk and E. Gornik. *Analysis of TM-polarized DFB laser structures with metal surface gratings*. *Quantum Electronics, IEEE Journal of* 36 (7): 780–786 (2000). doi:10.1109/3.848348
- [87] M. Schubert and F. Rana. *Analysis of terahertz surface emitting quantum-cascade lasers*. *Quantum Electronics, IEEE Journal of* 42 (3): 257–265 (2006). doi:10.1109/JQE.2005.863138
- [88] C. Sigler, J. D. Kirch, T. Earles, L. J. Mawst, Z. Yu and D. Botez. *Design for high-power, single-lobe, grating-surface-emitting quantum cascade lasers enabled by plasmon-enhanced absorption of antisymmetric modes*. *Applied Physics Letters* 104 (13): 131108 (2014). doi:10.1063/1.4869561
- [89] W. Streifer, D. Scifres and R. Burnham. *Coupled wave analysis of DFB and DBR lasers*. *IEEE Journal of Quantum Electronics* 13 (4): 134–141 (1977). doi:10.1109/JQE.1977.1069328
- [90] R. Kazarinov and C. Henry. *Second-order distributed feedback lasers with mode selection provided by first-order radiation losses*. *IEEE Journal of Quantum Electronics* 21 (2): 144–150 (1985). doi:10.1109/JQE.1985.1072627
- [91] H. Kogelnik. *Coupled wave theory for thick hologram gratings*. *The Bell System Technical Journal* 48 (9): 2909–2947 (1969). doi:10.1002/j.1538-7305.1969.tb01198.x
- [92] G. Wan-Hong, L. Jun-Qi, L. Quan-Yong, Z. Wei, L. Lu, W. Li-Jun, L. Feng-Qi and W. Zhan-Guo. *Design of surface emitting distributed feedback quantum cascade laser*

- with single-lobe far-field pattern and high outcoupling efficiency.* Chinese Physics B 19 (5): 054208 (2010). doi:10.1088/1674-1056/19/5/054208
- [93] C. Gourgon, J. Robadey, D. Martin, F. Filipowicz, L. Mahler, N. H. Ky, D. Deveaud and F. K. Reinhart. *Complex-coupled DFB lasers: advantages and drawbacks of gain and radiation loss grating.* IEEE Photonics Technology Letters 12 (7): 765–767 (2000). doi:10.1109/68.853493
- [94] E. Kapon, A. Hardy and A. Katzir. *The effect of complex coupling coefficients on distributed feedback lasers.* IEEE Journal of Quantum Electronics 18 (1): 66–71 (1982). doi:10.1109/JQE.1982.1071364
- [95] T. Hasegawa. *Quantitative Infrared Spectroscopy for Understanding of a Condensed Matter.* Springer Japan (2017)
- [96] <https://www.python.org/>
- [97] R. Kazarinov and R. Suris. *Possible amplification of electromagnetic waves in a semiconductor with a superlattice* 5: 707–709 (1971)
- [98] A. Cho and J. Arthur. *Molecular beam epitaxy.* Progress in Solid State Chemistry 10: 157 – 191 (1975). doi:[https://doi.org/10.1016/0079-6786\(75\)90005-9](https://doi.org/10.1016/0079-6786(75)90005-9)
- [99] W. P. McCray. *MBE deserves a place in the history books.* Nature Nanotechnology 2: 259– (2007). doi:10.1038/nnano.2007.121
- [100] M. Razeghi. *The MOCVD Challenge: A survey of GaInAsP-InP and GaInAsP-GaAs for photonic and electronic device applications, Second Edition.* Electronic materials and devices series. CRC Press (2010)
- [101] M. S. Vitiello, G. Scalari, B. Williams and P. D. Natale. *Quantum cascade lasers: 20 years of challenges.* Opt Express 23 (4): 5167–5182 (2015). doi:10.1364/OE.23.005167
- [102] M. Levinshtein, S. Rumyantsev and M. Shur. *Handbook Series on Semiconductor Parameters: Si, Ge, C (Diamond), GaAs, GaP, GaSb, InAs, InP, InSb.* Handbook Series on Semiconductor Parameters. World Scientific (1996)
- [103] T. P. Pearsall, R. Carles and J. C. Portal. *Single longitudinal-mode optical phonon scattering in Ga_{0.47}In_{0.53}As.* Applied Physics Letters 42 (5): 436–438 (1983). doi:10.1063/1.93962
- [104] J. Faist, C. Gmachl, F. Capasso, C. Sirtori, D. L. Sivco, J. N. Baillargeon and A. Y. Cho. *Distributed feedback quantum cascade lasers.* Applied Physics Letters 70 (20): 2670–2672 (1997). doi:10.1063/1.119208
- [105] M. Beck, D. Hofstetter, T. Aellen, J. Faist, U. Oesterle, M. Ilegems, E. Gini and H. Melchior. *Continuous Wave Operation of a Mid-Infrared Semiconductor Laser at Room Temperature.* Science 295 (5553): 301–305 (2002). doi:10.1126/science.1066408

- [106] G. Liang, T. Liu and Q. J. Wang. *Recent Developments of Terahertz Quantum Cascade Lasers*. IEEE Journal of Selected Topics in Quantum Electronics 23 (4): 1–18 (2017). doi:10.1109/JSTQE.2016.2625982
- [107] S. Jung, A. Jiang, Y. Jiang, K. Vijayraghavan, X. Wang, M. Troccoli and M. A. Belkin. *Broadly tunable monolithic room-temperature terahertz quantum cascade laser sources*. Nature Communications 5: 4267– (2014). doi:10.1038/ncomms5267
- [108] T. Udem, R. Holzwarth and T. W. Hänsch. *Optical frequency metrology*. Nature 416: 233– (2002). doi:10.1038/416233a
- [109] G. Villares, A. Hugi, S. Blaser and J. Faist. *Dual-comb spectroscopy based on quantum-cascade-laser frequency combs*. Nature Communications 5: 5192– (2014). doi:10.1038/ncomms6192
- [110] M. Razeghi, Q. Y. Lu, N. Bandyopadhyay, W. Zhou, D. Heydari, Y. Bai and S. Slivken. *Quantum cascade lasers: from tool to product*. Opt Express 23 (7): 8462–8475 (2015). doi:10.1364/OE.23.008462
- [111] O. Cathabard, R. Teissier, J. Devenson, J. C. Moreno and A. N. Baranov. *Quantum cascade lasers emitting near 2.6 μ m*. Applied Physics Letters 96 (14): 141110 (2010). doi:10.1063/1.3385778
- [112] A. Vizbaras, M. Anders, S. Katz, C. Grasse, G. Boehm, R. Meyer, M. A. Belkin and M. C. Amann. *Room-Temperature $\lambda \approx 2.7\mu$ m Quantum Cascade Laser Sources Based on Intracavity Second-Harmonic Generation*. IEEE Journal of Quantum Electronics 47 (5): 691–697 (2011). doi:10.1109/JQE.2011.2109372
- [113] Y. Bai, N. Bandyopadhyay, S. Tsao, S. Slivken and M. Razeghi. *Room temperature quantum cascade lasers with 27% wall plug efficiency*. Applied Physics Letters 98 (18): 181102 (2011). doi:10.1063/1.3586773
- [114] Y. Bai, S. Slivken, S. Kuboya, S. R. Darvish and M. Razeghi. *Quantum cascade lasers that emit more light than heat*. Nature Photonics 4: 99–102 (2010). doi:10.1038/nphoton.2009.263
- [115] B. Schwarz, P. Reininger, D. Ristanić, H. Detz, A. M. Andrews, W. Schrenk and G. Strasser. *Monolithically integrated mid-infrared lab-on-a-chip using plasmonics and quantum cascade structures*. Nat Commun 5 (2014). doi:10.1038/ncomms5085
- [116] S. Rudin and T. L. Reinecke. *Electron $\tilde{L}O$ -phonon scattering rates in semiconductor quantum wells*. Phys Rev B 41: 7713–7717 (1990). doi:10.1103/PhysRevB.41.7713
- [117] I. Vurgaftman, J. R. Meyer and L. R. Ram-Mohan. *Band parameters for III–V compound semiconductors and their alloys*. Journal of Applied Physics 89 (11): 5815–5875 (2001). doi:10.1063/1.1368156
- [118] R. Colombelli, K. Srinivasan, M. Troccoli, O. Painter, C. F. Gmachl, D. M. Tennant, A. M. Sergent, D. L. Sivco, A. Y. Cho and F. Capasso. *Quantum Cascade*

- Surface-Emitting Photonic Crystal Laser*. Science 302 (5649): 1374–1377 (2003). doi:10.1126/science.1090561
- [119] D. Hofstetter, J. Faist, M. Beck and U. Oesterle. *Surface-emitting 10.1 \hat{I}_4 m quantum-cascade distributed feedback lasers*. Applied Physics Letters 75 (24): 3769–3771 (1999). doi:10.1063/1.125450
- [120] W. Schrenk, N. Finger, S. Gianordoli, L. Hvozدارa, G. Strasser and E. Gornik. *Surface-emitting distributed feedback quantum-cascade lasers*. Applied Physics Letters 77 (14): 2086–2088 (2000). doi:10.1063/1.1313807
- [121] C. Pflügl, M. Austerer, W. Schrenk, S. Golka, G. Strasser, R. P. Green, L. R. Wilson, J. W. Cockburn, A. B. Krysa and J. S. Roberts. *Single-mode surface-emitting quantum-cascade lasers*. Applied Physics Letters 86 (21): 211102 (2005). doi:10.1063/1.1929070
- [122] C. Gmachl, J. Faist, F. Capasso, C. Sirtori, D. L. Sivco and A. Y. Cho. *Long-wavelength (9.5-11.5 μ m) microdisk quantum-cascade lasers*. IEEE Journal of Quantum Electronics 33 (9): 1567–1573 (1997). doi:10.1109/3.622638
- [123] E. Mujagić, S. Schartner, L. K. Hoffmann, W. Schrenk, M. P. Semtsiv, M. Wienold, W. T. Masselink and G. Strasser. *Grating-coupled surface emitting quantum cascade ring lasers*. Applied Physics Letters 93 (1): 011108 (2008). doi:10.1063/1.2958910
- [124] E. Mujagić, L. K. Hoffmann, S. Schartner, M. Nobile, W. Schrenk, M. P. Semtsiv, M. Wienold, W. T. Masselink and G. Strasser. *Low divergence single-mode surface emitting quantum cascade ring lasers*. Applied Physics Letters 93 (16): 161101 (2008). doi:10.1063/1.3000630
- [125] E. Mujagić, C. Deutsch, H. Detz, P. Klang, M. Nobile, A. M. Andrews, W. Schrenk, K. Unterrainer and G. Strasser. *Vertically emitting terahertz quantum cascade ring lasers*. Applied Physics Letters 95 (1): 011120 (2009). doi:10.1063/1.3176966
- [126] L. Mahler, M. I. Amanti, C. Walther, A. Tredicucci, F. Beltram, J. Faist, H. E. Beere and D. A. Ritchie. *Distributed feedback ring resonators for vertically emitting terahertz quantum cascade lasers*. Opt Express 17 (15): 13031–13039 (2009). doi:10.1364/OE.17.013031
- [127] C. Schwarzer, E. Mujagić, Y. Yao, W. Schrenk, J. Chen, C. Gmachl and G. Strasser. *Coherent coupling of ring cavity surface emitting quantum cascade lasers*. Applied Physics Letters 97 (7): 071103 (2010). doi:10.1063/1.3479913
- [128] E. Mujagić, M. Nobile, H. Detz, W. Schrenk, J. Chen, C. Gmachl and G. Strasser. *Ring cavity induced threshold reduction in single-mode surface emitting quantum cascade lasers*. Applied Physics Letters 96 (3): 031111 (2010). doi:10.1063/1.3292021
- [129] E. Mujagić, C. Schwarzer, W. Schrenk, J. Chen, C. Gmachl and G. Strasser. *Ring-cavity surface-emitting lasers as a building block for tunable and coherent quantum cascade laser arrays*. Semiconductor Science and Technology 26 (1): 014019 (2011). doi:10.1088/0268-1242/26/1/014019

- [130] E. Mujagić, C. Schwarzer, Y. Yao, J. Chen, C. Gmachl and G. Strasser. *Two-dimensional broadband distributed-feedback quantum cascade laser arrays*. Applied Physics Letters 98 (14): 141101 (2011). doi:10.1063/1.3574555
- [131] Y. Bai, S. Tsao, N. Bandyopadhyay, S. Slivken, Q. Y. Lu, D. Caffey, M. Pushkarsky, T. Day and M. Razeghi. *High power, continuous wave, quantum cascade ring laser*. Applied Physics Letters 99 (26): 261104 (2011). doi:10.1063/1.3672049
- [132] C. Schwarzer, R. Szedlak, S. Il Ahn, T. Zederbauer, H. Detz, A. Maxwell Andrews, W. Schrenk and G. Strasser. *Linearly polarized light from substrate emitting ring cavity quantum cascade lasers*. Applied Physics Letters 103 (8): 081101 (2013). doi:10.1063/1.4819034
- [133] R. Szedlak, C. Schwarzer, T. Zederbauer, H. Detz, A. Maxwell Andrews, W. Schrenk and G. Strasser. *On-chip focusing in the mid-infrared: Demonstrated with ring quantum cascade lasers*. Applied Physics Letters 104 (15): 151105 (2014). doi:10.1063/1.4871520
- [134] R. Szedlak, C. Schwarzer, T. Zederbauer, H. Detz, A. M. Andrews, W. Schrenk and G. Strasser. *Grating-based far field modifications of ring quantum cascade lasers*. Opt Express 22 (13): 15829–15836 (2014). doi:10.1364/OE.22.015829
- [135] M. Brandstetter, A. Genner, C. Schwarzer, E. Mujagic, G. Strasser and B. Lendl. *Time-resolved spectral characterization of ring cavity surface emitting and ridge-type distributed feedback quantum cascade lasers by step-scan FT-IR spectroscopy*. Opt Express 22 (3): 2656–2664 (2014). doi:10.1364/OE.22.002656
- [136] H. Moser, A. Genner, J. Ofner, C. Schwarzer, G. Strasser and B. Lendl. *Application of a ring cavity surface emitting quantum cascade laser (RCSE-QCL) on the measurement of H₂S in a CH₄ matrix for process analytics*. Opt Express 24 (6): 6572–6585 (2016). doi:10.1364/OE.24.006572
- [137] E. Tutuncu, V. Kokoric, R. Szedlak, D. MacFarland, T. Zederbauer, H. Detz, A. M. Andrews, W. Schrenk, G. Strasser and B. Mizaikoff. *Advanced gas sensors based on substrate-integrated hollow waveguides and dual-color ring quantum cascade lasers*. Analyst 141: 6202–6207 (2016). doi:10.1039/C6AN01130F
- [138] R. Szedlak. *On the Light Emission from Ring Quantum Cascade Lasers and their Application in Spectroscopic Sensing*. Ph.D. thesis, TU Wien (2017)
- [139] G. D. Gillen and S. Guha. *Modeling and propagation of near-field diffraction patterns: A more complete approach*. American Journal of Physics 72 (9): 1195–1201 (2004). doi:10.1119/1.1767102
- [140] G. Gillen, K. Gillen and S. Guha. *Light Propagation in Linear Optical Media*. Optics, Lasers et Photonics. Taylor & Francis (2013)
- [141] R. Szedlak, M. Holzbauer, P. Reininger, D. MacFarland, T. Zederbauer, H. Detz, A. M. Andrews, W. Schrenk and G. Strasser. *Ring quantum cascade lasers*

- with grating phase shifts and a light collimating dielectric metamaterial for enhanced infrared spectroscopy.* *Vibrational Spectroscopy* 84: 101 – 105 (2016). doi:10.1016/j.vibspec.2016.03.009
- [142] R. Szedlak, M. Holzbauer, D. MacFarland, T. Zederbauer, H. Detz, A. M. Andrews, C. Schwarzer, W. Schrenk and G. Strasser. *The influence of whispering gallery modes on the far field of ring lasers.* *Sci Rep* 5: 16668 (2015). doi:10.1038/srep16668
- [143] S. E. Yumin, K. Komori and S. Arai. *GaInAsP/InP semiconductor vertical GRIN-lens for semiconductor optical devices.* *IEEE Photonics Technology Letters* 6 (5): 601–604 (1994). doi:10.1109/68.285554
- [144] J. Neu, B. Krolla, O. Paul, B. Reinhard, R. Beigang and M. Rahm. *Metamaterial-based gradient index lens with strong focusing in the THz frequency range.* *Opt Express* 18 (26): 27748–27757 (2010). doi:10.1364/OE.18.027748
- [145] M. Calvo and V. Lakshminarayanan. *Optical Waveguides: From Theory to Applied Technologies.* Optical Science and Engineering. CRC Press (2007)
- [146] R. Szedlak, A. Harrer, M. Holzbauer, B. Schwarz, J. P. Waclawek, D. MacFarland, T. Zederbauer, H. Detz, A. M. Andrews, W. Schrenk, B. Lendl and G. Strasser. *Remote Sensing with Commutable Monolithic Laser and Detector.* *ACS Photonics* 3 (10): 1794–1798 (2016). doi:10.1021/acsp Photonics.6b00603
- [147] D. Hofstetter, M. Beck and J. Faist. *Quantum-cascade-laser structures as photodetectors.* *Applied Physics Letters* 81 (15): 2683–2685 (2002). doi:10.1063/1.1512954
- [148] F. Giorgetta, E. Baumann, M. Graf, Q. Yang, C. Manz, K. Kohler, H. Beere, D. Ritchie, E. Linfield, A. Davies, Y. Fedoryshyn, H. Jackel, M. Fischer, J. Faist and D. Hofstetter. *Quantum Cascade Detectors.* *Quantum Electronics, IEEE Journal of* 45 (8): 1039–1052 (2009). doi:10.1109/JQE.2009.2017929
- [149] L. Gendron, M. Carras, A. Huynh, V. Ortiz, C. Koeniguer and V. Berger. *Quantum cascade photodetector.* *Applied Physics Letters* 85 (14): 2824–2826 (2004). doi:10.1063/1.1781731
- [150] M. Graf, N. Hoyler, M. Giovannini, J. Faist and D. Hofstetter. *InP-based quantum cascade detectors in the mid-infrared.* *Applied Physics Letters* 88 (24): 241118 (2006). doi:10.1063/1.2210088
- [151] P. Reininger, B. Schwarz, H. Detz, D. MacFarland, T. Zederbauer, A. M. Andrews, W. Schrenk, O. Baumgartner, H. Kosina and G. Strasser. *Diagonal-transition quantum cascade detector.* *Applied Physics Letters* 105 (9): 091108 (2014). doi:10.1063/1.4894767
- [152] B. Schwarz, P. Reininger, H. Detz, T. Zederbauer, A. M. Andrews, S. Kalchmair, W. Schrenk, O. Baumgartner, H. Kosina and G. Strasser. *A bi-functional quantum cascade device for same-frequency lasing and detection.* *Applied Physics Letters* 101 (19): 191109 (2012). doi:10.1063/1.4767128

- [153] B. Schwarz, P. Reininger, H. Detz, T. Zederbauer, A. M. Andrews, W. Schrenk and G. Strasser. *Monolithically Integrated Mid-Infrared Quantum Cascade Laser and Detector*. *Sensors* 13 (2): 2196–2205 (2013). doi:10.3390/s130202196
- [154] D. Ristanic, B. Schwarz, P. Reininger, H. Detz, T. Zederbauer, A. M. Andrews, W. Schrenk and G. Strasser. *Monolithically integrated mid-infrared sensor using narrow mode operation and temperature feedback*. *Applied Physics Letters* 106 (4): 041101 (2015). doi:10.1063/1.4906802
- [155] A. Harrer, R. Szedlak, B. Schwarz, H. Moser, T. Zederbauer, D. MacFarland, H. Detz, A. M. Andrews, W. Schrenk, B. Lendl and G. Strasser. *Mid-infrared surface transmitting and detecting quantum cascade device for gas-sensing*. *Scientific Reports* 6: 21795– (2016). doi:10.1038/srep21795
- [156] B. Schwarz, D. Ristanic, P. Reininger, T. Zederbauer, D. MacFarland, H. Detz, A. M. Andrews, W. Schrenk and G. Strasser. *High performance bi-functional quantum cascade laser and detector*. *Applied Physics Letters* 107 (7): 071104 (2015). doi:10.1063/1.4927851
- [157] S. W. S. Timothy J. Johnson, Robert L. Sams. *The PNNL quantitative infrared database for gas-phase sensing: a spectral library for environmental, hazmat, and public safety standoff detection* (2004). doi:10.1117/12.515604
- [158] H. K. Lee, K. S. Chung, J. S. Yu and M. Razeghi. *Thermal analysis of buried heterostructure quantum cascade lasers for long-wavelength infrared emission using 2D anisotropic heat-dissipation model*. *physica status solidi (a)* 206 (2): 356–362 (2009). doi:10.1002/pssa.200824314
- [159] J. Faist, F. Capasso, C. Sirtori, D. L. Sivco, A. L. Hutchinson and A. Y. Cho. *Continuous wave operation of a vertical transition quantum cascade laser above $T=80$ K*. *Applied Physics Letters* 67 (21): 3057–3059 (1995). doi:10.1063/1.114863
- [160] A. Lops, V. Spagnolo and G. Scamarcio. *Thermal modeling of GaInAs/AlInAs quantum cascade lasers*. *Journal of Applied Physics* 100 (4): 043109 (2006). doi:10.1063/1.2222074
- [161] V. Spagnolo, A. Lops, G. Scamarcio, M. S. Vitiello and C. Di Franco. *Improved thermal management of mid-IR quantum cascade lasers*. *Journal of Applied Physics* 103 (4): 043103 (2008). doi:10.1063/1.2840136
- [162] K. Watari, M. E. Brito, M. Toriyama, K. Ishizaki, S. Cao and K. Mori. *Thermal conductivity of Y_2O_3 -doped Si_3N_4 ceramic at 4 to 1000 K*. *Journal of Materials Science Letters* 18 (11): 865–867 (1999). doi:10.1023/A:1006696126661
- [163] H. Lee and J. Yu. *Thermal analysis of short wavelength InGaAs/InAlAs quantum cascade lasers*. *Solid-State Electronics* 54 (8): 769 – 776 (2010). doi:10.1016/j.sse.2010.03.015
- [164] G. Chen. *Thermal conductivity and ballistic-phonon transport in the cross-*

- plane direction of superlattices.* Phys Rev B 57: 14958–14973 (1998). doi:10.1103/PhysRevB.57.14958
- [165] M. S. Vitiello, G. Scamarcio, V. Spagnolo, A. Lops, Q. Yang, C. Manz and J. Wagner. *Experimental investigation of the lattice and electronic temperatures in $Ga_{0.47}In_{0.53}As/Al_{0.62}Ga_{0.38}As_{1-x}Sb_x$ quantum-cascade lasers.* Applied Physics Letters 90 (12): 121109 (2007). doi:10.1063/1.2717018
- [166] E. T. Swartz and R. O. Pohl. *Thermal boundary resistance.* Rev Mod Phys 61: 605–668 (1989). doi:10.1103/RevModPhys.61.605
- [167] C. Zhu, Y.-g. Zhang, A.-z. Li and Z.-b. Tian. *Analysis of key parameters affecting the thermal behavior and performance of quantum cascade lasers.* Journal of Applied Physics 100 (5): 053105 (2006). doi:10.1063/1.2344812
- [168] M. Vitiello, G. Scamarcio and V. Spagnolo. *Temperature Dependence of Thermal Conductivity and Boundary Resistance in THz Quantum Cascade Lasers.* Selected Topics in Quantum Electronics, IEEE Journal of 14 (2): 431–435 (2008). doi:10.1109/JSTQE.2007.910102
- [169] K. Q. Le and S. Kim. *Model for cross-plane thermal conductivity of layered quantum semiconductor structures and application for thermal modeling of GaInAs/AlInAs-based quantum cascade lasers.* physica status solidi (a) 205 (2): 392–396 (2008). doi:10.1002/pssa.200723346
- [170] C. Evans, D. Indjin, Z. Ikonic, P. Harrison, M. Vitiello, V. Spagnolo and G. Scamarcio. *Thermal Modeling of Terahertz Quantum-Cascade Lasers: Comparison of Optical Waveguides.* Quantum Electronics, IEEE Journal of 44 (7): 680–685 (2008). doi:10.1109/JQE.2008.922327
- [171] D. G. Cahill and R. O. Pohl. *Thermal conductivity of amorphous solids above the plateau.* Phys Rev B 35: 4067–4073 (1987). doi:10.1103/PhysRevB.35.4067
- [172] Y. Flores, M. Elagin, S. Kurlov, A. Aleksandrova, G. Monastyrskyi, J. Kischkat, M. Semtsiv and W. Masselink. *Growth initiation for buried-heterostructure quantum-cascade laser regrowth by gas-source molecular-beam epitaxy.* Journal of Crystal Growth 398 (0): 40 – 44 (2014). doi:10.1016/j.jcrysgro.2014.04.010
- [173] A. Bismuto. *Mid-infrared quantum cascade lasers: active medium and waveguide engineering.* Ph.D. thesis, ETH (2011)
- [174] C. Gmachl, A. Sergent, A. Tredicucci, F. Capasso, A. Hutchinson, D. L. Sivco, J. N. Baillargeon, S. N. G. Chu and A. Y. Cho. *Improved CW operation of quantum cascade lasers with epitaxial-side heat-sinking.* Photonics Technology Letters, IEEE 11 (11): 1369–1371 (1999). doi:10.1109/68.803048
- [175] A. Wittmann, Y. Bonetti, M. Fischer, J. Faist, S. Blaser and E. Gini. *Distributed-Feedback Quantum-Cascade Lasers at $9\mu m$ Operating in Continuous Wave Up to 423 K.* Photonics Technology Letters, IEEE 21 (12): 814–816 (2009). doi:10.1109/LPT.2009.2019117

- [176] A. Evans, J. S. Yu, J. David, L. Doris, K. Mi, S. Slivken and M. Razeghi. *High-temperature, high-power, continuous-wave operation of buried heterostructure quantum-cascade lasers*. Applied Physics Letters 84 (3): 314–316 (2004). doi:10.1063/1.1641174
- [177] A. Evans, S. R. Darvish, S. Slivken, J. Nguyen, Y. Bai and M. Razeghi. *Buried heterostructure quantum cascade lasers with high continuous-wave wall plug efficiency*. Applied Physics Letters 91 (7): 071101 (2007). doi:10.1063/1.2770768
- [178] D. H. Wu and M. Razeghi. *High power, low divergent, substrate emitting quantum cascade ring laser in continuous wave operation*. APL Materials 5 (3): 035505 (2017). doi:10.1063/1.4978810
- [179] C. Boyle, C. Sigler, J. D. Kirch, D. F. Lindberg, T. Earles, D. Botez and L. J. Mawst. *High-power, surface-emitting quantum cascade laser operating in a symmetric grating mode*. Applied Physics Letters 108 (12): 121107 (2016). doi:10.1063/1.4944846
- [180] Z. Liu, D. Wasserman, S. Howard, A. Hoffman, C. Gmachl, X. Wang, T. Tanbun-Ek, L. Cheng and F.-S. Choa. *Room-temperature continuous-wave quantum cascade lasers grown by MOCVD without lateral regrowth*. Photonics Technology Letters, IEEE 18 (12): 1347–1349 (2006). doi:10.1109/LPT.2006.877006
- [181] H. Detz. *Thermal expansion of III-V materials in atomistic models using empirical Tersoff potentials*. Electronics Letters 51 (18): 1455–1457 (2015). doi:10.1049/el.2015.1302
- [182] B. W. Hakki and T. L. Paoli. *Gain spectra in GaAs double-heterostructure injection lasers*. Journal of Applied Physics 46 (3): 1299–1306 (1975). doi:10.1063/1.321696
- [183] A. Soibel, K. Mansour, Y. Qiu, C. J. Hill and R. Q. Yang. *Optical gain, loss, and transparency current in high performance mid-infrared interband cascade lasers*. Journal of Applied Physics 101 (9): 093104 (2007). doi:10.1063/1.2723188
- [184] J. Faist, F. Capasso, D. L. Sivco, A. L. Hutchinson, S.-N. G. Chu and A. Y. Cho. *Short wavelength ($\lambda \sim 3.4\mu\text{m}$) quantum cascade laser based on strained compensated InGaAs/AlInAs*. Applied Physics Letters 72 (6): 680–682 (1998). doi:10.1063/1.120843
- [185] N. Bandyopadhyay, Y. Bai, S. Tsao, S. Nida, S. Slivken and M. Razeghi. *Room temperature continuous wave operation of $\lambda \sim 3 - 3.2\mu\text{m}$ quantum cascade lasers*. Applied Physics Letters 101 (24): 241110 (2012). doi:10.1063/1.4769038
- [186] A. N. Baranov and R. Teissier. *Quantum Cascade Lasers in the InAs/AlSb Material System*. IEEE Journal of Selected Topics in Quantum Electronics 21 (6): 85–96 (2015). doi:10.1109/JSTQE.2015.2426412
- [187] J. R. Meyer, C. A. Hoffman, F. J. Bartoli and L. R. Ram-Mohan. *Type-II quantum-well lasers for the mid-wavelength infrared*. Applied Physics Letters 67 (6): 757–759 (1995). doi:10.1063/1.115216

- [188] A. Haug. *Free-carrier absorption in semiconductor lasers*. Semiconductor Science and Technology 7 (3): 373 (1992). doi:10.1088/0268-1242/7/3/017
- [189] J. R. Meyer, I. Vurgaftman, R. Q. Yang and L. R. Ram-Mohan. *Type-II and type-I interband cascade lasers*. Electronics Letters 32 (1): 45–46 (1996). doi:10.1049/el:19960064
- [190] G. Agrawal and N. Dutta. *Long wavelength semiconductor lasers*. Van Nostrand Reinhold Co. Inc., New York, NY (1986)
- [191] I. Vurgaftman, W. W. Bewley, C. L. Canedy, C. S. Kim, M. Kim, C. D. Merritt, J. Abell and J. R. Meyer. *Interband Cascade Lasers With Low Threshold Powers and High Output Powers*. IEEE Journal of Selected Topics in Quantum Electronics 19 (4): 1200210–1200210 (2013). doi:10.1109/JSTQE.2012.2237017
- [192] R. Q. Yang, J. L. Bradshaw, J. D. Bruno, J. T. Pham and D. E. Wortman. *Mid-infrared type-II interband cascade lasers*. IEEE Journal of Quantum Electronics 38 (6): 559–568 (2002). doi:10.1109/JQE.2002.1005406
- [193] I. Vurgaftman, J. R. Meyer and L. R. Ram-Mohan. *High-power/low-threshold type-II interband cascade mid-IR laser-design and modeling*. IEEE Photonics Technology Letters 9 (2): 170–172 (1997). doi:10.1109/68.553079
- [194] M. Sweeny and J. Xu. *Resonant interband tunnel diodes*. Applied Physics Letters 54 (6): 546–548 (1989). doi:10.1063/1.100926
- [195] R. Q. Yang, C. H. Lin, P. C. Chang, S. J. Murry, D. Zhang, S. S. Pei, S. R. Kurtz, A. N. Chu and F. Ren. *Mid-ir interband cascade electroluminescence in type-II quantum wells*. Electronics Letters 32 (17): 1621–1622 (1996). doi:10.1049/el:20030095
- [196] C.-H. Lin, R. Q. Yang, D. Zhang, S. J. Murry, S. S. Pei, A. A. Allerman and S. R. Kurtz. *Type-II interband quantum cascade laser at 3.8 μ m*. Electronics Letters 33 (7): 598–599 (1997). doi:10.1049/el:19970421
- [197] C. L. Felix, W. W. Bewley, I. Vurgaftman, J. R. Meyer, D. Zhang, C. H. Lin, R. Q. Yang and S. S. Pei. *Interband cascade laser emitting > 1 photon per injected electron*. IEEE Photonics Technology Letters 9 (11): 1433–1435 (1997). doi:10.1109/68.634699
- [198] C. L. Felix, W. W. Bewley, E. H. Aifer, I. Vurgaftman, J. R. Meyer, C. H. Lin, D. Zhang, S. J. Murry, R. Q. Yang and S. S. Pei. *Low threshold 3 μ m interband cascade “W” laser*. Journal of Electronic Materials 27 (2): 77–80 (1998). doi:10.1007/s11664-998-0192-2
- [199] L. J. Olafsen, E. H. Aifer, I. Vurgaftman, W. W. Bewley, C. L. Felix, J. R. Meyer, D. Zhang, C.-H. Lin and S. S. Pei. *Near-room-temperature mid-infrared interband cascade laser*. Applied Physics Letters 72 (19): 2370–2372 (1998). doi:10.1063/1.121359

- [200] R. Q. Yang, J. D. Bruno, J. L. Bradshaw, J. T. Pham and D. E. Wortman. *High-power interband cascade lasers with quantum efficiency > 450%*. Electronics Letters 35 (15): 1254–1255 (1999). doi:10.1049/el:19990880
- [201] D. Zhang, E. Dupont, R. Q. Yang, H. C. Liu, C.-H. Lin, M. Buchanan and S. S. Pei. *Long-wavelength infrared ($\sim 10\text{--}15\mu\text{m}$) electroluminescence from Sb-based interband cascade devices*. Opt Express 1 (4): 97–101 (1997). doi:10.1364/OE.1.000097
- [202] J. L. Bradshaw, J. T. Pham, R. Q. Yang, J. D. Bruno and D. E. Wortman. *Enhanced CW performance of the interband cascade laser using improved device fabrication*. IEEE Journal of Selected Topics in Quantum Electronics 7 (2): 102–105 (2001). doi:10.1109/2944.954117
- [203] J. L. Bradshaw, J. D. Bruno, J. T. Pham, D. E. Wortman, S. Zhang and S. R. J. Brueck. *Single-longitudinal-mode emission from interband cascade DFB laser with a grating fabricated by interferometric lithography*. IEE Proceedings - Optoelectronics 150 (4): 288–292 (2003). doi:10.1049/ip-opt:20030613
- [204] C. J. Hill, B. Yang and R. Q. Yang. *Low-threshold interband cascade lasers operating above room temperature*. Physica E: Low-dimensional Systems and Nanostructures 20 (3): 486 – 490 (2004). doi:10.1016/j.physe.2003.08.064
- [205] M. Kim, C. L. Canedy, W. W. Bewley, C. S. Kim, J. R. Lindle, J. Abell, I. Vurgaftman and J. R. Meyer. *Interband cascade laser emitting at $\lambda = 3.75\mu\text{m}$ in continuous wave above room temperature*. Applied Physics Letters 92 (19): 191110 (2008). doi:10.1063/1.2930685
- [206] M. Kim, W. W. Bewley, C. L. Canedy, C. S. Kim, C. D. Merritt, J. Abell, I. Vurgaftman and J. R. Meyer. *High-power continuous-wave interband cascade lasers with 10 active stages*. Opt Express 23 (8): 9664–9672 (2015). doi:10.1364/OE.23.009664
- [207] W. W. Bewley, C. L. Canedy, C. S. Kim, M. Kim, C. D. Merritt, J. Abell, I. Vurgaftman and J. R. Meyer. *High-power room-temperature continuous-wave mid-infrared interband cascade lasers*. Opt Express 20 (19): 20894–20901 (2012). doi:10.1364/OE.20.020894
- [208] J. Scheuermann, R. Weih, M. von Edlinger, L. Nähle, M. Fischer, J. Koeth, M. Kamp and S. Höfling. *Single-mode interband cascade lasers emitting below $\sim 2.8\mu\text{m}$* . Applied Physics Letters 106 (16): 161103 (2015). doi:10.1063/1.4918985
- [209] S. Höfling, R. Weih, M. Dallner, J. Scheuermann, M. von Edlinger, L. Nähle, M. Fischer, J. Koeth and M. Kamp. *Mid-infrared ($\sim 2.8\mu\text{m}$ to $\sim 7.1\mu\text{m}$) interband cascade lasers* (2015). doi:10.1117/12.2193657
- [210] M. Dallner, F. Hau, S. Höfling and M. Kamp. *InAs-based interband-cascade-lasers emitting around $7\mu\text{m}$ with threshold current densities below $1\text{kA}/\text{cm}^2$ at room temperature*. Applied Physics Letters 106 (4): 041108 (2015). doi:10.1063/1.4907002
- [211] J. T. Getty, E. J. Skogen, L. A. Johansson and L. A. Coldren. *CW operation of $1.55\mu\text{m}$ bipolar cascade laser with record differential efficiency, low threshold, and*

- 50-Ω matching*. IEEE Photonics Technology Letters 15 (11): 1513–1515 (2003). doi:10.1109/LPT.2003.818646
- [212] J. Singleton. *Band Theory and Electronic Properties of Solids*. Oxford Master Series in Condensed Matter Physics. OUP Oxford (2001)
- [213] N. Ashcroft and N. Mermin. *Solid State Physics*. HRW international editions. Holt, Rinehart and Winston (1976)
- [214] H.-S. Lan, S. T. Chang and C. W. Liu. *Semiconductor, topological semimetal, indirect semimetal, and topological Dirac semimetal phases of $\text{Ge}_{1-x}\text{Sn}_x$ alloys*. Phys Rev B 95: 201201 (2017). doi:10.1103/PhysRevB.95.201201
- [215] A. Bauer, K. Rößner, T. Lehnhardt, M. Kamp, S. Höfling, L. Worschech and A. Forchel. *Mid-infrared semiconductor heterostructure lasers for gas sensing applications*. Semiconductor Science and Technology 26 (1): 014032 (2011). doi:10.1088/0268-1242/26/1/014032
- [216] H. Kroemer. *The 6.1 Å family (InAs, GaSb, AlSb) and its heterostructures: a selective review*. Physica E: Low-dimensional Systems and Nanostructures 20 (3-4): 196 – 203 (2004). doi:10.1016/j.physe.2003.08.003
- [217] A. Rogalski, P. Martyniuk and M. Kopytko. *InAs/GaSb type-II superlattice infrared detectors: Future prospect*. Applied Physics Reviews 4 (3): 031304 (2017). doi:10.1063/1.4999077
- [218] P. YU and M. Cardona. *Fundamentals of Semiconductors: Physics and Materials Properties*. Number Bd. 3 in Advanced texts in physics. Springer Berlin Heidelberg (2005)
- [219] Y. Varshni. *Temperature dependence of the energy gap in semiconductors*. Physica 34 (1): 149 – 154 (1967). doi:10.1016/0031-8914(67)90062-6
- [220] A. Chandola, R. Pino and P. S. Dutta. *Below bandgap optical absorption in tellurium-doped GaSb*. Semiconductor Science and Technology 20 (8): 886 (2005). doi:10.1088/0268-1242/20/8/046
- [221] I. Vurgaftman, W. W. Bewley, C. D. Merritt, C. L. Canedy, C. S. Kim, J. Abell, J. R. Meyer and M. Kim. *Physics of interband cascade lasers* (2012). doi:10.1117/12.914577
- [222] S. Bhargava, H.-R. Blank, V. Narayanamurti and H. Kroemer. *Fermi-level pinning position at the Au-InAs interface determined using ballistic electron emission microscopy*. Applied Physics Letters 70 (6): 759–761 (1997). doi:10.1063/1.118271
- [223] Y. Jiang. *High-performance InAs-based interband cascade laser*. Ph.D. thesis, University of Oklahoma (2016)
- [224] R. Weih, A. Bauer, M. Kamp and S. Höfling. *Interband cascade lasers with AlGaAsSb bulk cladding layers*. Opt Mater Express 3 (10): 1624–1631 (2013). doi:10.1364/OME.3.001624

- [225] Z. Tian, R. Q. Yang, T. D. Mishima, M. B. Santos, R. T. Hinkey, M. E. Curtis and M. B. Johnson. *Inas-based interband cascade lasers near 6um*. Electronics Letters 45 (1): 48–49 (2009). doi:10.1049/el:20092779
- [226] Z. Tian, R. Q. Yang, T. D. Mishima, M. B. Santos and M. B. Johnson. *Plasmon-Waveguide Interband Cascade Lasers Near 7.5 μ m*. IEEE Photonics Technology Letters 21 (21): 1588–1590 (2009). doi:10.1109/LPT.2009.2030686
- [227] K. Ohtani and H. Ohno. *An InAs-Based Intersubband Quantum Cascade Laser*. Japanese Journal of Applied Physics 41 (11B): L1279 (2002). doi:10.1143/JJAP.41.L1279
- [228] Z. Tian, L. Li, H. Ye, R. Q. Yang, T. D. Mishima, M. B. Santos and M. B. Johnson. *InAs-based interband cascade lasers with emission wavelength at 10.4 um*. Electronics Letters 48 (2): 113–114 (2012). doi:10.1049/el.2011.3555
- [229] C. L. Canedy, M. V. Warren, C. D. Merritt, W. W. Bewley, C. S. Kim, M. Kim, I. Vurgaftman and J. R. Meyer. *Interband cascade lasers with longer wavelengths* (2017). doi:10.1117/12.2246450
- [230] Z. Tian, Y. Jiang, L. Li, R. T. Hinkey, Z. Yin, R. Q. Yang, T. D. Mishima, M. B. Santos and M. B. Johnson. *InAs-Based Mid-Infrared Interband Cascade Lasers Near 5.3 μ m*. IEEE Journal of Quantum Electronics 48 (7): 915–921 (2012). doi:10.1109/JQE.2012.2195477
- [231] M. Holzbauer, R. Szedlak, H. Detz, R. Weih, S. Höfling, W. Schrenk, J. Koeth and G. Strasser. *Substrate-emitting ring interband cascade lasers*. Applied Physics Letters 111 (17): 171101 (2017). doi:10.1063/1.4989514
- [232] L. Berger. *Semiconductor Materials*. Taylor & Francis (1996)
- [233] L. Piskorski and R. Sarzala. *Material parameters of antimonides and amorphous materials for modelling the mid-infrared lasers* 46: 227–240 (2016). doi:10.5277/oa160207
- [234] http://www.tf.uni-kiel.de/matwis/amat/semi_en/kap_2/backbone/r2_3_1.html
- [235] F. Bouzid and D. L. *Performance evaluation of a GaSb thermophotovoltaic converter*. Revue des Energies Renouvelables 15 (3): 383–397 (2012)
- [236] C. S. Kim, M. Kim, J. Abell, W. W. Bewley, C. D. Merritt, C. L. Canedy, I. Vurgaftman and J. R. Meyer. *Mid-infrared distributed-feedback interband cascade lasers with continuous-wave single-mode emission to 80 °C*. Applied Physics Letters 101 (6): 061104 (2012). doi:10.1063/1.4744445
- [237] C. Borgentun, C. Frez, R. M. Briggs, M. Fradet and S. Forouhar. *Single-mode high-power interband cascade lasers for mid-infrared absorption spectroscopy*. Opt Express 23 (3): 2446–2450 (2015). doi:10.1364/OE.23.002446

- [238] J. Faist, F. Capasso, D. L. Sivco, A. L. Hutchinson, C. Sirtori, S. N. G. Chu and A. Y. Cho. *Quantum cascade laser: Temperature dependence of the performance characteristics and high T_0 operation*. Applied Physics Letters 65 (23): 2901–2903 (1994). doi:10.1063/1.112524
- [239] D. Botez, C.-C. Chang and L. J. Mawst. *Temperature sensitivity of the electro-optical characteristics for mid-infrared ($\lambda = 3 - 16\mu\text{m}$)-emitting quantum cascade lasers*. Journal of Physics D: Applied Physics 49 (4): 043001 (2016). doi:10.1088/0022-3727/49/4/043001
- [240] A. Evans, S. R. Darvish, S. Slivken, J. Nguyen, Y. Bai and M. Razeghi. *Buried heterostructure quantum cascade lasers with high continuous-wave wall plug efficiency*. Applied Physics Letters 91 (7): 071101 (2007). doi:10.1063/1.2770768
- [241] W. W. Bewley, J. A. Nolde, D. C. Larrabee, C. L. Canedy, C. S. Kim, M. Kim, I. Vurgaftman and J. R. Meyer. *Interband cascade laser operating cw to 257K at $\lambda = 3.7\mu\text{m}$* . Applied Physics Letters 89 (16): 161106 (2006). doi:10.1063/1.2363169
- [242] R. Weih, L. Nähle, S. Höfling, J. Koeth and M. Kamp. *Single mode interband cascade lasers based on lateral metal gratings*. Applied Physics Letters 105 (7): 071111 (2014)
- [243] K. Ryczko and G. Sek. *Polarization-independent gain in mid-infrared interband cascade lasers*. AIP Advances 6 (11): 115020 (2016). doi:10.1063/1.4968190
- [244] <http://apps.webofknowledge.com>
- [245] A. Prechtl. *Vorlesungen über Elektrodynamik*. TU Wien (2005)
- [246] S. Chuang. *Physics of Photonic Devices*. Wiley Series in Pure and Applied Optics. Wiley (2012)
- [247] G. Lehner. *Elektromagnetische Feldtheorie: für Ingenieure und Physiker*. Springer-Lehrbuch. Springer Berlin Heidelberg (2013)
- [248] J. Pankove. *Optical Processes in Semiconductors*. Dover books explaining science and mathematics. Dover (1971)
- [249] F. Vasko and A. Kuznetsov. *Electronic States and Optical Transitions in Semiconductor Heterostructures*. Graduate Texts in Contemporary Physics. Springer New York (2012)
- [250] M. R. Lorenz, W. Reuter, W. P. Dumke, R. J. Chicotka, G. D. Pettit and J. M. Woodall. *BAND STRUCTURE AND DIRECT TRANSITION ELECTROLUMINESCENCE IN THE $\text{In}_{1-x}\text{Ga}_x\text{P}$ ALLOYS*. Applied Physics Letters 13 (12): 421–423 (1968). doi:10.1063/1.1652500
- [251] A. H. Kahn. *Theory of the Infrared Absorption of Carriers in Germanium and Silicon*. Phys Rev 97: 1647–1652 (1955). doi:10.1103/PhysRev.97.1647
- [252] M. Levinshtein, S. Rumyantsev, M. Shur and W. Scientific. *Handbook Series*

- on Semiconductor Parameters: Ternary and quaternary III-V compounds.* EBL-Schweitzer. World Scientific Publishing Company (1999)
- [253] C. Pidgeon, C. Ciesla and B. Murdin. *Suppression of non-radiative processes in semiconductor mid-infrared emitters and detectors.* Progress in Quantum Electronics 21 (5): 361 – 419 (1997). doi:10.1016/S0079-6727(97)00012-8
- [254] L. Coldren, S. Corzine and M. Mashanovitch. *Diode Lasers and Photonic Integrated Circuits.* Wiley Series in Microwave and Optical Engineering. Wiley (2012)
- [255] W. Shockley and W. T. Read. *Statistics of the Recombinations of Holes and Electrons.* Phys Rev 87: 835–842 (1952). doi:10.1103/PhysRev.87.835
- [256] R. N. Hall. *Electron-Hole Recombination in Germanium.* Phys Rev 87: 387–387 (1952). doi:10.1103/PhysRev.87.387
- [257] K. S. Gadedjisso-Tossou, S. Belahsene, M. A. Mohou, E. Tournié and Y. Rouillard. *Recombination channels in 2.4-3.2 μm GaInAsSb quantum-well lasers.* Semiconductor Science and Technology 28 (1): 015015 (2013). doi:10.1088/0268-1242/28/1/015015
- [258] T. D. Eales, I. P. Marko, B. A. Ikyo, A. R. Adams, S. Arafin, S. Sprengel, M. C. Amann and S. J. Sweeney. *Wavelength Dependence of Efficiency Limiting Mechanisms in Type-I Mid-Infrared GaInAsSb/GaSb Lasers.* IEEE Journal of Selected Topics in Quantum Electronics 23 (6): 1–9 (2017). doi:10.1109/JSTQE.2017.2687823
- [259] A. Haug. *Auger recombination in direct-gap semiconductors: band-structure effects.* Journal of Physics C: Solid State Physics 16 (21): 4159 (1983)
- [260] R. I. Taylor, R. A. Abram, M. G. Burt and C. Smith. *A detailed study of Auger recombination in 1.3 μm InGaAsP/InP quantum wells and quantum well wires.* Semiconductor Science and Technology 5 (1): 90 (1990). doi:10.1088/0268-1242/5/1/013
- [261] P. Landsberg. *Recombination in Semiconductors.* Cambridge University Press (2003)
- [262] C. H. Grein, M. E. Flatté, J. T. Olesberg, S. A. Anson, L. Zhang and T. F. Boguess. *Auger recombination in narrow-gap semiconductor superlattices incorporating antimony.* Journal of Applied Physics 92 (12): 7311–7316 (2002). doi:10.1063/1.1521255
- [263] W. W. Bewley, J. R. Lindle, C. S. Kim, M. Kim, C. L. Canedy, I. Vurgaftman and J. R. Meyer. *Lifetimes and Auger coefficients in type-II W interband cascade lasers.* Applied Physics Letters 93 (4): 041118 (2008). doi:10.1063/1.2967730

Acknowledgements

On this page I want to thank all the great people that supported and stimulated me during my time as PhD student at the Institute of Solid State Electronics. First of all, I want to thank Gottfried Strasser for his support and guidance. I'm grateful for his fruitful discussions and for enabling me to follow my own ideas. I really enjoyed the discussions with Erich Gornik, Jürgen Smoliner, Dionyz Pogany, Alois Lugstein, Werner Schrenk and Carlo Requiao, which sometimes were completely unrelated to science and brought fresh ideas to my mind.

Furthermore, I want to thank all the people I worked together at the TU Wien: Alexander Alexewicz, Maxwell Andrews, Maximilian Beiser, Martin Brandstetter, Mattia Capriotti, Hermann Detz, Christoph Deutsch, Clement Fleury, Roman Gansch, Andreas Harrer, Johannes David Hillbrand, Hedwig Knötig, Suzanne Lancaster, Anna Lardschneider, Donald MacFarland, Manuel Reichenpfader, Matteo Rigato, Daniela Ristanic, Clemens Schwarzer, Masiar Sistani and Tobias Zederbauer.

A very special thank to my entertaining office members Borislav Hinkov, Benedikt Schwarz and Peter Reininger. I'm still astonished that I could resist becoming a coffee junkie. In addition, I want to thank my collaborators at the Humboldt University Berlin: Ted Masselink and Mykhaylo Semtsiv for providing me overgrown quantum cascade laser samples. Many thanks to the people behind the very fruitful collaboration with the University of Würzburg and nanoplus: Sven Höfling, Johannes Koeth and Robert Weih.

Finally I want to thank my family and Corinna for her patience and support during this, sometimes very demanding, time. I'm sorry for the hours I spent in the cleanroom and the lab instead with you. Thanks for taking care of me not becoming a total nerd. Partially you may have been successful.

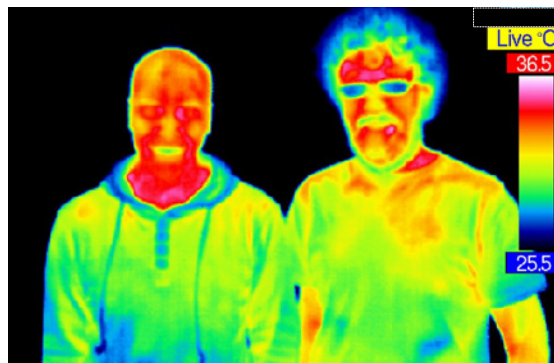


Fig. 1: Infrared image of me (left) and my colleague Clement Fléury (right). While my head is already optimized for surface-emission, Clement's curly hair provides good thermal insulation.

List of Publications

Journal publications

- J1** M. Holzbauer, R. Szedlak, H. Detz, R. Weih, S. Höfling, W. Schrenk, J. Koeth, and G. Strasser, "*Substrate-emitting ring interband cascade lasers*", *Appl. Phys. Lett.* **111**, 171101 (2017), doi:10.1063/1.4989514
- J2** R. Szedlak, J. Hayden, P. Martín-Mateos, M. Holzbauer, A. Harrer, B. Schwarz, B. Hinkov, D. MacFarland, T. Zederbauer, H. Detz, A.M. Andrews, W. Schrenk, P. Acedo, B. Lendl, and G. Strasser, "*Surface emitting ring quantum cascade lasers for chemical sensing*", *Opt. Eng.* **57**(1), 011005 (2017) doi:10.1117/1.OE.57.1.011005
- J3** M. Sistani, P. Staudinger, J. Greil, M. Holzbauer, H. Detz, E. Bertagnolli, and A. Lugstein, "*Room Temperature Quantum Ballistic Transport in Monolithic Ultra-scaled Al-Ge-Al Nanowire Heterostructures*", *Nano Lett.* **17** (8), 4556–4561 (2017) doi:10.1021/acs.nanolett.7b00425
- J4** R. Szedlak, A. Harrer, M. Holzbauer, B. Schwarz, J. Waclawek, D. MacFarland, T. Zederbauer, H. Detz, A.M. Andrews, W. Schrenk, B. Lendl, and G. Strasser, "*Remote sensing with commutable monolithic laser and detector*", *ACS Photonics* **3**, 1794–1798 (2016) doi:10.1021/acsp Photonics.6b00603
- J5** R. Szedlak, M. Holzbauer, P. Reininger, D. MacFarland, T. Zederbauer, H. Detz, A.M. Andrews, W. Schrenk, and G. Strasser, "*Ring quantum cascade lasers with grating phase shifts and a light collimating dielectric metamaterial for enhanced infrared spectroscopy*", *Vib Spectrosc* **84**, 101-105 (2016), doi:10.1016/j.vibspec.2016.03.009
- J6** R. Szedlak, M. Holzbauer, D. MacFarland, T. Zederbauer, H. Detz, A.M. Andrews, C. Schwarzer, W. Schrenk, and G. Strasser, "*The influence of whispering gallery modes on the far field of ring lasers*", *Sci. Rep.* **5**, 16668 (2015), doi:10.1038/srep16668
- J7** M. Holzbauer, P. Klang, H. Detz, A.M. Andrews, G. Strasser, P. Bakshi, and E. Gornik, "*Resonant intersubband plasmon induced current in InGaAs quantum wells on GaAs*", *Appl. Phys. Lett.* **104**, 122101 (2014), doi:10.1063/1.4869757

Oral presentations

- O1** M. Holzbauer, B. Hinkov, R. Szedlak, H. Detz, R. Weih, S. Höfling, W. Schrenk, E. Gornik, J. Koeth, and G. Strasser, "Ring Interband Cascade Lasers", CLEO 2018, San Jose, USA, May 13 - 18, 2018
- O2** M. Holzbauer, R. Weih, S. Höfling, W. Schrenk, J. Koeth, E. Gornik, and G. Strasser, "Interband cascade ring lasers", 2nd Int. Symp on Magnetic Excitations in Semiconductors, Buffalo, USA, Jul 13 - 15, 2018
- O3** R. Szedlak, A. Harrer, B. Schwarz, M. Holzbauer, J. P. Waclawek, D. MacFarland, T. Zederbauer, H. Detz, A. M. Andrews, W. Schrenk, B. Lendl, and G. Strasser: "*On-Chip Quantum Cascade Laser/Detector System for Remote Gas Sensing*", SCIX2017, Reno, USA, Oct 8 - 13, 2017
- O4** M. Holzbauer, B. Hinkov, R. Szedlak, H. Detz, R. Weih, S. Höfling, W. Schrenk, E. Gornik, J. Koeth, and G. Strasser: "*Ring cavity interband cascade lasers*", ITQW14, Singapore, Sep 10 - 15, 2017
- O5** R. Szedlak, A. Harrer, B. Schwarz, M. Holzbauer, J.P. Waclawek, E. Tütüncü, V. Kokoric, J. Hayden, D. Macfarland, T. Zederbauer, H. Detz, A.M. Andrews, W. Schrenk, B. Mizaikoff, B. Lendl, and G. Strasser: "*Commutable Monolithic QC Laser/Detector System for Remote Sensing*", ITQW14, Singapore, Sep 10 - 15, 2017
- O6** B. Hinkov, B. Schwarz, R. Szedlak, M. Holzbauer, A. Harrer, H. Detz, A. M. Andrews, and G. Strasser: "*Mid-infrared Quantum Cascade Lasers for spectroscopic applications*", Annual Meeting of the Austrian & Swiss Phys. Soc., Genf, Switzerland, Aug 21 - 25, 2017
- O7** M. Holzbauer, R. Szedlak, H. Detz, R. Weih, S. Höfling, W. Schrenk, J. Koeth, and G. Strasser: "*Substrate-emitting ring interband cascade lasers*", CLEO Europe, Munich, Jun 25 - 29, 2017
- O8** R. Szedlak, A. Harrer, B. Schwarz, M. Holzbauer, J. P. Waclawek, H. Moser, D. MacFarland, T. Zederbauer, H. Detz, A. M. Andrews, W. Schrenk, B. Lendl, and G. Strasser: "*Photonic Gas Sensing with Commutable Laser and Detector on the same Chip*", ICAVS 9, Victoria (BC), Canada., Jun 11 - 16, 2017
- O9** R. Szedlak, A. Harrer, B. Schwarz, M. Holzbauer, J.P. Waclawek, D. MacFarland, T. Zederbauer, H. Detz, A.M. Andrews, W. Schrenk, B. Lendl, and G. Strasser: "*Remote Gas Sensing with Quantum Cascade Systems*", Nano and Photonics, Mauterndorf, Austria, Mar 22 - 25, 2017 (invited)
- O10** A. Harrer, B. Schwarz, R. Szedlak, M. Holzbauer, D. Ristanic, H. Detz, D. MacFarland, T. Zederbauer, A.M. Andrews, W. Schrenk, and G. Strasser: "*Quantum cascade structures for sensing applications*", Daylight Solutions Seminar, San Diego, USA, Feb 10, 2017
- O11** R. Szedlak, A. Harrer, M. Holzbauer, B. Schwarz, J. P. Waclawek, H. Moser, D.

- MacFarland, T. Zederbauer, H. Detz, A. M. Andrews, W. Schrenk, B. Lendl, and G. Strasser: *"Compact mid-IR sensors based on bi-functional and commutable semiconductor lasers and detectors on the same chip"*, 3rd International WORKshop on Infrared Technologies, Olching, Germany, Nov 7 - 8, 2016 (invited)
- O12** M. Holzbauer, R. Szedlak, D. MacFarland, T. Zederbauer, H. Detz, A.M. Andrews, W. Schrenk, and G. Strasser: *"Sub-threshold measurements of the whispering gallery modes in ring quantum cascade lasers"*, 66th Yearly Meeting of the Austrian Physical Society, Vienna, Austria, Sep 27 - 29, 2016
- O13** R. Szedlak, A. Harrer, B. Schwarz, M. Holzbauer, J. P. Waclawek, D. MacFarland, T. Zederbauer, H. Detz, A. M. Andrews, W. Schrenk, B. Lendl, and G. Strasser: *"Remote gas sensing with commutable quantum cascade laser and detector on the same chip"*, IQCLSW, Cambridge, United Kingdom, Sep 04 - 09, 2016 (invited)
- O14** R. Szedlak, A. Harrer, M. Holzbauer, B. Schwarz, D. MacFarland, T. Zederbauer, H. Detz, A. M. Andrews, W. Schrenk, and G. Strasser: *"Mid-infrared ring lasers for sensing applications"*, 7th EPS-QEOD Europhoton Conference (EUROPHOTON 2016), Vienna, Austria, Aug 21 - 26, 2016
- O15** M. Holzbauer, R. Szedlak, D. MacFarland, T. Zederbauer, H. Detz, A.M. Andrews, W. Schrenk, and G. Strasser: *"Ring quantum cascade lasers with metal-covered distributed feedback gratings"*, ICPS, Beijing, China, Jul 31 - Aug 5, 2016
- O16** A. Harrer, R. Szedlak, B. Schwarz, M. Holzbauer, T. Zederbauer, H. Detz, A. M. Andrews, D. MacFarland, W. Schrenk, H. Moser, J. P. Waclawek, B. Lendl, and G. Strasser: *"Mid-infrared bi-functional quantum cascade sensor for long interaction regions"*, nanoFIS, Graz, Austria, Jun 27 - 29, 2016.
- O17** M. Holzbauer, R. Szedlak, D. MacFarland, T. Zederbauer, H. Detz, A.M. Andrews, W. Schrenk, M.P. Semtsiv, W.T. Masselink, and G. Strasser: *"Ring quantum cascade lasers for chemical sensing and spectroscopic applications"*, VIENNA young SCIENTISTS SYMPOSIUM VSS 2016, Vienna, Austria, Jun 9 - 10, 2016
- O18** R. Szedlak, A. Harrer, B. Schwarz, M. Holzbauer, H. Moser, D. MacFarland, T. Zederbauer, H. Detz, A. M. Andrews, W. Schrenk, B. Lendl, and G. Strasser: *"Highly Integrated Gas Sensors based on Bi-functional Quantum Cascade Structures"*, CLEO 2016, San Jose, USA, Jun 5 - 10, 2016
- O19** R. Szedlak, T. Hirsch, M. Holzbauer, D. MacFarland, T. Zederbauer, H. Detz, A.M. Andrews, W. Schrenk, S. Rotter, and G. Strasser: *"On-chip Generation of Infrared Orbital Angular Momentum Beams using a Dielectric Metamaterial"*, CLEO 2016, San Jose, USA, Jun 5 - 10, 2016
- O20** A. Harrer, B. Schwarz, R. Szedlak, M. Holzbauer, T. Zederbauer, H. Detz, A.M. Andrews, D. MacFarland, W. Schrenk, H. Moser, J.P. Waclawek, B. Lendl, and G. Strasser: *"Mid-infrared sensing based on quantum cascade structures"*, Next-Lite Workshop, Vienna, Austria, May 3 - 4, 2015
- O21** M. Holzbauer, R. Szedlak, D. MacFarland, T. Zederbauer, H. Detz, A.M. Andrews,

- W. Schrenk, and G. Strasser: *"Thermal optimization of ring quantum cascade lasers"*, Annual Meeting of the Austrian & Swiss Phys. Soc., Vienna, Austria, Sep 1 – 4, 2015
- O22** R. Szedlak, M. Holzbauer, D. MacFarland, T. Zederbauer, H. Detz, A.M. Andrews, W. Schrenk, and G. Strasser: *"Using the far field of ring lasers to characterize their whispering gallery modes"*, Annual Meeting of the Austrian & Swiss Phys. Soc., Vienna, Austria, Sep 1 – 4, 2015
- O23** R. Szedlak, M. Holzbauer, D. MacFarland, T. Zederbauer, H. Detz, A.M. Andrews, W. Schrenk, and G. Strasser: *"Ring quantum cascade lasers for infrared spectroscopy"*, 8th Int. Conf. on Advanced Vibrational Spectroscopy ICAVS8, Vienna, Austria, Jul 12 – 17, 2015
- O24** A. Harrer, R. Szedlak, M. Holzbauer, B. Schwarz, H. Moser, E. Mujagic, D. MacFarland, T. Zederbauer, H. Detz, A. M. Andrews, W. Schrenk, B. Lendl, and G. Strasser: *"Monolithic integrated on-chip sensing utilizing plasmonics"*, 1st Next-Lite Workshop, Hirschwang, Austria, Jun 18 - 19, 2015
- O25** R. Szedlak, M. Holzbauer, D. MacFarland, T. Zederbauer, H. Detz, A. M. Andrews, W. Schrenk, and G. Strasser: *"Probing whispering gallery modes in ring lasers"*, 1st Next-Lite Workshop, Hirschwang an der Rax, Austria, Jun 18 - 19, 2015
- O26** R. Szedlak, A. Harrer, M. Holzbauer, B. Schwarz, H. Moser, E. Mujagic, C. Deutsch, D. MacFarland, T. Zederbauer, H. Detz, A. M. Andrews, W. Schrenk, K. Unterrainer, B. Lendl, and G. Strasser: *"Infrared and terahertz spectroscopy with ring quantum cascade lasers"*, German THz Conference, Dresden, Germany, Jun 8 - 10, 2015
- O27** M. Holzbauer, R. Szedlak, D. MacFarland, T. Zederbauer, H. Detz, A. M. Andrews, W. Schrenk, and G. Strasser: *"Light extraction from ring quantum cascade lasers"*, Nanoforum 2015, Linz, Austria, Jun 8 - 9, 2015 (invited)
- O28** M. Holzbauer, R. Szedlak, C. Schwarzer, D. MacFarland, T. Zederbauer, H. Detz, A. M. Andrews, W. Schrenk, and G. Strasser: *"Mid-infrared Ring Cavities"*, 4th Int. Nanophotonics Meeting, Igls, Austria, Oct 23 – 25, 2014
- O29** M. Holzbauer, P. Klang, H. Detz, A.M. Maxwell, W. Schrenk, G. Strasser, P. Bakshi, and E. Gornik: *"Intersubband plasmon coupling enhanced current transport"*, 32nd ICPS, Austin (TX), USA, Aug 10 – 15, 2014

Poster presentations

- P1** H. Knötig, M. Holzbauer, R. Szedlak, H. Detz, R. Weih, S. Höfling, W. Schrenk, J. Koeth, and G. Strasser: *"Ring interband cascade lasers for spectroscopic applications"*, 20th International Winterschool on New Developments in Solid State Physics, Mauterndorf, Austria, Feb 25 - Mar 03, 2018

-
- P2** M. Holzbauer, R. Szedlak, H. Detz, R. Weih, S. Höfling, W. Schrenk, J. Koeth, and G. Strasser: *"The polarization of ring interband cascade lasers"*, Austrian MBE Workshop 2017, Vienna, Austria, Sep 28 - 29, 2017
- P3** R. Szedlak, M. Holzbauer, B. Schwarz, D. MacFarland, T. Zederbauer, H. Detz, A. M. Andrews, W. Schrenk, and G. Strasser: *"Ring Quantum Cascade Lasers: Versatile Light Emission and Applications in Spectroscopic Sensing"*, Austrian MBE Workshop 2017, Vienna, Austria, Sep 28 - 29, 2017
- P4** M. Beiser, B. Schwarz, M. Holzbauer, H. Detz, A. M. Andrews, and G. Strasser: *"Bi-functional Quantum Cascade Detectors/Lasers"*, Austrian MBE Workshop 2017, Vienna, Austria, Sep 28 - 29, 2017
- P5** M. Holzbauer, R. Szedlak, D. MacFarland, T. Zederbauer, H. Detz, A.M. Andrews, W. Schrenk, and G. Strasser: *"Substrate-emitting ring quantum cascade laser array with distributed feedback metal gratings"*, IQCLSW 2016, Cambridge, UK, Sep 4 - 9, 2016
- P6** R. Szedlak, A. Harrer, M. Holzbauer, B. Schwarz, J.P. Waclawek, D. MacFarland, T. Zederbauer, H. Detz, A. M. Andrews, W. Schrenk, B. Lendl, and G. Strasser: *"Laser Surface Emission and Detection from the same Quantum Cascade Element"*, ICPS, Beijing, China, Jul 31 - Aug 5, 2016
- P7** R. Szedlak, T. Hisch, M. Holzbauer, D. MacFarland, T. Zederbauer, H. Detz, A. M. Andrews, W. Schrenk, S. Rotter, and G. Strasser: *"Creation of Orbital Angular Momentum using an On-chip Dielectric Metamaterial for Beam Shaping"*, ICPS, Beijing, China, Jul 31 - Aug 5, 2016
- P8** R. Szedlak, A. Harrer, M. Holzbauer, B. Schwarz, J.P. Waclawek, D. MacFarland, T. Zederbauer, H. Detz, A.M. Andrews, W. Schrenk, B. Lendl, and G. Strasser: *"Gas sensing with bi-functional ring resonators as laser and detector"*, Microelectronic Systems Symposium MESS16, Vienna, Austria, Apr 28 - 29, 2016
- P9** R. Szedlak, M. Holzbauer, D. MacFarland, T. Zederbauer, H. Detz, A.M. Andrews, W. Schrenk, and G. Strasser: *"How whispering gallery modes can influence the far field of ring lasers"*, ITQW, Vienna, Austria, Sep 6 - 11, 2015
- P10** M. Holzbauer, R. Szedlak, D. MacFarland, T. Zederbauer, H. Detz, A.M. Andrews, W. Schrenk, and G. Strasser: *"Thermal management in ring quantum cascade lasers"*, ITQW, Vienna, Austria, Sep 6 - 11, 2015
- P11** M. Holzbauer, R. Szedlak, D. MacFarland, T. Zederbauer, H. Detz, A. M. Andrews, W. Schrenk, M. Semtsiv, W. Masselink, and G. Strasser: *"Towards continuous wave operation of ring cavity quantum cascade lasers"*, 7th EPS-QEOD Europhoton Conference (EUROPHOTON 2016), Vienna, Austria, Aug 21 - 26, 2016
- P12** M. Holzbauer, R. Szedlak, D. MacFarland, T. Zederbauer, H. Detz, A.M. Andrews, W. Schrenk, and G. Strasser: *"High performance ring quantum cascade laser for sensing applications"*, 8th Int. Conf. on Advanced Vibrational Spectroscopy ICAVS8, Vienna, Austria, Jul 12 - 17, 2015

- P13** R. Szedlak, C. Schwarzer, M. Holzbauer, T. Zederbauer, H. Detz, A. M. Andrews, W. Schrenk, and G. Strasser: "*Polarization and Far Field Modifications of Ring Lasers*", Infrared & Raman Discussion Group Spring Meeting, Vienna, Austria, Apr 24 – 25, 2014
- P14** M. Holzbauer, P. Klang, H. Detz, A.M. Andrews, P. Bakshi, G. Strasser, and E. Gornik: "*Resonant Intersubband Plasmon Enhanced Current Transport*", 18th Int. Winterschool on New Developments in Solid State Physics, Mauterndorf, Austria, Feb 23 - 28, 2014

Curriculum Vitae

Personal Data

Name	Martin Holzbauer
Date of Birth	29.09.1987
Place of Birth	Wr. Neustadt, Austria
Nationality	Austrian

Education

Since Sept 2012	PhD candidate in Electrical Engineering TU Wien, Vienna, Austria, Supervisors: Prof. Gottfried Strasser and Prof. Erich Gornik
2012 – 2012	MSc in Microelectronics TU Wien, Vienna, Austria Diploma thesis: "Coherent THz-Emission from Current-Driven Plasma Instabilities" Supervisor: Prof. Erich Gornik, Institute of Solid State Electronics
2006 – 2012	BSc in Electrical Engineering, TU Wien, Vienna, Austria
2001 – 2006	Matura Secondary technical high school for Electrical Engineering, HTBLuVA Wr. Neustadt, Austria